STRONGLY COUPLED LIGHT-MATTER PHENOMENA INVESTIGATED WITH ALGORITHMIC AND FORMALISTIC DENSITY FUNCTIONAL COUPLING SCHEMES

By

Justin Michael Malave

Dissertation

Submitted to the Faculty of the

Graduate School of Vanderbilt University

in partial fulfillment of the requirements

for the degree of

DOCTOR OF PHILOSOPHY

in

Physics

August, 2023

Nashville, Tennessee

Approved:

Kálmán Varga, Ph.D.

Sharon Weiss, Ph.D.

Momchil Velkovsky, Ph.D.

Sait Umar, Ph.D.

Richard Haglund, Ph.D.

To my parents and grandparents

ACKNOWLEDGMENTS

Constituting the core of this text are three publications: “Coupled Maxwell and time-dependent orbital-free density functional calculations” by Cody Covington, me, and Kálmán Varga, published in *Physical Review B*; “Harmonically confined N-electron systems coupled to light in a cavity” by me, Yetmgeta S. Aklilu, Matthew Beutel, Chenhang Huang, and Kálmán Varga, also published in *Physical Review B*; and “Real-space, real-time approach to quantum-electrodynamical time-dependent density functional theory” by mw, Alexander Ahrens, Daniel Pitagora, Cody Covington, and Kálmán Varga, published in *The Journal of Chemical Physics*. The latter two publications were supported by the National Science Foundation (NSF) under Grant No. IRES 1826917

Good research cannot be done in isolation. I thank members of the administration of the Vanderbilt University Department of Physics and Astronomy for their support over the years: Alyce Dobyns; Ashley Brammer; Libby Johnson; Peggy Lucas-McGowan; Alisha McCord; and Don Pickert. I also extend my gratitude to the faculties and staffs of: Sarah Shannon Stevenson Science and Engineering Library; Jean and Alexander Heard Library; the Vanderbilt Institute of Nanoscale Science and Engineering; and the Adventure Science Center.

It is with deep appreciation do I recognize the many scientists, both at Vanderbilt and elsewhere, I met along the way who helped me realize my project, build up my confidence, and return to my scientific skeptical roots: Atsushi Yamada and Kazuhiro Yabana for their hospitality and perspicuous publications; Thibault Derrien; Davis Welakuh; Paul Corkum; Sokrates Pantelides for his inspiring meticulousness; Sourish Dutta; Alfredo Gurrola; Shane Hutson; Thomas Kephart; Andreas Berlind; Jorge Salas; Savanna Rae Starko; Norman Tolk; Julia Velkovska; David Ernst for his guidance, honesty, and wisdom; Brenda Fabela Enriquez for the discussions and reflections; Vicki Greene; Bao Deliang; Hongbo Du; Xin Jin; Andrew O’Hara; Joseph Hamilton, especially for his taste in office decor; Richard Haglund for his shrewd observations and infectious enthusiasm for physics history; Momchil Velkovsky for helping me with pretty much every core subject of physics; Sait Umar for the pep and notes; Sharon Weiss for accepting the vacant position on my committee and elevating its experimental representation. I credit Daniel Kidd for making my move to Tennessee quick and easy. I single out Cody Covington for being there for me since day one, helping me along by answering my questions, grounding me with reality checks, and checking on my progress in his big brotherly way. And I extol my advisor Kálmán Varga for his insight, guidance, and a manifold of things I aspire to emulate as I mature as a researcher: his no-nonsense and forthright style of advising; his “killer instinct” for research projects; his scientific humility, which helped me harness my passion for scientific skepticism; his hands-on “in the trenches” approach to research; his empathy-based leadership style; and perhaps most of all, his patience. Thank you for not giving up on me.

This work would not have been possible without the immeasurable support of my friends. In Ohio: Gary, Luis, and Marissa Nogueras; Samuel and Shelby Gallagher; Julian and Rhi Gonzales; Vincent Longo; Chris Farrell; Russell Thorpe; Joey Cook; David Shinn; Matt, Rebecca, and Dominic Worcester; Mauren Schindler; Nicholas Hammond; Robert Hood and Doug Soltesz; Brent Strunk, Melissa Dennison, and Aaron Montgomery for helping me realize I had the chops; Russell Bartels; Gary Kader; Peter Hoekje; Meridith Witt; Edwin Meyer; Daniel Tonn; Kaylee Yuhas; and Liya Wang for nominating me for the Honors Program at Baldwin Wallace University, the opportunities of which revitalized my dormant feeling for the sciences. Luke Szumyckyj and Dan Jesensky. In Tennessee: Aaron and Nate for the fun; Kyle Hawkins; Michael Reynolds and Michael Padgett; Matthew Murrow; Noah Austin; Adam Cummings; David Curie; Kayla Johnson; and all my students over the years; Jethro Gaglione; Brandon Blankenship. All of the roommates I have had in graduate school: Dale Julson; Christian Ornelas and Elena Kovalik for the years of emotional and intellectual support; Luis Bichon for the many, many, many late nights and laughs; and Maria Lubag for the squatting. My friends in graduate school elsewhere: Paul Peters for “bringing me home” whenever we talked; Sarah Shapley for the encouragement, advice, and generosity; Michael Jeswald for the progressive rock; and Lauren Kasper for insightful lunch hours. My family: My mother and father who, time and time again, would take me to multiple bookstores in one day; my step-mother and step-father; all my sisters and brothers, especially Jessica and Christina. Brian and Cody; my dear niece Lucy; all of my cousins, aunts, and uncles, in Ohio, Pennsylvania, New Jersey, North Carolina, and Puerto Rico; my grandparents; Reese, Roxy, and Jolyne; Johnny Cash and the spunky Dorothy Joan.

And Tessa – thank you for everything.

You can normalize. Don't it make you feel alive?

- LCD Soundsystem, "Get Innocuous"

John Wilmot penned his poetry riddled with the pox
Nabokov wrote on index cards, at a lectern, in his socks
St. John of the Cross did his best stuff imprisoned in a box
And Johnny Thunders was half alive when he wrote Chinese Rocks

- Nick Cave & The Bad Seeds, "There She Goes My Beautiful World"

TABLE OF CONTENTS

LIST OF TABLES

LIST OF FIGURES

CHAPTER 1

Introduction

1.1 Some Thoughts

In the first chapter of the second edition of his popular monograph *Computational Electrodynamics* [2], Allen Taflove reservedly declares that the societal relevance of Maxwell's equations during World War II and the Cold War-era was in bolstering military might. Radar technology epitomized the applications of the theory, and in discussing its pressing demand during wartime, Taflove effectively outlines the table of contents in the canonical *Classical Electrodynamics*, by John David Jackson [3]. "Radar encompasses a wide range of needs in solving Maxwell's equations," Taflove writes. "At the radar site, microwave sources, circuits, wave guides, and antennas must be designed to generate, transport, radiate, receive, and process electromagnetic waves." Taflove goes on to discuss the penetration depth and armament of devices in context of nuclear bomb detonations above Earth's atmosphere. As the end of the Cold War heralded a minima in nuclear anxiety, there occurred a paradigm shift in the application of Maxwell's equations. Military applications did not become passé, but in anti-correlation with the number of minutes until midnight, and in correlation with computing performance, electrodynamics quickly became the bread and butter of commercial electrical engineering. The concurrent evolution of the computer made this inevitable: the unprecedented technological developments defining the twentieth century gave electrodynamics a platform on which it could thrive, and in contributing to computing and communication technology research, computational electrodynamics perpetuates the social relevance of Maxwell's equations. Solid-state physics delivered, so it delivered.

In 1972, Morris Brodwin held a graduate seminar, at Northwestern University, on bioelectromagnetic hazards. For an independent study associated with the seminar, Taflove conducted research on modeling ultra-high frequency and microwave penetration into the human eye. The motivation for this research was to understand the cause of the cataracts many radar technicians during World War II developed – presumably due to their repeated exposure to microwave radiation. Taflove sought to understand this process, requiring the solution of Maxwell's equations in biological matter, "three-dimensional biological tissue geometry represented by the eye, its surrounding muscle and fat tissues, and its embedding within the bony orbital of the skull." Generic, Helmholtz equation-friendly shapes fell short of modeling the tissue, and the geometry, according to Taflove, required the solution of approximately 100,000 field unknowns. A breakthrough occurred as Taflove scoured issues of *IEEE Transactions on Antennas and Propagation*, during which he found Kane Yee's 1966 paper, "Numerical Solution of Initial Boundary Value Problems Involving Maxwell's Equations in

Isotropic Media" [4]. With this paper as the key player to Taflove's work, he would go on to author two publications in *IEEE Transactions on Microwave Theory and Techniques*, elevating Yee's "forward-difference, time-domain" technique just high enough above the water line to catch the attention of some industry scientists and electromagnetic pulse researchers in the government [5, 6, 7]. A decade later, it would call many labs home, proving useful to materials scientists, electrical engineers, and physicists.

Before computing power swelled, physicists and electrical engineers had to get cozy with Bessel functions, Legendre polynomials, Green's functions, convergence tests, spherical harmonics, differential equations for surface harmonics, boundary value problems, and had to know how to solve Maxwell's equations by, paraphrasing Sait Umar at Vanderbilt University, breaking one's nose on Jackson. These days, students are wont to keep these tools at arm's length, a privilege begotten by processing power, terabyte hard drives, and the Internet. Written almost like a precaution, William R. Smythe's *Static and Dynamic Electricity* [8], written to weld together advanced electromagnetic theory with its application to experiment, as put by a contributor to a textbook list maintained by John C. Baez at the University of California, Riverside, is for "extreme masochists," containing "some of the most hair-raising [electromagnetism] problems you'll ever see," a dire warning for those who have taken a class that works out of Jackson's textbook. Smythe ostensibly sought to make research problems more tractable on paper, to discourage time-consuming first-principles approaches and questionable solutions resembling a pastiche and patchwork of archetypal textbook systems. Necessity is the mother of invention – working within the limits of contemporary mechanical calculators, not capable of taking the general form of Maxwell's equations as input, only pen, paper, wit, and resolve could put the equations to use, thus necessitating intense training regiments in the fastidious, scorched-Earth Smythe style. Of course, the mother of invention would appreciate advancements in computing. About a century later, the state of applied computational electrodynamics is leaps and bounds from the world Smythe's textbook served (though it is still an excellent textbook). This state would not exist without advancements in solid-state physics – advancements that would improve our calculators, save energy, save space, and release the bats of imagination.

Vacuum tubes were the defining anatomy of first-generation computers. Lattices of bulbous logical elements like markers of Space Age pulp fiction, they generated a prohibitive amount of heat and were easy to break. Worse, to make a powerful computer, one needed a lot of vacuum tubes – and a lot of room to store them. Such technology and real estate could only be afforded by big companies and universities, like IBM and Cambridge. Such machines were not fit for applying Maxwell's equations to complicated material systems. The community would need faster, preferably smaller devices as those made possible by transistors. The birth year of the transistor marked the beginning of a monotonic dive in computer size and an increase in speed: from vacuum tubes to transistor-based computers to integrated circuit-based computers to microprocessor-

based computers. In tandem, what problems computational physics could address swelled in lockstep with the ambition of theorists ready-set to seize algorithmic firepower. The gold rush of computational physics had begun. Taflove, again:

> ...the modeling of electromagnetic engineering systems was primarily implemented using solution techniques for the sinusoidal steady-state Maxwell's equations. Before about 1960, the principal approaches in this area involved closed-form and infinite-series analytical solutions, with numerical results from these analyses obtained using mechanical calculators. After 1960, the increasing availability of programmable electronic digital computers permitted such...approaches to rise markedly in sophistication. Researchers were able to take advantage of the capabilities afforded by powerful new high-level programming languages such as Fortran, rapid random-access storage of large arrays of numbers, and computational speeds of orders of magnitude faster than possible with mechanical calculators.

Unlike electromagnetism, the mathematical complexity of quantum mechanics seemed to depend on a future in which numerical techniques were capital, credit due to the mutual age of the disciplines and the fact that the material properties of large systems could be understood using classical physics. Graduate students of physics have heard it before: the hydrogen atom is the only physical system we can solve analytically using the Schrödinger equation. Larger atoms, never mind molecules, require something else. Even the Born-Oppenheimer approximation cannot shake an analytical solution out of these heavier structures. Yet, neither Smythe nor Jackson have cousins in the library of quantum mechanics, nothing in the pedagogical quantum canon raising a fist at a possible future without computers. Messiah, Schiff, Dirac, Sakurai, Shankar, and many others go without the technical and encyclopedic aura of Goldstein, for classical mechanics, and Jackson, for classical electrodynamics. (I cannot say the same for statistical physics, perhaps due to the dual-custody quantum mechanics and classical mechanics have over it.) In anecdote, it seems that no quantum mechanics textbook has enjoyed enough use to get its own colloquialism in the physics community. *Classical Mechanics* by Herbert Goldstein goes by Goldstein [9]. Jackson's textbook is either Jackson-red (the second edition) or Jackson-blue (the third edition). The Wikipedia page for "Principles of Optics" [10] by Max Born and Emil Wolf notes that the book is colloquially known as "Born and Wolf," as did an optical engineer, during an interview I had with Peak Nano, a capacitor and optics research company in Valley View, Ohio. With quantum mechanics maturing concurrently with computing power, perhaps a text discussing quantum theory in biblical detail was not needed. Many-body theory taken to its logical, human endpoint – reduced to quadrature or some complicated differential equation – would do because, not without growing pains, the computers could take it from there (See below and chapter 2).

The classical aspects of solid-state theory excepted, in brief, quantum chemistry and solid-state physics require sophisticated numerical techniques to solve for their wave equations. Historically, the most popular *wave function* method for solving the many-body problems of these disciplines is the Hartree-Fock approach [11, 12, 13, 14, 15]. Using the Hartree approximation, an assumption which strips electrons of their spin and fermionic character and describes the many-body wave function as a product of many single-particle wave functions, as a springboard, the Hartree-Fock method organizes the single-particle wave functions into a Slater determinant [16]. This determinant imposes the anti-symmetry affect of the Pauli exclusion principle. Less hard on computers is density functional theory, an exact approach based on the electron density, which mediates a *massive* reduction in the parameter space (see Chapter 2). In truncating this parameter space, the Hamiltonian loses resolving power, requiring fixer terms not known exactly. With physical insight, however, the approach can be shaped up to serve as an excellent approximation for many-body behavior.

In this thesis, density functional theory is used in every problem, and save for one case, it is featured in its time-dependent form. In *Time-Dependent Density-Functional Theory* by Carsten A. Ullrich [17], he defines three "typical, generic scenarios" in which time-dependent density functional theory would be useful: the dynamical response of a system perturbed from its ground state; the evolution of a nonequilibrium state; and the obtainment of excited state properties. This thesis concerns, in part, many-electron systems electrically zapped into an excited state. Note, however, that the Hamiltonian of time-dependent density functional theory is just a complicated Schrödinger equation. There's nothing about it that changes the relationship between Hamiltonians and perturbations from classically-treated sources. In principle, the character of an electric field can be included in the equation either in an external potential or the momentum – and that *external*-ness means that the source of the electric field comes from outside the system of interest. Yes, the *longitudinal* Coulomb interaction is there, but the incoming field is always *transverse* in structure. What's more is that the form of this external field doesn't deviate from its pre-programmed structure. That is, the oscillating electrons have no impact on its form at all.

This mirrors a situation in electrodynamics. There was no mention in the coverage of computational electrodynamics about a need to go beyond using basic expressions of permittivity and permeability to represent a material. Why complicate the problem of calculating material parameters in some electrodynamics simulation by involving quantum mechanics? If a material loses electrons somehow – either to an adjacent system or the continuum – for the sake of accuracy, it would do well for the material parameters to account for this. The fine structure is being changed, somehow, and the speed of light in the material is too. The nature of the damping forces would change. The nature of the system would change, and in the limit of nanoscale systems, this can have a noticeable impact on thet total material character.

This is telling us something about the degrees of separation between quantum matter and optical research.

The quest to understand matter, whether classically or quantum mechanically, benefited from computation just as much as it benefited electrodynamics. Solid-state physics research gave scientists powerful simulation tools. However – and perhaps for the better – with the exception of quantum electrodynamics, nothing in the great epiphanies of physics more than half a century ago demanded matter and light be dyadically studied, and not even the applications of quantum electrodynamics possessed built-in visions of reaching beyond quantum-scale systems. Like business partners going their separate ways, solid-state physics and optical physics, both in and out of computational garb, would grow independently, with overlapping concepts being deployed to make statements about either one or the other, rarely both.

In his dissertation, "Fully Coupled Maxwell-Kohn-Sham Systems," [18] René Jestädt writes, "One common way to describe the interaction of electromagnetic fields with matter relies on the reduction of the considered degrees of freedom. The choices for what is considered relevant depends on the aspects of interest. Historically as a consequence of this, the description of light-matter interactions has developed into different subfields." He goes on to write,

> In quantum chemistry and solid-state physics, the electromagnetic field is typically treated as as [sic] given environment that determines material science and a focus is on a detailed description of matter. On the other hand in quantum optics, certain matter properties are prescribed and a focus is placed on the electromagnetic fields. In this context, it becomes clear, that the theoretical methodology of considering the two topics depends on the corresponding subfield.

The Hamiltonian of an electron in an electric field, either in length or velocity gauge, is, in the end, an operator of a *quantum* eigenvalue equation, ultimately a support beam for the wave function. Likewise, solutions to Maxwell's equation, whether for biological tissue or some other complicated geometry, are informed of material properties through relative permittivity and permeability values, defined at every point on the Yee lattice for forward-difference time-domain approaches. The "coupling" of light and matter in this manner is extremely useful, and both the material sciences and optical sciences have enjoyed great success in carrying on in this way. Advancements in nanoscale engineering and nano-optics mutually glide along the theoretical interface separating material and optical disciplines. The industrial, semiconductor explosion initiated by the transistor laid down the bones of destiny: per decades of engineering cleverness, solid-state physics and electrodynamics would meet, once more with feeling, on the grounds the latter found so fertile.

Breaching the nanoscale regime in both material elements and gap sizes, the concerns of scientists and engineers are complicated by quantum effects. Interfaces spatially extended or otherwise, provided they are sufficiently small, permit gap tunneling, which can change the relative permittivity of both the gap and the interfacial material elements. Boundary quantum effects also impact the frequency and coherence of electron

oscillations. Nanoparticle geometry and the passage of mobile electron density packets may also affect field enhancement. Theoretically, the physics of the density is adequately described using time-dependent density functional theory. The outgoing radiation associated with the altered electron oscillations may be understood using the electron current. Even optical physics like high-harmonic generation may be described using solutions of a many-body, time-dependent current [17]. Well and good, but computational electrodynamics methods are not, by their nature, informed of these small-scale changes. If the size of the system is on the nanoscale – with non-negligible fluctuations in the relative material parameters, field enhancement effects, and more – one can expect the transmitted light to be impacted somehow.

Likewise, the more "intimate" discipline of quantum optics takes charge of a domain including the limit of a few photons. Here, one needs to go beyond semi-classical descriptions of the light and matter dynamics – but, to just understand the impact of the photons, one need not consider the granular, quantum structure of atoms to get at pressing questions. It is also worth mentioning that, despite the decades-old study of quantum electronics, semi-classical theories are usually enough. "Semi-classical theories are adequate for most purposes," says Mark Fox in his *Quantum Optics* [19]. "For example, when the theory of absorption of light by atoms is first considered, it is usual to apply quantum mechanics to the atoms, but treat the light as a classical electromagnetic wave. The question that we really have to ask to define the subject of quantum optics is whether there are any effects that cannot be explained in the semi-classical approach. It may come as a surprise to the reader that there are relatively few such phenomena." Semi-classical theories using a traditional light-matter coupling arrangement being enough for many light-matter problems, the loss of coupling information was just perceived as the cost of doing business. A subdiscipline that could include the full coupling character between electron and photons didn't need to be built up to account for anything but simplistic atomic systems.

The preface of *Optical Resonance and Two-Level Atoms* by Les Allen and Joseph H. Eberly [20], once the "Bible" of quantum optics at the University of Warsaw, according to Maciej Lewenstein [21], states that, "To the extent that a resonant interaction calls into play only a single transition in the atom, the atom has only two energy levels, and the laser may be taken to be monochromatic. Certainly, for most lasers and most atoms this can be an excellent pair of approximations..." Without having to invoke renormalization, the mechanism of the Lamb Shift may be understood, as can the mechanisms and factors determining the character of spontaneous emission. A possible addendum to Jestädt's comment on the field of quantum optics is that modern, theoretical quantum optics, also concerning strong light-matter coupling, requires, more or less, the treatment of light and matter on equal footing; however, the matter dynamics may be simplified enormously. What happens when one includes a fuller description of an atom or molecule? If the light-matter coupling is strong enough, for emitter-cavity coupled systems, the physical and chemical properties of the

matter are altered. Electron and photon states can hybridize to form so-called polariton states, their presence detectable in the splitting of absorption spectra peaks at frequencies allowed by the cavity [19]. To observe such effects, one must elevate their two-level atom model to a many-body theory, then inflame the new model by somehow including photons.

Let's take inventory of our bounty. Wieldy forms of the many-body Schrödinger equation, including external fields, describe excited electrons which do not influence the itinerant radiation, which is to say that the external field passes through the material as if it were transparent. Held in the other hand is our many-electron and photon dilemma. The field term of the Jaynes-Cummings Hamiltonian [20, 21] is a good start, but in all its forms the atom must be made more complicated. Density functional theory offers a solution to the both of these problems.

To make computational electrodynamics useful in situations involving nanoscale quantum dynamics, overlapping variables between the Schrödinger equation and Maxwell's equations are key: Maxwell's equations gives a vector potential, which gives an electron momentum, which gives a current, which affects a change in the vector potential, and so on – no new theory needed, and we wonder once more at the power of computers. *Algorithmic* techniques of this form employing the forward-difference time-domain method have been constructed [22, 23, 24, 25]. Methods using a "Maxwell-wave function" method have been made as well, and is the go-to approach for one of the projects detailed in this thesis [18, 26]. These numerical techniques function with a bidirectional line of communication between the matter and light dynamics, fitting computational electrodynamics for quantum effects.

But there's always another problem. Density functional theory makes amenable the many-electron problem, but this statement must be understood in context of the limits of wave function approaches to the many-body problem. *Weeks* of computation time, about the cost time-dependent density functional theory incurs describing Buckminsterfullerene, using the computing cluster responsible for generating the results in this thesis, looks attractive when considering the arms and legs needed for a wave function-based description (gory details in Chapter 2). Nanoscale devices, like IBM's two nanometer node chip, are too expensive to simulate with traditional density functional theory. As is tradition, we seek to make this calculation possible by reducing the degrees of freedom. The work this time, however, redirects the burden of this reduction: keep the line between the light and matter, and cut costs in the theory doing the most damage. The matter being the expensive part, in this thesis, we turn to it and use a less expensive form of density functional theory.

More good news: as far as electron-photon interactions are concerned – and theoretically, they, for the present, chiefly concern atoms and molecules coupled to cavities – density functional theory is up to the task. Computational *quantum* electrodynamics is coming of age, and all methods going beyond the two-level atom care to include the totality of the particle-particle interactions. The quantum electrodynamical density

functional theory is already the cheap option, so our aim, here, is not to get a discount. Instead, we look to elevate the accuracy of the approach *formalistically*, no new algorithms needed.

This thesis is filling within the ever-arborizing branches of computational electrodynamics. The results presented here come from the use of many numerical approaches, but the solutions to the problems at hand should be distinguished by their mutual nature. The semi-classical theory to be presented uses an approach called orbital-free density functional theory. Central to the coupling of the light and matter, though formally described, is a numerical algorithm propagating both the light and the matter in time as a dyad. The fully quantum approaches presented rely on traditional many-body and numerical methods, but are novel theories geared towards making electrons and photons equally granular.

1.2 About the Contents of this Thesis

The miniaturization of electronic and optical devices toward the nanoscale demands a computational electrodynamics informed by quantum mechanics, as their material environments breach thresholds beyond which quantum effects become important [27, 28, 29, 30, 31, 32]. Fields of study beyond this threshold, such as nanoplasmonics and nano-optics, have received a lot of computational and experimental interest in the last decade. Hitherto computational nanoscience literature shows the use of quantum simulations to investigate anisotropic electron spill-out, size, and geometrical effects on plasmonic resonances [33, 34, 35], laser irradiation [36], photoelectron circular dichroism [37, 38, 39], dielectric responses [40, 41], and light polarization effects on high harmonic generation (HHG) [42, 43, 44, 45, 46], as well HHG in solids [47, 48]. Experiments have imaged momentum space wave functions [49], visualized nanostructure plasmon couplings and modulation [50, 51, 52], and developed Raman scattering images of nanostructures [53, 54].

Quantum effects invariably manifest on the nanoscale, and their presence can be straightforwardly understood using quantum theory. Depending on the distribution of core and valence electrons, electron spill-out blue- and red-shifts metallic surface plasmon resonances [33]. Landau damping, yielded by a shift from plasmon-electron continuum-continuum state interactions to continuum-discrete state interactions, causes absorption spectra fragmentation [55]. Selection rules suppress harmonic orders in high harmonic generation spectra for circularly polarized light [56]. Surface scattering and charge diffusion may result in the formation of large, transient dipole fields, which describes the photo-Dember effect in semiconductors as electron-hole mobility asymmetries result in different scattering and diffusion times between the particles [57]. Multiple quantum effects can inform the optical properties of nanostructures, and so a cross fertilization of light and matter approaches is required. The domain of nanoplasmonic and nano-optics is then ideal for a coupled Maxwell-Schrodinger approach.

Nanoparticles and quantum emitters in optical cavities are examined using novel light-matter coupling

methods. Historically, treating light and matter on equal ab initio footing has not been necessary to advance the fields of optical and condensed matter physics; however, advancements in nanoplasmonics, quantum chemistry, and quantum optics present opportunities for more complex light-matter schemes, presenting questions not approachable using classical light propagation methods or many-body theories. Among the investigative opportunities are charge transfer observations in hybrid nanoparticles [52], ground state calculations for cavity-coupled atoms and molecules [58, 59, 60], and the time-dependent behavior of quantum emitters in optical cavities [61, 62]. In the "quantum-classical" regime, the current and density transfer dynamics of jellium and atomically-detailed nanoparticles are examined using coupled Maxwell and orbital-free density functional equations, in which all effective energy functionals are density-dependent, the Maxwell equations are propagated quantum mechanically, and a back-reaction of the induced current is detectable in the classical net field. In the "quantum-quantum" framework, many-electron systems, atoms, and molecules coupled to cavities are examined using the Pauli-Fierz Hamiltonian [61, 63, 64] of non-relativistic quantum electrodynamics (NR-QED). Specifically, density functional methods are employed to solve the NR-QED equations for these systems.

To start, chapter 2 is a discussion on the optical and quantum-many body methods necessary to address questions about the aforementioned systems. The many-electron problem and density functional theory are introduced, including orbital-free density functional theory [65]. Time-dependent density functional theories are discussed as well. Relevant to the application of orbital-free density functional theory, a brief discussion of the kinetic density energy functional problem is included. The Mi-Genova-Pavanello being the kinetic energy form of choice [66], it is given its own subsections, which cover the exact conditions necessary for the derivation of the functional and their imposition in the theory. The relevant classical optics and photon theory are then discussed. Finally, tying the first two sections together is a passage on the key theoretical schema – the non-relativistic limit of quantum electrodynamics being calculated to derive the Pauli-Fierz Hamiltonian and the Hamiltonian for a charged particle in a classical field.

Chapter 3 covers the coupling of the Maxwell and Schrodinger equations with an emphasis on the application of its orbital-free variant for lithium jellium and an aluminum-graphene hybrid nanoparticle. Due to the essential technical step of reconfiguring the time-dependent Maxwell equations into a Schrodinger-like form, the Riemann-Silberstein vector [67] is introduced then used to devise the coupling relationship. After a brief discussion of the orbital-free coupled equations, an application of the formalism to lithium jellium is compared to the identical application of Kohn-Sham TDDFT. This includes an introduction to real-space grid approaches and complex absorbing potentials. From here, we take a detour to exhibit the capabilities of traditional orbital-free equations when atoms are considered. This centers on research conducted to determine how orbital-free quantum physics compares to orbital-inclusive quantum physics, specifically in the

context of high harmonic generation for finite and periodic structures. We then apply coupled orbital-free equations to the problem of charge transfer frequency and net field dynamics of an aluminum and graphene hybrid nanoparticle, in which the modulation of the transfer frequency across the junction is detectable in the induced field around the nanoparticle.

Breaking away from quantum-classical problems to examine quantum-quantum problems, chapter 4 introduces the problem of many-electrons coupled to cavity photons, addressing questions involving strong light-matter coupling in optical cavities. A brief introduction to cavities and the strong coupling limit is provided. In this introduction, the two-level atom is used. We then pull focus on the research problem. The total Hamiltonian is separated into a center-of-mass Hamiltonian and a "relative" many-electron Hamiltonian, the former being the only component coupled to light and solved analytically. For the "relative" part, the density and the energy per harmonically confined electron is calculated using stationary density functional theory, then compared to the results of the wave function method known as the stochastic variational method. Plots of harmonically confined electron densities, one- and two-dimensional plots, calculated with density functional theory, are then shown.

Finally, in chapter 5, furthering the investigation of the physics of strong coupling in cavities, a novel form of the quantum electrodynamical density functional theory is introduced to reveal the specific impact of strong coupling on time-dependent phenomena and the optical properties of quantum particles [19]. Atom-cavity interactions are density functionalized using a tensor product of real-space electron and Fock space photon states. Calculations with this approach follow. Cavity polaritons are discussed, as are the relevance of the optical absorption and polarizability tensor. Cavity-coupling induced splitting in the absorption spectrum of benzene is then shown. The final discussion focuses on high harmonic generation from cavity-coupled molecules. A dipole acceleration technique for calculating high harmonic generation is explained. Upconversion effciency per virtue of cavity coupling is then shown, and its being attributed to interference across photon spaces is presented as well. Amid these discussions is commentary on the possibilities of the theory aiding research into photon exchange approximations, as well as curiosities observed in the geometry of coupling-split transition peaks.

The final chapter is dedicated to possible research opportunities pertaining to the presented methods and results. Atomic units are used in this text unless stated otherwise.

CHAPTER 2

Essential Theory

2.1 The Many-Electron Problem

Atomic and electronic structure determines the ground state properties of molecules, nanoparticles, clusters, and other, much larger structures sweeping all strata of scale and complexity. Provided accurate atomic and electronic structure information, numerous material observables beyond ground state energies are describable: molecular bond lengths, strengths, and geometry; nanoparticle shape and size; atomic and molecular orbital geometry; band structures and more. The dynamics following stimulation of the electronic structure by a general perturbation is principally determined by the separate, physical forms of the perturbation and the ground state of the target material. Without the rigorous, theoretical inclusion of the perturbation physics, however, observables normally encoded in back-reaction electromagnetic fields are theoretically accessible via the electron dynamics – electron currents in periodic boundary condition systems, or dipole oscillations in non-periodic boundary condition systems. Among these observables are absorption cross sections, oscillator strengths, susceptibilities, dielectric functions, refractive indicies, and even nonlinear optical processes like high harmonic generation.

Notice the focus on the electron dynamics for time-dependent phenomena. A dynamic electronic structure yields theoretical and experimental physical properties on femtosecond timescales while ionic motion occurs on picosecond timescales, owing to the tremendous difference in mass between electrons and nuclei. This timescale difference implies the many-body electron-nucelon wave function ansatz may be decoupled into two wave functions – one representing electron degrees of freedom, one representing ionic degrees of freedom – a separation called the Born-Oppenheimer Approximation (BOA) [15, 68]. In the literature, BOA is synonymous with electrons responding instantaneously to the motion of host ions: electrons mobile within an immovable lattice. The aforementioned observables are all calculable using BOA. And so noting the role of ions as spatially-fixed potentials, this thesis will concentrate on quantities engendered by electronic structure, methods for and solutions to the marginally simpler many-electron problem.

In possession of sufficient data on the ground state of a many-electron system has proven powerful, but the acquisition of this information is typically arduous, and ameliorative efforts to reduce calculation and storage expenses do not succeed without sacrificial, technical steps sullying physical properties. Still, it is in principal possible to calculate ground and excited state properties, and with enough computing power, the obstacles erected by formalism expenses are principally surmountable. In this thesis, such electronic structure

methods will be divided into two categories: wave function-based methods and density functional methods [69]. Thesis-relevant wave function-based methods will be described later. Density functional theory being relevant to multiple problems in this thesis, it and other variants will be discussed later in this chapter.

Electronic structure methods are approaches to solving the many-electron Schrodinger equation. "Many-electron," here, means anything larger than a system with one electron. Multielectron systems, even those with only two electrons, do not have known analytical solutions. Approximation schemes are then in order. Consider the general example of an atomic system of N interacting nonrelativistic electrons, the time-independent Schrodinger equation (TISE) is

$$\hat{H}\Psi_k(\mathbf{x}_1,\mathbf{x}_2,...,\mathbf{x}_N) = E_k\Psi_k(\mathbf{x}_1,\mathbf{x}_2,...,\mathbf{x}_N) \tag{2.1}$$

Wave function Ψ_k corresponds to the many-electron eigenstate k and is associated with the many-electron eigenvalue E_k. The parameters $\mathbf{x}_1,\mathbf{x}_2,...,\mathbf{x}_N$ individually represent the position and spin coordinates of a labeled electron: $\mathbf{x}_j \equiv (x_j, y_j, z_j, \sigma_j)$ for the jth electron.

Hamiltonian $\hat{H}$ is given by

$$\hat{H} = \hat{T} + \hat{V}_{ext} + \hat{U}_{ee}, \tag{2.2}$$

the first, second, and third terms being the kinetic energy operator, the external potential operator, and the electron-electron interaction operator, respectively. All operators are summations over the N electrons. The kinetic energy operator is a summation of the Laplacian of each spatial coordinate $\mathbf{x}_j$ in the wave function:

$$\hat{T} = -\sum_{j=1}^{N} \frac{\nabla_j^2}{2}. \tag{2.3}$$

Next, the external potential operator is the collective influence of the sources external to the electronic interactions: fixed ions in time-independent problems, fixed or itinerant ions, or perhaps light radiation in time-dependent ones. Therefore, its structure depends on environmental conditions. Since this multielectron system has been designated to be both static, the form the external potential operator takes is a Coulombic interaction between N electrons and M ions in some spatial configuration,

$$\hat{V}_{ext} = -\sum_{l=1}^{M}\sum_{j=1}^{N} \frac{Z_l}{|\mathbf{x}_j - \mathbf{X}_l|}, \tag{2.4}$$

where $\mathbf{X}_l$ are the ionic position vectors. Lastly, the electron-electron interaction operator is Coulombic, the summation indices assorted to prevent self-interaction, the division by two included to remove duplicate

interactions between every ith and jth electron:

$$\hat{U}_{ee} = \frac{1}{2} \sum_{i=1, i \neq j}^{N} \sum_{j=1}^{N} \frac{1}{|\mathbf{x}_i - \mathbf{x}_j|}. \tag{2.5}$$

An ionic kinetic energy operator and an ion-ion potential energy operator are absent due to the aforementioned BOA.

The summations in each term make the Hamiltonian and its corresponding many-body wave function unwieldy, necessitating the application of numerical (wave function) techniques: the popular Slater determinant-based Hartree-Fock method; quantum Monte Carlo [70]; coupled cluster theory [71]; and stochastic variational method [70]. Noting that Hartree-Fock method generally excludes electron correlations, these wave function approaches promise good accuracy [70, 72, 73, 74, 75, 76], but they share a memory storage problem – serious information overload Walter Kohn named the "exponential wall" in his 1999 Nobel Lecture [77].

A textbook exercise due to Ullrich quantifies this great disadvantage [17]:

> To get an impression of the "exponential wall" one encounters when dealing with many-body wave functions, let us do a back-of-the envelope calculation. Imagine that we represent a wave function...with 10 parameters for each spatial coordinate; these could be grid points, or coefficients of basis functions. Without any spatial symmetry, a one-electron system therefore requires $10^3 = 1000$ numbers to fully represent it. In single precision, this corresponds to 1 kilobyte of data that needs to be stored. How many bytes would you need to store the wave function of a two-electron system, and how many for a 10-electron system? Assume that a hard drive has a capacity of 1 Terabyte; how many hard drives would you need? How large could N be before the storage requirement exceeds the number of atoms in the universe (about 10^{80})?

The "exponential wall," here, in terms of bytes follows 10^{3N}, where N is the number of electrons. Calculating the bytes needed to store the two-electron wave function according to the specifications of Ullrich's exercise, one would need 1000 kilobyte storage. For the 10-electron system, in terms of single Terabyte hard drives, one would need 10^{18} Terabyte hard drives to store the information. For reference, the data from all the unique calculations performed in this thesis were stored in a 2.7 Terabyte hard drive.

The exponential wall leaves extended systems out of reach for contemporary wave function methods. Many interesting questions are addressable using wave function methods, as later chapters in this thesis will demonstrate; however, the simulation of the electron structure for large and realistic systems is highly desirable. The simulation of time-dependent phenomena is also desirable. For such systems, for a relatively inexpensive approach to solving many-electron variants of both TISE and the time-dependent Schrodinger

equation (TDSE), one must use a density functional approach.

2.1.1 Density Functional Theory

The essential operation of density functional theory is predicated on the one-to-one correspondence between the electronic number density and the external (ionic) potential, also known as the first Hohenberg-Kohn theorem. Formally presented the electron number density,

$$n(\mathbf{x}) = N \int d\mathbf{x}_2 \cdots \int d\mathbf{x}_N \, \Psi^*(\mathbf{x}, \mathbf{x}_2, \ldots, \mathbf{x}_N)\Psi(\mathbf{x}, \mathbf{x}_2, \ldots, \mathbf{x}_N), \tag{2.6}$$

is uniquely defined provided an external potential. A *reductio ad absurdum* argument leveled at the premise of two external potentials yielding identical, relaxed electron number densities is the traditional proof of the Hohenberg-Kohn theorem. Assuming no energetic degeneracy associated with $n(\mathbf{x})$ this proof is straightforward.

Consider the two external potentials previously mentioned: $\hat{V}$ and $\hat{V}'$. They are distinguished non-trivially, and so their difference is not constant. The Hamiltonians they are associated with are

$$\hat{H} = \hat{F} + \hat{V}$$

$$\hat{H}' = \hat{F} + \hat{V}',$$

where $\hat{F}$ is the same operator in both Hamiltonians – a grouping of all operators but the external potential. The premise specifies identical electron densities, but the potentials being distinguishable, the ground state energies must be different: $\langle\Psi|\hat{H}|\Psi\rangle \neq \langle\Psi'|\hat{H}'|\Psi'\rangle$, or $E \neq E'$. From this one may assume either expectation value is the larger of the other, making dissection via variational principle the obvious next step. Swapping Hamiltonians in these expectation values gives $\langle\Psi|\hat{H}'|\Psi\rangle$ and $\langle\Psi'|\hat{H}|\Psi'\rangle$, and expanding them both gives two similar inequalities,

$$E < E' + \langle\Psi'|\hat{V} - \hat{V}'|\Psi'\rangle$$

$$E' < E - \langle\Psi|\hat{V} - \hat{V}'|\Psi\rangle.$$

Permitting $\Psi = \Psi'$, a proxy declaration for identical electron densities, the addition of these inequalities tells all:

$$E + E' < E + E' + \langle\Psi'|\hat{V} - \hat{V}'|\Psi'\rangle - \langle\Psi|\hat{V} - \hat{V}'|\Psi\rangle$$

$$E + E' < E + E' + 0 \tag{2.7}$$

Euod erat demonstrandum. Inequality 2.7 is fallacious. Therefore, the ground state density and the external potential have a one-to-one correspondence. The theoretical essence for density functional theory (DFT) being demonstrated, a brief and technical introduction to its formalism follows.

Numerous textbooks and journal articles provide technical and historical coverage of DFT [15, 17, 69, 70, 77, 78]. The theory was developed by Hohenberg, Kohn, and Sham, the latter two being responsible for the key proof of concept just presented. Given the density-potential correspondence, one may present the corollary that the external potential determines the electron eigenvectors in the Schrodinger equation. Of course, the state vector would still be expensive to calculate and store. Therefore, for DFT, one moves from a multielectron picture to a single-electron picture in which none of the electrons are interacting with each other. The Coulombic forces and the antisymmetric properties of the many-body fermionic wave function dissipate, requiring the introduction of effective potentials engendering the real system electron dynamics. In other words, one takes the single-particle orbitals harbored in the Slater determinant of the many-electron wave function and solves the Schrodinger equation using them and their individual single-particle densities. The noninteracting and interacting Euler equations being identical in form, one ends up with the Kohn-Sham equations:

$$n(\mathbf{x}) = \sum_{j=1}^{N} |\phi_j(\mathbf{x})|^2 \tag{2.8}$$

$$\left(-\frac{\nabla^2}{2} + \hat{V}_{KS}[n(\mathbf{x})]\right)\phi_j(\mathbf{x}) = \varepsilon_j \phi_j(\mathbf{x}). \tag{2.9}$$

Eq. 2.8 is the single-particle density, which corresponds to the external potential. Eq. 2.9 is "the" Kohn-Sham (KS) equation – the wave equation ready set for many-electron systems – its terms, from left to right, all for the jth electron, being the single-particle kinetic energy, the Kohn-Sham potential, the single-particle wave function, and the Kohn-Sham eigenvalue.

The Kohn-Sham potential is

$$\hat{V}_{KS}[n(\mathbf{x})] = \hat{V}_{ext} + \hat{V}_H + \hat{V}_{XC}. \tag{2.10}$$

These are the effective potentials, the interactions for making the noninteracting electron system behave in numerical mimicry of a real system. Note that the BOA is at work as an ion-ion potential term is absent. $\hat{V}_{ext}$ is the external potential, its form unlike eq. 2.4 and which will be discussed later. $\hat{V}_H$ is the Hartree potential of the electrons. It handles the Coulombic electron-electron interactions, and it is defined as:

$$\hat{V}_H = \int \frac{n(\mathbf{x}')}{|\mathbf{x}-\mathbf{x}'|} d\mathbf{x}' \tag{2.11}$$

The first-order power of the denominator and the charge term in the numerator resemble the structure of a

Coulombic potential; however, eq. 2.11 being a density functional, the electron-electron interaction will turn out to be different than what eq. 2.5 produces. Furthermore, the rigidity of volume integration excludes assortment details describable using the summation approach – the Hartree term has duplicate electron-electron interactions. This raises another question: how does the single-particle kinetic energy produce the correct many-body kinetic energy? It actually does not do this, so one is met with two potential terms that fall short of proper mimicry. Also, how about the Pauli exclusion principle? One can no longer rely on the antisymmetry of a many-electron wave function. What is one to do?

Enter the exchange-correlation (XC) function:

$$\hat{V}_{XC} = \frac{\delta E_{XC}[n(\mathbf{x})]}{\delta[n(\mathbf{x})]}, \tag{2.12}$$

the panacea of virtually all density functional ills. A deficiency in approach is more or less addressed using this potential operator. In the traditional KS equation, this term has three tasks: the refinement of the kinetic energy; the refinement of the electron correlation; and the inclusion of an exchange "force" due to the exclusion principle. DFT would yield exact solutions if the XC energy were known, but in practice approximations of the XC energy are used. The approximations are numerous, but in this thesis the simplest approximation, the local density approximation (LDA), is used:

$$E_{XC}^{LDA} = \int d\mathbf{x}\varepsilon[n(\mathbf{x})]n(\mathbf{x}), \tag{2.13}$$

where $\varepsilon[n(\mathbf{x})]$ is the XC energy per unit volume for the homogeneous electron gas density, which is known.

Returning to the external potential, this thesis uses the psuedopotential approach to describe the ion-electron interaction. In the pseudopotential description of ion-electron interactions, the total charge of the nucelons in an atom and the core electrons are merged to form a single, weaker potential source partially determining the valence electron dynamics. This is justified by the fact that valence electrons are mostly responsible for the physics in nanostructures and solids, key to bonding, field back-reaction effects, density spill out effects, and more. A formal discussion of a general psuedopotential is involved and will not be included in this thesis, though one can be found here [15, 70]. In brief, replacing the ionic potential with a psuedopotential will impact the structure of the single particle, valence wave functions. These "pseudo wave functions" are single particle eigenstates whose critical dynamics manifest far from the core. The tail of the wave function is preserved, but the nodes at the core due to core-valence orthogonalization no longer exist – if the core electrons are "gone" there is no need to include them in a Gram-Schmidt process. That stated, the projection operator of the core states ends up in the general definition of the psuedopotential.

Furthermore, psuedopotentials are "semilocal," as they are parameterized with (local) radial and (nonlocal) angular quantities so that valence electrons are affected differently because of spatial separation and the atomic state shell geometry. In this thesis, the Trouiller-Martins psuedopotential form [79] is used unless stated otherwise.

With these terms in hand, one may express the Kohn-Sham total energy functional:

$$E[\phi_j] = \sum_j \int \phi_j \left(\frac{-\nabla^2}{2} \right) \phi_j d\mathbf{x} + \int V^{ext}(\mathbf{x}) n(\mathbf{x}) d\mathbf{x} + \frac{1}{2} \int \frac{n(\mathbf{x}) n(\mathbf{x}')}{\mathbf{x} - \mathbf{x}'} d\mathbf{x}' d\mathbf{x} + E^{XC}[n(\mathbf{x})]. \tag{2.14}$$

This functional may be solved self-consistently using an initial guess for the density. Solving the Kohn-Sham equation, one will compute single-particle orbitals ϕ_j that are used to calculate the new density according to eq. 2.8, which is then compared to the initial density. This two-way communication between eq. 2.8 and eq. 2.9 goes on until the density converges according to some convergence criterion. Density mixing, such as linear mixing, is used to prevent instabilities manifested in the nonlinearity of the Kohn-Sham equation. Upon convergence in the energy and density distribution, the minimum energy is found. General computational procedures solving the Kohn-Sham equation may be found here [70].

2.1.2 Time-Dependent Density Functional Theory

The time-dependent density functional theory (TDDFT) is a straightforward extension of "stationary" DFT, requiring only the inclusion of a time parameter in eqs. 2.8 and 2.9:

$$n(\mathbf{x},t) = \sum_{j=1}^{N} |\phi_j(\mathbf{x},t)|^2 \tag{2.15}$$

$$\left(-\frac{\nabla^2}{2} + \hat{V}_{KS}[n(\mathbf{x},t)] \right) \phi_j(\mathbf{x},t) = \varepsilon_j \phi_j(\mathbf{x},t). \tag{2.16}$$

These are the time-dependent Kohn-Sham (TDKS) equations. Objections raised concerning the continuity of the Hohenberg-Kohn theorem for TDDFT are addressed by two existence theorems: the Runge-Gross theorem [80] and the van Leeuwen theorem [81]. The former is a virtually identical statement to the Hohenberg-Kohn theorem but with the time-dependence tacked on to the external potential and single-particle density. The latter has no stationary analog and states the structure of the time-dependent density is not unique when interactions beyond those represented by the external potential are included – a time-dependent potential can always be added to the Hamiltonian which affects the observables of another potential.

All potentials included in the TDKS potential are similarly time-dependent, though the time-dependent XC potential has added complexity in TDDFT, encompassing historical information about $n(\mathbf{x},t)$, the interacting many-electron wave function at $t = 0$, and the Kohn-Sham wave function at $t = 0$. The Keldysh

formalism solves the problem of extending this potential to TDDFT [82], but the approximation of $\hat{V}_{XC}(\mathbf{x},t)$ for calculations is similarly difficult [83]. In this thesis, the adiabatic local density approximation (ALDA) is used to calculate the time-dependent XC potential:

$$\hat{V}_{XC}^{(ADLA)} = \frac{\delta e_{XC}[n(\mathbf{x})]}{\delta[n(\mathbf{x})]}|_{n(\mathbf{x})\rightarrow n(\mathbf{x},t)}, \tag{2.17}$$

where $\delta e_{XC}[n(\mathbf{x})]$ is the XC energy density of the HEG, which is dependent on the HEG density. This approximation uses the instantaneous density and the memory effects are ignored. Unfortunately, total adiabatic time evolution of real quantum systems occurs infrequently. Despite this, the approximation has worked well with the calculation of optical absorption, dielectric functions, electronic excitations, and transport calculations [17, 70].

Solving the TDKS gives one access to the time-dependent density and observables like the probability current density,

$$\mathbf{j}(\mathbf{r},t) = \frac{1}{2i}\sum_{j=1}^{N}(\phi_n^*\nabla\phi_n - \phi_n\nabla\phi_n^*). \tag{2.18}$$

Furthermore, optical absorption, oscillator strengths, and dielectric functions are calculable from dipole oscillations in time.

2.1.3 Orbital-Free Density Functional Theory

Returning to the nuts and bolts of stationary DFT, notice the role of the orbitals in eq. 2.14. One could play pedant by objecting to their inclusion. DFT is a "density" functional approach after all, and the only role the orbitals should play is in defining the single-electron density. A more sophisticated observation of the orbitals pulls the carpet out from beneath the expense comparison between DFT and wave function methods: DFT may be orders of magnitude less expensive, but it is *still* quite expensive. This criticism may also be leveled at TDDFT calculations – the calculation time scales cubically with the number of electrons. This leaves extended systems out of reach for any computer system ill-equipped for the time commitment. Returning to the early roots of DFT, however, exists a solution, though this solution follows the trend of sacrificing physical information for speed.

Many of the ideas characterizing DFT were introduced by Thomas-Fermi-Dirac (TFD) theory [84, 85], a prototypical density functional approach predating Hartree-Fock theory. For a non-interacting electron and ion system, the total TFD energy is,

$$E^{TFD} = \frac{3}{10}(3\pi^2)^{2/3}\int[n(\mathbf{x})]^{5/3}d\mathbf{x} - \frac{3}{2}\left(\frac{3}{\pi}\right)^{1/3}\int[n(\mathbf{x})]^{4/3}d\mathbf{x} + \int V(\mathbf{x})n(\mathbf{x})d\mathbf{x} + \frac{1}{2}\int\frac{n(\mathbf{x})n(\mathbf{x}')}{\mathbf{x}-\mathbf{x}'}d\mathbf{x}d\mathbf{x}'. \tag{2.19}$$

From left to right, the terms represent the kinetic energy, the exchange energy, the external potential energy, and the electron-electron Coulomb interaction. What Thomas, Fermi, and Dirac realized was that the electron density played a crucial role in describing electronic structure. This theory, however, is neither qualitatively nor quantitatively accurate. None of the terms constituting the total energy account for electron correlations. Traditional DFT uses orbitals, but TFD theory does not, meaning it cannot provide any information about single-particle states. In turn, TFD fails to describe atomic and molecular orbitals, meaning it fails to reproduce the bonding structure of diatomic molecules. This will also affect the ion-electron interaction in the psuedopotential description, forcing the psuedopotential to occupy a truncated parameter space without angular quantities. Lastly, ground state densities calculated with TFD do not decay exponentially from bulk structures. These are the failures of a "true" density functional approach. That said, provided the exchange-correlation effects are reliably approximated by LDA or some other XC potential, the usefulness of TFD is measured by the quality of the kinetic energy term, or the kinetic energy density functional (KEDF). The formalistic accounting of XC potentials *plus* KEDF using approximation functionals takes TFD to the study of orbital-free density functional theory (OF-DFT).

With BOA, the total energy of OF-DFT is

$$E_{OF} = \int [n(\mathbf{x})]^{1/2} \left(-\frac{\nabla^2}{2} \right) [n(\mathbf{x})]^{1/2} d\mathbf{x} + V_H[n] + E_{XC}[n] + T[n] - T_{vW}[n]. \tag{2.20}$$

From left to right, the terms are: the orthodox kinetic energy expectation value presented with the substitution $\phi_0 = [n(\mathbf{x})]^{1/2}$; the Hartree energy; the XC energy, represented by the LDA; the Kohn-Sham kinetic energy, and once more the orthodox kinetic energy expectation value. In OF-DFT the orthodox kinetic energy is called the von Weizsäcker (VW) term [86]. Condensing the potential terms into an OF effective potential, the effective equation of motion is superficially identical to the Kohn-Sham equation of eq. 2.9:

$$\left(-\frac{\nabla^2}{2} + \hat{V}_{OF}[n(\mathbf{x})] \right) \phi_0(\mathbf{x}) = \varepsilon_0 \phi_0(\mathbf{x}). \tag{2.21}$$

This is the orbital-free equation (Traditional DFT solutions being dictated the Kohn-Sham equation, it will be referred to as Kohn-Sham DFT, or KS-DFT, from here on). The indicies labeling the orbitals removed, the many-orbital set is truncated into one normalizable "orbital" containing all system electrons – the "orbital-free" in orbital-free DFT. Like how XC potentials mitigate the negative impacts manifested in the structures of the Hartree potential and the Kohn-Sham kinetic energy, the three kinetic energy terms, as well as the shortcomings of TFD, imply the necessity of a KEDF panacea – an approximation for the Kohn-Sham kinetic energy.

Numerous KEDFs have been developed over the years [66, 87, 88, 89, 90, 91]. The standard form of the KEDF uses some fraction of the VW term and some fraction of the TFD kinetic energy (commonly referred to as the Thomas-Fermi (TF) kinetic energy in the literature):

$$T[n] \approx \gamma T_{TF}[n] + \lambda T_{vW}[n] \tag{2.22}$$

$$T[n] - T_{vW}[n] \approx \gamma T_{TF}[n] + (\lambda - 1) T_{vW}[n], \tag{2.23}$$

where γ and λ are scalars systematically selected to reproduce material properties. These KEDF terms are "locally" parameterized, dependent on the electronic density at $\mathbf{x}$. Including semi-local parameters, a dependence on $\frac{\nabla n}{d\mathbf{x}}$, puts OF-DFT in good agreement with KS-DFT for warm dense matter simulations [92, 93]. Nonlocal KEDFs, a dependence on the density at $\mathbf{x}$ and $\mathbf{x}'$, have successfully and accurately described light metallic systems, like the nearly-free electron gas and aluminum dislocations [89, 94]. Their general form is defined as

$$T[n] \approx T_{TF}[n] + T_{vW}[n] + T_{NL}[n]$$

$$T_{NL}[n] = \int n^{\alpha}(\mathbf{x}) \omega_{T_{NL}}[p](\mathbf{x}, \mathbf{x}') n^{\beta}(\mathbf{x}') d\mathbf{x} d\mathbf{x}', \tag{2.24}$$

where $\omega_{T_{NL}}$ is a material- and density- dependent kernel and α and β are parameters systematically chosen for material property reproduction.

The nonlocal approaches vary in speed and applicability, though. The Huang-Carter approach yields reliable bulk properties for semiconductors, but does not do so with metals, unlike the Wang-Teter KEDF. In this thesis, a nonlocal KEDF is used unless. The KEDF of choice in this thesis is due to Mi, Genova, and Pavanello (MGP) its developmental aim of inexpensively simulating non-simple metal and semiconductor properties having been shown in [66].

2.1.4 Mi-Genova-Pavanello Kinetic Energy Density Functional

The implementation of MGP uses a kinetic electron-augmented density independent kernel, the kernel being the result of integration over the free-electron gas inverse response function. A detailed derivation, a discussion, and the MGP KEDF pilot calculations may be found in [66].

The formulation of the MGP KEDF depends on three *exact conditions*, mathematical relations satisfied by the real kinetic energy operator for OF-DFT, carefully selected by the authors. These conditions are: the existence of a "Kinetic electron," inter-potential hypercorrelation, and the Lindhard response in the free electron gas limit.

2.1.4.1 Exact Conditions for KEDF

The kinetic electron concept may be understood as follows. The sum of the potentials associated with the Kohn-Sham Hamiltonian equals a constant chemical potential. To see this, one need only vary the kinetic energy potential and take it to its logical conclusion. We start with the definition of the kinetic energy

$$T[n] = \sum_{i=1}^{N} t_i, \tag{2.25}$$

where t_i is the orbital kinetic energy. Varying this quantity yields,

$$\delta t_i = \int d\mathbf{x}\, \phi_i^*\, t_i\, \delta\phi_i + \int d\mathbf{x}\, \delta\phi_i^*\, t_i\, \phi_i. \tag{2.26}$$

Here, $\phi = \phi(\mathbf{x})$. The quantity t_i may be expressed as the difference between the orbital energy and the effective Kohn-Sham potential energy: $t_i = \varepsilon_i - V_{eff}^{KS}(\mathbf{x})$

$$\begin{aligned}
\delta t_i &= \int d\mathbf{x}\phi_i^* \left(\varepsilon_i - V_{eff}^{KS}(\mathbf{x})\right) \delta\phi_i + \int d\mathbf{x}\delta\phi_i^* \left(\varepsilon_i - V_{eff}^{KS}(\mathbf{x})\right) \phi_i && (2.27)\\
&= \int d\mathbf{x}\phi_i^*\, \varepsilon_i\, \delta\phi_i + \int d\mathbf{x}\delta\phi_i^*\, \varepsilon_i\, \phi_i - \int d\mathbf{x}\phi_i^*\, V_{eff}^{KS}(\mathbf{x})\, \delta\phi_i - \int d\mathbf{x}\delta\phi_i^*\, V_{eff}^{KS}(\mathbf{x})\, \phi_i && (2.28)\\
&= \varepsilon_i\, \delta \int d\mathbf{x}|\phi_i|^2 - \int d\mathbf{x} V_{eff}^{KS}(\mathbf{x})\delta|\phi_i|^2 && (2.29)\\
&= 0 - \int d\mathbf{x} V_{eff}^{KS}(\mathbf{x})\delta|\phi_i|^2. && (2.30)
\end{aligned}$$

Summing over all δt_i yields

$$\begin{aligned}
\delta T[n] &= \sum_{i=1}^{N} \delta t_i && (2.31)\\
&= -\int \sum_{i=1}^{N} d\mathbf{x} V_{eff}^{KS}(\mathbf{x})\delta|\phi_i|^2 && (2.32)\\
&= -\int d\mathbf{x} V_{eff}^{KS}(\mathbf{x})\delta n(\mathbf{x}) && (2.33)
\end{aligned}$$

Turning eq. 2.31 into a functional derivative with respect to $n(\mathbf{x})$ we get

$$\begin{aligned}
\frac{\delta T[n]}{\delta n(\mathbf{x})} &= -V_T && (2.34)\\
&= -\mu + V_{eff}^{KS}(\mathbf{x}) && (2.35)
\end{aligned}$$

where μ is a constant, and V_T is the kinetic energy potential. The effective Kohn-Sham potential is just the Kohn-Sham potential of eq. 2.10, though we do not treat the potentials as operators here. This leaves us with

the Euler equation of density functional theory [95]:

$$\mu = V_{ext} + V_H + V_{XC} + V_T \tag{2.36}$$

Taking the Laplacian of each term, then using Poisson's equation to evaluate each term yields

$$0 = \nabla^2 V_H + \nabla^2 V_{ext} + \nabla^2 V_{XC} + \nabla^2 V_T \tag{2.37}$$

$$= -4\pi n(\mathbf{x}) - 4\pi\, n_{ext}(\mathbf{x}) - 4\pi n_{XC}(\mathbf{x}) - 4\pi n_T(\mathbf{x}). \tag{2.38}$$

Here $n(\mathbf{x})$, $n_{ext}(\mathbf{x})$, $n_{XC}(\mathbf{x})$, and $n_T(\mathbf{x})$ are, respectively, the electron density, the external (ionic) density, a density associated with the "exchange-correlation hole" [17], and the density associated with the kinetic energy, which is to be interpreted here. Isolating the kinetic energy density term and integrating over all space, we obtain

$$4\pi n_T(\mathbf{x}) = -4\pi n(\mathbf{x}) - 4\pi\, n_{ext}(\mathbf{x}) - 4\pi n_{XC}(\mathbf{x}) \tag{2.39}$$

$$\int d\mathbf{x}\, n_T(\mathbf{x}) = -\int d\mathbf{x}\,(n(\mathbf{x}) + n_{ext}(\mathbf{x}) + n_{XC}(\mathbf{x})) \tag{2.40}$$

$$= -N_e + N_{ext} + 1 \tag{2.41}$$

$$= Q + 1, \tag{2.42}$$

where Q is the total charge. For neutral systems, in which $Q = 0$, the integral equals $+1$, the inverse result of integrating over the exchange-correlation hole. The term n_T is defined as the kinetic electron in [66].

The next condition, hypercorrelation, is a property of all functionals, and can be used to devise characteristic constraints for the KEDF [96, 97]. The namesake of the constraint, here, comes from [66], in which it is used to emphasize the relationship between the energy density and the physical potential for an electron density, from the vacuum to its true form.

Originally used to determine the form of the exchange-correlation energy from the exchange correlation potential in a general way, hypercorrelation may be used to determine the form of any energy from functionals when only supplied the functional derivatives. If we parameterize the electron densities using t, where t is some number on the path between 0 and 1, one may express the energy difference $E[n(\mathbf{x};t=1)] - E[n(\mathbf{x};t=0)]$ as the line integral

$$E[n(\mathbf{x};t=1)] - E[n(\mathbf{x};t=0)] = \int_0^1 dt\, \frac{dE}{dt} \tag{2.43}$$

Parameterizing the density using t allows us to express $\frac{dE}{dt}$ using the chain rule, which yields

$$E[n(\mathbf{x};1)] - E[n(\mathbf{x};0)] = \int_0^1 dt \int d\mathbf{x}\, \frac{\delta E[n(\mathbf{x};t)]}{\delta n(\mathbf{x};t)} \frac{dn(\mathbf{x};t)}{dt} \tag{2.44}$$

$$= \int_0^1 dt \int d\mathbf{x}\, V[n(\mathbf{x};t)] \frac{dn(\mathbf{x};t)}{dt}. \tag{2.45}$$

In recognizing $V[n(\mathbf{x};t)] = \frac{\delta E[n(\mathbf{x};t)]}{\delta n(\mathbf{x};t)}$, we also recognize that the t-parameterization of the electron density may take almost any form, as the equality signifies path independence. With this freedom, plus the freedom to choose whatever form of the energy difference, we may express the energy at the true electron density with respect to its functional derivative. Letting $n(\mathbf{x};t) = t\, n(\mathbf{x})$, which yields $E[n(\mathbf{x};0) = 0]$ (the vacuum condition), gives

$$E[n(\mathbf{x})] = \int_0^1 dt \int d\mathbf{x}\, V[n(\mathbf{x});t] n(\mathbf{x}) \tag{2.46}$$

Since hypercorrelation applies to all functionals, we take what is suggested in eqs. 2.44 and 2.45 and expand the potential in terms of its functional derivative. Keeping $n(\mathbf{x};t) = t\, n(\mathbf{x})$, we obtain

$$V[n(\mathbf{x})] = \int_0^1 dt \int d\mathbf{x}\, \frac{\delta V[n(\mathbf{x};t)]}{\delta n(\mathbf{x};t)} n(\mathbf{x}), \tag{2.47}$$

which gives

$$V[n(\mathbf{x})] = \int_0^1 dt \int d\mathbf{x}'\, \frac{\delta^2 E[n(\mathbf{x};t)]}{\delta n(\mathbf{x}) \delta n(\mathbf{x}';t)} n(\mathbf{x}'). \tag{2.48}$$

This is the hypercorrelation result one needs to construct the MGP functional.

The last exact condition for the kinetic energy functional is how it relates to the free electron gas linear response function [98, 99]. From eqs. 2.47 and 2.48, we can establish a relationship between the functional derivative the potential and the second functional derivative of the energy:

$$\frac{\delta V[n(\mathbf{x};t)]}{\delta n(\mathbf{x};t)} = \frac{\delta^2 E[n(\mathbf{x};t)]}{\delta n(\mathbf{x}) \delta n(\mathbf{x}';t)}. \tag{2.49}$$

Combining this with insight from eq. 2.34, one can see that the kinetic energy and the kinetic energy potential may be similarly related to each other,

$$\frac{\delta V_T[n]}{\delta n(\mathbf{x})} = -\frac{\delta^2 T[n]}{\delta n(\mathbf{x}) \delta n(\mathbf{x}')}. \tag{2.50}$$

The left-hand side of eq. 2.50 is what we recognize as the response function,

$$\chi_T(\mathbf{x},\mathbf{x}') = \left[\frac{\delta V^T[n]}{\delta n(\mathbf{x})}\right]^{-1} \tag{2.51}$$

To simplify the implementation of the response function, one may assume $\chi_T(\mathbf{x},\mathbf{x}') = \chi_T(|\mathbf{x}-\mathbf{x}'|)$, which yields a wieldy one-dimensional Fourier transform known as the Lindhard function [100],

$$\chi_L(\eta) = -\frac{k_f}{\pi^2}\left(\frac{1}{2} + \frac{1-\eta^2}{4\eta}\ln\left|\frac{1+\eta}{1-\eta}\right|\right), \tag{2.52}$$

where $\eta = q/2k_f$ is a dimensionless momentum parameter, $k_f = (3\pi^2 n_0)^{1/3}$ is the Fermi wavevector, and n_0 is the uniform electron density associated with the system. In the limit of a uniform electron gas, the Fourier transform of eq. 2.50 must be

$$\hat{F}\left[\frac{\delta V^T[n]}{\delta n(\mathbf{x})}\right]_{n(\mathbf{x})=n_0} = -\frac{1}{\chi_L}. \tag{2.53}$$

2.1.4.2 Imposition of Exact Conditions for nonlocal KEDF

To construct the MGP KEDF, we need to use the discussed exact conditions. The free electron gas response is imposed through hypercorrelation. We do this by expanding on eq. 2.50 by relating the lone kinetic energy potential term to the second derivative of the kinetic energy itself,

$$V_{NL}^T[n(\mathbf{x})] = \int_0^1 dt \int d\mathbf{x}' \, \frac{\delta^2 T_{NL}[n(\mathbf{x};t)]}{\delta n(\mathbf{x})\delta n(\mathbf{x}';t)} n(\mathbf{x}'), \tag{2.54}$$

which resembles eq. 2.48. Here, *NL* signifies nonlocality. From eq. 2.51, we may expand the kernel of this integral using the response function. Taking $n_0 \to t n_0$, and $\chi_L(\eta)^{-1} = \frac{\pi^2}{k_f} G_L(\eta)$

$$\frac{\delta^2 T_{NL}[n(\mathbf{x};t)]}{\delta n(\mathbf{x})\delta n(\mathbf{x}';t)} = \frac{\pi^2}{k_f} G_{NL} \tag{2.55}$$

$$= \frac{\pi^2}{(3\pi^2 n_0)^{\frac{1}{3}}} G_{NL} \tag{2.56}$$

$$= \frac{\pi^2}{(3\pi^2)^{\frac{1}{3}}} n_0^{-\frac{1}{6}} (t n_0)^{-\frac{1}{6}} G_{NL}, \tag{2.57}$$

where G_{NL} is a response-function dependent quantity to be defined shortly. Implementing the local density approximation ($n_0 \to n(\mathbf{x})$) gives

$$\frac{\delta^2 T_{NL}[n(\mathbf{x};t)]}{\delta n(\mathbf{x})\delta n(\mathbf{x}';t)} = \frac{\pi^2}{(3\pi^2)^{\frac{1}{3}}} n(\mathbf{x})^{-\frac{1}{6}} (t n(\mathbf{x}'))^{-\frac{1}{6}} G_{NL}(|\mathbf{x}-\mathbf{x}'|;t), \tag{2.58}$$

where $\hat{F}[G_{NL}(|\mathbf{x}-\mathbf{x}'|;t)]_{\mathbf{x}\to\eta} = G_L(\eta) - 3\eta^2 - 1$. This suggest for eq. 2.54 that

$$V_{NL}^T[n(\mathbf{x})] = \int_0^1 dt \int d\mathbf{x}' \, \frac{\pi^2}{(3\pi^2)^{\frac{1}{3}}} n(\mathbf{x})^{-\frac{1}{6}} (tn(\mathbf{x}'))^{-\frac{1}{6}} G_{NL}(|\mathbf{x}-\mathbf{x}'|;t) n(\mathbf{x}') \tag{2.59}$$

$$= \frac{\pi^2}{(3\pi^2)^{\frac{1}{3}}} n(\mathbf{x})^{-\frac{1}{6}} \int d\mathbf{x}' \, n(\mathbf{x}')^{\frac{5}{6}} \int_0^1 dt \, t^{-\frac{1}{6}} G_{NL}(|\mathbf{x}-\mathbf{x}'|;t) \tag{2.60}$$

$$= \frac{\pi^2}{(3\pi^2)^{\frac{1}{3}}} n(\mathbf{x})^{-\frac{1}{6}} \int d\mathbf{x}' \, n(\mathbf{x}')^{\frac{5}{6}} \times \frac{6}{5} \left[t^{\frac{6}{5}} G_{NL}(|\mathbf{x}-\mathbf{x}'|;t) \, |_0^1 - \int_0^1 dt \, t^{\frac{5}{6}} \dot{G}_{NL}(|\mathbf{x}-\mathbf{x}'|;t) \right] \tag{2.61}$$

$$= \frac{\pi^2}{(3\pi^2)^{\frac{1}{3}}} n(\mathbf{x})^{-\frac{1}{6}} \int d\mathbf{x}' \, n(\mathbf{x}')^{\frac{5}{6}} \times \frac{6}{5} \left[G_{NL}(|\mathbf{x}-\mathbf{x}'|) - \int_0^1 dt \, t^{\frac{5}{6}} \dot{G}_{NL}(|\mathbf{x}-\mathbf{x}'|;t) \right] \tag{2.62}$$

$$= n(\mathbf{x})^{-1/6} \hat{F}^{-1}[\hat{F}[n(\mathbf{x})^{5/6}](q) \times \omega_T(q)], \tag{2.63}$$

where $\omega_T(q)$ stores the constant and integral terms in the reciprocal transform,

$$\omega_T(q) = \frac{6}{5} \frac{\pi^2}{(3\pi^2)^{\frac{1}{3}}} \left[G_{NL}(\eta(q)) - \int_0^1 dt \, t^{\frac{5}{6}} \dot{G}_{NL}(\eta(q,t)) \right]. \tag{2.64}$$

In reciprocal space (q domain), eq. 2.63 vanishes in the low q limit, and so the Kinetic electron vanishes at this limit. To get around this, the authors of [66] model the Kinetic electron using a product of a basic Gaussian function and the square of the error function centered at $q = 0$. This yields the kernel,

$$\omega_{MGP}(q) = \omega_T(q) + \text{erf}^2(q) \frac{4\pi a}{q^2} \exp(-bq^2). \tag{2.65}$$

The shape of the kinetic electron may be adjusted by a and b. When $b \to$ inf, this results in a large volume, real-space Kinetic electron – suitable for modeling semiconductors. When $b \to 0$, its spatial extension is reduced – suitable for modeling metals.

Note the inclusion of $\omega_T(q)$. The Kinetic electron is a feature added to this kernel. This leaves the kinetic energy potential

$$V_T = V_{TF} + V_{vW} + V_{NL} \tag{2.66}$$

$$V_T = V_{TF} + V_{vW} + n(\mathbf{x})^{-1/6} \hat{F}^{-1}[\hat{F}[n(\mathbf{x})^{5/6}](q) \times \omega_{MGP}(q)](\mathbf{x}) \tag{2.67}$$

$$\tag{2.68}$$

The a and b parameters in $\omega_{MGP}(q)$ are free. To avoid dependency issues at $q = 0$, we set the boundary condition $\omega_{MGP}(q = 0) = 0$. Figs. 2.1 and 2.2 compare OF- and KS-DFT ground states for periodic aluminum,

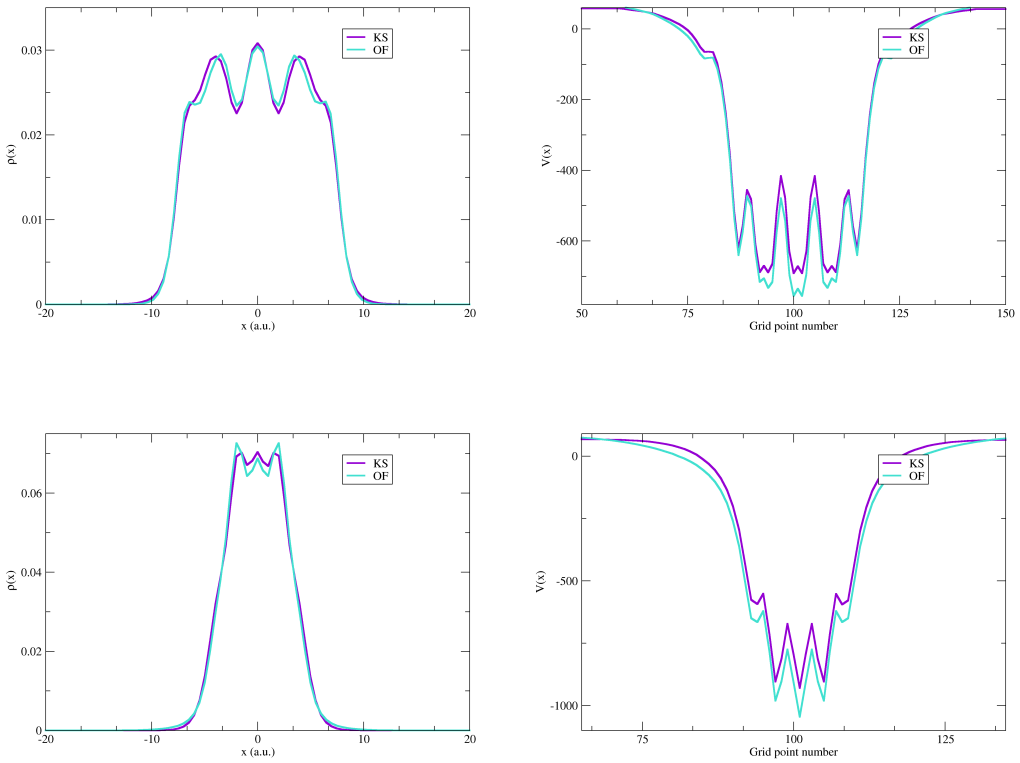

Figure 2.1: Ground state electron densities and potentials for a Al sheet (top) and Si sheet (bottom), calculated using OF-TDDFT, with MGP, and KS-TDDFT.

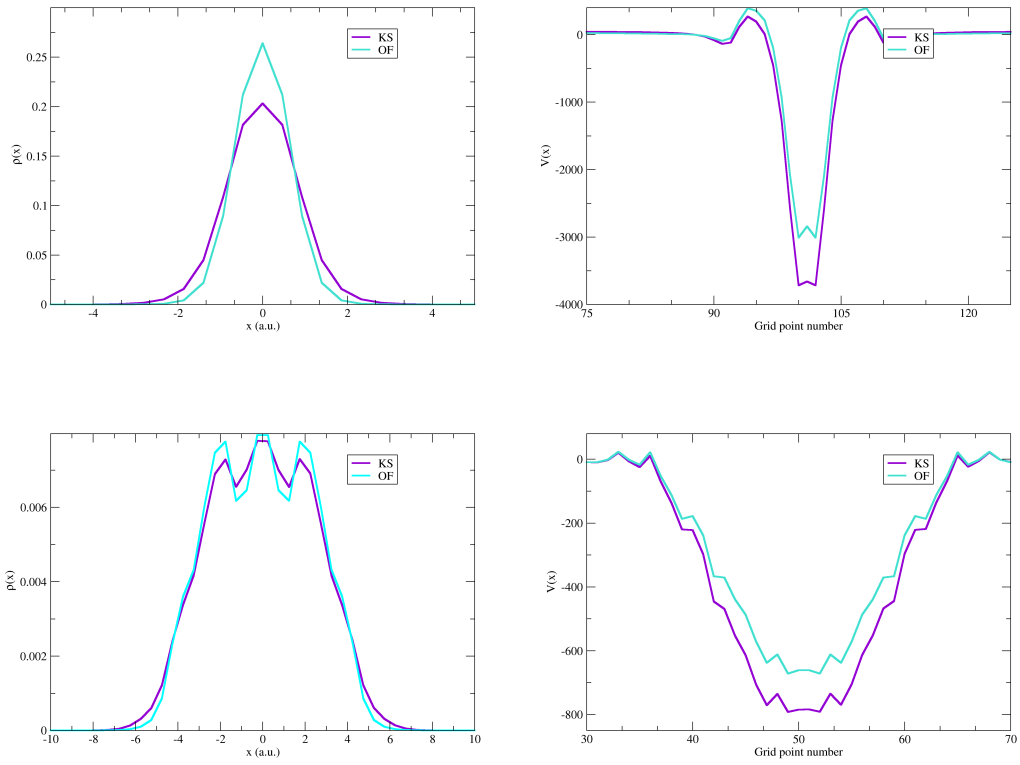

Figure 2.2: Ground state electron densities and potentials for graphene sheet (top) and C_{20} particle (bottom), calculated using OF-TDDFT, with MGP, and KS-TDDFT.

periodic silicon, periodic graphene, and C_{20}

2.1.5 Time-Dependent Orbital-Free Density Functional Theory

The last point to be made about OF-DFT is that its time-dependent variant, OF-TDDFT, is no larger a conceptual leap from its static variant than that which exists between KS-DFT and KS-TDDFT: add time to the parameter space and stay vigilant for the XC potential. In general, with a KEDF term, the time-dependent orbital-free wave equation is,

$$\left(-\frac{\nabla^2}{2}+\hat{V}_{OF}[n](\mathbf{x},t)\right)\phi_0(\mathbf{x},t)=\varepsilon_0\phi_0(\mathbf{x},t) \tag{2.69}$$

$$V_{OF}[n](\mathbf{x},t)=V_{KS}[n](\mathbf{x},t)+\gamma V_{TF}[n](\mathbf{x},t)+(\lambda-1)V_{vW}[n](\mathbf{x},t)+\sigma V_{NL}[n](\mathbf{x},t), \tag{2.70}$$

where $\sigma = 0$ or 1, where the nonlocality of the equation is established as needed. The nonlocal, MGP KEDF is used later in this thesis.

2.2 Classical and Quantum Light

As mentioned in [18], the theoretical description of light has historically been informed by solid-state physics with the academic stipulation that the solid-state physics occupy a secondary role, its formal acknowledgement ultimately favoring optical physics phenomena. Geometrical ray optics is informed only by lens geometry and refractive indicies. Time propagated Maxwell equations are informed by material permittivity and permeability. To be clear, this is not a theoretical deficiency, as computational electrodynamics and ray optics is enormously useful. Besides, informing Maxwell's equations with quantum material parameters is not a simple task considering the hurdles constituting the many-electron problem, even when the scale of the system is on the order of a cubic nanometer. In computational electrodynamics, methods like the forward-difference time-domain (FDTD) approach propagates Maxwell's equations on a Yee lattice requiring input of the medium dielectric parameters at every lattice grid point. Time-dependent dielectric parameters would require the electronic current, a quantum observable not available in this method. A system with two materials requires two dielectric parameters, the interfacial or overlapping regions at which one might take a weighted average of the dielectric parameters [55]. Therefore, to answer any question in which simulated quantum effects are important, an algorithmic light-matter coupling approach is needed.

Situations in which photonic resolution is important pose a separate challenge. Natural invariance requirements dictate the photon does not have a position operator [55, 101], a result in agreement with what the uncertainty principle suggests for photon motion. Therefore, building a Hilbert space-like photon wave function is not straightforward. Including the photon in a useful many-body framework, then, at least for

now, requires simplifications manifest in nanostructure symmetries, like optical cavities, or circuits.

In this thesis, the character of electromagnetic radiation is described using both Maxwell wave mechanics and standing wave cavity photons. In the domains of both descriptions will the theoretical structure of light be coupled to matter. Maxwell's equations are well understood and are a part of the standard of physics pedagogy, and so only thesis-relevant classical electrodynamical theory will be covered. Novel technical developments involving the Maxwell formalism will be presented. The quantum theory of light is not a part of the standard curriculum, but its discussion will be terse, though derivations will be provided. This will be done with the strict aim of describing cavity photons rather than general photonic states, realized by vector potential mode expansion in a finite volume. After this, a mathematically rigorous dissection of the quantum electrodynamics (QED) schema unifying the light-matter theories in this thesis will be presented – a derivation of the Pauli-Fierz Hamiltonian and the Hamiltonian for a charged particle in an electromagnetic field. Starting from the Lagrangian of QED the equations of motion for free photons and field-stimulated matter are separately solved, reduced in explanatory scope to their non-relativistic limits, then united in a general, wieldy, minimally-coupled Hamiltonian. It is from here one can include coupled electrons and photons formalistically, or coupled electrons and electromagnetic waves algorithmically.

2.2.1 Helmholtz Decomposed Electric Field

In atomic units ($\varepsilon_0 = 1/4\pi$), the Maxwell equations in a vacuum are

$$\nabla \cdot \mathbf{E} = \frac{\rho}{\varepsilon_0}$$

$$\nabla \cdot \mathbf{B} = 0$$

$$\nabla \times \mathbf{E} = -\frac{1}{c}\frac{\partial \mathbf{B}}{\partial t}$$

$$\nabla \times \mathbf{B} = \frac{1}{c}\left(\frac{\partial \mathbf{E}}{\partial t} + \frac{\mathbf{j}}{\varepsilon_0}\right),$$

where $\mathbf{E}$ and $\mathbf{B}$ are, respectively, the electric and magnetic fields, ρ is the charge density, c is the speed of light, and $\mathbf{j}$ is the electronic current. If source and itinerant radiation coexist, the electric field may be Helmholtz decomposed into transverse and longitudinal components:

$$\mathbf{E}(\mathbf{x},t) = \mathbf{E}_L(\mathbf{x},t) + \mathbf{E}_T(\mathbf{x},t), \tag{2.71}$$

where $\mathbf{E}_L(\mathbf{x},t)$ is the longitudinal, or "irrotational" component, and $\mathbf{E}_T(\mathbf{x},t)$ is the transverse, or "rotational" component. They are formally distinguished according to the differentiation conditions under which they

vanish. Explicitly,

$$\nabla \times \mathbf{E}_L(\mathbf{x},t) = 0 \tag{2.72}$$

$$\nabla \cdot \mathbf{E}_T(\mathbf{x},t) = 0. \tag{2.73}$$

The specification of source and itinerant fields required for eq. 2.71 and eq. 2.73 to coexist are manifest in the gradient of an electrical potential and the temporal derivative of a vector potential,

$$\mathbf{E}(\mathbf{x},t) = -\nabla\Phi - \frac{1}{c}\frac{\partial \mathbf{A}}{\partial t}. \tag{2.74}$$

It is straightforward to match these terms with their Helmholtz decomposed electric field components: a general property of the gradient yields $\nabla \times \nabla\Phi = 0$, and an ad hoc property of the vector potential known as the Coulomb gauge gives $\frac{\partial}{\partial t}(\nabla \cdot \mathbf{A}(\mathbf{x},t)) = 0$.

The Coulomb gauge, also known as the transverse or radiation gauge, is defined as:

$$\nabla \cdot \mathbf{A}(\mathbf{x},t) = 0, \tag{2.75}$$

and its chief function is to ensure the correct identification of the origins of the longitudinal and transverse field terms: longitudinal radiation comes from point sources while transverse radiation is normally external or "sourceless," like a laser field. It also ensures that the vector amplitudes of the itinerant field are perpendicular to the direction of the flux, or the Poynting vector. To show this, consider the plane wave electric field:

$$\mathbf{E}(\mathbf{x},t) = \mathbf{E}_0 e^{i(\mathbf{k}\cdot\mathbf{x}-\omega t)}. \tag{2.76}$$

According our conditions, this sourceless radiation should satisfy eq. 2.74 under the circumstances the gradient term is nonexistent. Using knowledge about the structure of plane waves – a structure with zero divergence – one may take the divergence of this electric field and get,

$$\nabla \cdot \mathbf{E}(\mathbf{x},t) = i\mathbf{k} \cdot \mathbf{E}(\mathbf{x},t). \tag{2.77}$$

Seeing that this divergence may also be described using the right-hand side of eq. 2.74, another way to write this divergence is,

$$\nabla \cdot \mathbf{E}(\mathbf{x},t) = \frac{1}{c}\frac{\partial}{\partial t}(\nabla \cdot \mathbf{A}(\mathbf{x},t)), \tag{2.78}$$

the right hand side of which vanishes. Therefore, equating eqs. 2.77 and 2.78 yields,

$$i\mathbf{k}\cdot\mathbf{E}(\mathbf{x},t)=0, \tag{2.79}$$

meaning that the amplitude vector of the electric field is perpendicular to the wave vector $\mathbf{k}$, its direction of motion.

This thesis will make extensive use of the vector potential, accounting for the transverse fields at play in our semi-classical calculations. Stating the integral implicit in the sourceless version of eq. 2.74,

$$\mathbf{A}(\mathbf{x},t)=-c\int_0^t \mathbf{E}_T(\mathbf{x},t')dt', \tag{2.80}$$

one sees a straightforward way to encode all the transverse radiation in a calculation using the vector potential. Obviously the inclusion of electrons, the intention of this thesis, would produce a field restricting the removal of the gradient term in eq. 2.74. Yet, the algorithimic coupling scheme to be discussed in chapter 3 requires dropping the gradient term to remove a redundancy, as the electric potential and its time evolution will be represented by the Hartree potential in KS-DFT/OF-DFT. Therefore, moving forward, *the electric fields we treat explicitly will be transverse.* The longitudinal terms will be contained within the Kohn-Sham potentials.

2.2.2 Photon Operators in Fock Space

The atomic units system is used in this section. Starting from the Lagrangian of the free electromagnetic field, $\mathscr{L}_{EM}=-\frac{1}{4}F^{\mu\nu}F_{\mu\nu}$, one may follow the recipe of canonical quantization: evaluate the momentum density and Hamiltonian density using $\mathscr{L}_{EM}$; swap the field space for its analogous operator space; establish commutation relations between field operators and the momentum; expand the field operator into energy modes; then evaluate the normal-ordered Hamiltonian. As mentioned earlier, the coverage of photon theory here will be terse. For helpful guides on how to quantize the electromagnetic field and the general canonical quantization procedure, see here [102, 103].

Canonical quantization and the Coulomb gauge yield the following forms for the vector potential, the *transverse* electric field, and the magnetic field:

$$\hat{\mathbf{A}}(\mathbf{x})=\sqrt{\left(\frac{c^2}{\varepsilon_0 L^3}\right)}\sum_{\mathbf{n},\lambda}\frac{\mathbf{e}_{\mathbf{n},\lambda}}{\sqrt{2\omega_{\mathbf{n}}}}[\hat{a}_{\mathbf{n},\lambda}e^{i\mathbf{k}_{\mathbf{n}}\cdot\mathbf{x}}+\hat{a}^{\dagger}_{\mathbf{n},\lambda}e^{-i\mathbf{k}_{\mathbf{n}}\cdot\mathbf{x}}] \tag{2.81}$$

$$\hat{\mathbf{E}}(\mathbf{x})=\sqrt{\left(\frac{1}{\varepsilon_0 L^3}\right)}\sum_{\mathbf{n},\lambda}i\mathbf{e}_{\mathbf{n},\lambda}\sqrt{\frac{\omega_{\mathbf{n}}}{2}}[\hat{a}_{\mathbf{n},\lambda}e^{i\mathbf{k}_{\mathbf{n}}\cdot\mathbf{x}}-\hat{a}^{\dagger}_{\mathbf{n},\lambda}e^{-i\mathbf{k}_{\mathbf{n}}\cdot\mathbf{x}}] \tag{2.82}$$

$$\hat{\mathbf{B}}(\mathbf{x}) = \sqrt{\left(\frac{c^2}{\varepsilon_0 L^3}\right)} \sum_{\mathbf{n},\lambda} \frac{i\mathbf{k_n} \times \mathbf{e}_{\mathbf{n},\lambda}}{\sqrt{2\omega_\mathbf{n}}} [\hat{a}_{\mathbf{n},\lambda} e^{i\mathbf{k_n}\cdot\mathbf{x}} - \hat{a}^\dagger_{\mathbf{n},\lambda} e^{-i\mathbf{k_n}\cdot\mathbf{x}}]. \tag{2.83}$$

These informationally dense operator equations are described using: a quantization cube of side length L; allowed photon frequencies of

$$\omega_\mathbf{n} = c|\mathbf{n}|\frac{2\pi}{L} \quad \text{with,} \quad n_x, n_y, n_z = 0, \pm 1, \pm 2, \pm 3, \pm 4, ...; \tag{2.84}$$

two transversal polarization directions in λ; a transverse polarization vector $\mathbf{e}_{\mathbf{n},\lambda}$ perpendicular to the wave vector $\mathbf{k_n}$ – due to the Coulomb gauge – in a matching photon mode, with magnitude $|\mathbf{k_n}| = \omega_\mathbf{n}/c$ (This vector naturally appears during the canonical quantization process. It being key to the description of quantized Maxwell fields, coincident with photons being spin-1 particles, are why particle physicists categorize photons as "vector bosons"). Perhaps the most important components are the photon creation and annihilation operators,

$$\hat{a}_{\mathbf{n},\lambda} = \sqrt{\frac{\omega_\mathbf{n}}{2}} \left(q_{\mathbf{n},\lambda} + \frac{i}{\omega_\mathbf{n}} \frac{\partial}{\partial q_{\mathbf{n},\lambda}} \right) \tag{2.85}$$

$$\hat{a}^\dagger_{\mathbf{n},\lambda} = \sqrt{\frac{\omega_\mathbf{n}}{2}} \left(q_{\mathbf{n},\lambda} - \frac{i}{\omega_\mathbf{n}} \frac{\partial}{\partial q_{\mathbf{n},\lambda}} \right), \tag{2.86}$$

where $q_{\mathbf{n},\lambda}$ are the photon displacement coordinates and $\frac{\partial}{\partial q_{\mathbf{n},\lambda}}$ are the conjugate momenta (formally analogous to the position and momentum operators of Hilbert space, but are fundamentally different). As their names imply, $\hat{a}^\dagger_{\mathbf{n},\lambda}$ creates and $\hat{a}_{\mathbf{n},\lambda}$ destroys photon modes in a Fock space, and since they are Fock space operators for photons, they obey boson commutation relations:

$$\left[\hat{a}^\dagger_{\mathbf{m},\sigma}, \hat{a}^\dagger_{\mathbf{n},\lambda}\right] = 0 \tag{2.87}$$

$$\left[\hat{a}_{\mathbf{m},\sigma}, \hat{a}_{\mathbf{n},\lambda}\right] = 0 \tag{2.88}$$

$$\left[\hat{a}_{\mathbf{m},\sigma}, \hat{a}^\dagger_{\mathbf{n},\lambda}\right] = \delta_{\sigma\lambda}\delta_{\mathbf{mn}}. \tag{2.89}$$

It is worth noting here that though the polarization directions are invariably discrete, the modes themselves could either be countably or not countably infinite, which would turn the summation over the modes in eqs. 2.81, 2.82, and 2.83 into an integral over a modal volume. See [18, 102].

The electromagnetic energy density operator is,

$$\hat{H} = \frac{\varepsilon_0}{2} \int_V [\hat{\mathbf{E}}(\mathbf{x})^2 + \hat{\mathbf{B}}(\mathbf{x})^2] d\mathbf{x}. \tag{2.90}$$

Plugging in for the definitions of the electric and magnetic fields eqs. 2.82 and 2.83 yields

$$\hat{H} = \frac{\varepsilon_0}{2}\int_V [\hat{\mathbf{E}}(\mathbf{x})^2 + \hat{\mathbf{B}}(\mathbf{x})^2] d\mathbf{x} \tag{2.91}$$

$$= -\sum_{\mathbf{n}} \frac{1}{2L^3}\left[\frac{\omega_{\mathbf{n}}}{2}(\mathbf{e}_{\mathbf{n},\lambda})^2 + \frac{c^2}{2\omega_{\mathbf{n}}}(\mathbf{k}_{\mathbf{n}} \times \mathbf{e}_{\mathbf{n},\lambda})^2\right]\int_V [\hat{a}_{\mathbf{n},\lambda} e^{i\mathbf{k}_{\mathbf{n}}\cdot\mathbf{x}} - \hat{a}^\dagger_{\mathbf{n},\lambda} e^{-i\mathbf{k}_{\mathbf{n}}\cdot\mathbf{x}}]^2 d\mathbf{x} \tag{2.92}$$

$$= \sum_{\mathbf{n}} \frac{\omega_{\mathbf{n}}}{2L^3}\int_V \hat{a}^\dagger_{\mathbf{n},\lambda}\hat{a}_{\mathbf{n},\lambda} + \hat{a}_{\mathbf{n},\lambda}\hat{a}^\dagger_{\mathbf{n},\lambda} - \hat{a}_{\mathbf{n},\lambda}\hat{a}_{\mathbf{n},\lambda} e^{2i\mathbf{k}_{\mathbf{n}}\cdot\mathbf{x}} - \hat{a}^\dagger_{\mathbf{n},\lambda}\hat{a}^\dagger_{\mathbf{n},\lambda} e^{-2i\mathbf{k}_{\mathbf{n}}\cdot\mathbf{x}} d\mathbf{x} \tag{2.93}$$

$$= \sum_{\mathbf{n}} \frac{\omega_{\mathbf{n}}}{2L^3}\int_V \hat{a}^\dagger_{\mathbf{n},\lambda}\hat{a}_{\mathbf{n},\lambda} + \hat{a}^\dagger_{\mathbf{n},\lambda}\hat{a}_{\mathbf{n},\lambda} + 1\, d\mathbf{x} \tag{2.94}$$

$$= \sum_{\mathbf{n}} \frac{\omega_{\mathbf{n}}}{2L^3}(2\hat{a}^\dagger_{\mathbf{n},\lambda}\hat{a}_{\mathbf{n},\lambda}L^3 + L^3) \tag{2.95}$$

$$= \sum_{\mathbf{n},\lambda} \omega_{\mathbf{n}}\left[\hat{a}^\dagger_{\mathbf{n},\lambda}\hat{a}_{\mathbf{n},\lambda} + \frac{1}{2}\right]. \tag{2.96}$$

Note that the terms carrying repeated operators in eq. 2.93 vanish, as neither term returns the Fock space state vector to its original state, thus giving two vanishing inner products. Expressing the creation and annihilation operators using eqs. 2.85 and 2.86 gives

$$\hat{H} = \sum_{\mathbf{n},\lambda} \frac{1}{2}\left[\frac{\partial^2}{\partial q^2_{\mathbf{n},\lambda}} + \omega^2_{\mathbf{n}} q^2_{\mathbf{n},\lambda}\right]. \tag{2.97}$$

The free photon Hamiltonian presented here is essential for the derivation of Hamiltonians describing photon-sensitive electron states. In practice, photon operators act on state vectors in a Fock space, so a tensorial mixture of Hilbert space and Fock space is required to describe electron and photon dynamics simultaneously. To pull this off, one can use occupation number bases and how they are affected by the creation and annihilation operators (see chapters 4 and 5).

Commonly, the Fock space for photons is referred to as the photon number space [19]. Working in this space, it is advantageous to express the photon displacement coordinates and conjugate momenta with respect to the creation and annihilation operators. Assuming the existence of only one photon mode and no others,

$$q_\lambda = \frac{1}{\sqrt{2\omega_\lambda}}(\hat{a}_\lambda + \hat{a}^\dagger_\lambda) \tag{2.98}$$

$$\frac{\partial}{\partial q_\lambda} = -i\sqrt{\frac{\omega_\lambda}{2}}(\hat{a}_\lambda - \hat{a}^\dagger_\lambda). \tag{2.99}$$

The vacuum state, in which no photons exist, being defined as $|0\rangle$, the eigenstates of the number operator $\hat{a}^\dagger_\lambda\hat{a}_\lambda$ may be expressed by multiple applications of the creation operators,

$$|n_\lambda\rangle = (n!)^{\frac{1}{2}}\hat{a}^{\dagger n}_\lambda|0\rangle, \tag{2.100}$$

where n_λ represented the excited state of the photon mode of frequency ω_λ, or rather the number of photons in said state. This permits the construction of a general Fock space basis over which a vector space field of bosonic operators are defined:

$$|n_1, n_2, ..., N\rangle = \frac{1}{\sqrt{n_1, n_2, ..., N}} \prod_{\sigma=1}^{N} [\hat{a}_\sigma^\dagger]^{n_\sigma} |0\rangle, \tag{2.101}$$

where N is the number of photons in the highest energy state allowed.

2.3 Derivation of Velocity Gauge Hamiltonian from Non-Relativistic Quantum Electrodynamics

Natural units are used in this section to keep charge and mass present in the equations. Note that the use of natural units here both illuminates the discussion and leads to a result easily translatable to atomic units.

Depending on the observables desired, semi-classical theories describe either the optical properties of solids using Maxwell's equations or the evolution of electronic structure using a quantum wave equation, but both cannot be formalistically implemented simultaneously. Therefore, one must take advantage of the parameter overlap between Maxwell and quantum theory – the current and the vector potential – and use them to algorithimically couple the two equations. For cases requiring only quantum mechanics, photons can be straightforwardly coupled to electrons using QED, but practical calculations require the imposition of energetic boundaries restricting the number of photons and photon modes that may exist. Later, this thesis will introduce an algorithimic coupling scheme for photons and the electronic density in a density functional method, which is to be constracted from another density functional method using an electron-photon ansatz to couple their dynamics.

What will now follow is a derivation of a general, minimally coupled electron Hamiltonian unifying the coupling schemes, starting from its associated quantum field theory. Neither the "quantum-classical" algorithmic (QCA) coupling scheme nor the "quantum-quantum" formalistic (QQF) coupling scheme are immediate or obvious consequences of the derived Schrodinger equation, but the velocity gauge Hamiltonian is the technical base from which all the light-matter treatments in this thesis emerge. Thus, it would be useful share the formal origins of the essential theoretical devices.

The subsections are split between the QCA and QQF devices needed for their individual coupling schemes. Section 2.3.1 covers the QCA Hamiltonian form, which is just the differential equation for a charged particle in a classical field. Section 2.3.2 covers the QQF Hamiltonian, the Pauli-Fierz Hamiltonian of non-relativistic QED.

Using the natural units of QED ($\hbar = 1, c = 1, m = 1$), but withholding the suppression of the mass for clarity, one starts with the Lagrangian of QED

$$\mathscr{L}_{QED} = -\frac{1}{4}F^{\mu\nu}F_{\mu\nu} + \bar{\psi}\left(i\gamma^{\mu}D_{\mu} - m\right)\psi. \tag{2.102}$$

Its many components are defined as:

- $F_{\mu\nu} = -\partial_{\mu}A_{\nu} - \partial_{\nu}A_{\mu}$, the electromagnetic field tensor. Its covariant and contravariant variants composing the first term in $\mathscr{L}_{QED}$ represent a free electromagnetic field.

- ψ is the bispinor electron-position field, called a Dirac spinor, containing all the information about the electron-positron field. Its four components are appropriately and evenly divided among wave function matrices of opposite handedness:

$$\psi = \begin{bmatrix} \psi_L \\ \psi_R \end{bmatrix} \tag{2.103}$$

  The questions addressed in this thesis are in the non-relativistic limit – meaning no positron production – so these will be referred to as electron spinors.

- γ^{μ}, the Dirac matrices. In nested matrix form, they are

$$\gamma^0 = \begin{bmatrix} 0 & I \\ I & 0 \end{bmatrix}, \quad \boldsymbol{\gamma} = \begin{bmatrix} 0 & \boldsymbol{\sigma} \\ -\boldsymbol{\sigma} & 0 \end{bmatrix},$$

  where $\boldsymbol{\sigma}$ are the Pauli matrices.

- $D_{\mu} = \partial_{\mu} + ie\chi_{\mu}$ is the gauge covariant derivative, the term mediating the minimal coupling between photons and electrons. The letter e is the coupling constant, the fundamental charge of the bispinor field. The Greek letter term is $\chi_{\mu} = A_{\mu} + Y_{\mu}$, where the first term is the external four-vector potential, generated by an external source, while the second is an internal four-vector potential, generated by the system electrons. How this term is expressed is key to distinguishing the light-matter coupling schemes in this thesis.

- The letter m is the mass of the electron.

Expanding the covariant derivative yields

$$\mathscr{L}_{QED} = \frac{1}{4}F_{\mu\nu}F^{\mu\nu} + i\bar{\psi}\gamma^{\mu}\partial_{\mu}\psi - e\bar{\psi}\gamma^{\mu}\chi_{\mu}\psi - m\bar{\psi}\psi, \tag{2.104}$$

which leads to the equation of motion $\mathscr{L}_{QED}/\partial\bar{\psi} = 0$. Differentiating with respect to the bispinor adjoint yields zero unlike differentiation with respect to ψ. Evaluating $\mathscr{L}_{QED}/\partial\bar{\psi}$ removes all information about

the free photon field represented by the electromagnetic tensor term, yielding the minimally coupled Dirac equation (assuming a (+,-,-,-) metric),

$$0 = (\gamma^{\mu}(i\partial_{\mu} - e\chi_{\mu}) - m)\psi \tag{2.105}$$

The free photon behavior requires the equations of motion dictated using another field in $\mathscr{L}_{QED}$, which will be covered later. The derivation will now proceed.

$$0 = \partial \mathscr{L}_{QED}/\partial \bar{\psi} \tag{2.106}$$

$$= (i\gamma^{\mu}\partial_{\mu} - e\gamma^{\mu}\chi_{\mu})\psi - m\psi \tag{2.107}$$

$$= \gamma^0(i\partial_0 - e\chi_0)\psi - \boldsymbol{\gamma}\cdot(i\nabla - e\boldsymbol{\chi})\psi - m\psi$$

$$= \left(\begin{bmatrix} 0 & i\partial_0 - e\chi_0 \\ i\partial_0 - e\chi_0 & 0 \end{bmatrix} + \begin{bmatrix} 0 & -\boldsymbol{\sigma}\cdot(i\nabla - e\boldsymbol{\chi}) \\ \boldsymbol{\sigma}\cdot(i\nabla - e\boldsymbol{\chi}) & 0 \end{bmatrix} + \begin{bmatrix} -m & 0 \\ 0 & -m \end{bmatrix} \right) \times \begin{bmatrix} \psi_L \\ \psi_R \end{bmatrix} \tag{2.108}$$

$$= \begin{bmatrix} -m & i\partial_0 - e\chi_0 - \boldsymbol{\sigma}\cdot(i\nabla - e\boldsymbol{\chi}) \\ i\partial_0 - e\chi_0 + \boldsymbol{\sigma}\cdot(i\nabla - e\boldsymbol{\chi}) & -m \end{bmatrix} \begin{bmatrix} \psi_L \\ \psi_R \end{bmatrix} \tag{2.109}$$

The entries of the 2×1 matrix in the last line are

$$0 = -m\psi_L + (i\partial_0 - e\chi_0 - \boldsymbol{\sigma}\cdot(i\nabla - e\boldsymbol{\chi}))\psi_R \tag{2.110}$$

$$0 = (i\partial_0 - e\chi_0 + \boldsymbol{\sigma}\cdot(i\nabla - e\boldsymbol{\chi}))\psi_L - m\psi_R. \tag{2.111}$$

Two steps follow. First, one performs non-relativistic limit extraction, factoring out the large (relativistic) mass contribution through the wavefunction: $\psi_Q = \phi_Q e^{-imt}$, where Q is either L or R. As is so common in solving differential equations, the exponential terms will cancel out. Second, one must capitalize on the coupled nature of the equations in the matrix and choose to express either ϕ_L or ϕ_R in terms of the opposite handedness. Setting $\hat{E} = i\partial_0$, and seeing how its operation on either wave function gives

$$\hat{E}\phi_Q e^{-imt} = (\hat{E} + m)\phi_Q e^{-imt}, \tag{2.112}$$

one can straightforwardly arrive at the following wave equation for ϕ_L:

$$0 = -m\phi_L + (m + \hat{E} - e\chi_0 - \boldsymbol{\sigma}\cdot(i\nabla - e\boldsymbol{\chi}))\left(1 + \frac{\hat{E} - e\chi_0}{m} + \frac{\boldsymbol{\sigma}\cdot(i\nabla - e\boldsymbol{\chi})}{m}\right)\phi_L \tag{2.113}$$

From eq. 2.113 one may algebraically proceed towards the conclusion:

$$0 = -m\phi_L + (m + \hat{E} - e\chi_0 - \boldsymbol{\sigma}\cdot(i\nabla - e\boldsymbol{\chi}))\left(1 + \frac{\hat{E} - e\chi_0}{m} + \frac{\boldsymbol{\sigma}\cdot(i\nabla - e\boldsymbol{\chi})}{m}\right)\phi_L \tag{2.114}$$

$$= -m\phi_L + \left(m + 2(\hat{E} - e\chi_0) + \underbrace{\frac{(\hat{E} - e\chi_0)^2}{m}}_{\approx 0} - \frac{(\boldsymbol{\sigma}\cdot(i\nabla - e\boldsymbol{\chi}))^2}{m}\right)\phi_L. \tag{2.115}$$

Therefore,

$$2(\hat{E} - e\chi_0)\phi_L = \frac{(\boldsymbol{\sigma}\cdot(i\nabla - e\boldsymbol{\chi}))^2}{m}\phi_L. \tag{2.116}$$

Applying the Pauli spin algebra identity $(\mathbf{a}\cdot\boldsymbol{\sigma})(\mathbf{b}\cdot\boldsymbol{\sigma}) = (\mathbf{a}\cdot\mathbf{b})I_{\mathbb{N}} + i(\mathbf{a}\times\mathbf{b})\cdot\boldsymbol{\sigma}$, where $I_{\mathbb{N}}$ is the identity matrix of suitable dimensionality, to the squared parenthetical term on the right-hand side of eq. 2.116 gives

$$(\boldsymbol{\sigma}\cdot(i\nabla - e\boldsymbol{\chi}))^2 = (i\nabla - e\boldsymbol{\chi})\cdot(i\nabla - e\boldsymbol{\chi}) + i(i\nabla - e\boldsymbol{\chi})\times(i\nabla - e\boldsymbol{\chi})\cdot\boldsymbol{\sigma}. \tag{2.117}$$

With some relabeling, $\hat{E} = \hat{H}$, $-i\nabla = \hat{p}$, $\phi_L = \phi$ and $e\chi_0 = U$, and identifying $\boldsymbol{\chi}$ as a composite field of longitudinal and transverse radiation, meaning $\mathbf{B} = \nabla\times\boldsymbol{\chi}$, eq. (2.58) becomes

$$\hat{H}\phi = \frac{(\hat{p} + e\boldsymbol{\chi})^2}{2m}\phi + U\phi - \frac{e}{2m}(\boldsymbol{\sigma}\cdot\mathbf{B})\phi, \tag{2.118}$$

This result is known as the Pauli equation. The first term is the velocity gauge momentum describing the interaction between the electron momentum and a vector potential (Depending on the sign convention of the metric tensor, the plus sign in this term could be a minus sign. Either way, the physics is the same). The second term is a general potential term. The third term is the magnetic spin-field interaction, which will be sufficiently small in the questions of the thesis to exclude. Also, the coupling constant e is the charge of the electron, and its sign must be included: $e \to -e$. Thus,

$$\hat{H}\phi = \frac{(\hat{p} - e\boldsymbol{\chi})^2}{2m}\phi + U\phi. \tag{2.119}$$

Without specifying the structure of $\boldsymbol{\chi}$ in the minimally coupled kinetic term, eq. 2.118 is the root of the light-matter coupling formalism concerning this thesis. What happens to the free photon portion of the Lagrangian will be discussed in section 2.3.2.

2.3.1 Quantum-Classical: Electrons in an Electric Field

The reader might be pleased to see that eq. 2.119 is already in the form of a particle in a classical field, or more specifically, an electron in a classical electric field. Though one may reconfigure eq. 2.119 to its length gauge form and use terms for a weak perturbative potential and the dipole operator instead, the velocity gauge form of the Hamiltonian streamlines the QCA procedure. Also, unlike the length gauge Hamiltonian, the velocity gauge expression has the benefit of being compatible with periodic boundary conditions. We now return to using Hartree atomic units: $\hbar = m = e = 1$.

The intention is to use eq. 2.119 in a semi-classical DFT-based approach. Therefore, one only requires that $\boldsymbol{\chi}$ represent an external classical electromagnetic field. This means that in $\boldsymbol{\chi} = \mathbf{A} + \mathbf{Y}$, only $\mathbf{A}$ is present, so $\mathbf{Y} = 0$. Setting $\mathbf{Y} = 0$ removes a redundancy in the total field. Specifically, the portion of the total field generated by the system electrons will be handled by the Hartree potential, stored in the general potential term of eq. 2.119, and not the general vector potential in the kinetic energy term.

Explicitly, the light-matter coupling is just one term in the expansion of the kinetic energy numerator (with $\boldsymbol{\chi} = \mathbf{A}$):

$$\begin{aligned}
(\hat{p} - \mathbf{A})^2 \phi(\mathbf{x}) &= (\hat{p}^2 - \hat{p}\cdot\mathbf{A} - \mathbf{A}\cdot\hat{p} + \underbrace{\mathbf{A}^2}_{\to 0})\phi(\mathbf{x}) \\
&= \hat{p}^2\phi(\mathbf{x}) - \hat{p}\cdot(\mathbf{A}\phi(\mathbf{x})) - (\mathbf{A}\cdot\hat{p})\phi(\mathbf{x}) \\
&= \hat{p}^2\phi(\mathbf{x}) - \underbrace{\phi(\mathbf{x})(\hat{p}\cdot\mathbf{A})}_{=0} - \mathbf{A}\cdot(\hat{p}\phi(\mathbf{x})) - (\mathbf{A}\cdot\hat{p})\phi(\mathbf{x}) \\
&= (\hat{p}^2 - 2\mathbf{A}\cdot\hat{p})\phi(\mathbf{x}),
\end{aligned}$$

where $\phi(\mathbf{x})\hat{p}\cdot\mathbf{A}$ vanishes due to the Coulomb gauge. The term $\mathbf{A}^2$ is dropped because its contribution to the total kinetic energy is negligible. This term corresponds to two-photon interactions between the matter and electric field. $\mathbf{A}^2$ is responsible for Rayleigh scattering [104], and its contribution is worth including only when the incident radiation is intense. Also, why $\hat{p}\cdot\mathbf{A}$ does not automatically vanish in apparent agreement with the Coulomb gauge is due to the operation of this term on a wave function. The term $\hat{p}\cdot\mathbf{A}$ being a part of a Hamiltonian *operator*, the radiation gauge condition cannot be activated until it acts on a state function. After all, if $\phi(\mathbf{x})$ satisfies the criteria necessary to be a part of a Hilbert space, $\hat{p}\cdot\mathbf{A}\phi(\mathbf{x})$ will not vanish, so one must expand this dot product using the chain rule to properly exact the gauge simplification. We note that this is identical to claiming that the Coulomb gauge incidentally validates the commutation expression $\hat{p}\cdot\mathbf{A} = \mathbf{A}\cdot\hat{p}$. This permits the grouping of like terms, leading to the $2\mathbf{A}\cdot\hat{p}$ term in the kinetic energy [15, 104].

The result of the expansion is a momentum term and a coupling term. This coupling term is the semi-

classical light-matter interaction Hamiltonian:

$$\hat{H}_{int} = \mathbf{A} \cdot \hat{p} \tag{2.120}$$

The matrix elements of this term may be used to calculate the optical response of solids. To see this, one may analyze the interaction Hamiltonian as a time-dependent perturbation to be treated with time-dependent perturbation theory. One expresses the vector potential as a plane wave with a real-valued amplitude: $\mathbf{A} = \mathbf{A}_0 e^{i(\mathbf{k}\cdot\mathbf{x}-\omega t)}$. The matrix elements of the interaction Hamiltonian are

$$\langle \phi_f | \hat{H}_{int} | \phi_i \rangle = \langle \phi_f | \mathbf{A} \cdot \hat{p} | \phi_i \rangle, \tag{2.121}$$

where the state vectors are eigenvectors of the unperturbed Hamiltonian $\hat{H}_0$, corresponding to eigenstates E_f and E_i. Using the commutation relation $[\hat{H}_0, \mathbf{x}] = -i\hat{p}$, the matrix elements become

$$\langle \phi_f | \hat{H}_{int} | \phi_i \rangle = i \left[e^{-i\omega t} \mathbf{A}_0 \cdot \langle \phi_f | e^{i(\mathbf{k}\cdot\mathbf{x})} (\hat{H}_0 \mathbf{x} - \mathbf{x}\hat{H}_0) | \phi_i \rangle \right]. \tag{2.122}$$

In the long wavelength limit, where $\boldsymbol{\lambda} \to \infty$, wave vector $\mathbf{k}$ vanishes. Factoring in the electron charge to make the dipole operator $\mathbf{d} = -\mathbf{x}$, one has

$$\langle \phi_f | \hat{H}_{int} | \phi_i \rangle = -i \left[e^{-i\omega t} \mathbf{A}_0 \cdot \langle \phi_f | \mathbf{d} | \phi_i \rangle (E_f - E_i) \right]. \tag{2.123}$$

In general this term describes the interaction between a time-dependent vector potential and the dipole moment of the system. The matrix elements $\mathbf{d}_{fi} = \langle \phi_f | \mathbf{d} | \phi_i \rangle$ may be used to calculated the optical absorption. In KS-TDDFT and OF-TDDFT, these matrix elements are not used to calculate the dipole moment. Instead, the dipole moment is an integral over the product of the time-dependent density and position operator:

$$\mathbf{d} = \int \mathbf{x} \rho(\mathbf{x}, t) \; d\mathbf{x}, \tag{2.124}$$

where $\rho(\mathbf{x}, t)$ is understood to be the KS density of eq. 2.8. The density being propagated in time, one may directly acquire information about the dipole moment of the system from it.

The definition of the dipole operator used in density functional theory may be derived by representing the total wave function as a Slater determinant containing one-electron wave functions. Letting the state vector

be represented using Ψ, the dipole transition matrix element is defined as

$$\mathbf{d}_{ab} = \langle \Psi_a(t) | \mathbf{x} | \Psi_b(t) \rangle. \tag{2.125}$$

To start, one must project the state vectors into position space.

$$|\Psi_a(t)\rangle = \int d\mathbf{x} \, |\mathbf{x}\rangle \langle \mathbf{x} | \Psi_a(t) \rangle \;\text{ with }\; \langle \mathbf{x} | \Psi_a(t) \rangle = \Psi_a(\mathbf{x}, t). \tag{2.126}$$

Substituting this expression for the state vectors yields

$$\mathbf{d}_{ab} = \int d\mathbf{x} \int d\mathbf{x}' \langle \Psi_a(t) | \mathbf{x} \rangle \, \mathbf{x} \, \delta(\mathbf{x} - \mathbf{x}') \langle \mathbf{x}' | \Psi_b(t) \rangle \tag{2.127}$$

$$= \int d\mathbf{x} \, \langle \Psi_a(t) | \mathbf{x} \rangle \, \mathbf{x} \int d\mathbf{x}' \, \delta(\mathbf{x} - \mathbf{x}') \langle \mathbf{x}' | \Psi_b(t) \rangle \tag{2.128}$$

$$= \int d\mathbf{x} \, \mathbf{x} \, \Psi_a^*(\mathbf{x}, t) \Psi_b(\mathbf{x}, t). \tag{2.129}$$

In the single-particle approximation, the properties of the many-body wave function are dispersed among multiple, non-interacting wave functions. To include the necessary antisymmetry properties of the wave functions, the wave functions may be described using the Slater determinant. Letting $\mathbf{x}$ represent a set of position configurations $\{\mathbf{x}_1, \mathbf{x}_2, ..., \mathbf{x}_N\}$, the Slater determinant is

$$\Psi_k(\{\mathbf{x}\}, t) = \frac{1}{\sqrt{N!}} \begin{vmatrix} \eta_1^{(k)}(\mathbf{x}_1, t) & \eta_1^{(k)}(\mathbf{x}_2, t) & \cdots & \eta_1^{(k)}(\mathbf{x}_N, t) \\ \eta_2^{(k)}(\mathbf{x}_1, t) & \eta_2^{(k)}(\mathbf{x}_2, t) & \cdots & \eta_2^{(k)}(\mathbf{x}_N, t) \\ \vdots & \vdots & \ddots & \vdots \\ \eta_N^{(k)}(\mathbf{x}_1, t) & \eta_N^{(k)}(\mathbf{x}_2, t) & \cdots & \eta_N^{(k)}(\mathbf{x}_N, t) \end{vmatrix}. \tag{2.130}$$

The $\frac{1}{\sqrt{N!}}$ being a normalization constant, as η_l represents single-particle wave function l. The k signifies that all the single-particle wave functions are associated with the many-body wave function in state k. Assuming the dipole operator corresponds to $\mathbf{x}_1$, the substitution of the Slater determinant definition of the wave function into eq. 2.129 yields

$$\mathbf{d}_{ab}(t) = \sum_{i=1}^{N} \int d\mathbf{x}_1 \eta_i^{(a)*}(\mathbf{x}_1, t) \mathbf{x}_1 \eta_i^{(b)}(\mathbf{x}_1, t) \prod_{j>1}^{N} \prod_{h \neq i}^{N} \int d\mathbf{x}_j \eta_h^{(a)*}(\mathbf{x}_j, t) \eta_h^{(b)}(\mathbf{x}_j, t). \tag{2.131}$$

The single-particle wave functions are indexed using j and h, and this index is not to be confused with the state label. Here one must assign a meaning of the state labels a and b to suit the non-interacting electrons. The many-body wave function carries the state labels used to elucidate the system selection rules. Particular

transition trajectories, however, are an emergent property of a many-electron system *with* interactions inert to generalization for non-interacting cases. Nicely lending itself to this idea is the structure of the Slater determinant: nullifying interactions allows for the distribution of all remnant properties among numerous orbitals. Therefore, emergent phenomena are deconstructed into disparate, unrecognizable parts, a physicality incongruous with the symmetry functionality of the original many-body wave function. This requires that the symmetries responsible for the selection rules must be injected into the Hamiltonian some other way, such as through the core, Hartree, and exchange-correlation potentials in the KS equation of motion. With this, one may drop labels a and b

In dropping the state labels, the double product term becomes unity for each i, making

$$\mathbf{d}_{ab}(t) = \sum_{i=1}^{N} \int d\mathbf{x}_1 \eta_i^{(a)*}(\mathbf{x}_1,t)\mathbf{x}_1\eta_i^{(b)}(\mathbf{x}_1,t) \underbrace{\prod_{j>1}^{N}\prod_{h\neq i}^{N}\int d\mathbf{x}_j \eta_h^{(a)*}(\mathbf{x}_j,t)\eta_h^{(b)}(\mathbf{x}_j,t)}_{=1} \tag{2.132}$$

$$\therefore \quad \mathbf{d}(t) = \sum_{i=1}^{N} \int d\mathbf{x}_1 \eta_i^{*}(\mathbf{x}_1,t)\mathbf{x}_1\eta_i(\mathbf{x}_1,t), \tag{2.133}$$

which contains a substructure identical to the entirety of eq. 2.15. Acknowledging this, one obtains

$$\mathbf{d}(t) = \sum_{i=1}^{N} \int d\mathbf{x}_1 \eta_i^{*}(\mathbf{x}_1,t)\mathbf{x}_1\eta_i(\mathbf{x}_1,t) \tag{2.134}$$

$$= \int d\mathbf{x}_1\mathbf{x}_1 \sum_{i=1}^{N} |\eta_i(\mathbf{x}_1,t)|^2 \tag{2.135}$$

$$= \int d\mathbf{x}_1\mathbf{x}_1 \rho(\mathbf{x}_1,t) \tag{2.136}$$

the dipole operator used in time-dependent density functional theory.

2.3.2 Quantum-Quantum: The Pauli-Fierz Hamiltonian

The Pauli-Fierz Hamiltonian is eq. 2.119 but with a quantized vector potential and an extra term representing the free photon field, from the component excluded in the evaluation of the selected QED equation of motion. To avoid the redundancy in the longitudinal field terms, the electron source term in the general vector potential is once again excluded. For simplicity, eq. 2.81 is expressed using one photon polarization here:

$$\hat{\mathbf{A}}(\mathbf{x}) = \sqrt{\left(\frac{c^2}{\varepsilon_0 L^3}\right)} \sum_n \frac{\mathbf{e}_n}{\sqrt{2\omega_n}} [\hat{a}_n e^{i\mathbf{k_n}\cdot\mathbf{x}} + \hat{a}_n^{\dagger} e^{-i\mathbf{k_n}\cdot\mathbf{x}}], \tag{2.137}$$

where $\mathbf{n} \to n$ for convenience. Taking the long wavelength limit ($e^{i\mathbf{k_n}\cdot\mathbf{x}} \approx 1$), grouping squared terms, and factoring the cavity term $\frac{1}{\sqrt{L^3}}$ and the polarization vector into the parenthetical term yields an even more

wieldy version of the vector potential,

$$\hat{\mathbf{A}}(\mathbf{x}) = \sum_n \sqrt{\frac{1}{2\varepsilon_0 \omega_n}} [\hat{a}_n \mathbf{u}_n(\mathbf{x}) + \hat{a}_n^\dagger \mathbf{u}_n(\mathbf{x})^*], \tag{2.138}$$

where the cavity mode function has been defined as $\mathbf{u}_n(\mathbf{x}) = \mathbf{e}_n/\sqrt{L^3}$. In general, the cavity mode function would contain the mode expansion exponential term. Lastly, since this thesis concerns only cavity QED problems (see chapters 4 and 5), it is useful to put the quantum emitter (the many-electron system) in the center of the cavity, then establish a novel polarization vector storing all the constants and vectors defining the vector potential:

$$\hat{\mathbf{A}}(\mathbf{x}_0) = \sum_n \boldsymbol{\lambda}_n q_n, \tag{2.139}$$

where $\boldsymbol{\lambda}_n = \sqrt{\frac{1}{\varepsilon_0}}\,\mathbf{u}_n(\mathbf{x}_0)$, $\mathbf{x}_0$ is the center of the cavity, and q_n is the photon displacement coordinate. Recall that in Hartree atomic units, $\varepsilon_0 = \frac{1}{4\pi}$. These specifications give the Hamiltonian the form

$$\hat{H}_V = \frac{(\hat{p} - \hat{\mathbf{A}})^2}{2m} + U + \sum_n \frac{1}{2}\left[\frac{\partial^2}{\partial q_n^2} + \omega_n^2 q_n^2\right], \tag{2.140}$$

where U is of appropriate form and stores external terms. The third term is eq. 2.97, the quantized electromagnetic energy density operator, also known as the photon field Hamiltonian. It is easiest to derive this term separately, without using $\mathscr{L}_{QED}$, then add it to the total energy Hamiltonian. Eq. 2.119 is the Pauli-Fierz Hamiltonian in velocity gauge. The m is the mass of the electron, and though in our selected units system $m = 1$, it is included for clarity.

The phenomena concerning this thesis will use eq. (2.119) in length gauge. The unitary transformation needed to change the Hamiltonian into length gauge is

$$\Psi = T\Phi \;\;\rightarrow\;\; \hat{H}_V\Psi = \hat{H}_V T\Phi \;\;\rightarrow\;\; \hat{H}_V\Psi = \hat{H}_L\Phi \tag{2.141}$$

where $T = \exp\{i\hat{\mathbf{A}}(\mathbf{x}_0)\cdot\mathbf{D}\}$, and $\mathbf{D}$ is the total dipole operator $\mathbf{D} = \sum_i \mathbf{x}_i$. In this context, this transformation is known as the Power-Zienau-Woolley gauge transformation [105, 106, 107]. We note here two ways to transform the Hamiltonian into its length gauge form. Hamiltonian equations consisting of both electron and photon operators require Φ states that are Hilbert-Fock tensor products. Φ in eq. 2.141 must therefore be receptive to both Hilbert and Fock space operators. This is what we assume in eq. 2.141, and it is our transformation method of choice. The general form of this tensor product is,

$$\Psi = \Gamma_{\text{Hilbert}} \otimes \Gamma_{\text{Fock}}, \tag{2.142}$$

where Γ_{Hilbert} is the Hilbert space (electron) state and Γ_{Fock} is the Fock space (photon) state. It is this tensor product state that is transformed by the appropriate exponential factor affecting the gauge transformation. The transformation method used in [108] is an active transformation of the operators,

$$\hat{H}_L = T^\dagger \hat{H}_V T. \tag{2.143}$$

The following shows the specific effect the transformation. Letting index α represent the mode suitable to execute the derivative, the first kinetic energy term transforms as,

$$\begin{aligned}
\hat{p}_\alpha^2 \Psi &= \hat{p}_\alpha^2 T\Phi && (2.144)\\
&= -\nabla_\alpha^2 e^{i\hat{\mathbf{A}}(\mathbf{x}_0)\cdot\mathbf{D}}\Phi && (2.145)\\
&= -\nabla_\alpha \cdot (e^{i\hat{\mathbf{A}}(\mathbf{x}_0)\cdot\mathbf{D}}\nabla_\alpha\Phi + i\hat{\mathbf{A}}e^{i\hat{\mathbf{A}}(\mathbf{x}_0)\cdot\mathbf{D}}\Phi) && (2.146)\\
&= -(e^{i\hat{\mathbf{A}}(\mathbf{x}_0)\cdot\mathbf{D}}\nabla_\alpha^2\Phi + i\hat{\mathbf{A}}e^{i\hat{\mathbf{A}}(\mathbf{x}_0)\cdot\mathbf{D}}\cdot\nabla_\alpha\Phi - \hat{\mathbf{A}}^2 e^{i\hat{\mathbf{A}}(\mathbf{x}_0)\cdot\mathbf{D}}\Phi + i\hat{\mathbf{A}}e^{i\hat{\mathbf{A}}(\mathbf{x}_0)\cdot\mathbf{D}}\cdot\nabla_\alpha\Phi) && (2.147)\\
&= -(e^{i\hat{\mathbf{A}}(\mathbf{x}_0)\cdot\mathbf{D}}\nabla_\alpha^2\Phi + 2i\hat{\mathbf{A}}e^{i\hat{\mathbf{A}}(\mathbf{x}_0)\cdot\mathbf{D}}\cdot\nabla_\alpha\Phi - \hat{\mathbf{A}}^2 e^{i\hat{\mathbf{A}}(\mathbf{x}_0)\cdot\mathbf{D}}\Phi) && (2.148)\\
&= -e^{i\hat{\mathbf{A}}(\mathbf{x}_0)\cdot\mathbf{D}}(\nabla_\alpha^2 + 2i\hat{\mathbf{A}}\cdot\nabla_\alpha - \hat{\mathbf{A}}^2)\Phi && (2.149)\\
\therefore\quad \hat{p}_\alpha^2 &\to \hat{p}_\alpha^2 - 2i\hat{\mathbf{A}}\cdot\nabla_\alpha + \hat{\mathbf{A}}^2. && (2.150)
\end{aligned}$$

The second kinetic energy term transforms as,

$$\begin{aligned}
-2\hat{\mathbf{A}}\cdot\hat{p}_\alpha\Psi &= -2\hat{\mathbf{A}}\cdot\hat{p}_\alpha T\Phi && (2.151)\\
&= 2i\hat{\mathbf{A}}\cdot\nabla_\alpha e^{i\hat{\mathbf{A}}(\mathbf{x}_0)\cdot\mathbf{D}}\Phi && (2.152)\\
&= 2i\hat{\mathbf{A}}\cdot(e^{i\hat{\mathbf{A}}(\mathbf{x}_0)\cdot\mathbf{D}}\nabla_\alpha\Phi + i\hat{\mathbf{A}}e^{i\hat{\mathbf{A}}(\mathbf{x}_0)\cdot\mathbf{D}}\Phi) && (2.153)\\
&= (2ie^{i\hat{\mathbf{A}}(\mathbf{x}_0)\cdot\mathbf{D}}\hat{\mathbf{A}}\cdot\nabla_\alpha\Phi - 2\hat{\mathbf{A}}^2 e^{i\hat{\mathbf{A}}(\mathbf{x}_0)\cdot\mathbf{D}}\Phi) && (2.154)\\
&= e^{i\hat{\mathbf{A}}(\mathbf{x}_0)\cdot\mathbf{D}}(2i\hat{\mathbf{A}}\cdot\nabla_\alpha - 2\hat{\mathbf{A}}^2)\Phi && (2.155)\\
\therefore\quad -2\hat{\mathbf{A}}\cdot\hat{p}_\alpha &\to 2i\hat{\mathbf{A}}\cdot\nabla_\alpha - 2\hat{\mathbf{A}}^2. && (2.156)
\end{aligned}$$

We drop the $\hat{\mathbf{A}}^2$, but note that keeping it, and keeping the $\hat{\mathbf{A}}^2$ term in the kinetic energy expansion, would result in the cancellation of these terms. Also, we assume U is unaffected by the transformation.

Moving on to the terms in the photon Hamiltonian, we are presented with a fork in the road leading toward the Pauli-Fierz Hamiltonian. One fork would have us proceed with the derivation as we have, using a

transformed Hilbert-Fock wave function. Doing this leaves the photon coordinate operator unaffected,

$$\omega_n^2 q_n^2 T\Phi \rightarrow \omega_n^2 q_n^2. \tag{2.157}$$

Expressing $\frac{\partial^2}{\partial q_n^2}$ as $\partial_{q_n}^2$, the momentum operator transforms like so:

$$\begin{aligned}
\partial_{q_n}^2 e^{i\hat{\mathbf{A}}\cdot\mathbf{D}}\Phi &= \partial_{q_n}(\Phi\partial_{q_n}e^{i\hat{\mathbf{A}}\cdot\mathbf{D}} + e^{i\hat{\mathbf{A}}\cdot\mathbf{D}}\partial_{q_n}\Phi) && (2.158)\\
&= \partial_{q_n}(\Phi^{i\hat{\mathbf{A}}\cdot\mathbf{D}}\partial_{q_n} i\hat{\mathbf{A}}\cdot\mathbf{D} + e^{i\hat{\mathbf{A}}\cdot\mathbf{D}}\partial_{q_n}\Phi) && (2.159)\\
&= \partial_{q_n}(\Phi e^{i\hat{\mathbf{A}}\cdot\mathbf{D}} i\sum_n \boldsymbol{\lambda}_n\cdot\mathbf{D} + e^{i\hat{\mathbf{A}}\cdot\mathbf{D}}\partial_{q_n}\Phi) && (2.160)\\
&= (\partial_{q_n}\{\Phi e^{i\hat{\mathbf{A}}\cdot\mathbf{D}}\} i\sum_n \boldsymbol{\lambda}_n\cdot\mathbf{D} + \partial_{q_n}\{e^{i\hat{\mathbf{A}}\cdot\mathbf{D}}\partial_{q_n}\Phi\}) && (2.161)\\
&= (\{\Phi\partial_{q_n}e^{i\hat{\mathbf{A}}\cdot\mathbf{D}} + e^{i\hat{\mathbf{A}}\cdot\mathbf{D}}\partial_{q_n}\Phi\} i\sum_n \boldsymbol{\lambda}_n\cdot\mathbf{D} + \{e^{i\hat{\mathbf{A}}\cdot\mathbf{D}}\partial_{q_n}^2\Phi + \partial_{q_n}e^{i\hat{\mathbf{A}}\cdot\mathbf{D}}\partial_{q_n}\Phi\}) && (2.162)\\
&= (\{\Phi e^{i\hat{\mathbf{A}}\cdot\mathbf{D}} i\sum_n(\boldsymbol{\lambda}_n\cdot\mathbf{D}) + e^{i\hat{\mathbf{A}}\cdot\mathbf{D}}\partial_{q_n}\Phi\} i\sum_n(\boldsymbol{\lambda}_n\cdot\mathbf{D}) + \{e^{i\hat{\mathbf{A}}\cdot\mathbf{D}}\partial_{q_n}^2\Phi + e^{i\hat{\mathbf{A}}\cdot\mathbf{D}} i\sum_n \boldsymbol{\lambda}_n\cdot\mathbf{D}\partial_{q_n}\Phi\}) && (2.163)\\
&= (-\Phi e^{i\hat{\mathbf{A}}\cdot\mathbf{D}}\sum_n(\boldsymbol{\lambda}_n\cdot\mathbf{D})^2 + e^{i\hat{\mathbf{A}}\cdot\mathbf{D}}\partial_{q_n}\Phi\, i\sum_n(\boldsymbol{\lambda}_n\cdot\mathbf{D}) + e^{i\hat{\mathbf{A}}\cdot\mathbf{D}}\partial_{q_n}^2\Phi + e^{i\hat{\mathbf{A}}\cdot\mathbf{D}} i\sum_n(\boldsymbol{\lambda}_n\cdot\mathbf{D})\partial_{q_n}\Phi) && (2.164)\\
&= \sum_n e^{i\hat{\mathbf{A}}\cdot\mathbf{D}}(2i\boldsymbol{\lambda}_n\cdot\mathbf{D}\partial_{q_n} + \partial_{q_n}^2 - (\boldsymbol{\lambda}_n\cdot\mathbf{D})^2)\Phi && (2.165)\\
\therefore\quad \partial_{q_n}^2 &\rightarrow 2i\boldsymbol{\lambda}_n\cdot\mathbf{D}\partial_{q_n} + \partial_{q_n}^2 - (\boldsymbol{\lambda}_n\cdot\mathbf{D})^2. && (2.166)
\end{aligned}$$

The form of the transformed photon momentum operator is in agreement with what can be found in the literature [61, 108], though it is common to transform the photon operators according to,

$$\begin{aligned}
i\partial_{q_n} &\rightarrow p_n && (2.167)\\
q_n &\rightarrow -i\partial_{p_n}, && (2.168)
\end{aligned}$$

which maintains the commutation relationship between the operators. In this thesis, it is our preference to include an explicit light-matter coupling term in our electron-photon Hamiltonian. None of our transformations meet this preference, so we refer to the other side of the fork – transform the operator directly with the expression for T. In doing this, to simplify the mathematics, we use the ladder operator definition of the photon Hamiltonian, rewritten below for reference.

$$\sum_n \frac{1}{2}\left[\partial_{q_n}^2 + \omega_n^2 q_n^2\right] = \sum_n \omega_n\left[\hat{a}_n^\dagger\hat{a}_n + \frac{1}{2}\right] \tag{2.169}$$

To successfully transform the photon Hamiltonian, we make use of the Baker-Hausdorf lemma [109],

$$e^{iG\lambda}Ae^{-iG\lambda} = A + i\lambda[G,A] + \frac{i^2\lambda^2}{2!}[G,[G,A]] + \cdots + \left(\frac{i^n\lambda^n}{n!}\right)[G,[G,G[G,\ldots[G,A]]]] + \ldots, \tag{2.170}$$

in which A and G are operators, and λ is a real number not to be confused with the photon polarization vector. One may also use a method dependent on the identities for quasi-classical states (called coherent states in other textbooks [19, 105], explained in great detail in [105].

Using the lemma of eq. 2.170 up to its second order, and by setting $G = -i\hat{\mathbf{A}}\cdot\mathbf{D}$, one may transform the photon Hamiltonian as follow:

$$e^{-i\hat{\mathbf{A}}\cdot\mathbf{D}}\left[\hat{a}_n^\dagger\hat{a}_n - \frac{1}{2}\right]e^{i\hat{\mathbf{A}}\cdot\mathbf{D}} = \left[e^{-i\hat{\mathbf{A}}\cdot\mathbf{D}}\hat{a}_n^\dagger\hat{a}_n e^{i\hat{\mathbf{A}}\cdot\mathbf{D}} - \frac{1}{2}\right] \tag{2.171}$$

$$= \hat{a}_n^\dagger\hat{a}_n - i\mathbf{D}\cdot[\hat{\mathbf{A}},\hat{a}_n^\dagger\hat{a}_n] + \frac{\mathbf{D}^2}{2}[\hat{\mathbf{A}},[\hat{\mathbf{A}},\hat{a}_n^\dagger\hat{a}_n]] + \frac{1}{2} \tag{2.172}$$

$$= \hat{a}_n^\dagger\hat{a}_n - i\mathbf{D}\cdot[\hat{\mathbf{A}}\hat{a}_n^\dagger\hat{a}_n - \hat{a}_n^\dagger\hat{a}_n\hat{\mathbf{A}}] + \frac{\mathbf{D}^2}{2}[\hat{\mathbf{A}},\hat{\mathbf{A}}\hat{a}_n^\dagger\hat{a}_n - \hat{a}_n^\dagger\hat{a}_n\hat{\mathbf{A}}] + \frac{1}{2} \tag{2.173}$$

$$= \hat{a}_n^\dagger\hat{a}_n - i\mathbf{D}\cdot[\boldsymbol{\lambda}_n q_n\hat{a}_n^\dagger\hat{a}_n - \hat{a}_n^\dagger\hat{a}_n\boldsymbol{\lambda}_n q_n] + \frac{\mathbf{D}^2}{2}[\boldsymbol{\lambda}_n q_n,\boldsymbol{\lambda}_n q_n\hat{a}_n^\dagger\hat{a}_n - \hat{a}_n^\dagger\hat{a}_n\boldsymbol{\lambda}_n q_n] + \frac{1}{2}. \tag{2.174}$$

For the sake of clarity, we will expand the commutator terms individually and include the summation symbol.

Recalling that $q_n = \sqrt{\frac{1}{2\omega_n}}(\hat{a}_n + \hat{a}_n^\dagger)$, the first commutator term becomes,

$$\sum_n i\boldsymbol{\lambda}_n\cdot\mathbf{D}[q_n\hat{a}_n^\dagger\hat{a}_n - \hat{a}_n^\dagger\hat{a}_n q_n] = \sum_n i\sqrt{\frac{1}{2\omega_n}}\boldsymbol{\lambda}_n\cdot\mathbf{D}[(\hat{a}_n+\hat{a}_n^\dagger)\hat{a}_n^\dagger\hat{a}_n - \hat{a}_n^\dagger\hat{a}_n(\hat{a}_n+\hat{a}_n^\dagger)] \tag{2.175}$$

$$= \sum_n i\sqrt{\frac{1}{2\omega_n}}\boldsymbol{\lambda}_n\cdot\mathbf{D}[(\hat{a}_n\hat{a}_n^\dagger\hat{a}_n + \hat{a}_n^\dagger\hat{a}_n^\dagger\hat{a}_n) - (\hat{a}_n^\dagger\hat{a}_n\hat{a}_n + \hat{a}_n^\dagger\hat{a}_n\hat{a}_n^\dagger)] \tag{2.176}$$

$$= \sum_n i\sqrt{\frac{1}{2\omega_n}}\boldsymbol{\lambda}_n\cdot\mathbf{D}[((1+\hat{a}_n^\dagger\hat{a}_n)\hat{a}_n + \hat{a}_n^\dagger\hat{a}_n^\dagger\hat{a}_n) - (\hat{a}_n^\dagger\hat{a}_n\hat{a}_n + \hat{a}_n^\dagger(1+\hat{a}_n^\dagger\hat{a}_n))] \tag{2.177}$$

$$= \sum_n i\sqrt{\frac{1}{2\omega_n}}\boldsymbol{\lambda}_n\cdot\mathbf{D}[(\hat{a}_n + \hat{a}_n^\dagger\hat{a}_n\hat{a}_n + \hat{a}_n^\dagger\hat{a}_n^\dagger\hat{a}_n - \hat{a}_n^\dagger\hat{a}_n\hat{a}_n - \hat{a}_n^\dagger - \hat{a}_n^\dagger\hat{a}_n^\dagger\hat{a}_n)] \tag{2.178}$$

$$= \sum_n i\sqrt{\frac{1}{2\omega_n}}\boldsymbol{\lambda}_n\cdot\mathbf{D}[\hat{a}_n - \hat{a}_n^\dagger]. \tag{2.179}$$

This result helps to elucidate the second commutator term. The second commutator term becomes,

$$\sum_n \frac{\mathbf{D}^2}{2}[\boldsymbol{\lambda}_n q_n, \boldsymbol{\lambda}_n q_n \hat{a}_n^\dagger \hat{a}_n - \hat{a}_n^\dagger \hat{a}_n \boldsymbol{\lambda}_n q_n] = \sum_n \sqrt{\frac{1}{2\omega_n}} \frac{\boldsymbol{\lambda}_n^2 \cdot \mathbf{D}^2}{2}[q_n, \hat{a}_n - \hat{a}_n^\dagger] \tag{2.180}$$

$$= \sum_n \sqrt{\frac{1}{2\omega_n}} \frac{\boldsymbol{\lambda}_n^2 \cdot \mathbf{D}^2}{2}[q_n(\hat{a}_n - \hat{a}_n^\dagger) - (\hat{a}_n - \hat{a}_n^\dagger)q_n] \tag{2.181}$$

$$= \sum_n \frac{1}{2\omega_n} \frac{(\boldsymbol{\lambda}_n \cdot \mathbf{D})^2}{2}[(\hat{a}_n + \hat{a}_n^\dagger)(\hat{a}_n - \hat{a}_n^\dagger) - (\hat{a}_n - \hat{a}_n^\dagger)(\hat{a}_n + \hat{a}_n^\dagger)] \tag{2.182}$$

$$= \sum_n \frac{1}{2\omega_n} \frac{(\boldsymbol{\lambda}_n \cdot \mathbf{D})^2}{2}[2\hat{a}^\dagger \hat{a} - 2\hat{a}\hat{a}^\dagger] \tag{2.183}$$

$$= \sum_n \frac{1}{2\omega_n} (\boldsymbol{\lambda}_n \cdot \mathbf{D})^2 [\hat{a}^\dagger \hat{a} - (1 + \hat{a}^\dagger \hat{a})] \tag{2.184}$$

$$= \sum_n \frac{1}{2\omega_n} (\boldsymbol{\lambda}_n \cdot \mathbf{D})^2. \tag{2.185}$$

This nearly concludes the transformation of the electron and photon Hamiltonians. All together,

$$\frac{(\hat{p} - \hat{\mathbf{A}})^2}{2m} + U + \sum_n \frac{1}{2}\left[\frac{\partial^2}{\partial q_n^2} + \omega_n^2 q_n^2\right] \rightarrow \tag{2.186}$$

$$\frac{\hat{p}^2}{2m} + U + \sum_n \omega_n \left[\left(\hat{a}_n^\dagger \hat{a}_n + \frac{1}{2}\right) - i\sqrt{\frac{1}{2\omega_n}} \boldsymbol{\lambda}_n \cdot \mathbf{D}(\hat{a}_n - \hat{a}_n^\dagger) + \frac{1}{2\omega_n}(\boldsymbol{\lambda}_n \cdot \mathbf{D})^2\right]$$

This does not include the real light-matter coupling we want, but it is quite close. Including this preference is the last step, and to achieve this we use the following transformation – a unitary phase transformation operator:

$$\hat{U}_\theta = \mathrm{e}^{i\frac{\pi}{2}\hat{a}^\dagger \hat{a}}, \tag{2.187}$$

the effect of which is

$$\hat{U}_\theta^\dagger \hat{a} \hat{U}_\theta \rightarrow i\hat{a} \tag{2.188}$$

$$\hat{U}_\theta^\dagger \hat{a}^\dagger \hat{U}_\theta \rightarrow -i\hat{a}^\dagger. \tag{2.189}$$

This relation is best used in reverse, by distributing the i in $i\sqrt{\frac{1}{2\omega_n}}\boldsymbol{\lambda}_n \cdot \mathbf{D}(\hat{a}_n - \hat{a}_n^\dagger)$ term of eq. 2.186 so that the ladder operators are carry it. In doing this, one may swap these terms out for their associated values in eqs. 2.188 and 2.189. Mathematically,

$$i\sqrt{\frac{1}{2\omega_n}}\boldsymbol{\lambda}_n \cdot \mathbf{D}(\hat{a}_n - \hat{a}_n^\dagger) = \sqrt{\frac{1}{2\omega_n}}\boldsymbol{\lambda}_n \cdot \mathbf{D}(i\hat{a}_n - i\hat{a}_n^\dagger) \tag{2.190}$$

$$\sqrt{\frac{1}{2\omega_n}}\boldsymbol{\lambda}_n \cdot \mathbf{D}(i\hat{a}_n - i\hat{a}_n^\dagger) \rightarrow \sqrt{\frac{1}{2\omega_n}}\boldsymbol{\lambda}_n \cdot \mathbf{D}(\hat{a}_n + \hat{a}_n^\dagger), \tag{2.191}$$

giving,

$$\sqrt{\frac{1}{2\omega_n}}\boldsymbol{\lambda}_n \cdot \mathbf{D}(\hat{a}_n + \hat{a}_n^\dagger) = q_n \boldsymbol{\lambda}_n \cdot \mathbf{D}. \tag{2.192}$$

With this change, we get the coveted length gauge form of the Pauli-Fierz Hamiltonian,

$$\hat{H}_L = \frac{\hat{p}^2}{2m} + U + \sum_n \left[\omega_n \left(\hat{a}_n^\dagger \hat{a}_n + \frac{1}{2} \right) - \omega_n q_n \boldsymbol{\lambda}_n \cdot \mathbf{D} + \frac{1}{2} (\boldsymbol{\lambda}_n \cdot \mathbf{D})^2 \right], \tag{2.193}$$

where the enclosed terms, from left to right, are the photon field, the photon-electron coupling term, and the dipole self-interaction. In this thesis the simultaneous treatment of classical and quantized electromagnetic fields will be required. For this situation, the perturbation due to an external classical field will be stored in the general potential term, U, of eq. 2.193.

2.4 Appendix for Chapter 2

2.4.1 Comments on the Total Dipole Operator

In the *study* of time-dependent density functional theory, the total dipole operator possesses two forms – a true operator variant and the density functionalized variant presented in section 2.3.1. Its operator form, to be denoted $\hat{\mathbf{D}}$, is a sum over position operators,

$$\hat{\mathbf{D}} = \sum_i \mathbf{x}_i. \tag{2.194}$$

The demarcation of definitions falls on the same line differentiating classical and quantum electrodynamics. For a charge density distribution $\rho(\mathbf{x})$, the total dipole moment of (time-independent) eq. 2.136 contains a linear combination of delta functions, presented generally as

$$\mathbf{D}(\mathbf{x}) = \int_V \rho(\mathbf{x}')(\mathbf{x}' - \mathbf{x}) d\mathbf{x}', \tag{2.195}$$

which should look familiar – if not from canonical texts, then from section 2.3.1. The particle distribution contributes the delta functions:

$$\rho(\mathbf{x}') = \sum_i^N q_i \delta(\mathbf{x} - \mathbf{x}_i), \tag{2.196}$$

where q_i is the charge of particle i. Substitution of the right-hand side of eq. 2.195 for the density in eq. 2.196 gives

$$\mathbf{D}(\mathbf{x}) = \int_V \rho(\mathbf{x}')(\mathbf{x}' - \mathbf{x}) d\mathbf{x}' \tag{2.197}$$

$$= \int_V \sum_i^N q_i \delta(\mathbf{x} - \mathbf{x}_i)(\mathbf{x}' - \mathbf{x}) d\mathbf{x}' \tag{2.198}$$

$$= \sum_i^N q_i (\mathbf{x} - \mathbf{x}_i). \tag{2.199}$$

We are free to pick a set of reference coordinates, and to minimize notational clutter, we set $\mathbf{x} = \mathbf{0}$, the origin. In addition, the charges of concern being electrons, we may replace q_i with the fundamental unit of charge – so $q_i = 1$ for all i. This returns the operator of eq. 2.194.

This definition of the operator is to be compared and contrasted from the definition of the dipole operator in eq. 2.136. Both definitions play a role in this thesis. The definitions may be explicitly connected by evaluating the many-body expectation value of the product of the density "operator" in eq. 2.196 and the position operator, and in turn, eqs. 2.125, 2.136, and 2.194 may be united beyond the nominal. Explicitly,

$$\langle \Psi | \mathbf{x} \rho(\mathbf{x}) | \Psi \rangle = \langle \Psi | \sum_i^N \mathbf{x} \delta(\mathbf{x} - \mathbf{x}_i) | \Psi \rangle \tag{2.200}$$

$$= \sum_i^N \int d\mathbf{x}_1, ..., \int d\mathbf{x}_N \langle \Psi | \mathbf{x}_1, ..., \mathbf{x}_N \rangle \mathbf{x} \delta(\mathbf{x} - \mathbf{x}_i) \mathbf{x} \langle \mathbf{x}_1, ..., \mathbf{x}_N | \Psi \rangle \tag{2.201}$$

$$= \int d\mathbf{x}_1, ..., \int d\mathbf{x}_N \langle \Psi | \mathbf{x}_1, ..., \mathbf{x}_N \rangle \mathbf{x} \delta(\mathbf{x} - \mathbf{x}_1) \mathbf{x} \langle \mathbf{x}_1, ..., \mathbf{x}_N | \Psi \rangle \tag{2.202}$$

$$= N \int d\mathbf{x}_1, ..., \int d\mathbf{x}_N \langle \Psi | \mathbf{x}_1, ..., \mathbf{x}_N \rangle \mathbf{x} \langle \mathbf{x}_1, ..., \mathbf{x}_N | \Psi \rangle \tag{2.203}$$

$$= \mathbf{x} n(\mathbf{x}), \tag{2.204}$$

where $n(\mathbf{x})$ is defined by eq. 2.8, from chapter 2, and may be expanded in terms of Slater determinants projected in position space to affect the single-particle approximation. The step of eq. 2.203 shows a coordinate substitution over all indicies. Specifically, due to coordinate symmetry, we may use $\mathbf{x}_i \rightarrow \mathbf{x}_1$. This eliminates the sum and requires multiplication by N, as every delta function induced change in the many-body wave function coordinates may be redirected from some r_i to r_1, without sacrificing generality.

The three definitions of the dipole operator being connected, caution should be exercised whenever it appears in an equation to avoid misinterpretation. Sometimes it will not be necessary to elucidate the exact form of the dipole operator, but depending on the context, the form chosen will be specified; however, the following rule of thumb is useful: if the equation does not assume the single-particle approximation for density functional theory, the dipole operator should be defined with respect to the density operator of eq.

2.194; if the equation does assume the single-particle approximation, then it should be safe to assume the dipole operator is defined by eq. 2.136. This hair-splitting will manifest in an important way in chapter 5, when we consider the forms of electron-photon terms in a quantum electrodynamical density functional theory.

CHAPTER 3

Light-Matter Coupled Time-Dependent Density Functional Theory

3.1 Structure of Quantum-Classical Algorithmic Coupling

The construction of a light-matter QCA scheme capitalizes on the variables shared by the coupled equations. The KS equation in length gauge has a kinetic term which uses the vector potential as input, which may be used to describe the real part of eq. 2.18,

$$\mathbf{j}(\mathbf{x},t) = \mathrm{Re}\left[\sum_{j=1}^{N}[\phi_j^*(\hat{p}+\mathbf{A}(\mathbf{x},t))\phi_j]\right], \tag{3.1}$$

where N is the number of KS orbitals. The value of the vector potential is calculated using Maxwell's equations, where the current is input for the curl of the magnetic field. The essence of QCA is the alternate and staggered time propagation of the Maxwell and electron waves, to accommodate a information loop between two inputs – the source current and vector potential.

A diagrammatic presentation of the general structure of QCA is shown in fig. 3.1. M and N, respectively, are functions of (j,A) and $(\bar{j},\bar{A})$. These functions generally represent any function implicitly dependent on j and A, letters selected to represent, respectively, the current and vector potential. Parameters j and $\bar{j}$ are general currents sharing a system and region in spacetime. For the same system and region in spacetime, there exists general vector potentials A and $\bar{A}$. Starting with $M(j(t);A(t))$, its current parameter is propagated in time to $j(t+\delta t)$, then introduced into the function N with the substitution $\bar{j} = j(t+\delta t)$. Likewise, after the current substitution, the vector potential in $N(\bar{j};\bar{A}(t)$ is time propagated from $\bar{A}(t)$ to $\bar{A}(t+\delta t)$. The time propagated vector potential is then introduced to function M with the vector potential substitution $A = \bar{A}(t+\delta t)$. From here the cycle starts over, and for each time step δt, there is a single loop through the cycle. The loop is broken when the designated maximum number of time steps has been reached.

Several theoretical and computational issues have to be addressed in the implementation of this time-propagation approach. QCA methods which time propagate both the EM and matter waves using FDTD have been developed [22, 23, 24, 25]. These approaches are interested in properties of the EM fields, neglecting atomic detail and electron correlations. In following the QCA scheme, the calculated EM field, codified by its vector potential, enters the kinetic energy term of the Schrodinger equation. Upon solving the matter equation of motion, the polarization current density may be calculated from the wave function. This current density is then used as input for the Maxwell equations.

What these approaches have in common is the incorporation of both EM and matter waves in FDTD,

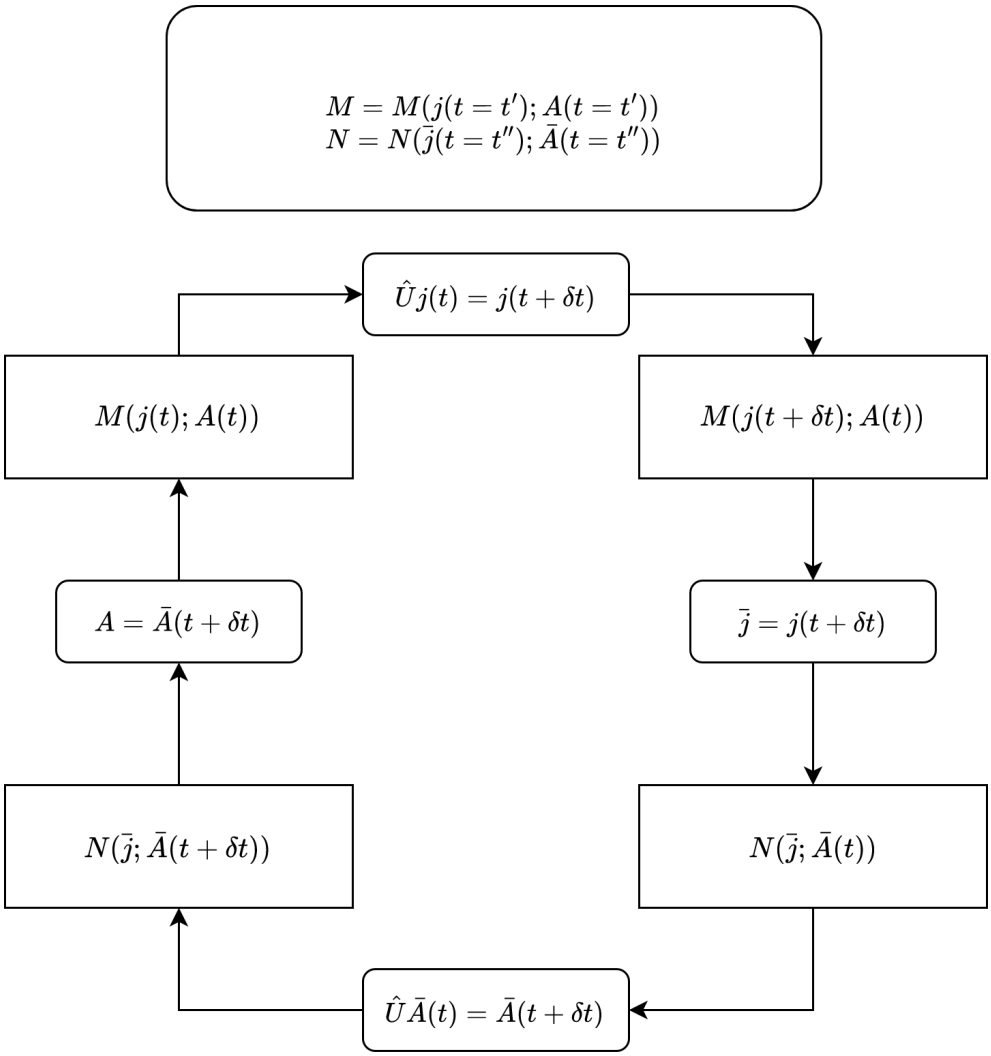

Figure 3.1: General structure of QCA scheme. M and N are defined as $M(j,A)$ and $N(\bar{j},\bar{A})$, where parameters j and $\bar{j}$ are general currents in the same system, and A and $\bar{A}$ are general vector potentials for the same system. $M(j(t);A(t))$ is propagated in time in its current to $j(t+\delta t)$, then introduced into the function N with the substitution $\bar{j} = j(t+\delta t)$. $N(\bar{j};\bar{A}(t))$ is then time propagated in its vector potential to $\bar{A}(t+\delta t)$. The time propagated vector potential is then introduced to function M with the vector potential substitution $A = \bar{A}(t+\delta t)$. The cycle then starts over.

where wave functions are propagated in a light wave propagation framework [110, 111, 112]. However, due to enormous spatiotemporal differences in the resolution of electronic and photonic phenomena – manifested of the speeds and wavelengths typical of their mutual dynamics – time propagating electrons and EM radiation on the same discretized grid poses a problem, and the time step Δt and grid spacing Δh are co-constrained by the Courant condition, $c\Delta t/\Delta h < 1$.

This inflexibility was brought up here [18, 26], and the solutions they offer is to reconfigure Maxwell's equations into a Schrodinger-like equation capable of being propagated by a unitary time evolution operator: instead of using the classical propagation device of FDTD on the coupled equations, one may use a quantum propagation device instead. Before doing this, however, one needs to make a Schrodinger-like equation out of Maxwell's equations, defining a wave function-like object as needed. The tool to do this is a complex, bilinear vector known as the Riemann-Silberstein (RS) vector [113, 114, 115, 116].

3.1.1 Riemann-Silberstein Electrodynamics

The RS vector is given by

$$\mathbf{F}(\mathbf{x},t) = \sqrt{\frac{\varepsilon_0}{2}}\mathbf{E}(\mathbf{x},t) \pm i\sqrt{\frac{\varepsilon_0}{2}}\mathbf{B}(\mathbf{x},t), \tag{3.2}$$

where $\mathbf{E}$ and $\mathbf{B}$ are, respectively, the electric and magnetic fields in a common region. The imaginary part of the RS vector represents different EM wave helicities. One can evaluate the divergence of eq. 3.2 using Maxwell's equations. Doing this gives

$$\nabla \cdot \mathbf{F} = \frac{\rho}{\sqrt{2\varepsilon_0}}. \tag{3.3}$$

This is the RS vector form of Maxwell's divergence equations. Taking the curl of eq 3.2 informed by Maxwell's equations yields

$$\nabla \times \mathbf{F} = -\sqrt{\frac{\varepsilon_0}{2c^2}}\frac{\partial \mathbf{B}}{\partial t} \pm i\sqrt{\frac{\varepsilon_0}{2c^2}}\left(\frac{\partial \mathbf{E}}{\partial t} + \frac{\mathbf{j}}{\varepsilon_0}\right), \tag{3.4}$$

where $\dot{\mathbf{E}}$ and $\dot{\mathbf{B}}$ are, respectively, the electric and magnetic fields in a common region. Eq 3.4 may be rewritten as

$$c\nabla \times \mathbf{F}(\mathbf{x},t) = i\frac{\partial}{\partial t}\mathbf{F}(\mathbf{x},t) + \frac{i}{\sqrt{2\varepsilon_0}}\mathbf{j}. \tag{3.5}$$

Presumably consistent with the spin-1 statistics of the photon [117], one may use spin-1 matrix identity $\mathbf{a}\times\mathbf{b} = -i(\hat{\mathbf{S}}\cdot\mathbf{a})\mathbf{b}$, where,

$$\hat{\mathbf{S}} = \begin{bmatrix} \hat{\mathbf{S}}_1 \\ \hat{\mathbf{S}}_2 \\ \hat{\mathbf{S}}_3 \end{bmatrix}, \tag{3.6}$$

and

$$\hat{\mathbf{S}}_1 = \begin{bmatrix} 0 & 0 & 0 \\ 0 & 0 & -i \\ 0 & i & 0 \end{bmatrix}, \ \hat{\mathbf{S}}_2 = \begin{bmatrix} 0 & 0 & i \\ 0 & 0 & 0 \\ -i & 0 & 0 \end{bmatrix}, \ \hat{\mathbf{S}}_3 = \begin{bmatrix} 0 & -i & 0 \\ i & 0 & 0 \\ 0 & 0 & 0 \end{bmatrix}, \tag{3.7}$$

to decompose the curl of the complex field into the spin projection of the RS vector momentum. Doing this and multiplying the entire result by $\hbar$ gives

$$i\hbar\frac{\partial \mathbf{F}}{\partial t} = c\left(\hat{\mathbf{S}}\cdot\frac{\hbar}{i}\nabla\right)\mathbf{F} - \frac{i\hbar}{\sqrt{2\varepsilon_0}}\mathbf{j}. \tag{3.8}$$

Recall that $\hbar = 1$, but is shown here for clarity. This inhomogenous, Schrodinger-like equation may be interpreted as the sum of an effective, "Maxwell Hamiltonian" and a source term, where the parenthetical term is the effective Hamiltonian: $\hat{H}_{MX} = c\left(\hat{\mathbf{S}}\cdot\frac{\hbar}{i}\nabla\right)$. Eq 3.3 and 3.8 constitute the equations of RS electrodynamics, where eq. 3.3 identifies the electromagnetic composition of the system (vacuum, electron gas, etc.) and eq. 3.8 encodes time-dependent behavior of the system in a quantum-friendly way. It is eq. 3.8 that can be propagated in time using the time evolution operator of quantum mechanics,

$$U(\hat{H};\Delta t) = \exp\left(-\frac{i\mathbf{H}\Delta t}{\hbar}\right). \tag{3.9}$$

As presented in [26], the solution for eq. 3.8 using a discretized, small time step approach is

$$\mathbf{F}(\mathbf{x},t+\Delta t_{MX}) = U(\hat{H}_{MX};\Delta t_{MX})\mathbf{F}(\mathbf{x},t) - \frac{i}{\hbar}U(\hat{H}_{MX};\Delta t_{MX})\int_0^{\Delta t_{MX}} U(\hat{H}_{MX};\tau)\frac{i\hbar}{\sqrt{2\varepsilon_0}}\mathbf{j}(\mathbf{x},t+\tau)\,d\tau, \tag{3.10}$$

where Δt_{MX} is the time step in the calculation. If the time step is sufficiently small then the integrand is approximately constant, giving

$$\mathbf{F}(\mathbf{x},t+\Delta t_{MX}) = U(\hat{H}_{MX};\Delta t_{MX})\mathbf{F}(\mathbf{x},t) - \frac{i\hbar}{\sqrt{2\varepsilon_0}}\mathbf{j}(\mathbf{x},t)\Delta t_{MX}. \tag{3.11}$$

This equation takes a virtually identical form in momentum space, where $\hat{H}_{MX}$ is diagonal:

$$\bar{\mathbf{F}}(\mathbf{k},t+\Delta t_{MX}) = U(\hat{H}_{MX};\Delta t_{MX})\bar{\mathbf{F}}(\mathbf{k},t) - \frac{i\hbar}{\sqrt{2\varepsilon_0}}\bar{\mathbf{j}}(\mathbf{k},t)\Delta t_{MX}. \tag{3.12}$$

Eq. 3.12 is an analytical approach and the EM time propagation equation that will be used in this chapter.

3.1.2 Coupled Maxwell-Schrodinger Formalism

With the general structure of the QCA as a guide, one may fashion an algorithm that propagates the Maxwell and Schrodinger equations simultaneously. To do so, one employs eq. 3.12 for the EM field and the following, numerical, real-space time propagation scheme for the electron orbitals $\phi_i(\mathbf{x},t)$:

$$\phi_i(\mathbf{x},t) = U(\hat{H}_{QM};0,t)\phi_i(\mathbf{x},0)$$

$$U(\hat{H}_{QM};0,t) = \bar{T}\exp\left[-\frac{i}{\hbar}\int_0^t \hat{H}_{QM}(\mathbf{x},\tau)d\tau\right], \tag{3.13}$$

where $\hat{H}_{QM}$ is the electron Hamiltonian and $\bar{T}$ is the time-ordering instruction to arrange affected time-dependent parameters in proper temporal sequence. In practice, one must time propagate the electrons incrementally, time step by time step. From the qth time step, $q\delta t$, the electron orbital is evolved to time step $q\delta t + \delta t$. The time evolution operator affecting this is

$$U(\hat{H}_{QM};0,t) = \prod_q U(\hat{H}_{QM};q\delta t, q\delta t+\delta t) \tag{3.14}$$

$$= \prod_q \exp\left[-\frac{i\delta t}{\hbar}\hat{H}_{QM}(\mathbf{x},q\delta t)\right], \tag{3.15}$$

where the time step is selected to be small enough to render the Hamiltonian constant over a single step. This thesis uses the Taylor time propagation approach [70] is used to represent the exponential term in eq. (3.15). Taylor expanding eq. 3.15 to the fourth-order,

$$U(\hat{H}_{QM};q\delta t, q\delta t+\delta t) \approx \sum_{m=0}^{4}\frac{1}{n!}\left[-\frac{i\delta}{\hbar}\hat{H}_{QM}(\mathbf{x},q\delta t)\right]^n, \tag{3.16}$$

where the unitarity of eq. (3.16) is preserved by the selection of a sufficiently small time step.

With the time propagation tools selected, the electrodynamics and quantum theory of choice determined, a sophisticated QCA based on fig. 3.1 conscious of the separate treatments of the light and matter time evolution may be constructed. Eqs. 3.12 and 3.16 use different time steps. In addition, they are executed in different parameter spaces. Therefore, to prevent instabilities, the time steps must obey the constraint $\frac{\delta t}{\Delta t_{MX}} \geq 20$. For ease, the same spatial grid is used for both the electrons and the EM fields.

The Leapfrog Algorithm, a temporally staggered QCA used in this thesis, is shown in table 3.1. It goes as follows: (0) for a many-electron system in a common region of spacetime, matter variables informed by a previously calculated ground state are initialized at time t, while EM variables are initialized at time $t-\delta t/2$; (1) the momentum space RS vector is calculated; (2) The momentum space current vector is calculated; (3)

Maxwell-Schrodinger QCA: Leapfrog Algorithm

Step Number: Command	**Input → Output**
0: Initialize Variables	$\phi(t), \mathbf{j}(t), \mathbf{A}(t-\delta t/2), \mathbf{F}(t-\delta t/2), V(t)$
1: FFT $\mathbf{x}$-space RS vector	$\text{FFT}\{\mathbf{F}(t-\delta t/2)\} \rightarrow \tilde{\mathbf{F}}(t-\delta t/2)$
2: FFT $\mathbf{x}$-space current	$\text{FFT}\{\mathbf{j}(t)\} \rightarrow \tilde{\mathbf{j}}(t)$
3: Propagate $\tilde{\mathbf{F}}$, add $\tilde{\mathbf{j}}$	$\tilde{\mathbf{j}}(t), \tilde{\mathbf{F}}(t-\delta t/2) \rightarrow \tilde{\mathbf{F}}(t+\delta t/2)$
4: Extract rotational component of $\tilde{\mathbf{F}}$	$\tilde{\mathbf{F}}(t+\delta t/2)\} \rightarrow \tilde{\mathbf{F}}_R(t+\delta t/2)$
5: FFT $\mathbf{p}$-space RS vectors	$\text{FFT}\{\tilde{\mathbf{F}}(t+\delta t/2)\}, \text{FFT}\{\tilde{\mathbf{F}}_R(t+\delta t/2)\} \rightarrow \mathbf{F}(t+\delta t/2), \mathbf{F}_R(t+\delta t/2)$
6: Use $\mathbf{F}_R$ to propagate $\mathbf{A}$	$\mathbf{A}(t), \mathbf{F}_R(t+\delta t/2) \rightarrow \mathbf{A}(t+\delta t)$
7: Interpolate $\mathbf{A}(t+\delta t/2)$ using $\mathbf{A}(t+\delta t)$ and $\mathbf{A}(t)$	$\mathbf{A}(t), \mathbf{A}(t+\delta t) \rightarrow \mathbf{A}(t+\delta t/2)$
8: Use $\mathbf{A}(t+\delta t/2)$ and $V(t)$ to evaluate $U(\hat{H}_{QM}, t+\delta t)\phi(t)$	$\mathbf{A}(t+\delta t/2), V(t), \phi(t) \rightarrow \phi(t+\delta t)$
9: Calculate $\mathbf{j}(t+\delta t)$ using $\hat{p}$, $\mathbf{A}(t+\delta t)$, and $\phi(t+\delta t)$	$\mathbf{A}(t+\delta t), \phi(t+\delta t) \rightarrow \mathbf{j}(t+\delta t)$
10: Solve Poisson equation using $\lvert\phi(t+\delta t)\rvert^2$	$\phi(t+\delta t) \rightarrow \mathbf{V}(t+\delta t)$

Table 3.1: The Leapfrog QCA for Maxwell-Schrodinger Coupling. The general form of this may be understood in terms of the general QCA scheme, with functions M and N being replaced with whatever quantum and electromagnetic functions are dependent on the current and vector potentials. The left column are the commands in human language, in order of execution. The right column sequentially lists the commands in a flow-like form.

The RS vector is propagated in time using Eq. 3.12, then the current term is subtracted from the result; (4) the divergence-less term is then extracted from the RS vector; (5) The full RS vector and its divergence-less term are returned to position space; (6) The rotational electric field in the rotational RS vector term is used to propagate the vector potential; (7) A new vector potential is temporally interpolated using the pre- and post-propagation vector potentials; (8) A new time evolution operator is constructed using the interpolated vector and scalar potentials, and is used to propagate the electron orbitals; (9) The vector potential calculated in step 6, the electron orbitals, and the momentum operator are used to calculated the new current; (10) the Poisson equation is solved by using the density of the propagated electron orbitals.

In Leapfrog QCA, the inclusion of RS electrodynamics is invariable as it must be propagated using the time evolution operator; however, any time-dependent quantum theory which includes an input for a vector potential is compatible with the algorithm, in principle. The calculations in this chapter use velocity gauge KS-TDDFT and OF-TDDFT, their formal differences only important to the vertices, if not the circuitry, of Leapfrog QCA: the I/O may have different internal structures, but the listed commands in table 3.1 do not change.

Before moving on to detailed applications of QCA coupling, it is useful to graphically represent the

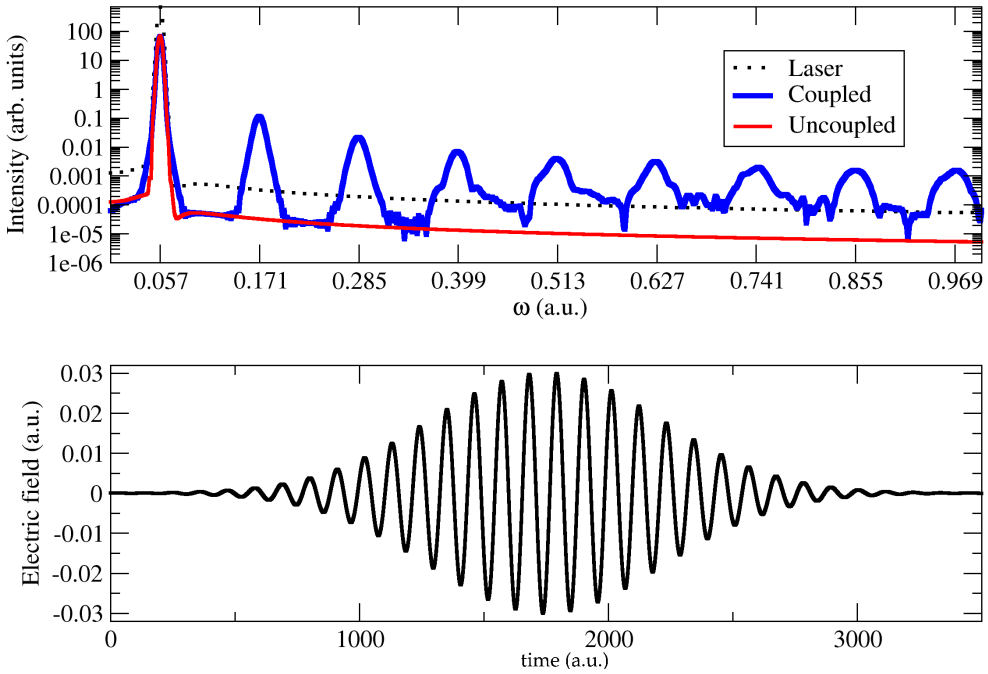

Figure 3.2: Coupled and uncoupled high harmonic generation spectra (top) of radiation transmitted through an aluminum sheet with a thickness of 0.6 nm. The laser pulse (bottom) has a wavelength of 800 nm, an amplitude of $E_0 = 0.03$ a.u., and a pulse duration of 3500 a.u. The spectra were generated using Fast Fourier transforms of outgoing radiation. Only the coupled case shows activity. The baseline difference between the uncoupled case and the laser is due to differences in temporal sampling.

impact QCA coupling has on the current and the outgoing radiation. In fig. 3.2, the high harmonic generation spectra (top) of laser light transmitted through an aluminum sheet are shown. The aluminum sheet has a thickness of 0.6 nm. The laser pulse has a wavelength of 800 nm, an amplitude of $E_0 = 0.03$ a.u., and a pulse duration of 3500 a.u. (bottom). As this exact simulation and others like it will come up later in this chapter, the reader will be spared its full computational details here.

Both spectra in the fig. 3.2 were generated using OF-TDDFT. As one can see, the coupling has the immediate impact of the net outgoing radiation being affected by the induced dipole field of the material. The uncoupled case has only one peak, at the frequency of the laser, showing that it effectively passed through a transparent medium. The intensity baseline difference between the uncoupled, outgoing radiation and the laser is due to its temporal sampling: for every ten time steps in the laser, the outgoing radiation was sampled. The application of OF-TDDFT to high harmonic generation is covered in section 3.3.

The coupled case shows that the electron-controlled back-reaction introduces into the field a dipole response. Traditionally, one would acquire HHG spectra using TDDFT by taking the Fouriert transform of the calculated electronic current. Here, one may calculate the HHG from the outgoing radiation instead, using the simulation box boundaries as "detectors." This better represents reality, as it is only through spectroscopy

can any investigator learn about the HHG spectra of a system. This is not to imply that we have simply added the laser field to the dipole field to make some trivial displacement field. The coupling itself can have an impact on the form of the high harmonic generation.

3.2 QCA coupled OF-TDDFT and KS-TDDFT Treatments of Stimulated Lithium Jellium Sheet

Computational electrodynamics has had great success modeling macroscopic systems (see citations in [2]). As electronic and optical devices get smaller, however, quantum effects become important, requiring computational electrodynamics techniques informed by quantum mechanics: an algorithimic light matter coupling approach. Such an approach is ideal for investigating nano-optical and nanoplasmonic phenomena, and the QCA Maxwell-Schrodinger coupling is, in principal, capable of this undertaking. To handle many-electron systems, though, one needs to tailor a density functional approach to the QCA coupling scheme.

Coupled Maxwell and TDDFT equations will now be used to examine excited state properties of a lithium jellium sheet. The predictions of the currents and fields by the coupled forms of KS-TDDFT and OF-TDDFT are found to be in close agreement with each other. The abilities of coupled OF-TDDFT are emphasized as it is the approach which makes nanostructures of experimental and industrial relevance computationally feasible to describe.

3.2.1 OF-TDDFT and Jellium for Quantum Simulation Feasibility Concerns

Recall the general, cubic scaling of KS-TDDFT approaches imposes an upper limit on the number of electrons that are computationally feasible to describe. This poses the problem of experimentally relevant systems being out of reach for any QCA employing KS-TDDFT, and because of quantum effects one cannot rely on the scaled-down versions of nanostructures of interest to replicate the results of the ideal. If one were to approximate the volume of the smallest device on the scale of relevant nano-engineering devices as a cubic nanometer, then an hollowed body centered cubic (BCC) lattice, with a lattice constant of 7 Bohr, filling the region would make 343 atoms. Generously assuming a single-valence electron atom, and ignoring the single unpaired electron, one would have 171 orbitals to normalize and make orthogonal to each other. Now assume an sp-atom and or fill the hollowed unit cell to make a proper BCC lattice – more electrons, more computation time. For real world reference, a stable 16,000 time step simulation on the computers used for this thesis, using only 80 electrons, takes about 80 hours. With the cubic scaling, attempts at simulating time-dependent physics for in-lab devices quickly becomes futile. Per this thesis, the most obvious solution is to use an OF-TDDFT QCA.

The introduction mentioned several quantum plasmonic-related successes with OF-TDDFT. Traditional OF-TDDFT has been used to investigate electron spill-out effects on nanorod and nanoparticle plasmons

[33, 35]. It has also been used to investigate quantum plasmonic field enhancement in nano-dimers [34]. Exploration in quantum plasmonics with OF-TDDFT is still in its infancy, but the promise having been demonstrated, it makes an ideal candidate for modeling strongly coupled light-matter systems, augmented with QCA. Yet OF-TDDFT has its weaknesses, as mentioned in chapter 2. The idea is to inform computational electrodynamics with, at least, qualitatively accurate quantum mechanics. Therefore, while coupled, one should ensure it works with longstanding popular toy models for nanoscience as well as system inexpensively treated with KS-TDDFT.

In this subsection, the toy model of choice is jellium, the simplest model of interacting electrons. In the jellium model [118, 119], the positive ions are smeared out to form a uniform background charge field in which the electrons interact with each other. Fitted into KS-TDDFT, the jellium model is useful for investigating the optical properties of numerous metallic nano-geometries [120]: optical absorption properties of spherical clusters [121, 122] and simple sp-metals [121, 122, 123, 124, 125]; vacuum and gap spill-out [55, 120, 126, 127, 128, 129, 130]; and tunneling current effects [120]. The main issue with the jellium model is its deliberate neglect of atomistic details [131, 132, 133]. For instance, in [120], the electric field enhancement at Mie LSPRs for sodium NPs is fragmented in the atomistic simulations, but whole and smooth in the jellium simulation. Nonetheless, the jellium is still effective at describing NP quantum behavior. The reluctance one might have about forgoing both orbital and atomic resolution is sensible; however, the critical heuristic of OF-TDDFT being geared toward applications for NPs of many atoms, and with subnanometric length scales not being the only scales of importance in experimentally relevant nanodevices, the wedding of QCA OF-TDDFT and jellium seems – and will prove – promising.

3.2.2 Computational Details

The KS-TDDFT and OF-TDDFT are separately coupled to the Maxwell equations using QCA. The KS equations are used as shown in Eqs. 2.8 and 2.9. The OF equations are used as shown in Eqs. 2.15 and 2.16. Since the ions – the protons and core electrons – are smeared to form a uniform, positively charged background to form jellium, psuedopotentials are not used. Using OF-TDDFT and jellium, however, is not all that needs discussing, as there still exists multiple computational obstacles that need to be addressed.

3.2.2.1 Real-Space Grid Approach

It should not be a surprise that a move from KS-TDDFT to OF-TDDFT does not mark the end of the storage dilemmas. Here, the OF-TDDFT and KS-TDDFT calculations are executed identically on a discretized real-space grid [70], the first of three devices to be introduced that help reduce simulation expenses. Mathematical functions are generally defined in domains of infinite size and resolution. Since computers have finite storage,

we are motivated to make mathematical domains and codomains computationally tractable by sampling points along both continua – defining the mathematical function only at the sampled points, between two endpoints – and excluding the remainder.

For example, to discretize a one-dimensional grid, one selects a starting point a, an ending point b, and a fixed distance between adjacent grid points h (the grid spacing). These values give a total grid point number N of

$$N = 1 + \frac{b-a}{h}. \tag{3.17}$$

Grid point x_i may be located using

$$x_i = a + (i-1)h. \tag{3.18}$$

This may be generalized to three dimensions, in which it is convenient to establish an indexing system for each grid point:

$$k = N_x N_y (i_x + 1 - 1) + N_y (i_y - 1) + i_z, \tag{3.19}$$

where k is the index for a point on a grid with $N = N_x N_y N_z$ points. N_x, N_y, and N_z are the respective number of grid points in the x, y, and z directions. Eq. 3.17 defines the grid spacing, and the three cardinal directions may have unique grid spacing values. In this thesis the grid spacings in all three directions will be the same. The mapping and inverse mapping between k and (i_x, i_y, i_z) helps store information, like functions, in vectors rather than higher-order tensors. Details on how the differential, integral, and vector calculus are performed on the grid may be found in [70, 134]

3.2.2.2 Complex Absorbing Potentials

Unfortunately, with grids being finite, a confrontation with boundary conditions is inevitable. Waves may reflect off the boundary and further stimulate the system as an undesirable consequence, but it is not efficient to make a grid extremely long in the direction of outgoing radiation. One may avoid making enormous grids to accommodate outgoing waves and their reflections off the grid boundary by using a complex absorbing potential (CAP) [70, 135, 136]. In the direction, say, an electron pulse is traveling, one may commit several layers of grid points lining the target boundary plane to absorbing the pulse, thus simulating outgoing radiation.

To understand how CAPs work for electrons waves, start with the continuity equation of quantum mechanics,

$$\nabla \cdot \mathbf{j} + \frac{\partial}{\partial t} |\Psi|^2 = 0, \tag{3.20}$$

where $\mathbf{j}$ is the current defined by eq. 2.18, and Ψ is the wave function for a single electron. If the wave

function corresponds to a non-Hermitian Hamiltonian containing a complex potential term, the continuity equation gets a conservation disrupting term

$$\nabla \cdot \mathbf{j} + \frac{\partial}{\partial t}|\Psi|^2 = 2|\Psi|^2 \mathrm{Im}(V), \tag{3.21}$$

where V is the complex potential. If the probability density is not changing in time, then

$$\nabla \cdot \mathbf{j} = 2|\Psi|^2 \mathrm{Im}(V). \tag{3.22}$$

Therefore, the current is not conserved, and depending on the sign of the imaginary part of the complex potential, probability density is either absorbed from or injected into the system.

Lastly, to simulate the physics of systems infinitely large in one or more directions – devices of experimental interest perhaps – if the lattice of the system has long-range translational symmetry, then one can use periodic boundary conditions (PBCs) instead of a large grid. Given a one-dimensional periodic potential,

$$V(x+L) = V(x), \tag{3.23}$$

which roughly captures the behavior of the symmetry of the material in one direction, according to Bloch's Theorem, the solutions for the Hamiltonian defined by the periodic potential are plane waves:

$$\psi_k(x) = e^{ikx}\phi_k(x), \tag{3.24}$$

where k is the crystal momentum, and $\phi_k(x)$ and its first derivative possesses the periodicity of $V(x)$. Explicitly,

$$\phi_k(x) = \phi_k(x+L) \tag{3.25}$$

and

$$\frac{d}{dx}\phi_k(x) = \frac{d}{dx}\phi_k(x+L), \tag{3.26}$$

and enforcing PBCs allows one to use the preparation and simulation of a "supercell" – the cell repeatedly imaged in the directions permitting PBCs – instead of the entire extended system without information loss. Supercells usually need only a minute fraction of the grid points required to simulate a complete material system; however, they come with the disadvantage of not being compatible with some operators, like the dipole operator (see Chapter 5).

The lithium jellium system is a 328-Bohr-wide sheet (17.35 nm) consisting of 36 electrons. The sheet

is contained in an isotropic simulation box of dimensions $(N_x, N_y, N_z) = (1152, 8, 8)$, with a grid spacing of $h = 0.5$ Bohr. PBCs were used for the y and z directions. The general form of the laser pulse is,

$$\mathbf{E}_{ext}(\mathbf{x}, t) = \hat{\mathbf{z}} E_0 e^{-(-t-t_0-x/c)^2/\alpha^2} \tag{3.27}$$

where t_0 is the pulse shift and α represents the width of the pulse. The electric field amplitude is parallel to the z-axis while the wave vector of the pulse itself is parallel to the x-axis. The laser parameters are E_0 = 0.02 a.u., α = 2.0 a.u. and t_0 = 6 a.u. To prevent EM wave reflection effects at the boundaries of the grid, a CAP of the following form is implemented in the x-direction:

$$\hat{H} = \hat{H}_{MX} + i\hat{W}_{MX}, \tag{3.28}$$

where $\hat{H}_{MX}$ is the RS vector Hamiltonian and $i\hat{W}_{MX}$ is of suitable form to absorb the outgoing electric field.

The time dependence of the electric field and currents are defined as averages over the grid points not in the CAP region:

$$\mathbf{E}(t) = \sum_{\mathbf{x}} \mathbf{E}(\mathbf{x}, t) \tag{3.29}$$

$$\mathbf{j}(t) = \sum_{\mathbf{x}} \mathbf{j}(\mathbf{x}, t). \tag{3.30}$$

Since the laser is in the z-direction, only the z-direction electric fields – E_z and components in its linear combination – and J_z are shown.

3.2.3 Results and Discussion

Fig. 3.3 shows the electronic properties of the stimulated lithium jellium sheet in the coupled and uncoupled cases. The coupled case is the application of the Maxwell-TDDFT QCA scheme. The uncoupled case is a traditional excited state TDDFT calculation, in which the Maxwell equations are not time propagated, reduced to the role of only stimulating the valence electrons. Recall the separate development of optical and solid-state theories – TDDFT is a matter-only approach, and therefore there is no need introduce into it the electronic feedback. Since there is no back-reaction on the field, the light transmits through the medium unaffected by internal, electronic changes. Therefore, there is no reason to propagate the Maxwell equations in time.

For QCA OF-TDDFT and QCA KS-TDDFT, the coupled and uncoupled current in the jellium system is shown in the top image of fig. 3.3. The coupling conditions yield mutually diverging results. After excitation, the uncoupled current is sustained, and the excited state persists for the remainder of the simulation. In the

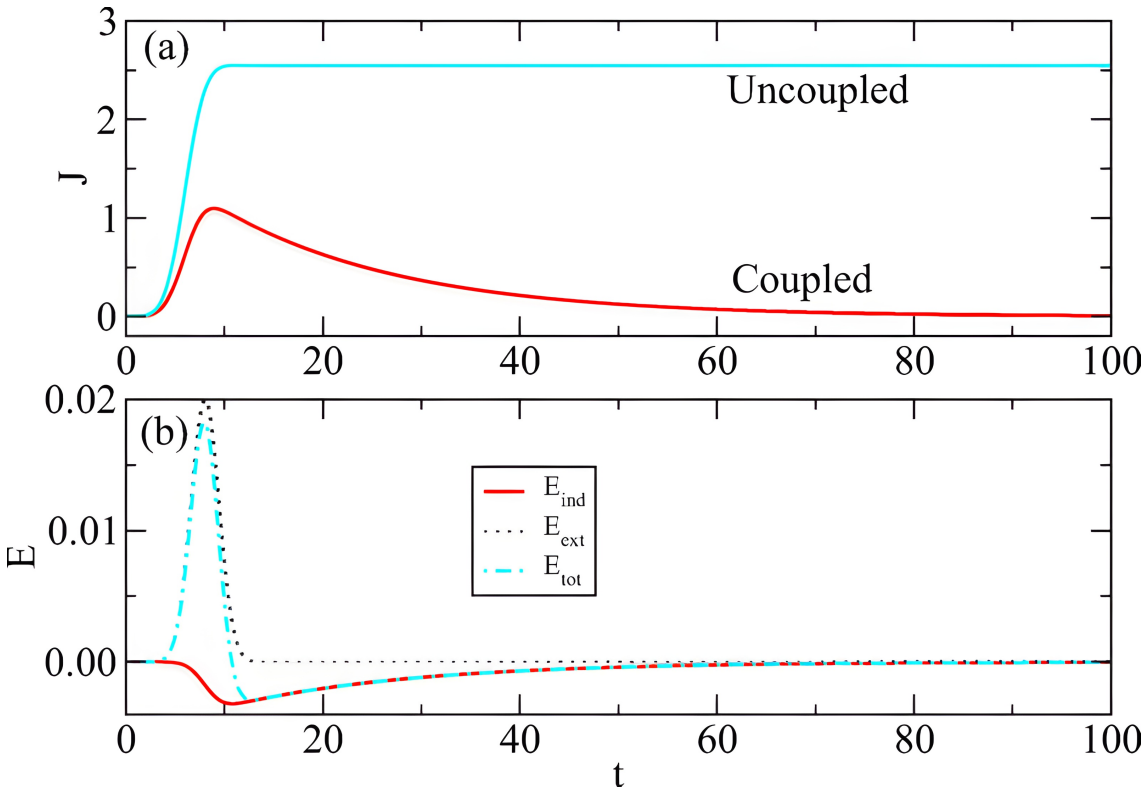

Figure 3.3: Comparison of OF-TDDFT and KS-TDDFT calculated averaged currents (top) and electric fields (bottom). The induced currents agree with each other up to four significant digits, as do the induced fields. 36 valence electrons are used. The thickness of the sheet is 328 Bohr. The grid dimensions are $(N_x, N_y, N_z) = (1152, 8, 8)$, with a grid spacing of $h = 0.5$ Bohr. PBCs were used for the y and z directions. The Gaussian pulse used to stimulate the system has the parameters E_0 = 0.02 a.u., a width of α = 2.0 a.u., and a shift of t_0 = 6 a.u.

coupled case, the current is reduced to zero. This is because the induced dipole field de-excites the electrons and quenches the current. For both versions of the QCA scheme, the dynamics are the same: identical up to four significant digits. As discussed in [137] this is due to periodic sheet symmetry. A finite system causes reflections yielding slight disagreements between OF- and KS-TDDFT.

The bottom image of fig. 3.3 shows the jellium electric field components for QCA OF-TDDFT. The external electric pulse – that is, the laser – appears in the total field. Shown is basic field superposition: the external field induces a dipole field, and the two combine to form a displacement field. The induced dipole field opposes the direction of the laser field, and after the laser pulse passes through the medium, the field of the displaced electrons slowly vanishes, which in turn leads to the depletion of the current. The displacement being the sum of the external and induced fields, the passing of the delta pulse means the only field determining the electron displacement is the field of the density itself, which should act to return the electrons to their ground state.

3.3 Interlude: High Harmonic Generation with Orbital-Free Time-Dependent Density Functional Theory

The success of QCA coupling in representing jellium is useful for describing the physics of simple metals; however, devices of relevance to nanoscale engineering are generally multifaceted, polyatomic structures with inhomogeneous components, anisotropic optical properties, and non-trivial valence electron distributions. At this stage the jellium model breaks down, requiring one to invoke atomistic details. The inclusion of atomistic details not only permits proper modeling of realistic multi-species nanostructures, but phenomena of physical descriptions within which ions are essential. Before applying coupled OF-TDDFT to an atomistic system, we take a detour to consider its fitness for describing the dynamics of atomistic in its uncoupled form.

One example of a phenomenon which relies on atomistic details is high harmonic generation (HHG). Earlier in this chapter we considered the effect coupling has on the outgoing radiation field, seeing that without the coupling no trace of the electron dynamics can be found in its HHG spectrum. That spectrum was generated using OF-TDDFT, and the differences between coupled and uncoupled OF-TDDFT pertaining to HHG will be covered here.

HHG is a highly nonlinear optical effect capable of generating coherent broadband radiation spanning frequencies from that of the driving laser to attosecond timescale pulses. Being crucial to the bedrock of attoscience, gas-phase HHG has helped advance methods probing molecular orbitals [138, 139] and techniques for generating isolated attosecond pulses [140]. More recently, solid-state HHG has been investigated [141, 142, 143, 144, 145, 146], opening the doors to engineered platforms for photonics in the attosecond domain.

Key to light-matter coupling is the information transfer of the matter dipole moment, induced by the laser field, from the excited electrons to the vector potential describing the radiation. If the intensity of the external radiation is high enough, an extreme nonlinear response may be seen in the photoemission spectrum. The form of the response is multiple, conspicuous signals at frequencies equal to an integer multiple of the laser driving frequency. HHG has been observed in numerous bodies of matter [147], including but not limited to doped systems [148], nanostructures, monolayer structures [149, 150, 151], and semi-conductors [152, 153].

The principals at work here are strictly quantum mechanical, but HHG may be understood semi-classically. In the "three-step picture" [154, 155, 156, 157] of the semi-classical model for HHG, the high-intensity radiation distorts the ionic potential containing the electron. The electron then tunnels through the thinned walls of the potential, picking up kinetic energy in the continuum due to the laser field. During this time, if the conditions are right, the field accelerates the electron back towards its parent ion. Finally, the electron is reabsorbed by the ion, and the energy picked up by the electron on its journey is released as energetic

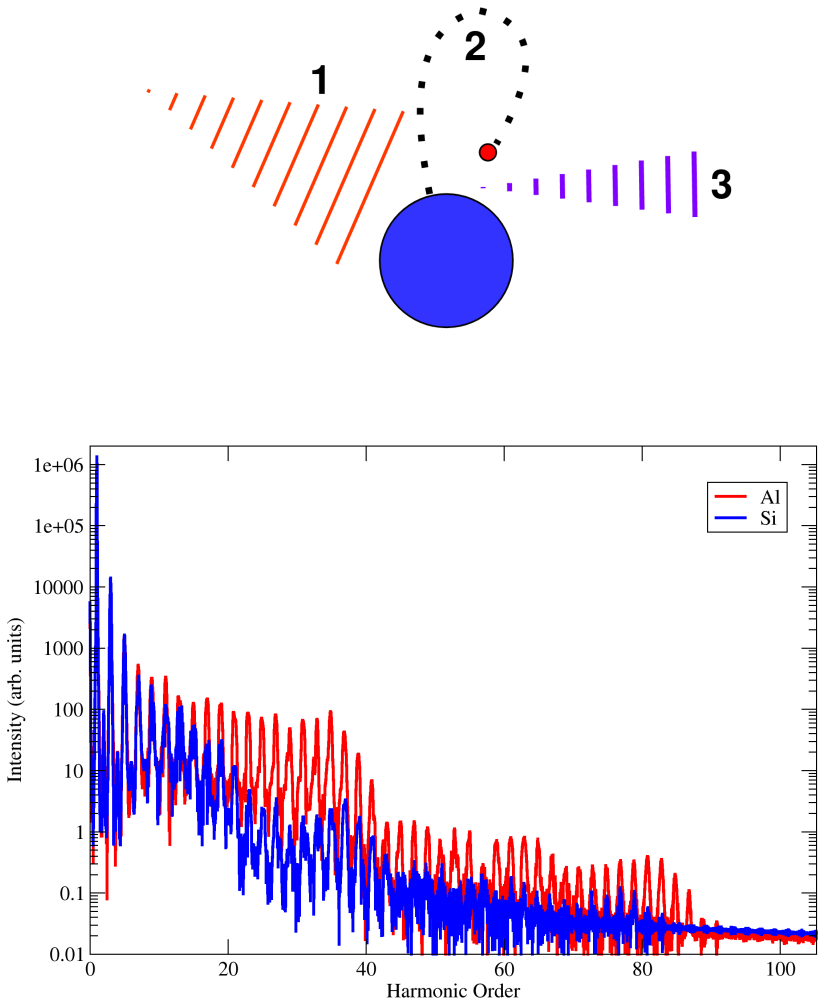

Figure 3.4: (Top) An diagram showing the three-step model of high harmonic generation. Step 1 shows the ionization of the electron (red circle) from an atom (blue circle) by incoming light. Step 2 shows the round trip of the ionized electron, its ponderomotive path and acceleration back towards the parent ion. Step 3 shows the recombination of the electron and ion, as well as the photon emission generated by the recombination. (Bottom) The OF-TDDFT-calculated HHG spectra of a 0.6 nm Al sheet and 0.3 nm Si sheet. The parameters are the same as those used for fig. 3.5 below.

light. In the wave function picture, a bound state function tunnels through the skewed potential, forming a bound and continuum state pair. The temporary reversal of the laser field recondenses the wave function by returning the tunneled, continuum portion to where the bound state portion is concentrated. From this, light is radiated possessing an energy bounded by a cutoff determined by the ionization energy and the incoming kinetic energy of the electron.

The character of the harmonic yields for a single atom may be determined using the dipole acceleration, which may be obtained from the time-dependent Schrodinger equation. For atomic and ionic HHG, the energetic upper limit E_{max} of the energy was explored in [155], and was shown to be

$$E_{max} = I_p + 3.17U_p(E_0, \omega), \tag{3.31}$$

where I_p is the ionization energy of the atom and $U_p(I, \omega) \propto {E_0}^2/\omega^2$ is the laser amplitude- and laser frequency-dependent *ponderomotive* energy the electron obtains, from the pump laser field, after its ionization and before its reabsorption. In HHG spectra, this upper limit is a cutoff at which the harmonics drop quickly to zero. HHG being a strong field response, it is a non-perturbative phenomenon. In principle, one may use the TDSE to numerically analyze the dynamics of the system, but not without incurring high computational costs. In [158], an approach based on the condition that the ponderomotive energy dominates the ionization energy is developed.

3.3.1 Time-Dependent Density Functional Theory for High Harmonic Generation

Localized jellium models have been used to explore second and multiple harmonic generation [159, 160]. By design, however, jellium should not be able to model high harmonic generation from solids. Both OF- and KS-TDDFT are capable of handling atomistic cases and are therefore well-equipped to describe HHG, but it is here that we present the effectiveness of the former. Whatever form the laser takes in the Hamiltonian, and no matter the time-dependent approach, in principal one need only extract the HHG spectra using the stimulated electron oscillations.

TDDFT has been used to investigate a plethora of HHG-related phenomena, such as: HHG in graphene driven by near-infrared light [161], band structure effects in solid-state HHG [48], shell activity in the HHG spectra of Xe [162], bound-bound and bound-continuum transition signs in the spectra of circularly-driven benzene [163], carbon chains and nanotubes [164]; circularly polarized XUV harmonic spectra in graphene [42]; and anisotropic effects for the harmonic yields of CO_2 [165]. Pertaining to bidirectional light-matter coupling, propagation effects in the HHG spectra of dielectrics has been researched as well [166].

Presently attractive in experimental and theoretical nanoscience is solid-state HHG, as is implied in the

TDDFT applications above. This is in part due to the expenses of gas-phase HHG, which requires an intricate and delicate arrangement involving vacuum pumps, structures to confine the gas, numerous optical elements, and amplified femtosecond laser systems. Moreover, energy cutoffs from solids deviate from semi-classical predictions by scaling linearly with the peak intensity of the driving field, demanding investigation into what mechanism affects that relationship [167].

TDDFT has been used to investigate some of the possibilities of solid-state HHG, and in its real-space form, might also be used to probe the nature of the mechanisms driving solid-state HHG. The results of such an investigation could inform the HHG-guided probing of atomic-scale structure, assisting with pursuits like vacancy inspection and impurity inspection, valence charge density inspection, and the imaging of condensed-phase wave functions [167]. Perhaps most exciting of all, however, are the possibilities of harmonics from nanostructures [149, 150, 168, 169, 170], which involve bespoke platforms of varied dimensionality purposed to control HHG properties. Results in [168, 170] demonstrate that such processes pave the way toward manipulating the spatiotemporal character of nanostructure harmonic yields, as well as their polarization and upconversion efficiency. Opportunities in confining the dynamics responsible for HHG might be offered by two-dimensional materials, such as graphene, the structure of which exhibits both atomic and solid-state HHG processes [171].

In starting a new decade in attoscience, theoretical research of nanostructure HHG could help inform nano-optical research and development decisions and nanoscale – both of which would naturally benefit from OF-TDDFT. KS-TDDFT, while fit to investigate HHG mechanisms for structures capable of being represented using a small cellular composition, would be an expensive approach to employ in dissecting emergent phenomena affecting and impacting nanostructure HHG. The comparatively inexpensive OF-TDDFT can be used to calculate HHG in periodic and finite structures. We note here that while not all mechanisms for solid-state HHG can be represented by real-space OF-TDDFT – such as interband polarization and intraband Bloch oscillations [167] – the complete, many-body process of collective electron ionization and reabsorption, which presents itself as an oscillating electron density in OF-TDDFT, occurs to yield HHG.

We now move on to preliminary OF-TDDFT calculations of HHG. We compare the results to KS-TDDFT HHG calculations. Three periodic structures – Al, Si, and graphene – and one finite structure, C_{20}, are used. Methods and specific parameters are discussed first, followed by results and a brief discussion about them. After that, preliminary results of coupling effects are presented.

3.3.2 External Field Parameters for Periodic and Finite Systems

Fig. 3.5a shows the HHG spectrum of the 0.6 nm aluminum sheet, consisting of 96 electrons. The simulation box has the dimensions (N_x, N_y, N_z) = (200, 31, 31), is periodic in y and z, and uses an EM and quantum CAP

in the x-direction. The grid spacing is $h = 0.493$ Bohr. The laser is a Gaussian pulse, distinguishable from the laser pulse shown in the bottom figure of Fig. 3.2 only in electric field amplitude. The mathematical form of this pulse is

$$\mathbf{E}_{ext}(\mathbf{x},t) = \hat{\mathbf{z}}E_0 e^{-(-t-t_0-x/c)^2/\alpha^2}\sin(\omega(t-x/c))\Gamma(x,t), \tag{3.32}$$

where, like eq. 3.27, t_0 is the pulse shift, α controls the pulse width, and ω gives the frequency. $\Gamma(x,t)$ is a ramping function that acts as a switch for the laser. It is used to ensure the external field is zero at the beginning of the calculation. It takes a piecewise form:

$$\Gamma(x,t) = \begin{cases} (t-x/c)/t_\gamma & \text{if } t-x/c \leq t_\gamma \\ 1 & \text{if } t-x/c > t_\gamma, \end{cases} \tag{3.33}$$

where t_γ is the ramping time. 0.5 a.u. was used for both fig. 3.5a calculations. The laser parameters are: t_0 = 1750 a.u.; α = 660 a.u.; ω = 0.057 a.u. There is no difference between the OF- and KS-TDDFT simulations except for in the amplitude of their lasers, which, respectively, are E_0^{OF} = 0.03 a.u. and E_0^{KS} = 0.005 a.u. OF-TDDFT. The amplitude difference between the KS- and OF-TDDFT calculations is common to the periodic calculations. This is discussed in the following section.

Fig. 3.5b shows the HHG spectrum of the 0.3 nm silicon sheet, consisting of 128 electrons. The simulation box has the dimensions (N_x, N_y, N_z) = (200, 31, 31), is periodic in y and z, and uses an EM and quantum CAP in the x-direction. The grid spacing is h = 0.498 Bohr. A Gaussian laser pulse of the following parameters were used: t_0 = 1750 a.u.; α = 660 a.u.; ω = 0.057 a.u.; t_γ = 0.5 a.u.; E_0^{OF} = 0.0275 a.u.; E_0^{KS} = 0.005 a.u.

Fig. 3.5c shows the HHG spectrum of a single layer of graphene, consisting of 192 electrons. The simulation box has the dimensions (N_x, N_y, N_z) = (200, 40, 52), is periodic in y and z, and uses an EM and quantum CAP in the x-direction. The grid spacing is h = 0.464 Bohr. A Gaussian laser pulse of the following parameters were used: t_0 = 1750 a.u.; α = 660 a.u.; ω = 0.057 a.u.; t_γ = 0.5 a.u.; E_0^{OF} = 0.028 a.u.; E_0^{KS} = 0.005 a.u.

Fig. 3.5d shows the HHG spectrum of a carbon-20 fullerene molecule, consisting of 80 electrons. The simulation box has the dimensions (N_x, N_y, N_z) = (200, 40, 52). PBCs are not used here. The calculation uses an EM CAP in the x-direction, while quantum CAPs are set up in the x- and z-directions to catch ionized portions of the density. The grid spacing is h = 0.5 Bohr. A Gaussian laser pulse of the following parameters were used: t_0 = 400 a.u.; α = 150 a.u.; ω = 0.057 a.u.; t_γ = 0.5 a.u.; E_0^{OF} = 0.03 a.u.; E_0^{KS} = 0.03 a.u.

All OF-TDDFT calculations use the MGP functional to represent the KEDF (see chapter 2). All vertical

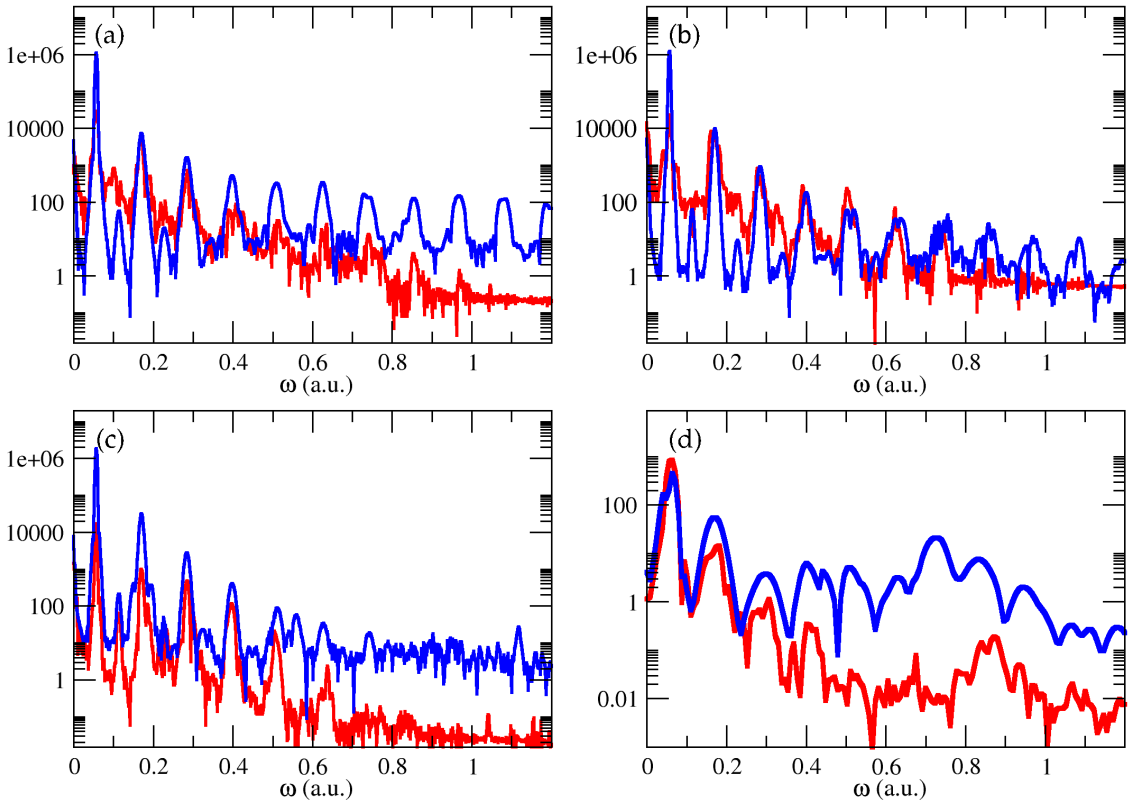

Figure 3.5: Comparisons of OF-TDDFT (blue) and KS-TDDFT (red) HHG spectra for (a) 0.6 nm Al (b) 0.3 nm Si (c) graphene, and (d) C_{20}. Due to the varied nature of the simulations, their specifications have been delegated to the body of subsection 3.3.2. OF-TDDFT requires much higher laser intensities to achieve HHG for the periodic cases, but the profiles of the presented OF- and KS-TDDFT spectra are in agreement.

axes represent current amplitudes of arbitrary accounting. Lastly, all OF- and KS-TDDFT calculations here use local pseudopotentials [15, 172, 173, 174, 175], a pseudopotential approximation which reduces electron-ion interactions from a multivariate potential to a radial one.

3.3.3 Harmonic Yields of Kohn-Sham and Orbital-Free Equations

A qualitative comparison of (uncoupled) OF- and KS-TDDFT in calculating HHG is shown fig. 3.5, in which all OF-TDDFT and KS-TDDFT data are blue and red, respectively, and the major ticks represent the positions of the harmonics. We immediately find that, OF- and KS-TDDFT are not equally equipped to handle HHG. Ponderomotive and cutoff energies cannot yet be compared between the theories, as the theories generally require different laser intensities for coherent harmonic generation. For now, we emphasize the unique axis of fig. 3.5d and make other observations.

Figs. 3.5a, 3.5b, 3.5c, and 3.5d respectively show the HHG spectra of a 0.6 nm aluminum sheet, a 0.3 nm silicon sheet, a single-layer graphene sheet, and a C_{20} fullerene molecule. For each system, like KS-TDDFT,

OF-TDDFT predicts odd-ordered harmonic yields, properly indicating centrosymmetry. The theories agree on the relative positions of the harmonics. Furthermore, OF-TDDFT properly shows the inverse relationship between harmonic intensity and harmonic order. The ability OF-TDDFT to accurately calculate HHG shows promise for investigating the harmonic generation properties of faceted, many-atom nanostructures like bulk solids, crystals, and metamaterials [176], the feasibility of plasmon-enhanced harmonic generation [177, 178], and cavity-enhanced harmonic generation [179, 180].

Figs. 3.5a, 3.5b, and 3.5c are the periodic system cases. Though we obtain coherent harmonic alignment between both theories, we emphasize here that, for the present, this can only be done by using a higher laser amplitude for the OF-TDDFT calculations. Fig. 3.6 shows the impact laser intensity has on the amplitude of the electron currents: the top image shows multiple results for the Si sheet, while the bottom image shows two results for the Al sheet. In both cases, an electric field amplitude of 0.005 a.u. – an amplitude at which KS-TDDFT yields harmonics – shows only two harmonics, plus minor disturbances at other locations. This is not to imply HHG calculated using KS-TDDFT does *not* coherently persist past 0.005 a.u., but both the coherence and maxima of the KS spectra, as shown in figs. 3.5a, 3.5b, and 3.5c, suggest the KS yields become noisy well before 0.01 a.u., while OF-TDDFT only resembles the low-intensity KS-TDDFT spectrum around much higher laser amplitudes. Conversely fig. 3.5d, the fullerene, the finite example, shows similar HHG between KS- and OF-TDDFT at identical intensities. In the future, the relationship between the laser intensity and the selected form of the MGP functional, as well as the relationship between the intensity and the cellular character of the matter system, should be investigated.

Graphene HHG with circularly polarized light was also investigated. Fig. 3.7 shows graphene HHG for linear (dotted) and circularly polarized fields, with the y- and z-directions being the solid violet and magenta lines, respectively. The parameters describing the system are the same for the graphene represented in fig 3.5c. Like other spectra, the odd-ordered harmonics are the most prominent. The present even-ordered harmonics, though coherent, are of low intensity – suppressed, as one would expect, due to the inversion symmetry of the lattice. Also worthy of note is the suppressed intensity of the third harmonic. This is a selection rule effect of circularly polarized HHG [56]. The six-fold symmetry of the graphene leads to the suppression of the third and ninth harmonics. The ability of OF-TDDFT to capture the Hamiltonian symmetries engendering the proper harmonic suppression is expected, and it shows the promise of the method to accurately represent HHG spectra generated using fields of various organized polarizations.

3.3.4 Subtotal Harmonic Suppression: Propagation Effects and Dimensionality

Regarding the subtotal harmonic suppression of the even-ordered harmonics, as well as the third harmonic in graphene excited by circularly polarized light, we must consider two things: electromagnetic propagation

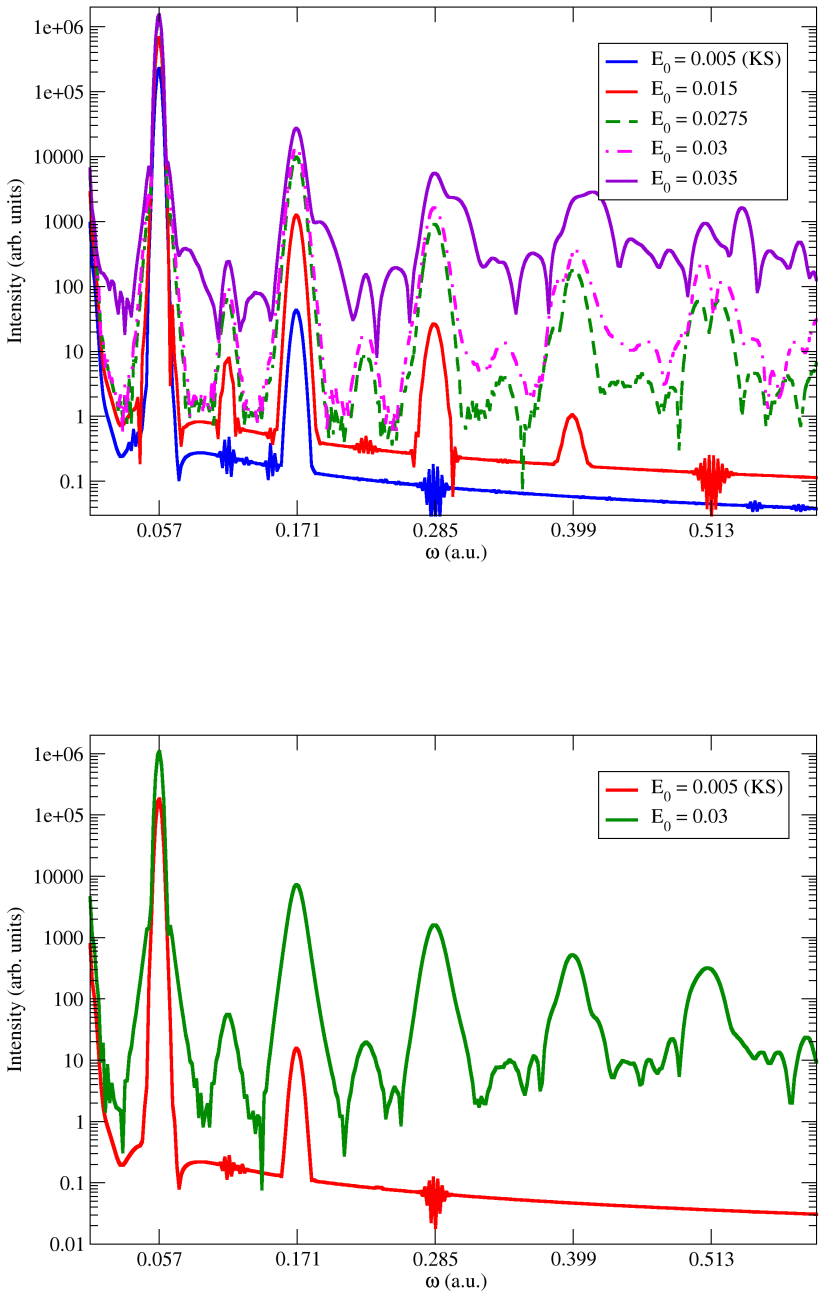

Figure 3.6: OF-TDDFT HHG of 0.3 nm Si sheet (top), at five electric amplitudes, and 0.6 nm Al sheet (bottom) at two electric amplitudes. The 0.005 a.u. electric field amplitude corresponds to the field intensity beyond which KS-TDDFT HHG spectra nears incoherence. At this intensity, in both cases, the yields are coherent but too few, requiring OF-TDDFT calculations to use higher laser intensities.

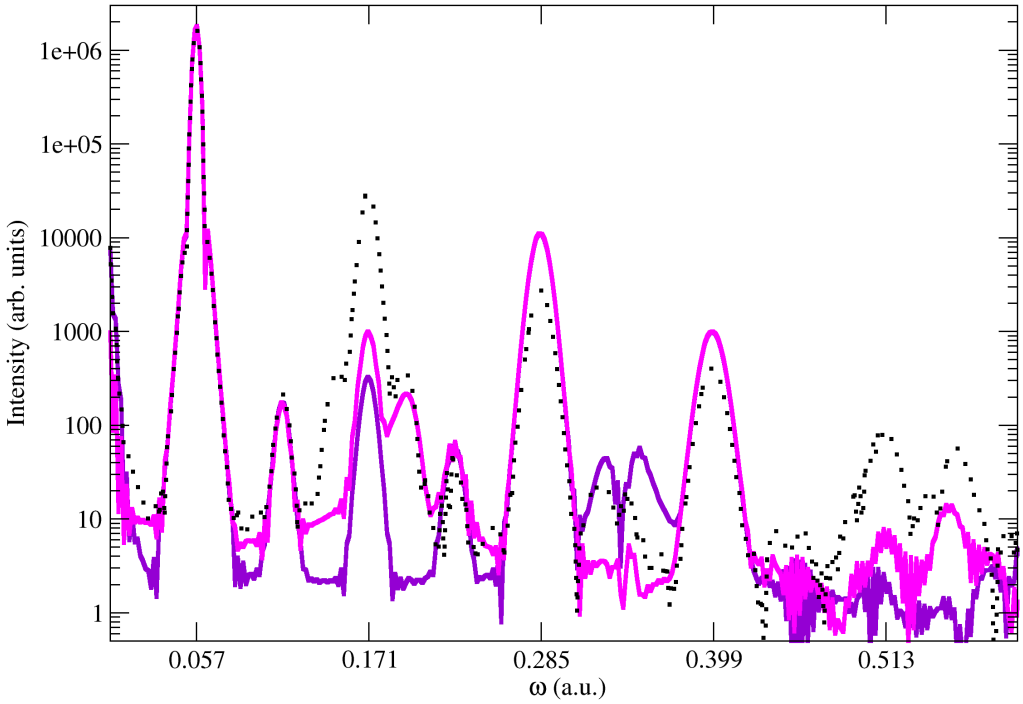

Figure 3.7: OF-TDDFT HHG of graphene, presented in the z-direction (magenta) and y-direction (violet), stimulated by circularly polarized light. OF-TDDFT graphene HHG from linearly polarized light (dotted) is shown for comparison. Both circularly polarized HHG spectra show (subtotal) even-ordered and third-order harmonic suppression, indicating inversion and six-point symmetry.

effects and the dimensionality of the target material. In attempting to remedy our picture of nanostructure HHG by including propagation effects, one should use the orbital-free equations coupled to light. The dimensionality concern need only be addressed by thickening the sheet.

Fig. 3.8 shows the HHG spectra from the same simulation that generated fig. 3.2, but this time the HHG is calculated using the current. As one can see, QCA coupling has an impact on the oscillations of the electrons. In fig. 3.2, the prominent harmonic orders are of odd parity. The even-ordered harmonics are suppressed due to the inversion symmetry of the lattice. Like the coupled outgoing radiation, the HHG spectrum for the coupled current properly suppresses the even-ordered harmonics. The uncoupled case only partially suppresses them, showing that the upconversion between the first harmonic and any even-ordered one is noticeably inefficient and sullied completely beyond the sixth harmonic.

It is possible the appearance of the low efficiency even-ordered harmonics are due to the subnanometer

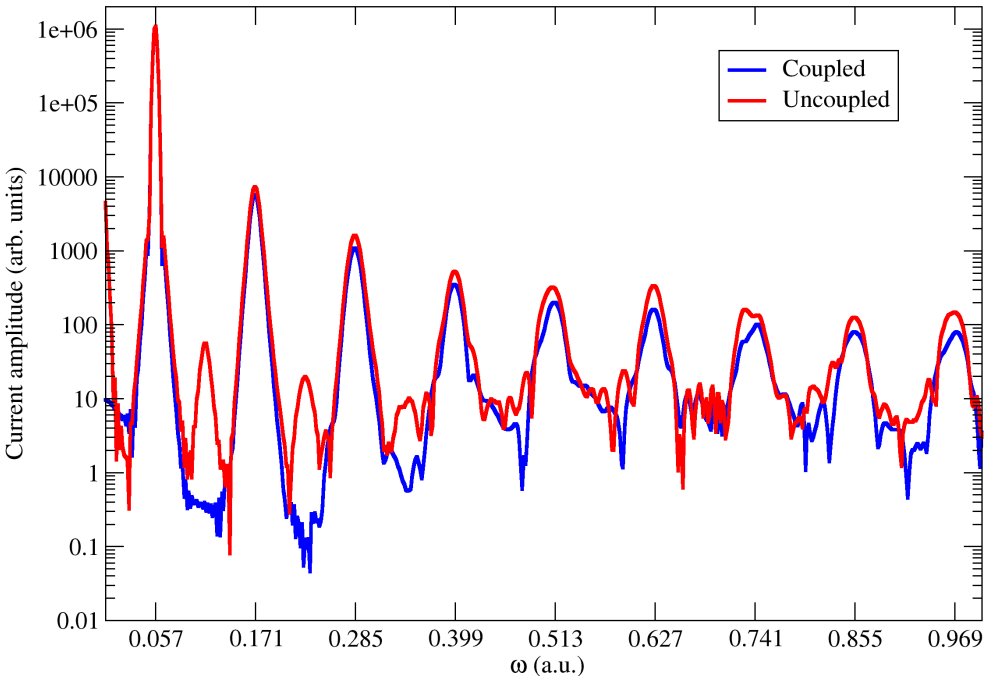

Figure 3.8: Coupled and uncoupled OF-TDDFT HHG spectra of the current in the aluminum sheet of thickness of 0.6 nm. The laser pulse has a wavelength of 800 nm, an amplitude of E_0 = 0.03 a.u., and a pulse duration of 3500 a.u. The spectra were generated using Fast Fourier transforms of the current, which is why both cases, and not just the coupled case, show activity. The imperfect suppression in the uncoupled case likely comes from the small thickness of the sheet. The suppression in the coupled cases likely comes from the periodic reinforcement of the lattice symmetries communicated between the electrons and the vector potential.

thickness of the Al sheet – an observation that should extend to all periodic systems under consideration (the dimensionality effect). With all three sheets being less than one nanometer thick, inversion symmetry effects may manifest weakly. Evidence of this can be found in fig. 3.9, which shows the OF-TDDFT HHG of Al at different thicknesses. However, it is possible that the etiology of the subtotal suppression also involves the propagation of a net field through the material. The complete suppression of the even-ordered harmonics when the coupling is turned on is likely due to the successive, field-mediated accentuation of the inversion symmetry of the lattice (the propagation effect). The induced vector potential communicates dynamic information about the lattice symmetry to the electrons with every laser cycle. This repetition elucidates the inversion symmetry already present in the electron density, which in turn alters the upconversion efficiency shown in the HHG spectrum. In other words, only electron-ion recombination informs uncoupled oscillations of the lattice symmetry, where as coupled oscillations are informed of these symmetries by both electron-ion recombination and the vector potential of the stimulated density.

The reader's attention is now drawn to the specific wording of the first paragraph of this section: "In attempting to remedy our picture of nanostructure HHG..." The implication here is that simultaneously in-

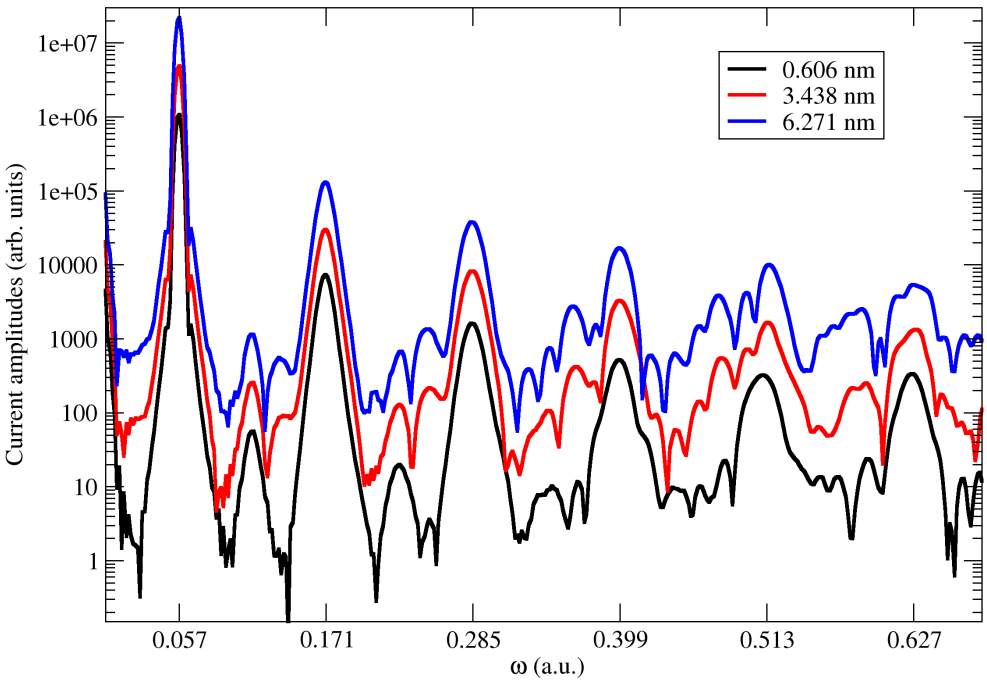

Figure 3.9: Multiple uncoupled OF-TDDFT HHG spectra in an aluminum sheet of thickness of 0.6 nm. The effect of the harmonic suppression increases with the thickness of the sheet. The laser pulse has a wavelength of 800 nm, an amplitude of $E_0 = 0.03$ a.u., and a pulse duration of 3500 a.u. The spectra were generated using Fast Fourier transforms of the current.

creasing sheet thickness and including light-matter coupling might not, in general, suppress the physically anomalous harmonics. With fig. 3.10, we consider circularly polarized light coupled to the electron dynamics of the graphene sheet. In both the y- and z-response cases, though the intensity of the partially suppressed harmonics are nearly identical, the baseline of the signal is elevated by the coupling, thereby having the effect of further suppressing the harmonics. The fourth harmonic in both cases, as well as later harmonics normally suppressed by symmetry, are eliminated. Still, the second and third harmonics, both of which should be completely suppressed, are both present and coherent. This suggests a mechanism besides propagation is responsible for the subtotal suppression, and the atomic-thickness of graphene strongly suggests that these harmonics are not a dimensionality effect. The use of a local pseudopotential may also have an impact on the suppression of certain harmonics.

Here, the reader is reminded once more that fig. 3.5 is shared for its qualitative value. We hypothesize that the need to vary the intensities between the KS- and OF-TDDFT calculations for the periodic systems are due

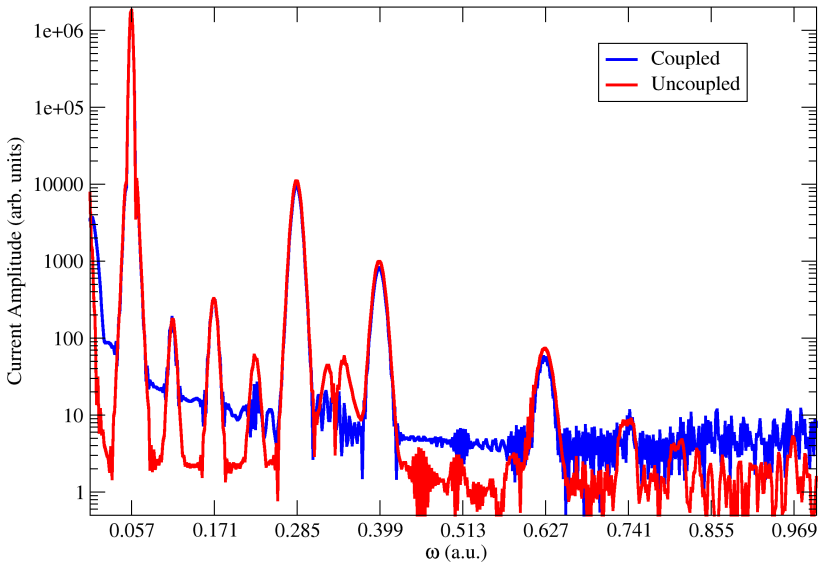

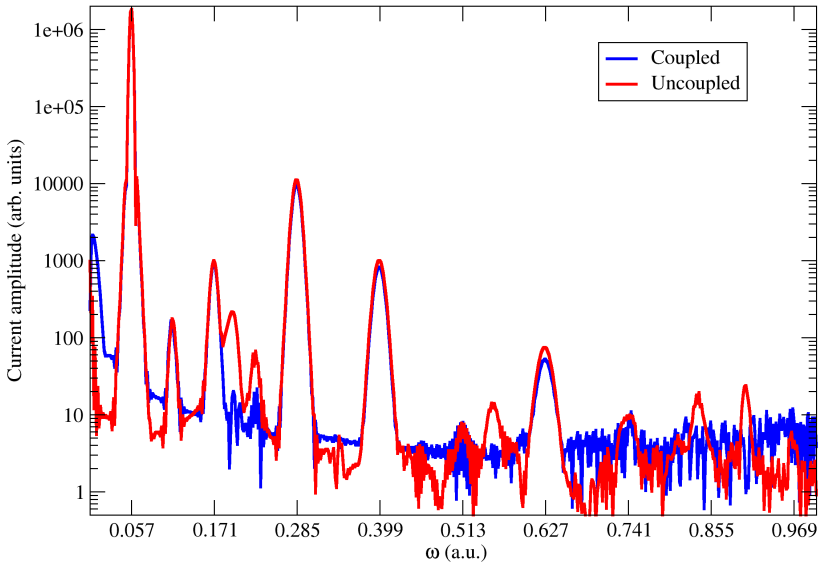

Figure 3.10: Coupled and uncoupled OF-TDDFT HHG spectra of graphene, generated in the (top) y-direction and (bottom) z-direction by circularly polarized light. In both cases, the coupling elevates the baseline of the response and thereby reduces the baseline-to-peak length of the subtotally suppressed harmonics. Noisy frequency bands replace somewhat coherent harmonic behavior in both cases.

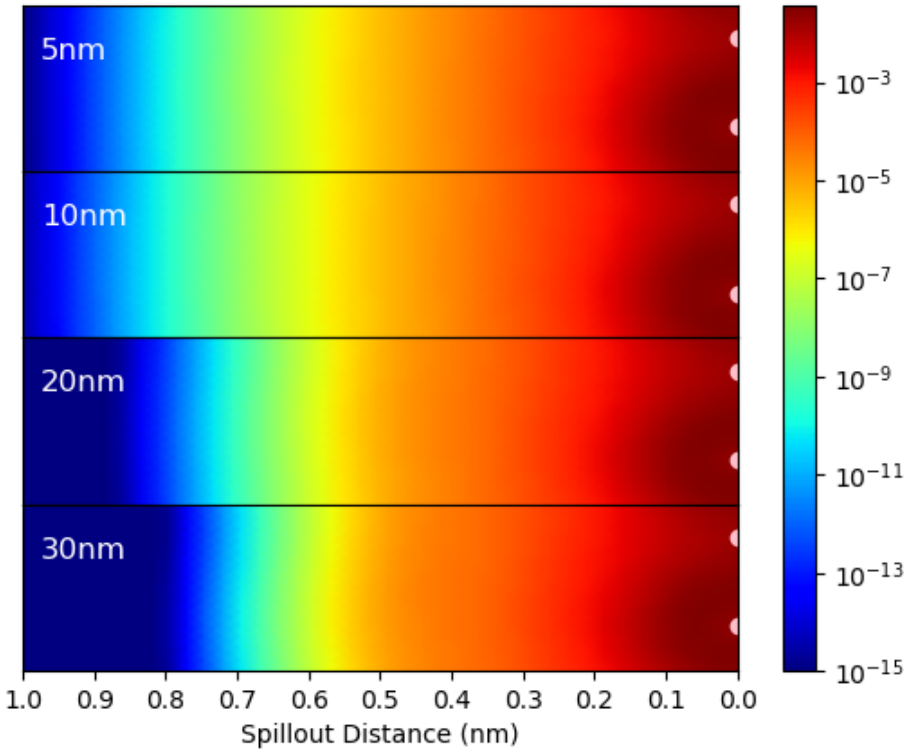

Figure 3.11: The electron spill out from aluminum sheets of varying thickness (in nanometers), calculated using OF-DFT. The pink dots lining the right side of the plot represent the aluminum surface. Here, the spill out length is defined as the distance the density reaches out from the surface-most atoms. The apparent inverse proportionality between nanosheet thickness and spill out length is in agreement with both theory and experiment.

to differences in the material susceptibilities predicted by the theories. The most important difference between OF-TDDFT and KS-TDDFT in calculating HHG is manifest in this intensity threshold duality for periodic systems. The usefulness of KS-TDDFT in calculating HHG has been well-established by the literature, but the interpretation of ponderomotive and cut-off energies, as well as harmonic order plateaus, calculated using OF-TDDFT are unclear for the present. In addition, why C_{20} is apparently immune to this amplitude limitation has yet to be investigated.

3.4 Induced Field Frequency Modulation with Graphene-Cantilevered Aluminum

3.4.1 Background

Direct access to observables make first-principles approaches attractive. Using TDDFT, in simulating high harmonic generation, one may trace the emission of integer frequency radiation back to the real-time dynamics of the electrons. Fig. 3.11 compares OF-DFT calculated electron spill outs between aluminum sheets of different thicknesses. Even without coupling, one can traceback the curious shift of the plasmon resonance of an aluminum rod to this surface effect [55]. In [133], the QCA OF-TDDFT scheme is used to show that atom-

istic structure can alter the electron motion in a nanogap, delivering insight into the mechanisms responsible for the observed dynamics.

Using a light-matter coupling scheme, key physical information should be accessible in electromagnetic field observables too. In [133], the QCA coupling scheme is justified due to the size of the bowtie system and the tunneling across the junction responsible for modulating the dielectric function of the gap. The field enhancement of the gap is calculated using output radiation, which, in the paper, is traced directly to the high density flux between the nanobowties.

The novel use of OF-TDDFT in quantum plasmonics was discussed in subsection 3.2.1. Then, jellium model simulations of current and atomistically-detailed HHG calculations proved OF-TDDFT useful in describing nanoscale quantum dynamics. The invocation of nanoplasmonics and atomistic details suggesting the investigation of relatively sophisticated nanoscale devices, we finally arrive at the simulation of a scaled-down hybrid nanoparticle to demonstrate how the structure of outgoing radiation is direclty influenced by the structure of the electron oscillations.

An aluminum nanorod is laid atop tri-layered graphene, the interfacial graphene layer being inhomogeneous by having a step aligned with one edge of the nanorod. The entire system is then excited by a single-cycle laser pulse, inducing charge transfer across the hybrid NP junction. The position of the rod is then varied longitudinally, along its principal axis. We find that this modulates the electron flux across the junction in quasi-linear fashion, which in turn modulates the frequency of the induced field.

3.4.2 Computational Details

The hybrid NP system consists of an Al nanorod of dimensions 11.46-by-11.64-by-26.76, in Bohr, and three graphene sheets, bounded by the extent of the grid volume, their interlayer spacing equaling a graphitic 6.47 Bohr. The Al-interfacial graphene layer terminates at the edge of the aluminum, which is positioned beside this terminated layer (see figs 3.12 and 3.13).

Atomic coordinates accepted, the five calculations performed use identical input. The dimensions of the Cartesian grid are $(N_x, N_y, N_z) = (142, 82, 213)$, and to properly affect PBCs, the grid spacing is 0.4535 Bohr. The PBCs are implemented in the $y-$ and $z-$directions to maximize the extent of the graphene with respect to the Al rod. An electromagnetic complex absorbing potential is set up in the x-direction to absorb outgoing radiation. The total number of valence electrons used – the sum of the C atom and Al atom valence electrons – is 4224.

The MGP kinetic energy potential is used with selected material-density dependent kernels $(\alpha, \beta) = (0.5, 0.3)$. These parameters are used for both the ground state and time-dependent calculation. To calculate the total electron crossing across the hybrid NP junction, we use

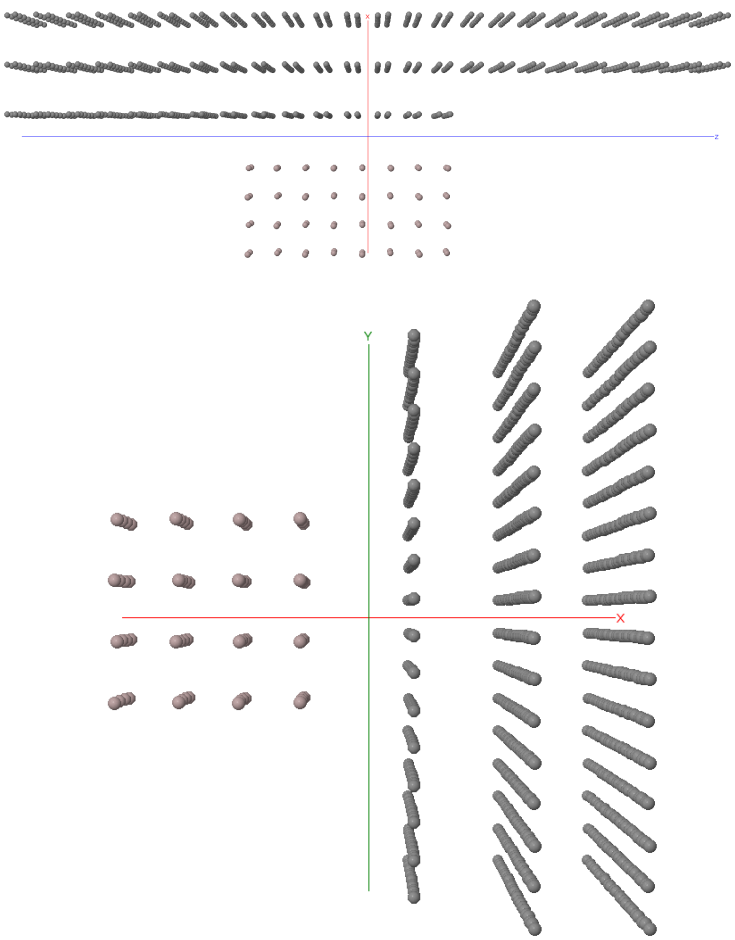

Figure 3.12: The structure of the Al-graphene hybrid nanoparticle supercell shown from the $x-z$ plane (top) and the $x-y$ plane (bottom).

$$\Phi_T = \int_0^T dt \left(- \int dy\, dz J_x(\mathbf{x}, t) \right), \tag{3.34}$$

with the parenthetical integral representing the instantaneous flux of the electrons.

Next, a 0.02 time step was used, with the total number of time steps being 25,000. The time step used for light propagation is 0.001. And lastly, the system was excited by a laser of a form described by eq. 3.7, direction included: with a peak electric field of E_0 = 0.0005 a.u., a width of α = 25 a.u., a shift of t_0 = 35 a.u., and a wavelength of 400 nm.

Periodic boundary conditions image the contents of Fig. 3.12 into infinity in directions not constrained by the complex absorbing potential. The two homogeneous graphene sheets extend into the PBC directions, continuing unbroken into infinity. The terminated graphene layer and the Al rod extend into the PBC directions too, but in a broken manner. One may think of the full system as being two layers of graphene periodically

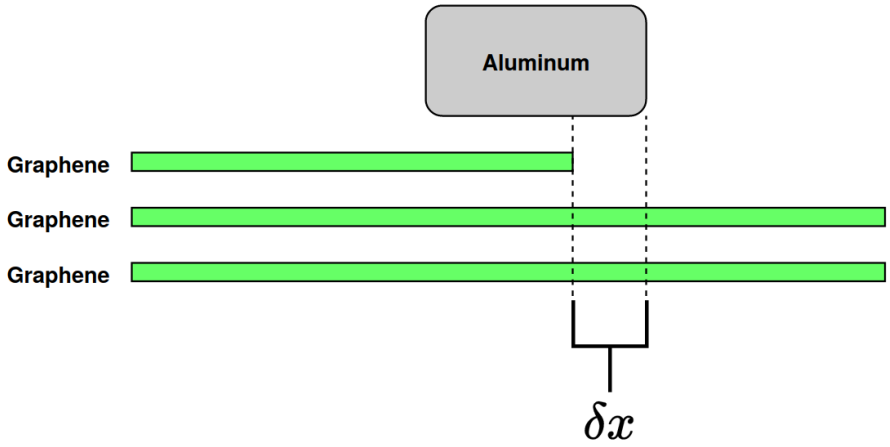

Figure 3.13: A diagram of the Al-graphene hybrid nanoparticle. The grey block is the aluminum, while the green lines represent the graphene. The shift δx represents the length beyond the graphene ribbon edge the Al rod extends.

covered by a graphene ribbon, with an Al rod sitting above the ribbon. If the gap between graphene ribbons is too small, then too large of a δx may induced image interactions between the rod and an image of the graphene ribbon. The largest δx being 2.0 a_{Al}, here, before performing calculations, the ground state density was used to detect a non-negligible density connecting the rod and the ribbon.

This density is shown in log scale in Fig. 3.16. Notice how a small fraction of the image ribbon density sits in the supercell around $(x,z) \approx (0,45)$. Excepting how the densities overlap at the junction, no density above the colorbar minimum extends along the axial length of the rod to interact with the image density of the ribbon. The weak time-dependent perturbations resulting in only a slight volume change, the ground state density provides sufficient assurance that the densities never overlap.

3.4.3 Results and Discussion

The resulting dynamics along the x-direction are shown in Figs. 3.14 and 3.15. Reacknowledging the main idea of this demonstration to connect electron dynamics to more experimentally accessible observables, we start with looking at the induced flux of Fig. 3.14. The size of the amplitudes correspond to the fraction of the electron density crossing the junction. By varying δx, one may modulate the frequency and transfer magnitude of the flux. Physically, this shows a correlation between the shift and the flux frequency exists. Seeing how eq. 3.34 depends on the x-direction current, one may expect the current to display similar behavior – as it does. Fig. 3.14c shows the current following the same trend as the flux.

We connect the electrons dynamics to an outgoing electric field. Fig. 3.14b shows the sum of the x-direction of the total electric field over the volume of the grid. The oscillations follow the same trend. Overall

δx (a_0)	Current ω	Junction Flux ω	Induced Field ω
0.0	1.065	1.066	1.066
0.5	1.026	1.026	1.022
1.0	0.947	0.947	0.943
1.5	0.868	0.868	0.865
2.0	0.789	0.868	0.786

Table 3.2: The location of frequency peaks in the Fast Fourier transforms of the current, the junction flux, and the induced field. The size of the shift is in units of the lattice constant of Al, represented as a_0. The frequency values are in atomic units.

the electric field amplitude increases as the shift increases, and with the shift the frequency of the radiation changes as well. The amount by which the frequency of the outgoing light changes is summarized in fig. 3.15, which shows the Fast Fourier transformations of these fields.

The top plot of fig. 3.15 shows the FFT of the total fields, while the bottom plot shows the FFT of the current. Quantitative amplitude information is discarded as only the frequency locations are relevant. The peaks are, naturally, in close alignment, suggestive of the origin of the oscillations in the outgoing electric field. This is no surprise, as the light-matter coupling appropriately passes density oscillations on to the electric field. The form of the current in the x-direction, however, is driven by the junction charge transfer. Therefore, with QCA coupling, one can properly tether real-time quantum dynamics to outgoing radiation rather than use dipole and current output to make inferences about outgoing fields. Table 3.2 shows the shift and peak frequency locations for the current, junction flux, and the fields.

Like how QCA coupling has been used to investigate the impact atomistic and quantum effects have on field enhancement in nanobowties, plasmonic couplings may also be investigated in terms of the quantum effects which contribute to their structure. For example, in [181], the NP structure of which inspired this demonstration, junction charge transfer asymmetries along the axial length of a gold nanocapsule drive asymmetries in the field enhancement. In the paper, the discrete dipole approximation [182, 183, 184, 185] is used to simulate the *field* asymmetry, but the electron dynamics speculated to be responsible for yielding the character of the plasmonic couplings have yet to be explored. QCA coupling could assist with realizing the exact nature of this charge-coupling-enhancement relationship.

3.5 Appendix for Chapter 3

3.5.1 Inversion Symmetry Impacts Dynamic Polarizability Terms

How even harmonics are suppressed in HHG is due to inversion symmetry. If the atomic coordinates of a structure, defined with respect to some center known as the center of inversion, are replaced with their inverse coordinates, and if this transformation yields structure unchanged, the structure is said to possess an inversion

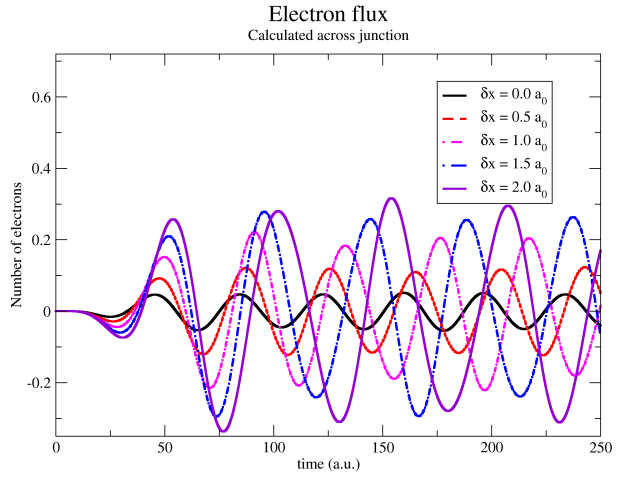

(a)

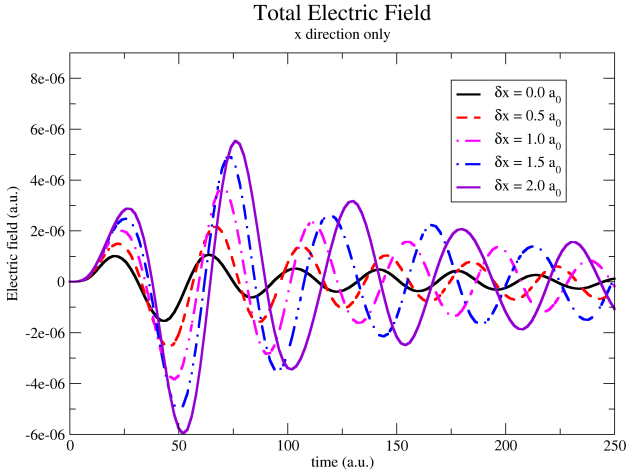

(b)

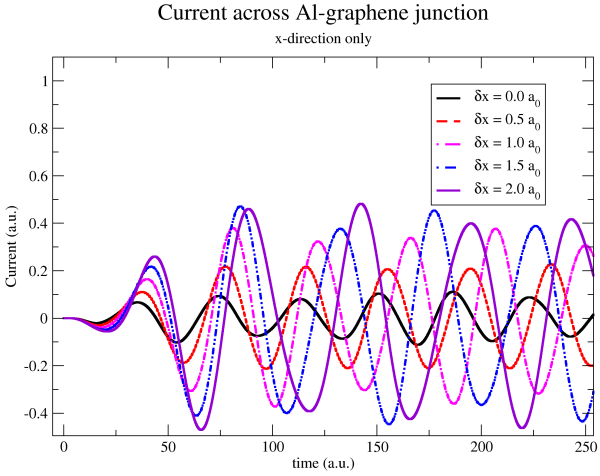

(c)

Figure 3.14: Induced current and total electric field behavior in stimulated Al-graphene nanoparticle: (a) the density oscillations across the junction; (b) Current in the x-direction; (c) Total, x-direction electric field. The unit a_0 represents the lattice constant of Al.

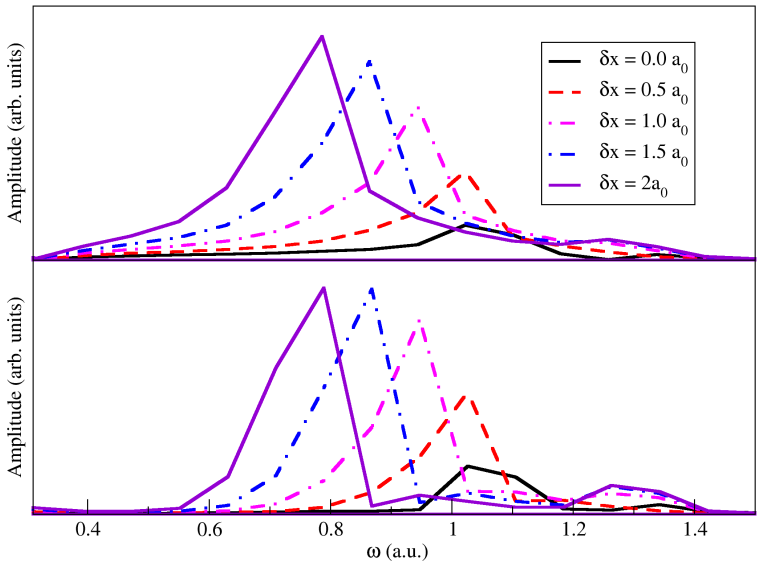

Figure 3.15: The location of frequency peaks in the Fast Fourier transforms of the total field (top) and the induced current (bottom). The unit a_0 represents the lattice constant of Al. Quantitative alignment information is provided in Table 3.2.

symmetry. This manifests in the HHG spectrum as a selection rule requirement of the dynamic polarizability. To keep things simple, we consider the effect inversion symmetry has on a general dipole matrix element.

Recall the electric dipole moment $\mathbf{x}$. Its selection rules determine which transition pathways are permitted. By definition, the dipole operator is odd under parity:

$$\Pi^\dagger \mathbf{x} \Pi = \Pi^\dagger(x,y,z)\Pi \tag{3.35}$$

$$= (-x,-y,-z) \tag{3.36}$$

$$= -\mathbf{x}. \tag{3.37}$$

This has an effect on the transition elements of the dipole matrix. For states $|n,l,m\rangle$ and $|n',l',m'\rangle$, the dipole matrix takes the form of

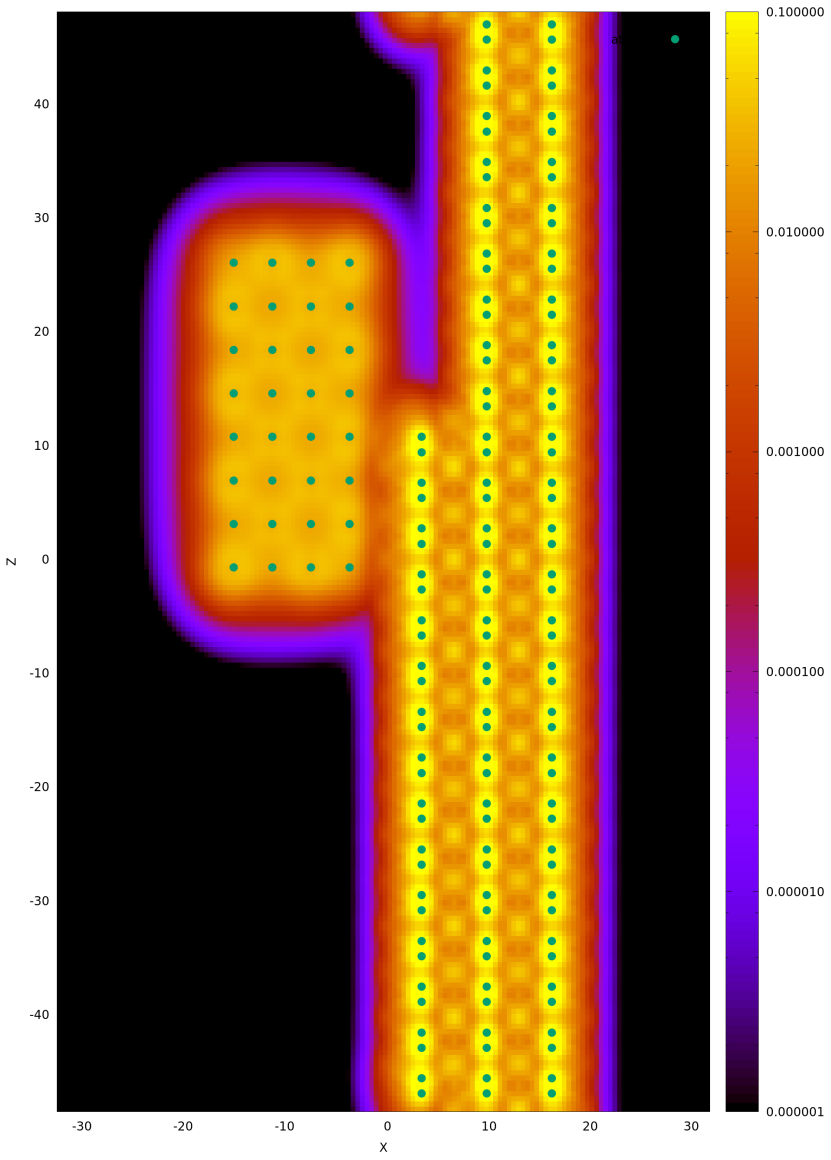

Figure 3.16: A $x-z$ density slice of the Al-graphene hybrid supercell, with $x = 2.0a_0$. The green dots represent the approximate locations of the atoms. Atoms located $x < 0$ are Al atoms, while atoms located $z > 0$ are C atoms. The image of the graphene layer closest to $x = 0$ intrudes around $(x,z) \approx (0,45)$. Real-image density interactions threatening the integrity of the junction dynamics are present.

$$\langle n,l,m|\mathbf{x}|n',l',m'\rangle = -\langle n,l,m|\Pi^{\dagger}\mathbf{x}\Pi|n',l',m'\rangle \tag{3.38}$$

$$= -\langle n,l,m|(-1)^{l}\mathbf{x}(-1)^{l'}|n',l',m'\rangle \tag{3.39}$$

$$= (-1)^{l+l'+1}\langle n,l,m|\mathbf{x}|n',l',m'\rangle \tag{3.40}$$

If $l+l'$ equals an even number, the matrix element vanishes, as it and its inverse would equal each other. This result demonstrates Laporte's rule [186, 187]: parity-conserving electronic transition are forbidden. It is a straightforward application of Laporte's rule which shows why even-ordered harmonics vanish under inversion symmetry.

Using perturbation theory, one can show that the dipole response to an oscillating electric field yields a first-order dynamic polarizability term corresponding to first-harmonic generation [17]. Assuming monochromatic incident radiation and no phonon losses, this term looks like

$$\text{First-harmonic generation} \propto \langle 0|\mathbf{x}|1\rangle\langle 1|\mathbf{x}|0\rangle, \tag{3.41}$$

where 0 is the ground state and 1 represents the excited state due to one photon. Note how this is expressed: an electron in its ground state absorbs a photon, jumps to state 1, and then returns to the ground state by releasing a photon. Second-harmonic generation, determined by the second-order dynamic polarizability, is expressed similarly:

$$\text{Second-harmonic generation} \propto \langle 0|\mathbf{x}|1\rangle\langle 1|\mathbf{x}|2\rangle\langle 2|\mathbf{x}|0\rangle. \tag{3.42}$$

Here, 2 represents the electron excited state due to two photons. An electron in its ground state absorbs a photon, jumps to state 1, then absorbs another photon to get to state 2. The electron then releases this gathered radiation as an energetic photon with a momentum equal to the two photons the electron absorbed: the electron jumps from state 2 to 0. For the third-order dynamic polarizability (third-harmonic generation) and higher terms, this pattern persists. If $f_{\text{HHG}}^{(N)}$ represents harmonic generation of order N, then

$$f_{\text{HHG}}^{(N)} \propto \langle N|\mathbf{x}|0\rangle \prod_{i=0}^{N-1}\langle i|\mathbf{x}|i+1\rangle. \tag{3.43}$$

The term $\langle N|\mathbf{x}|0\rangle$ is the electron-ion recombination term, which is responsible for communicating the release of the energetic photon. It is also the only term that matters in determining the impossibility of a transition.

If states 0 and N differ in parity, eq. 3.43 vanishes and the harmonic does not feature among the other yields. All transitions in the product term obey the selection rules, and if the electron can absorb the incoming

photon and transition successfully, it will be able to do so continuously until it arrives at state N. If a single photon-induced transition is acceptable, then provided the field remains monochromatic, all the transitions must be acceptable too. Therefore, the feasibility of the photon emission comes down to $\langle N|\mathbf{x}|0\rangle$, and it shows immediately that even-ordered harmonics vanish.

Making this more explicit, none of the $\langle i|\mathbf{x}|i+1\rangle$ terms will vanish due to Laporte's rule because each i to $i+1$ transition is permissible. This means that, for all i, i and $i+1$ will have different parities. Therefore, and again, the presence of a harmonic at order N depends on the term $\langle N|\mathbf{x}|0\rangle$. Dissecting the character of its parity,

$$\langle N|\mathbf{x}|0\rangle = -\langle N|\Pi^{\dagger}\mathbf{x}\Pi|0\rangle \tag{3.44}$$

$$= (-1)^{l_N+l_0+1}\langle N|\mathbf{x}|0\rangle, \tag{3.45}$$

where l_N and l_0 are parity-related state labels for states N and 0, respectively. Similarly,

$$\langle i|\mathbf{x}|i+1\rangle = -\langle i|\Pi^{\dagger}\mathbf{x}\Pi|i+1\rangle \tag{3.46}$$

$$= (-1)^{l_i+l_{i+1}+1}\langle i|\mathbf{x}|i+1\rangle, \tag{3.47}$$

where l_{i+1} and l_i are parity-related state labels for states $i+1$ and i, respectively. With eq. 3.47 being constrained by $l_{i+1}+l_i$ always equaling an odd number, it is a positive definite term. The exponential term l_N+l_0 has no such constraint, so it does not generally yield a positive definite term. And as one can see, with every iteration, l_N+l_0 alternates between odd and even values. The specific even and odd values are not important, however, and we can take advantage of this fact by setting $N = l_N+l_0$, which conveniently codifies the parity alteration of the exponential term: if $N+1$ is odd, $N+2$ is even, $N+3$ is odd, $N+4$ is even, and so on. Explicitly,

$$\langle N|\mathbf{x}|0\rangle = (-1)^{N+1}\langle N|\mathbf{x}|0\rangle, \tag{3.48}$$

which vanishes whenever N is even. Therefore, due to both the iterative nature of photon absorption in a monochromatic field and the parity character of the dipole operator, all even-ordered harmonics vanish.

CHAPTER 4

Harmonically Confined N-electron Systems Coupled to Light in a Cavity

Note: We will suppress the hat notation for operators (i.e. $\hat{O} \rightarrow O$) from here on.

4.1 Background

4.1.1 Optical Cavities and the Strong Coupling Limit

We now concern ourselves with problems requiring formalistic light-matter coupling, in which light and matter are directly coupled and or time-propagated in a single theory uniting them, rather than coupled through overlapping variables in separate theories. EM radiation and many-electron systems are both treated quantum mechanically, with the former representing Fock space bases. The light-matter theoretical framework is the Pauli-Fierz Hamiltonian, which may be decoupled into electron and electron-photon components. The electron-photon system concerning this thesis is the optical cavity [19], specifically in situations of strong coupling.

In general, optical cavities are arrangements of nanoscale optical elements, like reflective surfaces, which form an EM resonator. The resolving power of planar cavities, like the Fabry-Pérot optical cavity [188], is determined by its finesse. For cavities of a general geometry, the finesse is referred to as the quality factor (Q-factor), named after the wave mechanics terminology. The Q-factor equals the ratio of a mode frequency and its full-width half-maximum amplitude (FWHM): the smaller the intensity of a mode and or the more dispersed the mode energies are, the less effective the cavity is at preserving a mode in the neighborhood of that frequency. Photon lifetimes inside a cavity are determined by the refractive index, reflecting element separation length, and element reflectivity. Therefore, entertaining a point particle picture of the photon, whenever a photon of a specific frequency exits the cavity or changes frequency between interactions with reflective elements, it "decays," which shows up as mode decay in spectral data. If a photon exits the cavity, one would see amplitude reduction at the frequency of that photon. If a photon decays to another frequency, one might see in the optical absorption fragmentation and or spectral broadening at the frequency of that photon.

Coupling an atom to the cavity is a matter of nesting the atom within the cavity, and their interaction may be understood using the two-level energy picture [20, 21]. The strength of the atom-cavity interaction is determined by the relationship between the photon decay rate γ, the non-resonant decay rate κ, and a coupling parameter g_0. Acknowledging cavity- and inter-atomic energetic decay as separate decay channels, γ is determined by the same factors determining the cavity Q-factor. The non-resonant decay rate κ is

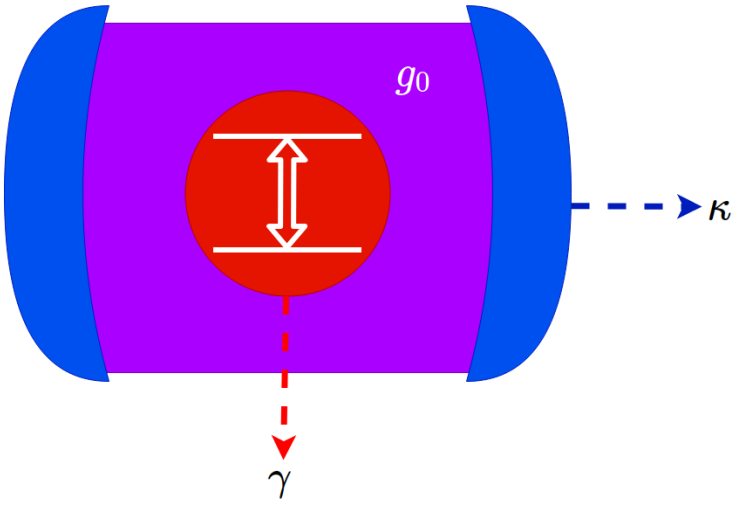

Figure 4.1: A schematic of a emitter-cavity coupled system with its energetic decay channels. The cavity walls (blue) surround a two-level atom (red). Their coupling is mediated by a photon field (purple). The strength of the coupling depends on the photon lifetime, which depends on the size of the decay channels characteristic of the optical elements: γ is due to atomic losses, such as photon emission outside the cavity and relaxations to intermediate energy levels (excluded by the two-level picture); κ represents cavity decay channels, such as refractive index, mirror separation length, and element reflectivity.

determined by multiple factors. Once again entertaining the point particle description of photons, an excited atom could eject photons from the cavity. Also, relaxation of an energized atom to intermediate energy levels could release non-resonant photon modes. Lastly, phonon scattering could decrease photon emission rates.

All forms of decay compete with the coupling strength g_0, and the relationship between the two determines the atom-cavity coupling limit. Here, the coupling strength is [19]

$$g_0 = \sqrt{\frac{2\pi\mu_{12}^2\omega}{V_0}}, \tag{4.1}$$

where μ_{12} is the dipole matrix element of the two-state transition, ω is the angular frequency of the photon, ε_0 is the free space permittivity, and V_0 is the modal volume. In general, when $\sqrt{N}g_0 << (\gamma, \kappa)$, where N is the number of quantum emitters in the cavity, the system occupies the weak coupling limit ($N = 1$ for atom-cavity case). In words, the mathematical statement refers to when the coupling parameter is much smaller than the larger of either γ or κ. Interesting phenomena occur in this regime, such as the alteration of spontaneous emission transition rates of quantum emitters known as the Purcell Effect [19, 189, 190]. This thesis concerns the strong coupling regime: $\sqrt{N}g_0 >> (\gamma, \kappa)$.

In this regime, the energy exchange rate between the atom and optical cavity is much higher than the dissipation rate. The photon is emitted and absorbed repeatedly by the atom, turning what is an irreversible process in free space into a reversible process. The theoretical domain of this electron-photon interaction loop is

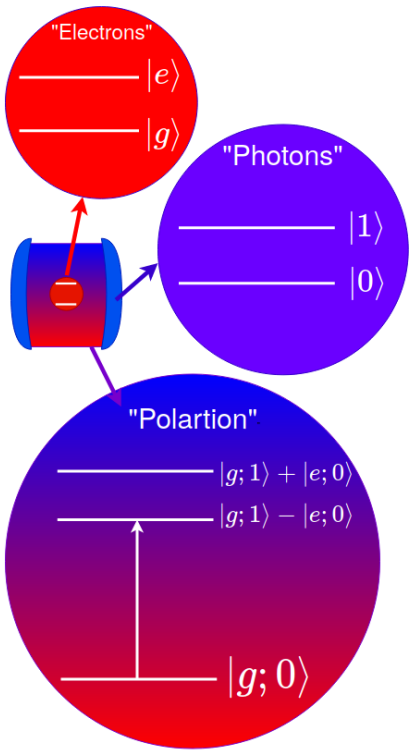

Figure 4.2: A particle-centric schematic of the emitter-cavity system. The electron energies of quantum emitters are represented by the toy two-level atom. The complete photon profile is determined by the structure of the cavity, which is represented by a two-level model corresponding to absorbed and free photon states. The coupling of the electron and photon may be understood as the hybridization of a pair of two-level toy models, leading to the formation of polariton doublets.

known as cavity quantum electrodynamics [191, 192], or cQED, named so because it explicitly handles electronic and photonic states simultaneously. The key ideas of cQED are elucidated by the Jaynes-Cummings model [21, 193], a two-state electron-photon interaction picture, and its main conclusion is that the atomic and photonic energy states couple to form newly dressed energy states: hybrid light-matter particles, or quasiparticles, known as polaritons.

The polariton energy states form with the lifting of a ground state degeneracy describing the uncoupled atom and photon states. The new energy states are doublets with a splitting size directly proportional to the coupling magnitude. What was formerly Fock and Hilbert space vector pairs becomes a coupled product of them both, forming a superposition consisting of terms describing the polariton states. Mathematically, assuming just one photon and a two-level atom, the polariton states are:

$$\Psi^{\pm}_{0,1} = \frac{1}{\sqrt{2}}(|g;1\rangle + |e;0\rangle). \tag{4.2}$$

The formation of polariton states is the hallmark of strong coupling, and they show up as splittings in the

optical absorption spectra of the quantum emitters. This splitting, known as Rabi splitting, conveys the frequency line locations of the polariton states. It is worth noting, however, these splittings in optical absorption spectra may occur with the presence of any kind of coupling field – that is, energy level splittings do not necessarily indicate the formation of polaritons [19, 194, 195, 196]. We will have no need to worry about this ostensibility, and we take our coverage of optics and strong coupling to the problem of calculating the ground state of a harmonically confined, many-electron system coupled to light in a cavity.

4.1.2 The Research Problem

Strong light-matter coupling in cavities leads to the formation of polariton states, which can demonstrate behavior wildly different than that of the uncoupled systems. Such coupling has been shown to impact optical nonlinearities [197, 198], affect photon frequency conversion [199], modify potential energy surfaces [200], modify molecular structures [201], change chemical properties [202] and do much more, which has attracted much experimental and theoretical interest [1, 203, 204, 205, 206, 207, 208]. The state-of-the-art of theory offers multiple approaches [58, 209, 210]. At present, however, no simple method for calculating observables related to strong coupling exist, and the light-matter coupling cannot be treated perturbatively per virtue of the hybridization. That said, like how we used RS electrodynamics and DFT to separately address the physical character of light and matter in the previous chapter, one can take advantage of the fundamentally decoupled nature of a problem and represent the disparate parts with different, well-established theories. Therefore, the idea here is to simplify a troublesome calculation for an interesting physical system in hopes to study its behavior and set benchmarks for generally faster, effective potential-based theories for strong light-matter coupling.

Here, we present a solution for the cQED problem of a harmonically confined, many-electron system coupled to light in a cavity. The general form of the harmonic well is a quadratic potential, which permits the decoupling of the electron motion into center-of-mass (CM) and relative parts, the former being the sole coordinate the cavity photons couple to. The solutions to the CM part are analytical. The solution to the relative motion, a many-electron problem, is not analytical. Therefore, we employ numerical approaches, one of which is density functional theory. The other approach is a wave function-based method known as stochastic variational method (SVM). Their electron densities and ground state energies are compared.

4.2 Computational Details

4.2.1 Relative and CM Hamiltonian Decoupling

The Hamiltonian decoupling process for a two-electron case is shown here [211]. We start with the Hamiltonian in eq. 2.193, the kinetic energy and general potential term being replaced with the N-body electronic

Hamiltonian containing electron-electron Coulomb and harmonic oscillator potential terms:

$$H = \frac{1}{2}\sum_{i=1}^{N}\mathbf{p}_i^2 + \frac{1}{2}{\omega_0}^2\sum_{i=1}^{N}\mathbf{x}_i^2 + \frac{1}{2}\sum_{i<j}^{N}\frac{1}{|\mathbf{x}_i-\mathbf{x}_j|} + \sum_n\left[\omega_n\left(\hat{a}_n^\dagger\hat{a}_n+\frac{1}{2}\right) - \omega_n q_n\boldsymbol{\lambda}_n\cdot\mathbf{D} + \frac{1}{2}(\boldsymbol{\lambda}_n\cdot\mathbf{D})^2\right], \tag{4.3}$$

where the first term is the total momentum of the N-electron system, the second term is the harmonic confinement potential, the third term is the Coulomb interaction, and the bracketed term, from left to right, is the free photon Hamiltonian, the photon-dipole interaction, and the dipole-self energy [108]. Eq. 4.3 may be split into a CM Hamiltonian and a relative motion Hamiltonian. To do this, we pull focus on the electronic Hamiltonian. Using only the electron terms, one can define relative coordinates like so,

$$\bar{\mathbf{x}}_i = \mathbf{x}_i - \mathbf{X}, \quad \mathbf{X} = \frac{1}{N}\sum_{i=1}^{N}\mathbf{x}_i, \tag{4.4}$$

then use them to reconfigure the electronic Hamiltonian into a CM and relative coordinate part. These Hamiltonians are defined as:

$$H_{REL} = \frac{1}{2}\sum_{i=1}^{N}\boldsymbol{\pi}_i^2 + \frac{1}{2}\frac{\omega_0^2}{N}\sum_{i<j}^{N}(\bar{\mathbf{x}}_i-\bar{\mathbf{x}}_j)^2 + \frac{1}{2}\sum_{i<j}^{N}\frac{1}{|\bar{\mathbf{x}}_i-\bar{\mathbf{x}}_j|} \tag{4.5}$$

$$H_{CM} = \frac{1}{2N}\boldsymbol{\Pi}^2 + \frac{1}{2}N\omega_0^2\mathbf{X}^2, \tag{4.6}$$

where $\boldsymbol{\Pi}$ is the canonically conjugate momentum to the CM coordinate $\mathbf{X}$, and $\boldsymbol{\pi}_i$ are the canonically conjugate momenta to the relative coordinates $\bar{\mathbf{x}}_i$. Recalling the definition of the total dipole operator established for eq. 2.194,

$$\begin{aligned}\mathbf{D} &= \sum_{i=1}^{N}\mathbf{d}_i \\ &= \sum_{i=1}^{N}\mathbf{x}_i,\end{aligned}$$

we may construct a form of the Pauli-Fierz Hamiltonian which capitalizes on this decoupling and reveals information about the photon coupling. Assuming only one photon mode, the need to sum over modes n vanishes, making eq. 4.3 a total, decoupled Hamiltonian of the form

$$H = H_{REL} + \omega\left(\hat{a}^\dagger\hat{a}+\frac{1}{2}\right) - N\omega q\boldsymbol{\lambda}\cdot\mathbf{X} + H_{CM} + \frac{1}{2}(N\boldsymbol{\lambda}\cdot\mathbf{X})^2. \tag{4.7}$$

The N is needed to cancel out its reciprocal in the definition of $\mathbf{X}$.

Looking at eq. 4.7 it might not come as a surprise that the photon couples to the CM term only. The photon-electron coupling in the Pauli-Fierz Hamiltonian is expressed as a dot product between the photon

coordinates (the coordinate operator and the polarization vector) and the total dipole – and the latter is a many-body operator in this context. Therefore, the photon interacts with each electron orbital simultaneously. This is desirable, as it agrees with the delocalized interaction of photons with a many-body system and captures the delocalized character of polariton states [212]

The CM Hamiltonian may be decoupled further. To do this, with $\mathbf{X} = (X,Y,Z)$ we introduce substitutions

$$u = \sqrt{N}\frac{X+Y}{\sqrt{2}} \tag{4.8}$$

$$v = \sqrt{N}\frac{Y-X}{\sqrt{2}} \tag{4.9}$$

$$z = \sqrt{N}Z. \tag{4.10}$$

These coordinate substitutions have the useful effect of reconfiguring a part of the Hamiltonian: $\hat{H}_{CM} + \frac{1}{2}(N\boldsymbol{\lambda}\cdot\mathbf{X})^2$, which explicitly

$$\hat{H}_{CM} + \frac{1}{2}(N\boldsymbol{\lambda}\cdot\mathbf{X})^2 = \frac{1}{2N}\boldsymbol{\Pi}^2 + \frac{1}{2}N\omega_0^2\mathbf{X}^2 + \frac{1}{2}(N\boldsymbol{\lambda}\cdot\mathbf{X})^2. \tag{4.11}$$

The momentum being the most complicated term to transform, we will perform its transformation last. We start with,

$$\frac{1}{2}N\omega_0^2\mathbf{X}^2 = \frac{1}{2}N\omega_0^2(X^2+Y^2+Z^2). \tag{4.12}$$

The simplest way to transform this term is by taking the squares of eqs. 4.8, 4.9, and 4.10, like so,

$$u^2 = \frac{N}{2}(X^2+Y^2+2XY) \tag{4.13}$$

$$v^2 = \frac{N}{2}(X^2+Y^2-2XY) \tag{4.14}$$

$$z^2 = NZ^2, \tag{4.15}$$

and then adding them together,

$$u^2+v^2+z^2 = \frac{N}{2}(X^2+Y^2+2XY) + \frac{N}{2}(X^2+Y^2-2XY) + NZ^2 \tag{4.16}$$

$$= NX^2 + NY^2 + (NXY - NXY) + NZ^2 \tag{4.17}$$

$$= N(X^2+Y^2+Z^2). \tag{4.18}$$

This gives us our first transformation, summarized as

$$\frac{1}{2}N\omega_0^2(X^2+Y^2+Z^2)=\frac{1}{2}\omega_0^2(u^2+v^2+z^2). \tag{4.19}$$

The next term we will transform is the dipole self-interaction term. Recalling that $\boldsymbol{\lambda}=\lambda(1,1,0)$, the total dipole-self interaction term is expanded as,

$$\frac{1}{2}(N\boldsymbol{\lambda}\cdot\mathbf{X})^2=\frac{1}{2}N^2\boldsymbol{\lambda}^2(X^2+Y^2+2XY). \tag{4.20}$$

Noting our expansion of the individual transformations, we can see immediately the expansion may be straightforwardly related to u^2,

$$\frac{1}{2}N^2\boldsymbol{\lambda}^2(X^2+Y^2+2XY)=N\boldsymbol{\lambda}^2\left[\frac{N}{2}(X^2+Y^2+2XY)\right] \tag{4.21}$$

$$=N\boldsymbol{\lambda}^2u^2. \tag{4.22}$$

The reconfiguration of the momentum term is somewhat tedious, but may be understood in analogy to the Cartesian-to-spherical coordinate transformation of the Laplacian. That is, one may follow the same steps needed to transform the Laplacian to spherical coordinates to transform the momentum to the new (u,v,z)-coordinate system. Observe that expressing an arbitrary function in Cartesian coordinate space, $f(X,Y,Z)$, as an arbitrary function in the new-coordinate space, $f(u(X,Y),v(X,Y),z(Z))$, with the mapping dependencies made explicit hinges the transformation on the chain rule. First, we take inventory of the structure of the momentum,

$$\frac{1}{2N}\boldsymbol{\Pi}^2=\frac{1}{2N}\left(\frac{\partial^2}{\partial X^2}+\frac{\partial^2}{\partial Y^2}+\frac{\partial^2}{\partial Z^2}\right). \tag{4.23}$$

Second, because we will have need of them, we express the derivatives of the coordinate transformations:

$$\because\quad u=\sqrt{\frac{N}{2}}(X+Y) \tag{4.24}$$

$$\frac{\partial u}{\partial X}=\sqrt{\frac{N}{2}} \tag{4.25}$$

$$\frac{\partial u}{\partial Y}=\sqrt{\frac{N}{2}} \tag{4.26}$$

$$\frac{\partial u}{\partial Z}=0, \tag{4.27}$$

and

$$\because \quad v = \sqrt{\frac{N}{2}}(Y - X) \tag{4.28}$$

$$\frac{\partial v}{\partial X} = -\sqrt{\frac{N}{2}} \tag{4.29}$$

$$\frac{\partial v}{\partial Y} = \sqrt{\frac{N}{2}} \tag{4.30}$$

$$\frac{\partial v}{\partial Z} = 0, \tag{4.31}$$

and

$$\because \quad z = \sqrt{N}Z \tag{4.32}$$

$$\frac{\partial z}{\partial X} = 0 \tag{4.33}$$

$$\frac{\partial z}{\partial Y} = 0 \tag{4.34}$$

$$\frac{\partial z}{\partial Z} = \sqrt{N}. \tag{4.35}$$

Third, using the chain rule we express the Cartesian coordinate derivatives of the arbitrary function $f(u(X,Y), v(X,Y), z(Z))$. Expanding $\frac{\partial f}{\partial X}$ we get

$$\frac{\partial f}{\partial X} = \frac{\partial f}{\partial u}\frac{\partial u}{\partial X} + \frac{\partial f}{\partial v}\frac{\partial v}{\partial X} + \frac{\partial f}{\partial z}\frac{\partial z}{\partial X} \tag{4.36}$$

$$= \sqrt{\frac{N}{2}}\frac{\partial f}{\partial u} - \sqrt{\frac{N}{2}}\frac{\partial f}{\partial v}, \tag{4.37}$$

where both $\frac{\partial u}{\partial X}$ and $\frac{\partial v}{\partial X}$ are expressed explicitly, and the third term vanishes because of the definition of z. Now, using the well-known second derivative identity of $\frac{\partial^2}{\partial X \partial Y} = \frac{\partial^2}{\partial Y \partial X}$, we can cleverly eliminate Cartesian derivatives while evaluating $\frac{\partial^2 f}{\partial X^2}$. Demonstrated,

$$\frac{\partial^2 f}{\partial X^2} = \frac{\partial}{\partial X}\left[\sqrt{\frac{N}{2}}\frac{\partial f}{\partial u} - \sqrt{\frac{N}{2}}\frac{\partial f}{\partial v}\right] \tag{4.38}$$

$$= \sqrt{\frac{N}{2}}\frac{\partial}{\partial u}\left[\frac{\partial f}{\partial u}\frac{\partial u}{\partial X} + \frac{\partial f}{\partial v}\frac{\partial v}{\partial X}\right] - \sqrt{\frac{N}{2}}\frac{\partial}{\partial v}\left[\frac{\partial f}{\partial u}\frac{\partial u}{\partial X} + \frac{\partial f}{\partial v}\frac{\partial v}{\partial X}\right] \tag{4.39}$$

$$= \sqrt{\frac{N}{2}}\frac{\partial}{\partial u}\left[\frac{\partial f}{\partial u}\sqrt{\frac{N}{2}} - \frac{\partial f}{\partial v}\sqrt{\frac{N}{2}}\right] - \sqrt{\frac{N}{2}}\frac{\partial}{\partial v}\left[\frac{\partial f}{\partial u}\sqrt{\frac{N}{2}} - \frac{\partial f}{\partial v}\sqrt{\frac{N}{2}}\right] \tag{4.40}$$

$$= \frac{N}{2}\frac{\partial}{\partial u}\left[\frac{\partial f}{\partial u} - \frac{\partial f}{\partial v}\right] - \frac{N}{2}\frac{\partial}{\partial v}\left[\frac{\partial f}{\partial u} - \frac{\partial f}{\partial v}\right] \tag{4.41}$$

$$= \frac{N}{2}\left[\frac{\partial^2 f}{\partial u^2} + \frac{\partial^2 f}{\partial v^2}\right]. \tag{4.42}$$

The same steps are taken to evaluate $\frac{\partial f}{\partial Y}$ and $\frac{\partial^2 f}{\partial Y^2}$:

$$\frac{\partial f}{\partial Y} = \frac{\partial f}{\partial u}\frac{\partial u}{\partial Y} + \frac{\partial f}{\partial v}\frac{\partial v}{\partial Y} + \frac{\partial f}{\partial z}\frac{\partial z}{\partial Y} \tag{4.43}$$

$$= \sqrt{\frac{N}{2}}\frac{\partial f}{\partial u} + \sqrt{\frac{N}{2}}\frac{\partial f}{\partial v}, \tag{4.44}$$

and

$$\frac{\partial^2 f}{\partial Y^2} = \frac{\partial}{\partial Y}\left[\sqrt{\frac{N}{2}}\frac{\partial f}{\partial u} + \sqrt{\frac{N}{2}}\frac{\partial f}{\partial v}\right] \tag{4.45}$$

$$= \sqrt{\frac{N}{2}}\frac{\partial}{\partial u}\left[\frac{\partial f}{\partial u}\frac{\partial u}{\partial Y} + \frac{\partial f}{\partial v}\frac{\partial v}{\partial Y}\right] + \sqrt{\frac{N}{2}}\frac{\partial}{\partial v}\left[\frac{\partial f}{\partial u}\frac{\partial u}{\partial Y} + \frac{\partial f}{\partial v}\frac{\partial v}{\partial Y}\right] \tag{4.46}$$

$$= \sqrt{\frac{N}{2}}\frac{\partial}{\partial u}\left[\frac{\partial f}{\partial u}\sqrt{\frac{N}{2}} + \frac{\partial f}{\partial v}\sqrt{\frac{N}{2}}\right] + \sqrt{\frac{N}{2}}\frac{\partial}{\partial v}\left[\frac{\partial f}{\partial u}\sqrt{\frac{N}{2}} + \frac{\partial f}{\partial v}\sqrt{\frac{N}{2}}\right] \tag{4.47}$$

$$= \frac{N}{2}\frac{\partial}{\partial u}\left[\frac{\partial f}{\partial u} + \frac{\partial f}{\partial v}\right] + \frac{N}{2}\frac{\partial}{\partial v}\left[\frac{\partial f}{\partial u} + \frac{\partial f}{\partial v}\right] \tag{4.48}$$

$$= \frac{N}{2}\left[\frac{\partial^2 f}{\partial u^2} + \frac{\partial^2 f}{\partial v^2}\right]. \tag{4.49}$$

And one more time with feeling, and with fewer necessary steps, $\frac{\partial f}{\partial Z}$ and $\frac{\partial^2 f}{\partial Z^2}$:

$$\frac{\partial f}{\partial Z} = \frac{\partial f}{\partial u}\frac{\partial u}{\partial Z} + \frac{\partial f}{\partial v}\frac{\partial v}{\partial Z} + \frac{\partial f}{\partial z}\frac{\partial z}{\partial Z} \tag{4.50}$$

$$= \sqrt{N}\frac{\partial f}{\partial z}, \tag{4.51}$$

$$\tag{4.52}$$

and

$$\frac{\partial^2 f}{\partial Z^2} = \sqrt{N}\frac{\partial}{\partial Z}\frac{\partial f}{\partial z} \tag{4.53}$$

$$= N\frac{\partial^2 f}{\partial z^2}. \tag{4.54}$$

All together, the momentum is

$$\frac{1}{2N}\left(\frac{\partial^2}{\partial X^2} + \frac{\partial^2}{\partial Y^2} + \frac{\partial^2}{\partial Z^2}\right) = \frac{1}{2N}\left(\frac{N}{2}\left[\frac{\partial^2 f}{\partial u^2} + \frac{\partial^2 f}{\partial v^2}\right] + \frac{N}{2}\left[\frac{\partial^2 f}{\partial u^2} + \frac{\partial^2 f}{\partial v^2}\right] + N\frac{\partial^2 f}{\partial z^2}\right) \tag{4.55}$$

$$= \frac{1}{2N}\left(N\left[\frac{\partial^2 f}{\partial u^2} + \frac{\partial^2 f}{\partial v^2}\right] + N\frac{\partial^2 f}{\partial z^2}\right) \tag{4.56}$$

$$= \frac{1}{2}\left(\frac{\partial^2 f}{\partial u^2} + \frac{\partial^2 f}{\partial v^2} + \frac{\partial^2 f}{\partial z^2}\right). \tag{4.57}$$

And when the smoke clears, the transformed Hamiltonian is

$$\frac{1}{2N}\mathbf{\Pi}^2+\frac{1}{2}N\omega_0^2\mathbf{X}^2+\frac{1}{2}(N\boldsymbol{\lambda}\cdot\mathbf{X})^2=\frac{1}{2}\left(\frac{\partial^2 f}{\partial u^2}+\frac{\partial^2 f}{\partial v^2}+\frac{\partial^2 f}{\partial z^2}\right)+\frac{1}{2}\omega_0^2(u^2+v^2+z^2)+N\boldsymbol{\lambda}^2u^2 \tag{4.58}$$

We may condense the Hamiltonian further according to the new variables. That is,

$$H_u=\frac{1}{2}\frac{\partial^2 f}{\partial u^2}+\frac{1}{2}\omega_0^2u^2+N\boldsymbol{\lambda}^2u^2 \tag{4.59}$$

$$H_v=\frac{1}{2}\frac{\partial^2 f}{\partial v^2}+\frac{1}{2}\omega_0^2v^2 \tag{4.60}$$

$$H_z=\frac{1}{2}\frac{\partial^2 f}{\partial z^2}+\frac{1}{2}\omega_0^2z^2, \tag{4.61}$$

and recognizing the frequency shift exclusive to u, we may write the Hamiltonians as

$$H_u=\frac{1}{2}\frac{\partial^2 f}{\partial u^2}+\frac{1}{2}(\omega_0^2+2N\boldsymbol{\lambda}^2)u^2 \tag{4.62}$$

$$=\frac{1}{2}\frac{\partial^2 f}{\partial u^2}+\frac{1}{2}\omega_u^2u^2 \tag{4.63}$$

$$H_v=\frac{1}{2}\frac{\partial^2 f}{\partial v^2}+\frac{1}{2}\omega_v^2v^2 \tag{4.64}$$

$$H_z=\frac{1}{2}\frac{\partial^2 f}{\partial z^2}+\frac{1}{2}\omega_z^2z^2. \tag{4.65}$$

Here $\omega_0=\omega_v=\omega_z$ and $\omega_u^2=\omega_0^2+2N\lambda^2$. Finally, we have the decoupled CM Hamiltonian,

$$\hat{H}_{CM}+\frac{1}{2}(N\boldsymbol{\lambda}\cdot\mathbf{X})^2=H_u+H_v+H_z \tag{4.66}$$

We now have three independent harmonic oscillators. Noting that H_u is structurally different from H_v and H_z, we see that, due to $\boldsymbol{\lambda}^2$ it is the only part of the CM Hamiltonian coupled to light. Being free of this coupling, the H_v and H_z terms correspond to quantum harmonic oscillator solutions.

$$H_v\phi_k(v)=\left(k+\frac{1}{2}\right)\omega_v\phi_k(v) \tag{4.67}$$

$$H_z\phi_l(z)=\left(l+\frac{1}{2}\right)\omega_z\phi_l(z) \tag{4.68}$$

Using H_u we can simplify the coupling Hamiltonian as

$$H_c = \omega\left(\hat{a}^\dagger\hat{a}+\frac{1}{2}\right) - N\omega q\boldsymbol{\lambda}\cdot\mathbf{X}+H_u \tag{4.69}$$

$$= \omega\left(\hat{a}^\dagger\hat{a}+\frac{1}{2}\right) - N\omega q\lambda(X+Y)+H_u \tag{4.70}$$

$$= \omega\left(\hat{a}^\dagger\hat{a}+\frac{1}{2}\right) - N\omega q\lambda\sqrt{\frac{2}{N}}u+H_u \tag{4.71}$$

$$= \omega\left(\hat{a}^\dagger\hat{a}+\frac{1}{2}\right) - \sqrt{2N}\omega q\lambda u+H_u. \tag{4.72}$$

Finally, we have the totally decoupled Hamiltonian

$$H = H_{REL}+H_v+H_z+H_c, \tag{4.73}$$

with energies

$$E = E_{REL}+E_v+E_z+E_c, \tag{4.74}$$

corresponding to product ansatz

$$\Psi = \Phi(\bar{\mathbf{x}})\phi_k(v)\phi_l(z)\Phi_{\mathrm{c}}(u) \tag{4.75}$$

We see that the total wave function Ψ is decoupled too. The CM wave function is $\phi_k(v)\phi_l(z)\Phi_{\mathrm{c}}(u)$, and is solvable using either exact diagonalization or shifted Fock states. The relative wave function must be solved numerically.

4.2.2 DFT and SVM for Relative Motion Hamiltonian

We will use the SVM and DFT approaches to solve for $\Phi(\bar{\mathbf{x}})$. The SVM approach is a wave function-based approach which expands the spatial component of $\Phi(\bar{\mathbf{x}})$ into explicitly correlated Gaussians

$$\Phi_k(\bar{\mathbf{x}}) = \hat{A}\left(\exp\left[-\frac{1}{2}\sum_{i<j}^{N}\alpha_{ij}^k(\mathbf{x}_i-\mathbf{x}_j)^2-\frac{1}{2}\sum_{i=1}^{N}\beta_i^k(\mathbf{x}_i-\mathbf{s}_i^k)^2\right]\chi_S\right). \tag{4.76}$$

The operator $\hat{A}$ is the antisymmetrizer, χ_S is the N-electron spin function which couples the spin to S. Symbols α_{ij}^k, β_i^k, and $\mathbf{s}_i^k$ are nonlinear parameters. Fuller explanations of this approach may be found [70, 75]. Here, matrix elements can be analytically calculated. The SVM is used to optimize the basis functions by settling on the best spatial basis parameters, selecting candidates which minimize the energy from an enormous batch of procedurally generated parameters. After generating a basis, it undergoes refinement via the replacement of states with randomly chosen basis functions superior to their predecessors. Adding the best states one by

one may be done to increase the size of the basis.

The DFT approach just takes the relative motion Hamiltonian and puts it into a spin-sensitive, density functionalized form:

$$H_{REL} = -\frac{1}{2}\nabla^2 + V_H[p(\bar{\mathbf{x}})] + V_{EX}[\rho_\uparrow(\mathbf{x}), \rho_\downarrow(\bar{\mathbf{x}})] + V_C(\bar{\mathbf{x}}) \tag{4.77}$$

. From left to right, the first term is the kinetic energy, the second term is the Hartree potential, the third term is the exchange correlation potential, and the fourth term, V_C, is the confining potential. The exchange-correlation potential is approximated using the local density approximation. The system being spin polarized, the orbitals and their corresponding densities are separated according to their orientation:

$$\rho_\uparrow = \sum_i \phi_{\uparrow,i}(\mathbf{x})^2, \qquad \rho_\downarrow = \sum_i \phi_{\downarrow,i}(\mathbf{x})^2 \tag{4.78}$$

The DFT equations are solved on a real-space grid – with grid spacing $h = 0.2$ Bohr – with a finite difference representation of its derivatives.

4.3 Results and Discussion

The DFT and SVM energy calculations follow similar trends dependent on spin and particle number. The SVM energies are always smaller than the DFT energies, and the SVM energies are accurate upper bounds of the exact energy. The electron densities predicted by both approaches are similar, though the SVM and DFT figures are rotated with respect to each other because the ground state is rotationally invariant (see fig. 4.3). This is due to the photon vector polarization – in x and y, nullifying any preference in direction. The SVM energies are accurate up to three significant digits passed the decimal. The disagreement between the approaches might be due to the typical DFT shortcomings, the form of the exchange-correlation potential. The relative motion part of the system is not informed by the CM coordinate and photon coupling, so the relative motion energy is just a constant shift to the CM motion energy.

Table 4.1 shows the energy of the relative motion calculated by SVM and DFT for different confinement strengths, spins, and electron numbers. Fig 4.4 shows the DFT-calculated ground state energy, for the cases with no spin polarization, as a function of electron number.

N	S	ω_0	DFT	SVM
2	0	0.5	1.743	1.659
		1.0	3.232	3.000
		1.5	4.626	4.268
2	1	0.5	1.980	1.913
		1.0	3.837	3.596
		1.5	5.627	5.236
3	0.5	0.5	3.703	3.583
		1.0	6.727	6.369
		1.5	9.544	8.982
3	1.5	0.5	3.840	3.714
		1.0	7.173	6.760
		1.5	10.34	9.681
4	0	0.5	6.074	6.071
		1.0	10.83	10.62
		1.5	15.23	14.57
4	1	0.5	6.049	5.964
		1.0	10.79	10.34
		1.5	15.18	14.48
4	2	0.5	6.493	6.349
		1.0	11.94	11.63
		1.5	17.10	16.27
5	0.5	0.5	8.905	8.880
		1.0	15.64	15.27
		1.5	21.81	21.39
5	1.5	0.5	9.092	9.074
		1.0	16.15	15.78
		1.5	22.67	22.04
5	2.5	0.5	9.476	9.287
		1.0	17.19	16.57
		1.5	24.45	23.50

Table 4.1: The SVM- and DFT-calculated energies for the relative motion. The parameters: N is the electron number; S is the spin; ω_0 is the frequency.

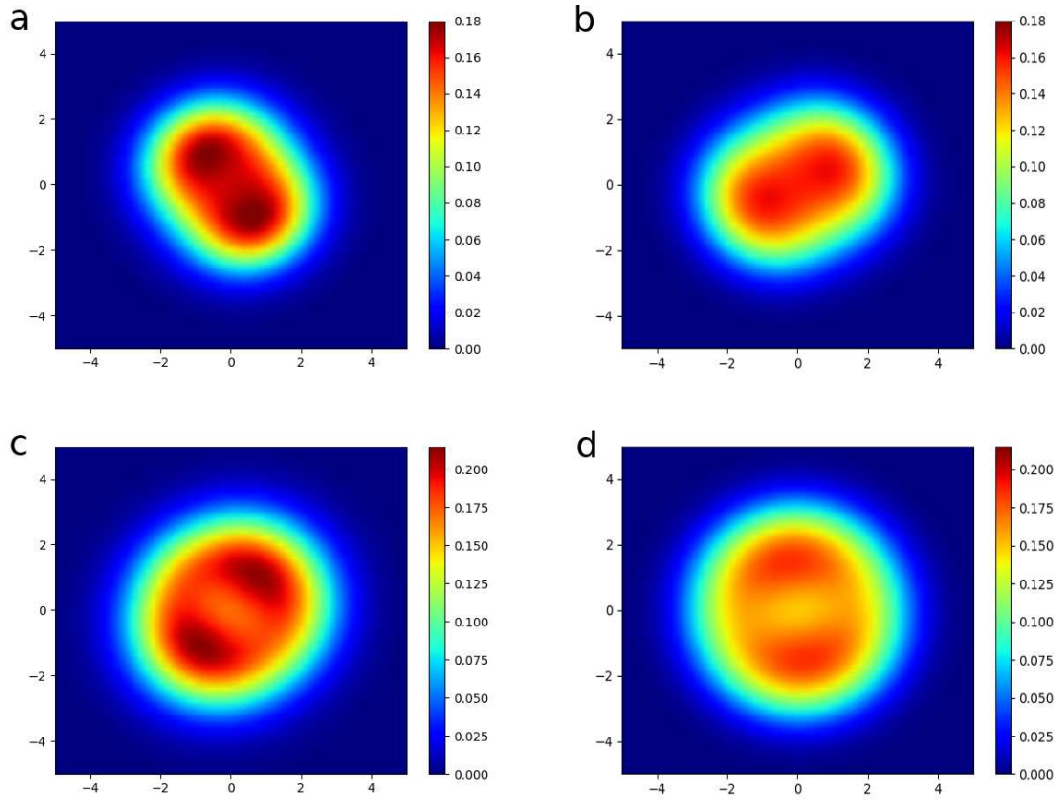

Figure 4.3: Electron density for three electrons (a) SVM, (b) DFT and five electrons (c) SVM, (d) DFT for $\omega_0 = 0.5$.

4.4 Appendix for Chapter 4

4.4.1 Exact Diagonalization of Light-Matter Coupled Hamiltonian

The CM Hamiltonian in the form of eq. 4.72 may be solved using exact diagonalization. The form of the basis function is a tensor product of CM wave functions and photon states (see Chapter 5):

$$|n_u\rangle \otimes |n_q\rangle = \phi_{n_u}(u)|n_q\rangle. \tag{4.79}$$

Where $|n_u\rangle$ and ϕ_{n_u} are, respectively, the electron state (Hilbert space) vector and the electron wave function. The term $|n_q\rangle$ is the photon state (Fock space) vector. In evaluating their eigenvalues, one must separate the operators by what space they exist in. The Fock space operator is q. The Hilbert space operators are H_u and u.

Despite this, the matrix elements of H_c are straightforward to calculate. Arguably the simplest term, H_u

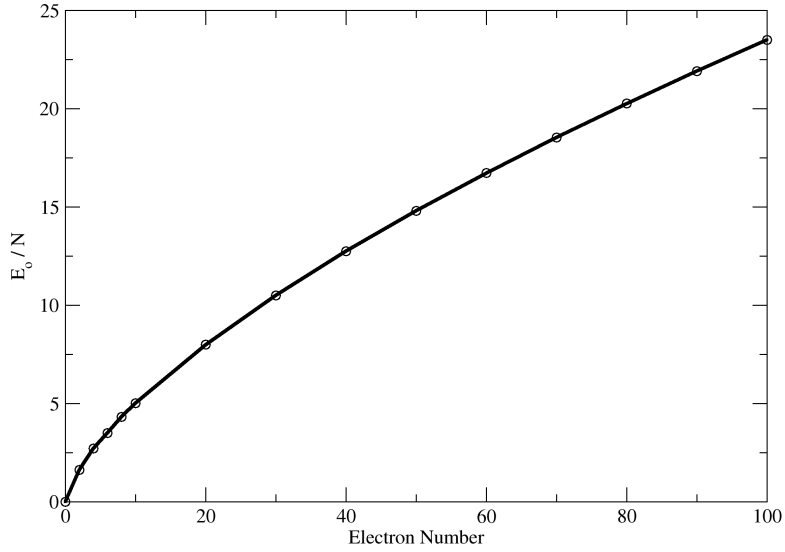

Figure 4.4: DFT-calculated ground state energy per electron in harmonically confined N-electron system.

yields the eigenvalues of the quantum harmonic oscillator,

$$\langle n'_u| \otimes \langle n'_q|H_u|n_u\rangle \otimes |n_q\rangle = \langle n'_u| \otimes \langle n'_q| \left(\frac{1}{2}\frac{\partial^2 f}{\partial u^2} + \frac{1}{2}\omega_u^2 u^2\right)|n_u\rangle \otimes |n_q\rangle \tag{4.80}$$

$$= \langle n'_u|n_u\rangle \langle n'_q| \left(\frac{1}{2}\frac{\partial^2 f}{\partial u^2} + \frac{1}{2}\omega_u^2 u^2\right)|n_q\rangle \tag{4.81}$$

$$= \delta_{n'_u n_u}\delta_{n'_q n_q}\left(n_u + \frac{1}{2}\right)\omega_u, \tag{4.82}$$

where δ_{ij} is the Kronecker delta. The operation on the free photon term yields the same result for photon energy levels:

$$\langle n'_u| \otimes \langle n'_q| \left(\hat{a}^\dagger \hat{a} + \frac{1}{2}\right)|n_u\rangle \otimes |n_q\rangle = \langle n'_u|n_u\rangle \langle n'_q| \left(\hat{a}^\dagger \hat{a} + \frac{1}{2}\right)|n_q\rangle \tag{4.83}$$

$$= \delta_{n'_u n_u}\delta_{n'_q n_q}\left(n_q + \frac{1}{2}\right). \tag{4.84}$$

The $\sqrt{2N}\omega q\lambda u$ term is more complicated. Clearly, from the other terms, the electron and photon states may be understood with the theory of the quantum harmonic oscillator. We are then permitted to express u as a ladder operator like so,

$$u = \frac{1}{\sqrt{2\omega_u}}(\hat{a}_u^\dagger + \hat{a}_u), \tag{4.85}$$

where $\hat{a}_u^\dagger$ and $\hat{a}_u$ are creation and annihilation operators for the electron states. This puts u in an electron Fock space separate from the photon Fock space. Due to the identical physicality of the Fock and Hilbert space solutions for the electron harmonic oscillator, a contradiction does not arise by changing the definition of u. Operating on $\sqrt{2N}\omega q\lambda u$ then yields,

$$\langle n'_u| \otimes \langle n'_q| \left(\sqrt{2N}\omega q\lambda u\right) |n_u\rangle \otimes |n_q\rangle = \sqrt{2N}\omega\lambda \langle n'_q|q|n_q\rangle \langle n'_u|u|n_u\rangle \tag{4.86}$$

$$= \sqrt{2N}\omega\lambda \langle n'_q| \frac{1}{\sqrt{2\omega}}(\hat{a}^\dagger + \hat{a})|n_q\rangle \langle n'_u| \frac{1}{\sqrt{2\omega_u}}(\hat{a}_u^\dagger + \hat{a}_u)|n_u\rangle \tag{4.87}$$

$$= \sqrt{\frac{N\omega}{2\omega_u}}\lambda \langle n'_q|(\hat{a}^\dagger + \hat{a})|n_q\rangle \langle n'_u|(\hat{a}_u^\dagger + \hat{a}_u)|n_u\rangle, \tag{4.88}$$

which expands into

$$\begin{aligned}\sqrt{\frac{N\omega}{2\omega_u}}\lambda \langle n'_q|(\hat{a}^\dagger + \hat{a})|n_q\rangle \langle n'_u|(\hat{a}_u^\dagger + \hat{a}_u)|n_u\rangle = \sqrt{\frac{N\omega}{2\omega_u}}\lambda \langle n'_q|(\sqrt{n_q+1}|n_q+1\rangle + \sqrt{n_q}|n_q-1\rangle) \\ \times \langle n'_u|(\sqrt{n_u+1}|n_u+1\rangle + \sqrt{n_u}|n_u-1\rangle).\end{aligned} \tag{4.89}$$

The parenthetical terms of the right-hand side of eq. 4.89 are structurally identical – evaluating one elucidates both. Generalizing the Fock states as $|n\rangle$, the matrix elements follow

$$D_{n'n} = \langle n'|\sqrt{n+1}|n+1\rangle + \langle n'|\sqrt{n}|n-1\rangle \tag{4.90}$$

$$= \sqrt{n+1}\langle n'|n+1\rangle + \sqrt{n}\langle n'|n-1\rangle, \tag{4.91}$$

giving elements

$$D_{00} = \sqrt{1}\langle 0|1\rangle + \sqrt{0}\langle 0|0-1\rangle = 0 \tag{4.92}$$

$$D_{01} = \sqrt{2}\langle 0|2\rangle + \sqrt{1}\langle 0|0\rangle = \sqrt{1} \tag{4.93}$$

$$D_{10} = \sqrt{1}\langle 1|1\rangle + \sqrt{0}\langle 1|0-1\rangle = \sqrt{1} \tag{4.94}$$

$$D_{11} = \sqrt{2}\langle 2|3\rangle + \sqrt{2}\langle 2|1\rangle = 0, \tag{4.95}$$

and so on. Following the pattern delineated above, we obtain

$$D_{mn} = \begin{bmatrix} 0 & \sqrt{1} & 0 & 0 & 0 & \dots \\ \sqrt{1} & 0 & \sqrt{2} & 0 & 0 & \dots \\ 0 & \sqrt{2} & 0 & \sqrt{3} & 0 & \dots \\ 0 & 0 & \sqrt{3} & 0 & \sqrt{4} & \dots \\ 0 & 0 & 0 & \sqrt{4} & 0 & \dots \\ \vdots & \vdots & \vdots & \vdots & \vdots & \ddots \end{bmatrix} \tag{4.96}$$

With eq. 4.96, we may rewrite eq. 4.86 as

$$\langle n'_u| \otimes \langle n'_q| \left(\sqrt{2N}\omega q \lambda u \right) |n_u\rangle \otimes |n_q\rangle = \sqrt{\frac{N\omega}{2\omega_u}} \lambda D_{n'_q n_q} D_{n'_u n_u}. \tag{4.97}$$

All together, the matrix elements of the CM Hamiltonian are

$$\langle n'_u| \otimes \langle n'_q|H_c|n_u\rangle \otimes |n_q\rangle = \delta_{n'_u n_u}\delta_{n'_q n_q} \left(n_u + \frac{1}{2} \right) \omega_u + \delta_{n'_u n_u}\delta_{n'_q n_q} \left(n_q + \frac{1}{2} \right) \omega + \sqrt{\frac{N\omega}{2\omega_u}} \lambda D_{n'_q n_q} D_{n'_u n_u}. \tag{4.98}$$

The eigenproducts which follow from eq. 4.98 are

$$\Phi_c = \sum_{n_u, n_q} c_{n_u, n_q} \phi_{n_u}(u) |n_q\rangle, \tag{4.99}$$

where c_{n_u, n_q} are the eigenproduct components.

4.5 Supplement for Chapter 4

4.5.1 Plots of Harmonically Confined DFT-calculated Electron Densities

Presented here are one- and two-dimensional plots for a multitude of harmonically confined electron populations and spin cases. All plots were generated using DFT ground states.

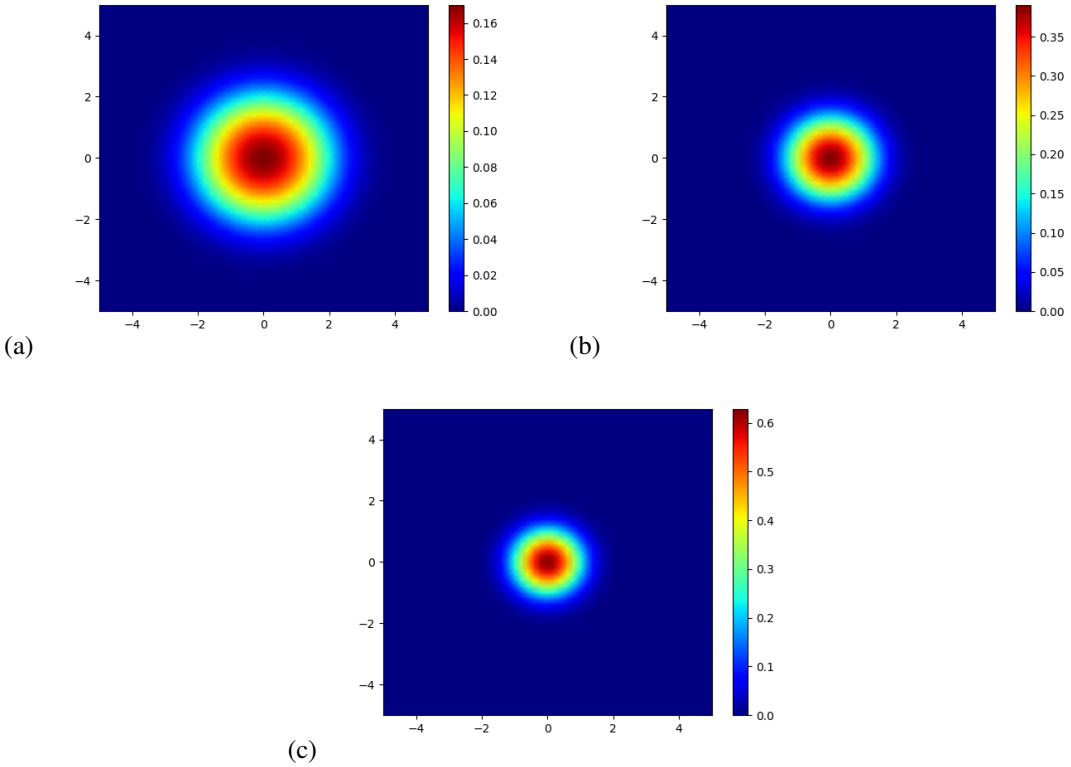

Figure 4.5: Relative motion DFT calculation of electron density for two electrons with total spin 0: $\uparrow + \downarrow = 0$. (a) $\omega_0 = 0.5$ (b) $\omega_0 = 1.0$ (c) $\omega_0 = 1.5$. Note that each plot has a unique color bar scale.

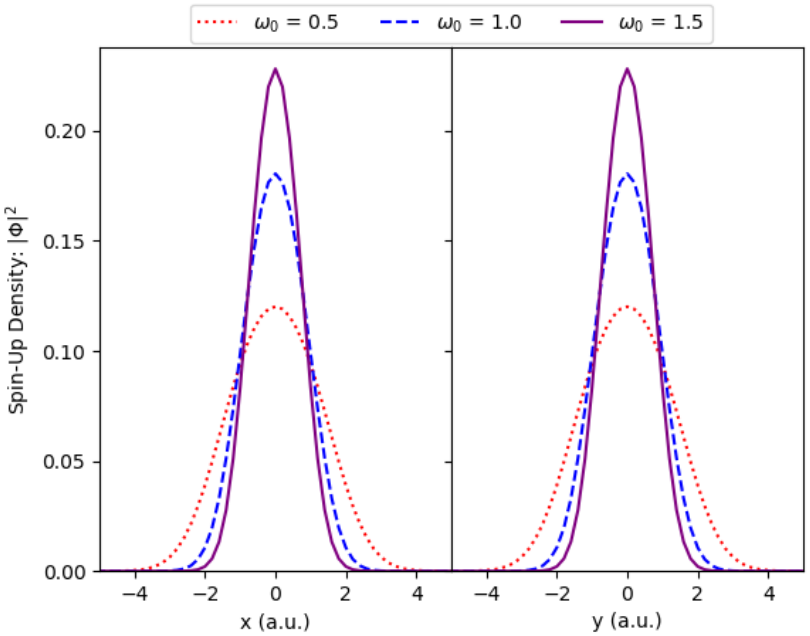

Figure 4.6: Spin-up electron density slices of two-electron system (S = 0) at different confining potential frequencies.

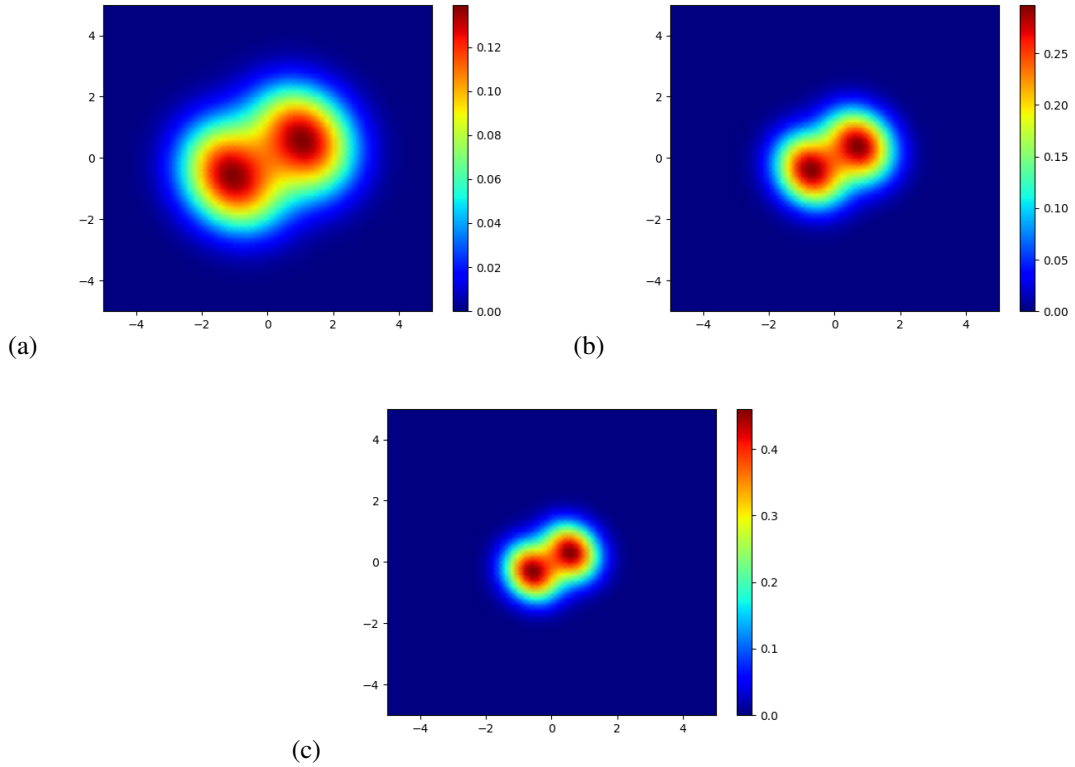

Figure 4.7: Relative motion DFT calculation of electron density for two electrons with total spin 1: $\uparrow + \uparrow = 1$. (a) $\omega_0 = 0.5$ (b) $\omega_0 = 1.0$ (c) $\omega_0 = 1.5$. Note that each plot has a unique color bar scale.

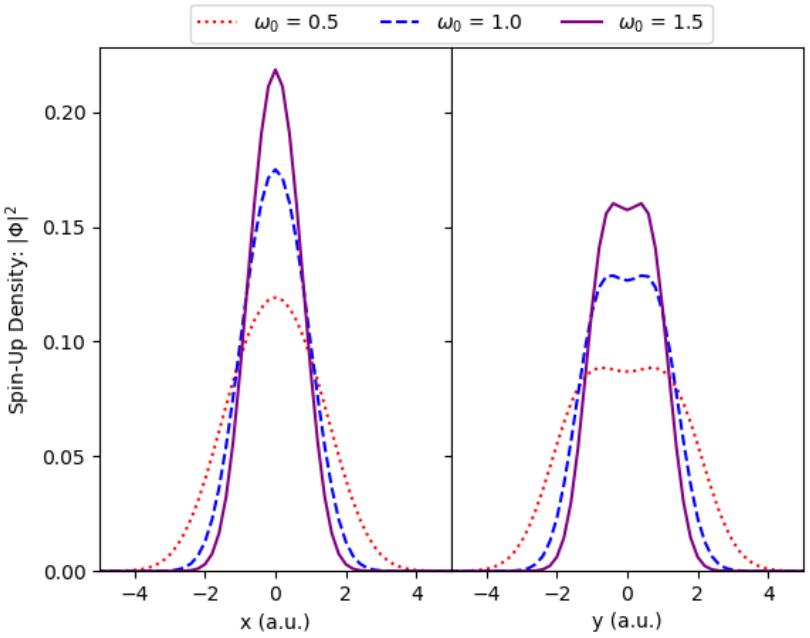

Figure 4.8: Spin-up electron density slices of two-electron system (S = 1) at different confining potential frequencies.

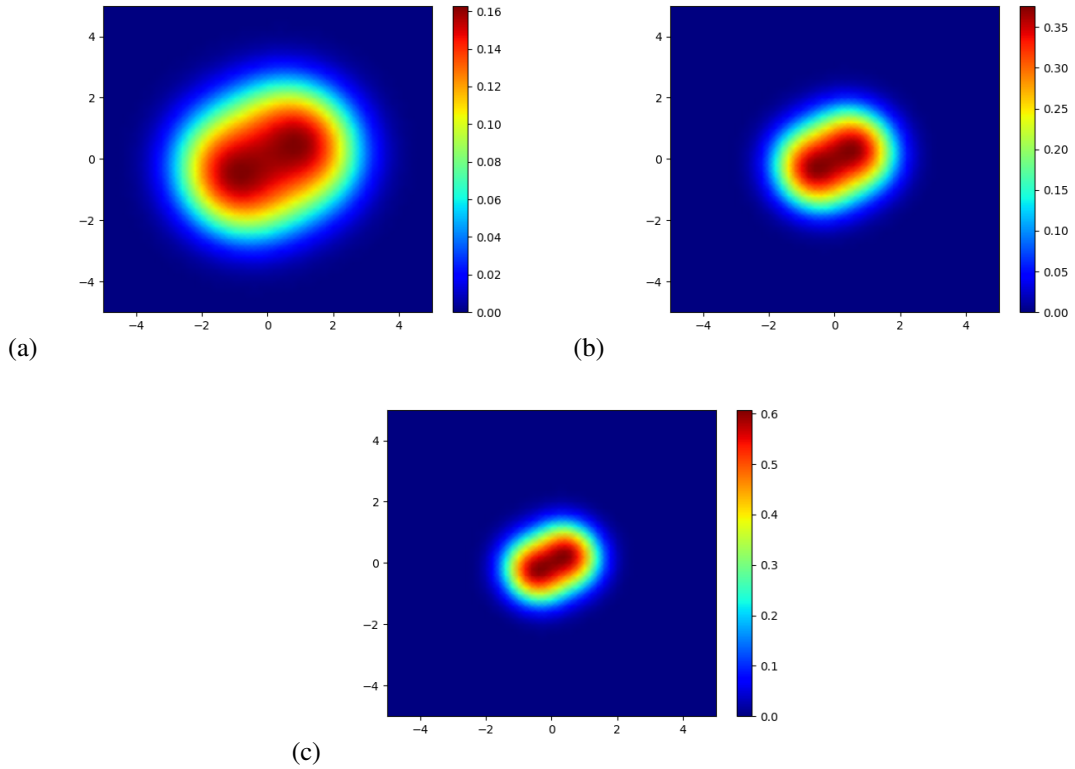

Figure 4.9: Relative motion DFT calculation of electron density for three electrons with total spin $\frac{1}{2}$: $\uparrow + \uparrow + \downarrow = \frac{1}{2}$. (a) $\omega_0 = 0.5$ (b) $\omega_0 = 1.0$ (c) $\omega_0 = 1.5$. Note that each plot has a unique color bar scale.

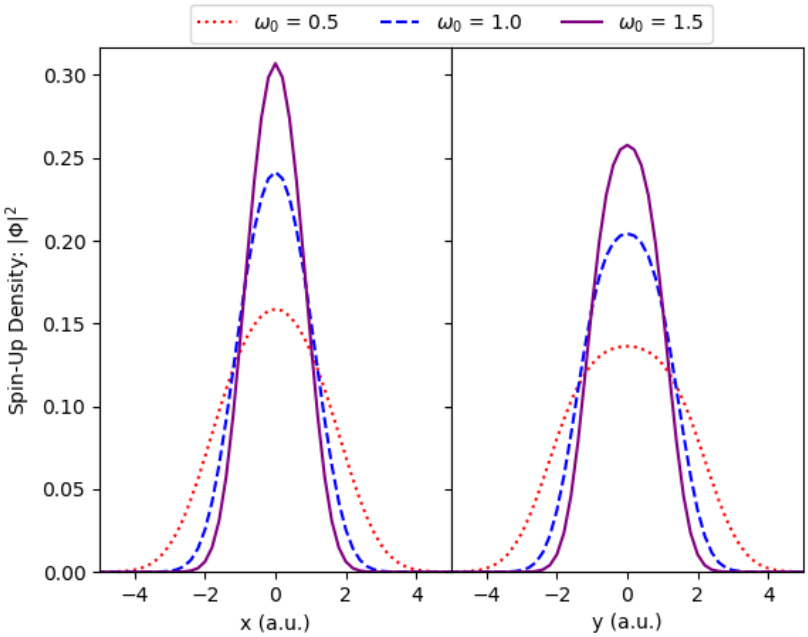

Figure 4.10: Spin-up electron density slices of three-electron system (S = $\frac{1}{2}$) at different confining potential frequencies.

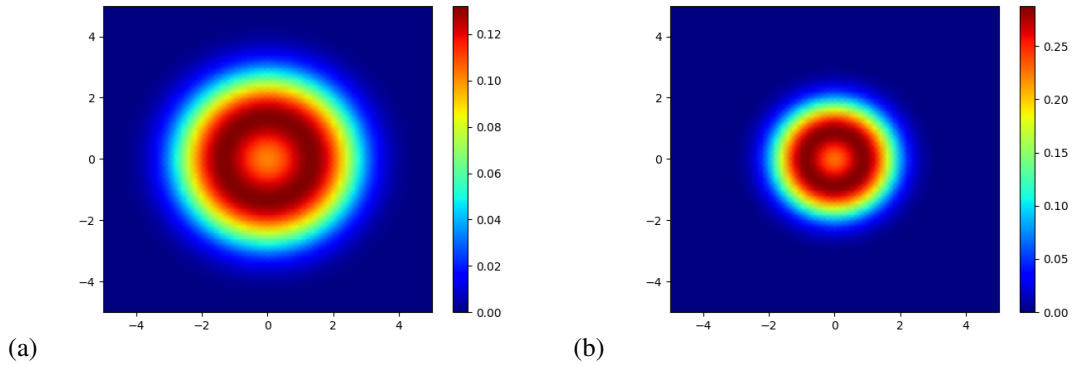

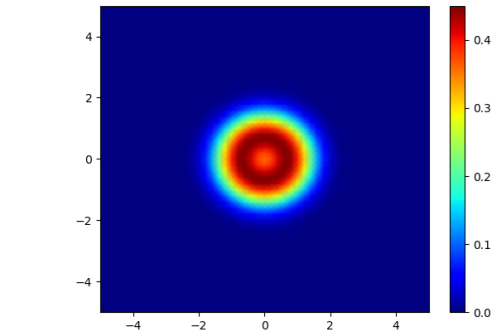

Figure 4.11: Relative motion DFT calculation of electron density for three electrons with total spin $\frac{3}{2}$: $\uparrow + \uparrow + \uparrow = \frac{3}{2}$. (a) $\omega_0 = 0.5$ (b) $\omega_0 = 1.0$ (c) $\omega_0 = 1.5$. Note that each plot has a unique color bar scale.

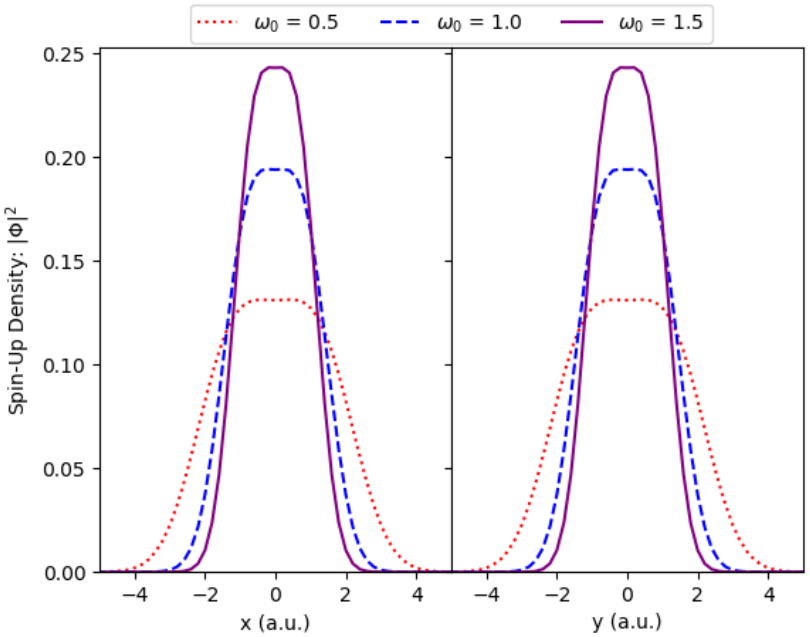

Figure 4.12: Spin-up electron density slices of three-electron system (S = $\frac{3}{2}$) at different confining potential frequencies.

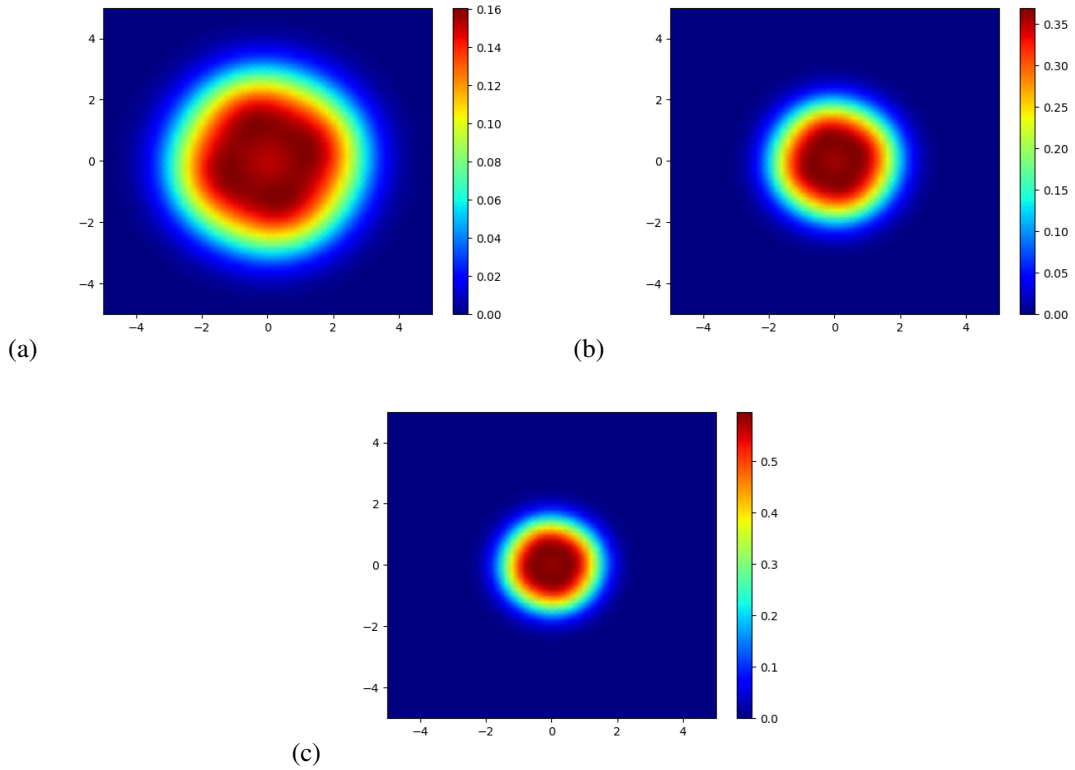

Figure 4.13: Relative motion DFT calculation of electron density for four electrons with total spin 0: $\uparrow + \uparrow + \downarrow + \downarrow = 0$. (a) $\omega_0 = 0.5$ (b) $\omega_0 = 1.0$ (c) $\omega_0 = 1.5$. Note that each plot has a unique color bar scale.

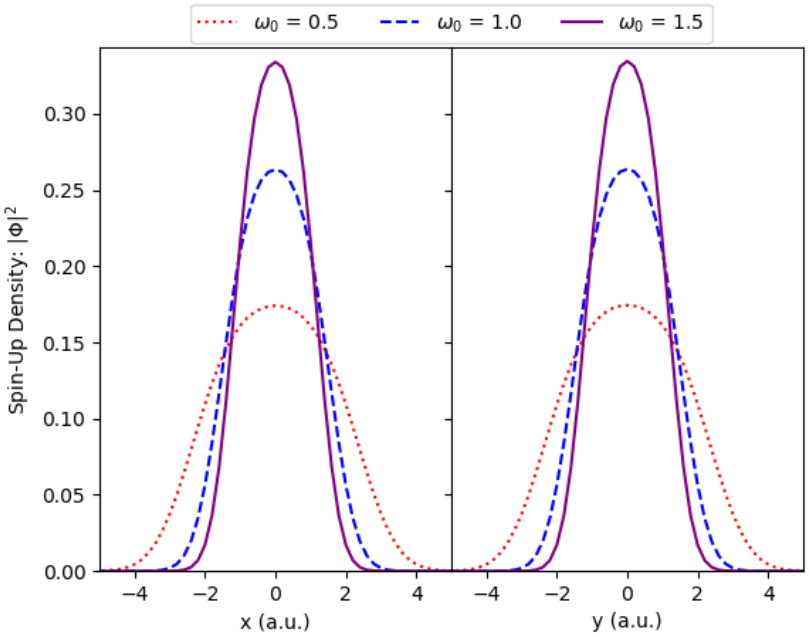

Figure 4.14: Spin-up electron density slices of four-electron system (S = 0) at different confining potential frequencies.

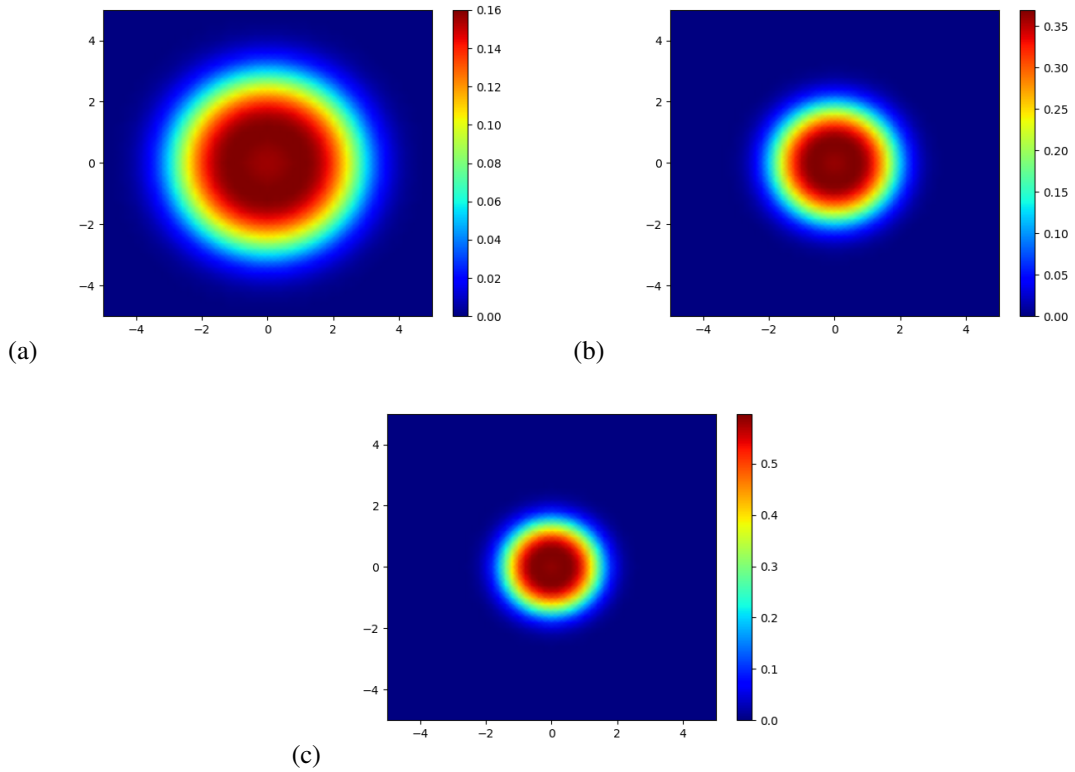

Figure 4.15: Relative motion DFT calculation of electron density for four electrons with total spin 1: $\uparrow + \uparrow + \uparrow - \downarrow = 1$. (a) $\omega_0 = 0.5$ (b) $\omega_0 = 1.0$ (c) $\omega_0 = 1.5$. Note that each plot has a unique color bar scale.

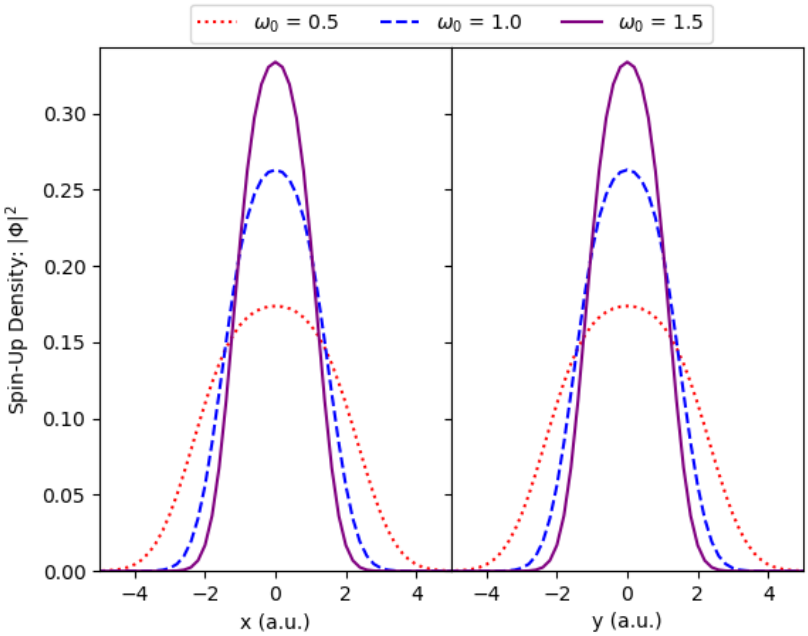

Figure 4.16: Spin-up electron density slices of four-electron system (S = 1) at different confining potential frequencies.

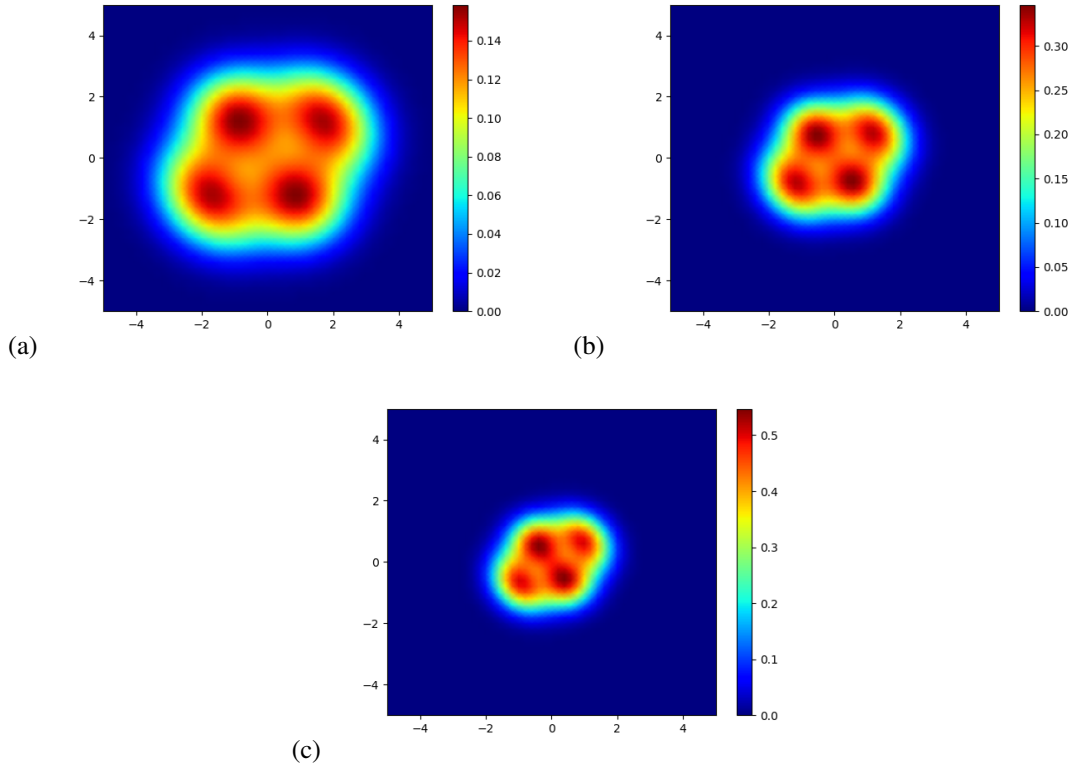

Figure 4.17: Relative motion DFT calculation of electron density for four electrons with total spin 2: $\uparrow + \uparrow + \uparrow + \uparrow = 2$. (a) $\omega_0 = 0.5$ (b) $\omega_0 = 1.0$ (c) $\omega_0 = 1.5$. Note that each plot has a unique color bar scale.

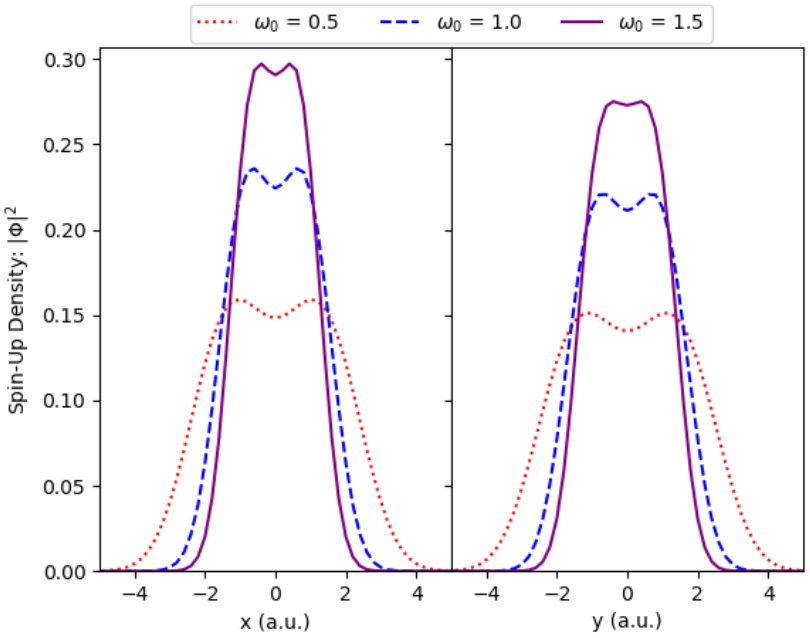

Figure 4.18: Spin-up electron density slices of four-electron system (S = 2) at different confining potential frequencies.

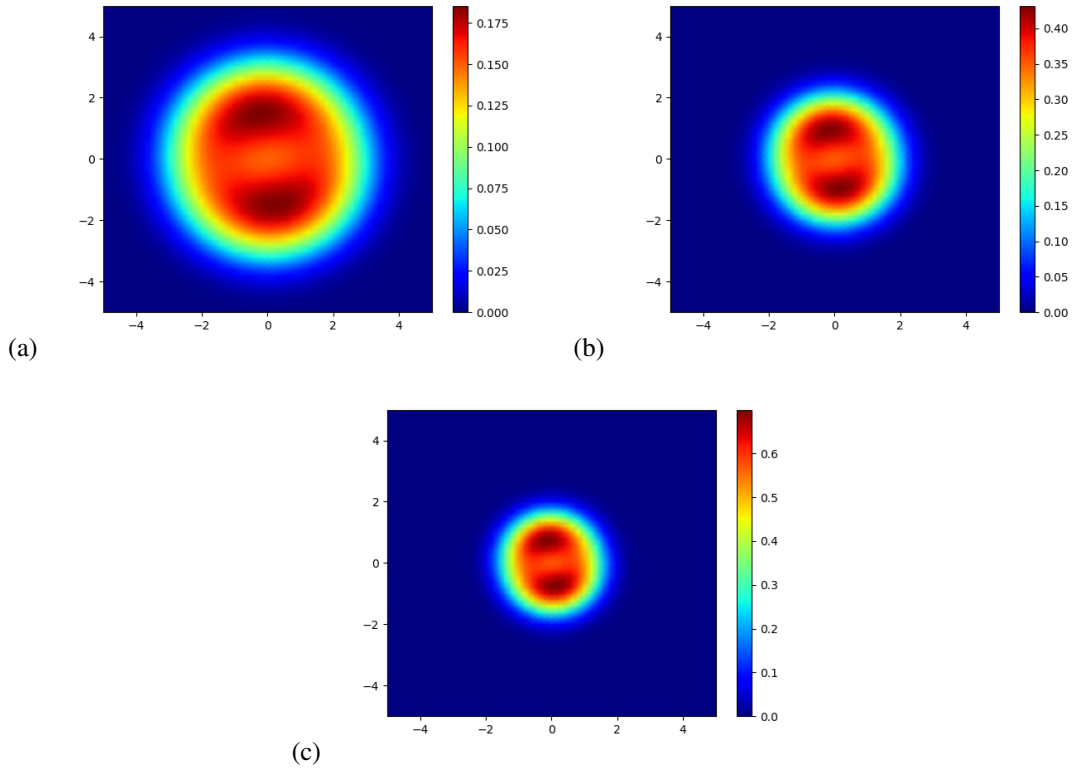

Figure 4.19: Relative motion DFT calculation of electron density for five electrons with total spin $\frac{1}{2}$: $\uparrow+\uparrow+\uparrow+\downarrow+\downarrow=\frac{1}{2}$. (a) $\omega_0 = 0.5$ (b) $\omega_0 = 1.0$ (c) $\omega_0 = 1.5$. Note that each plot has a unique color bar scale.

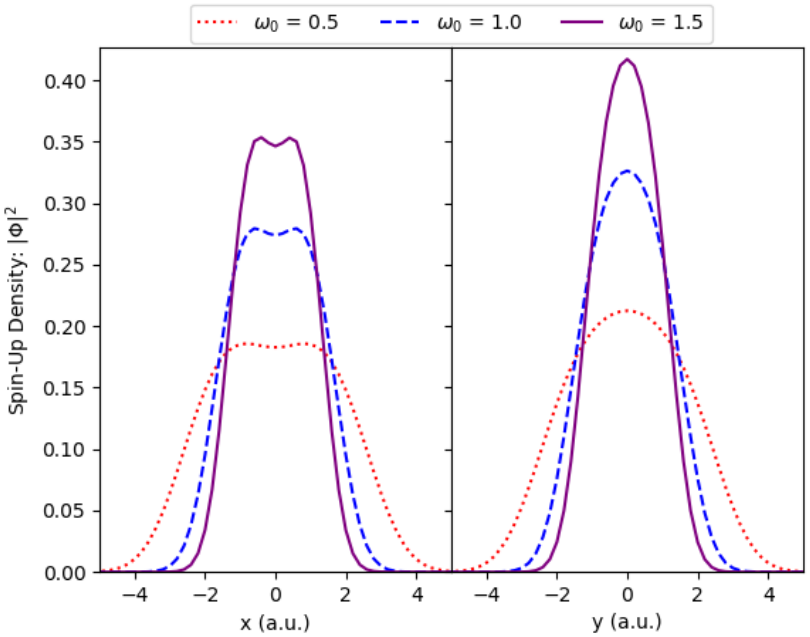

Figure 4.20: Spin-up electron density slices of five-electron system (S = $\frac{1}{2}$) at different confining potential frequencies.

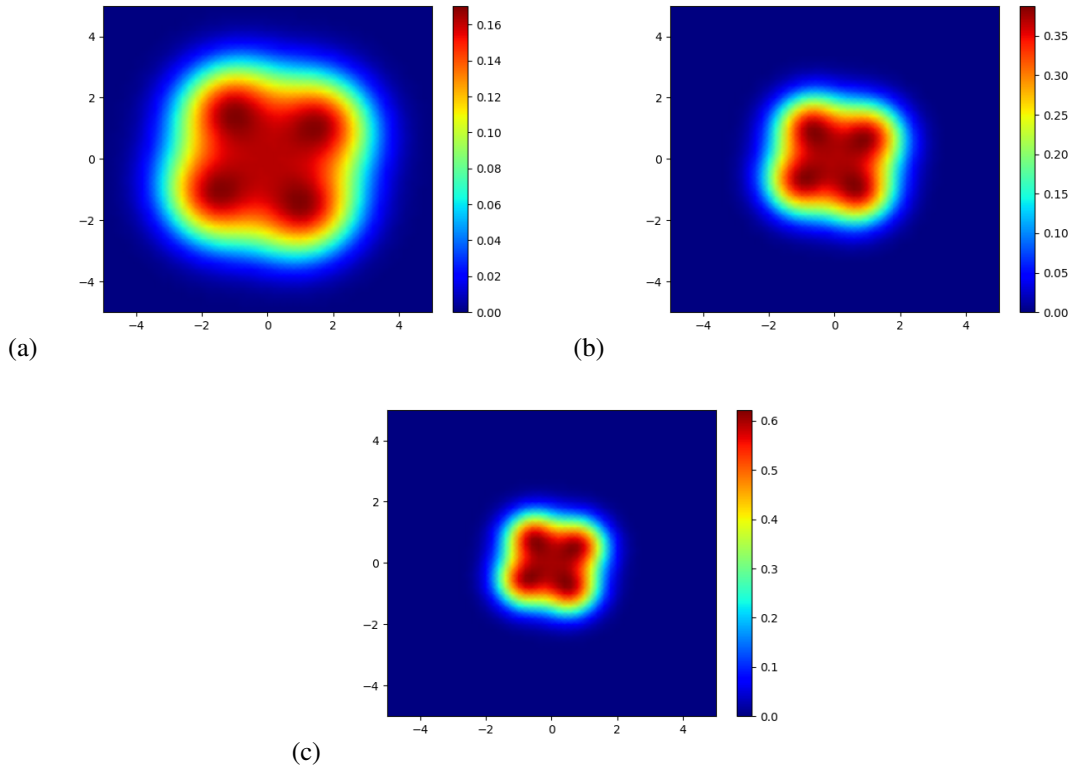

Figure 4.21: Relative motion DFT calculation of electron density for five electrons with total spin $\frac{3}{2}$: $\uparrow+\uparrow+\uparrow+\uparrow+\downarrow=\frac{3}{2}$. (a) $\omega_0 = 0.5$ (b) $\omega_0 = 1.0$ (c) $\omega_0 = 1.5$. Note that each plot has a unique color bar scale.

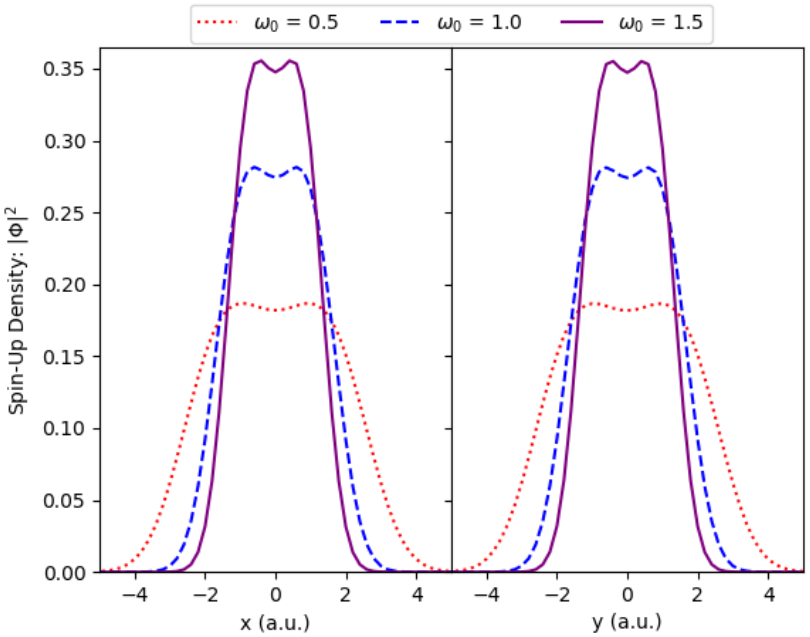

Figure 4.22: Spin-up electron density slices of five-electron system (S = $\frac{3}{2}$) at different confining potential frequencies.

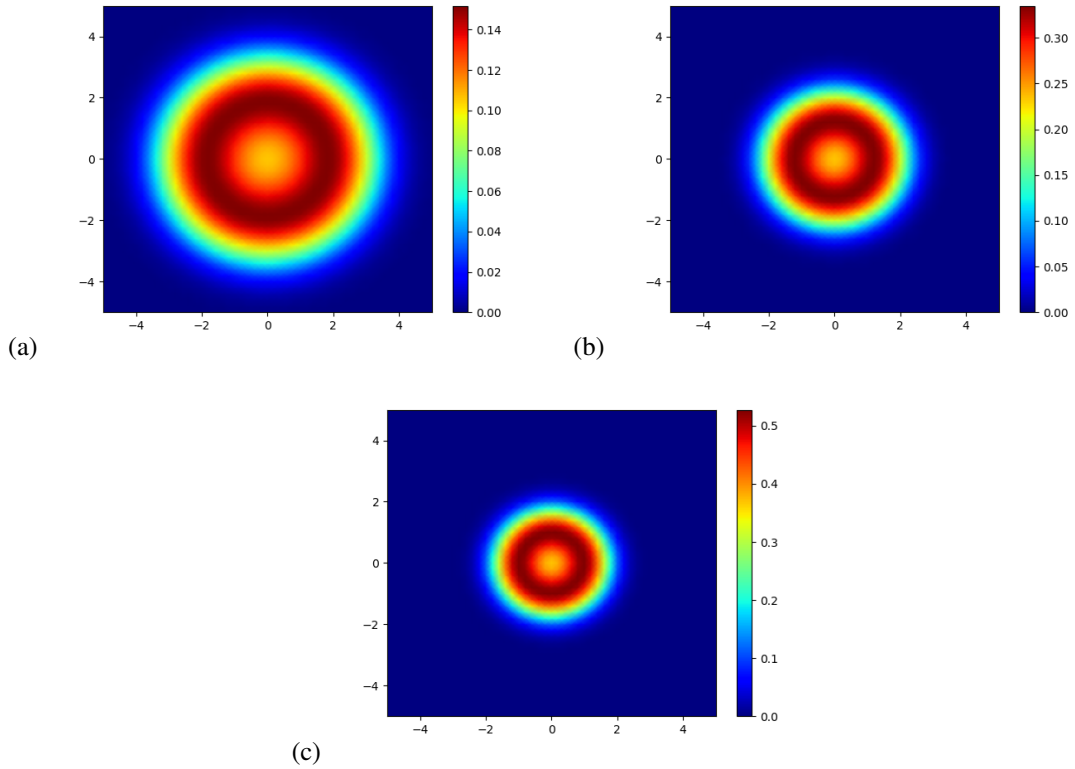

Figure 4.23: Relative motion DFT calculation of electron density for five electrons with total spin $\frac{5}{2}$: $\uparrow+\uparrow+\uparrow+\uparrow+\uparrow=\frac{5}{2}$. (a) $\omega_0 = 0.5$ (b) $\omega_0 = 1.0$ (c) $\omega_0 = 1.5$. Note that each plot has a unique color bar scale.

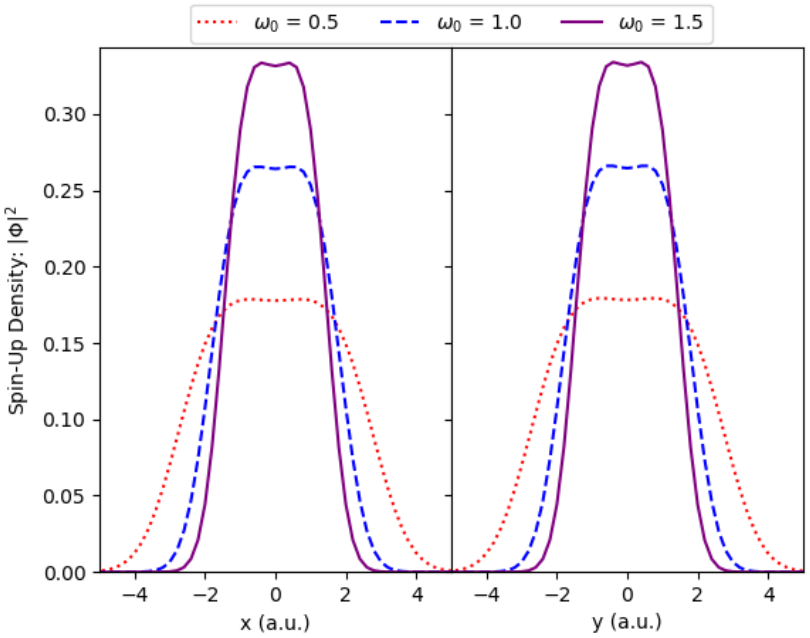

Figure 4.24: Spin-up electron density slices of five-electron system (S = $\frac{5}{2}$) at different confining potential frequencies.

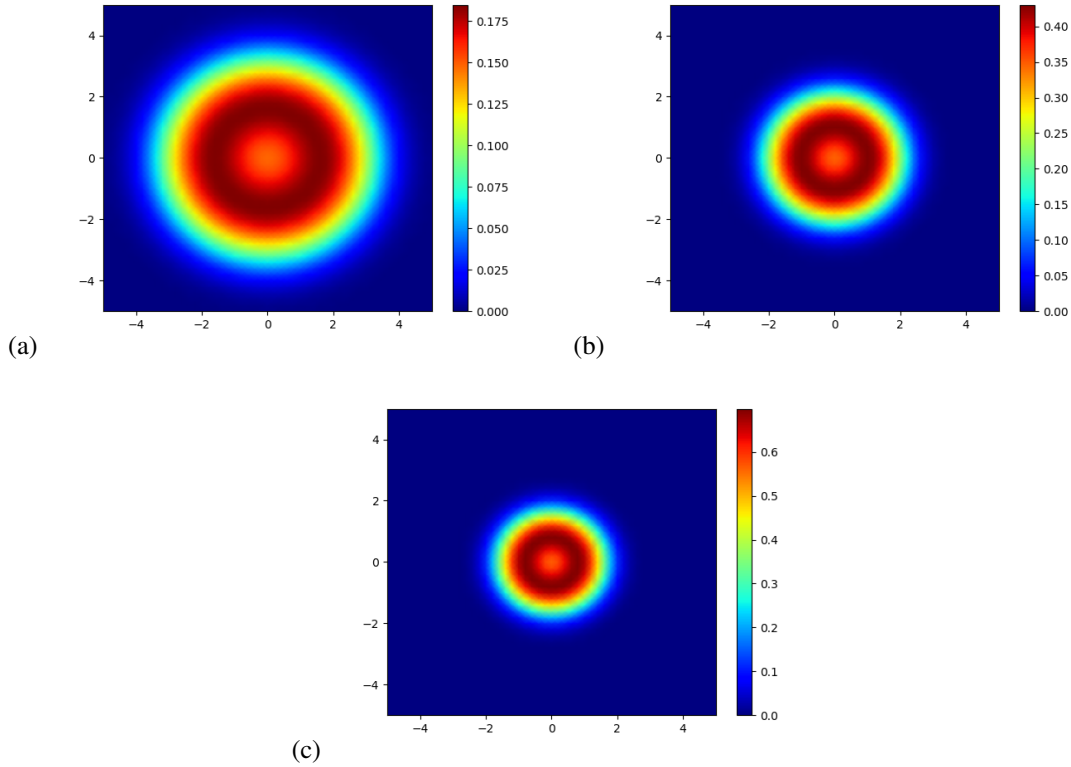

Figure 4.25: Relative motion DFT calculation of electron density for six electrons with total spin 0: $\uparrow+\uparrow+\uparrow+\downarrow+\downarrow+\downarrow=0$. (a) $\omega_0 = 0.5$ (b) $\omega_0 = 1.0$ (c) $\omega_0 = 1.5$. Note that each plot has a unique color bar scale.

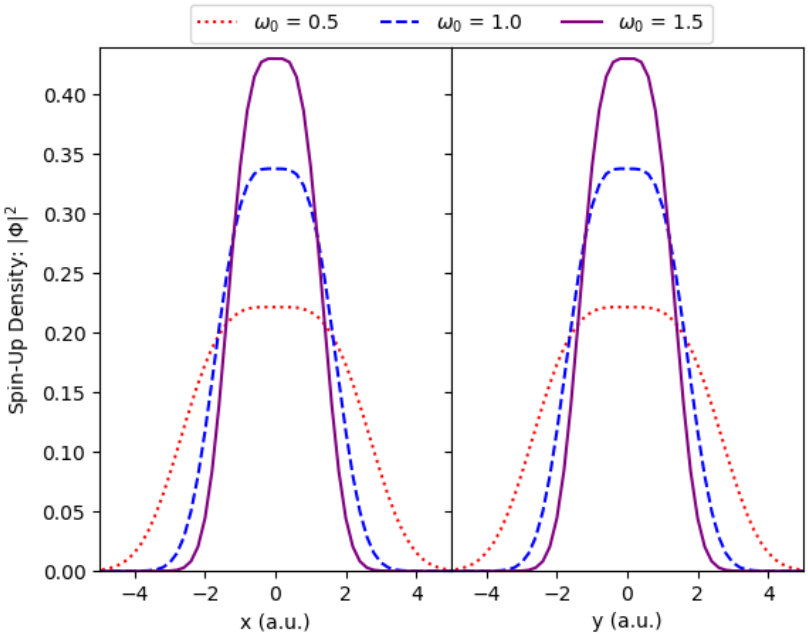

Figure 4.26: Spin-up electron density slices of six-electron system (S = 0) at different confining potential frequencies.

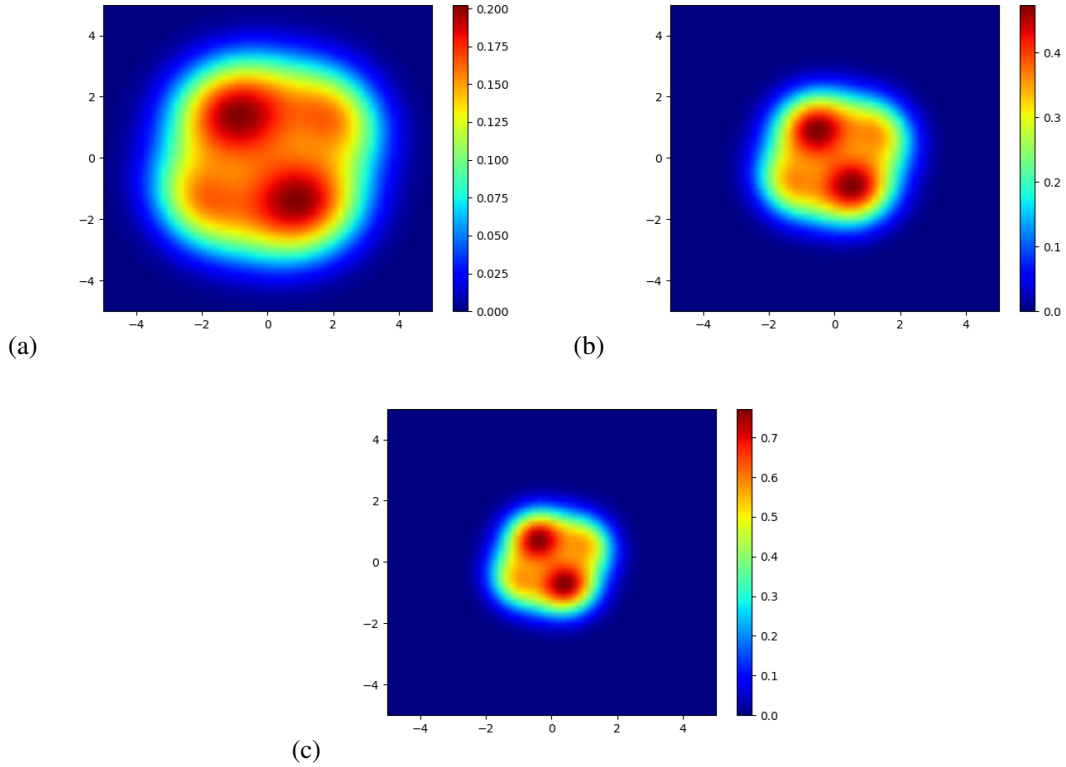

Figure 4.27: Relative motion DFT calculation of electron density for six electrons with total spin 1: $\uparrow + \uparrow + \uparrow + \uparrow + \downarrow + \downarrow = 1$. (a) $\omega_0 = 0.5$ (b) $\omega_0 = 1.0$ (c) $\omega_0 = 1.5$. Note that each plot has a unique color bar scale.

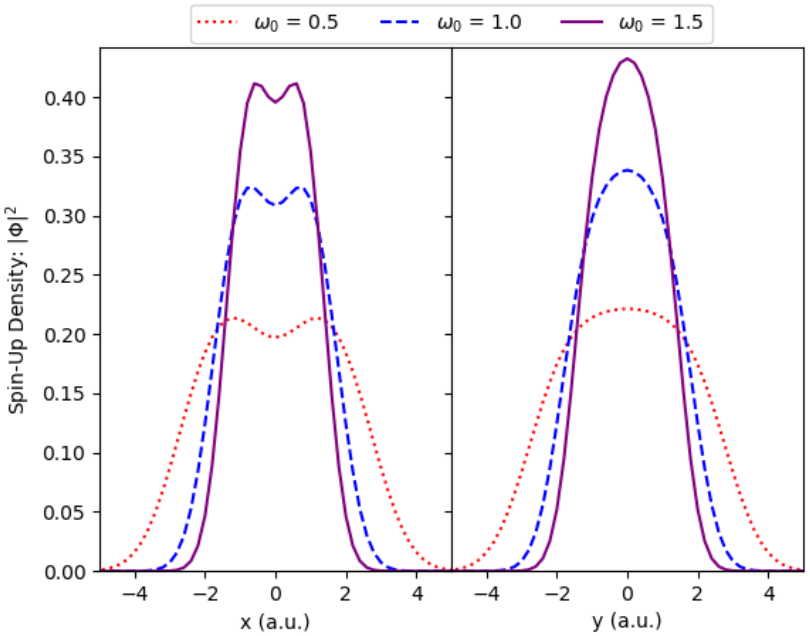

Figure 4.28: Spin-up electron density slices of six-electron system (S = 1) at different confining potential frequencies.

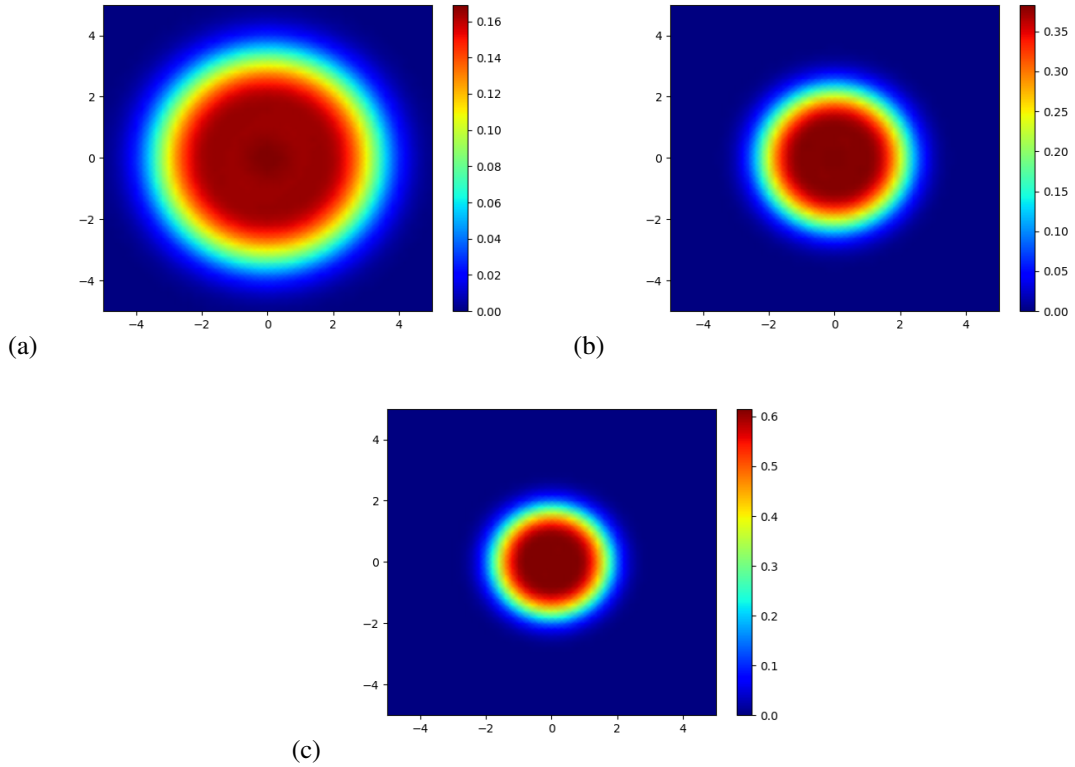

Figure 4.29: Relative motion DFT calculation of electron density for six electrons with total spin 2: $\uparrow+\uparrow+\uparrow+\uparrow+\uparrow+\downarrow=2$. (a) $\omega_0 = 0.5$ (b) $\omega_0 = 1.0$ (c) $\omega_0 = 1.5$. Note that each plot has a unique color bar scale.

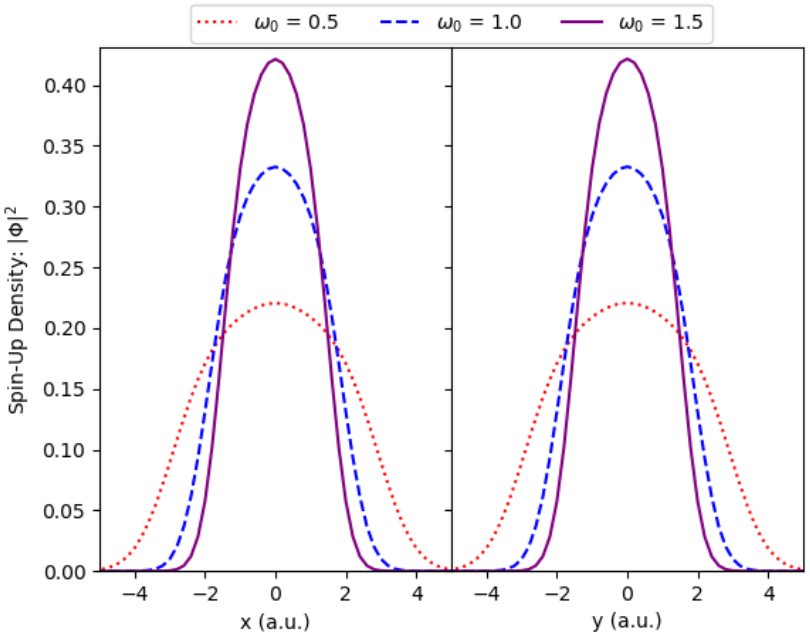

Figure 4.30: Spin-up electron density slices of six-electron system (S = 2) at different confining potential frequencies.

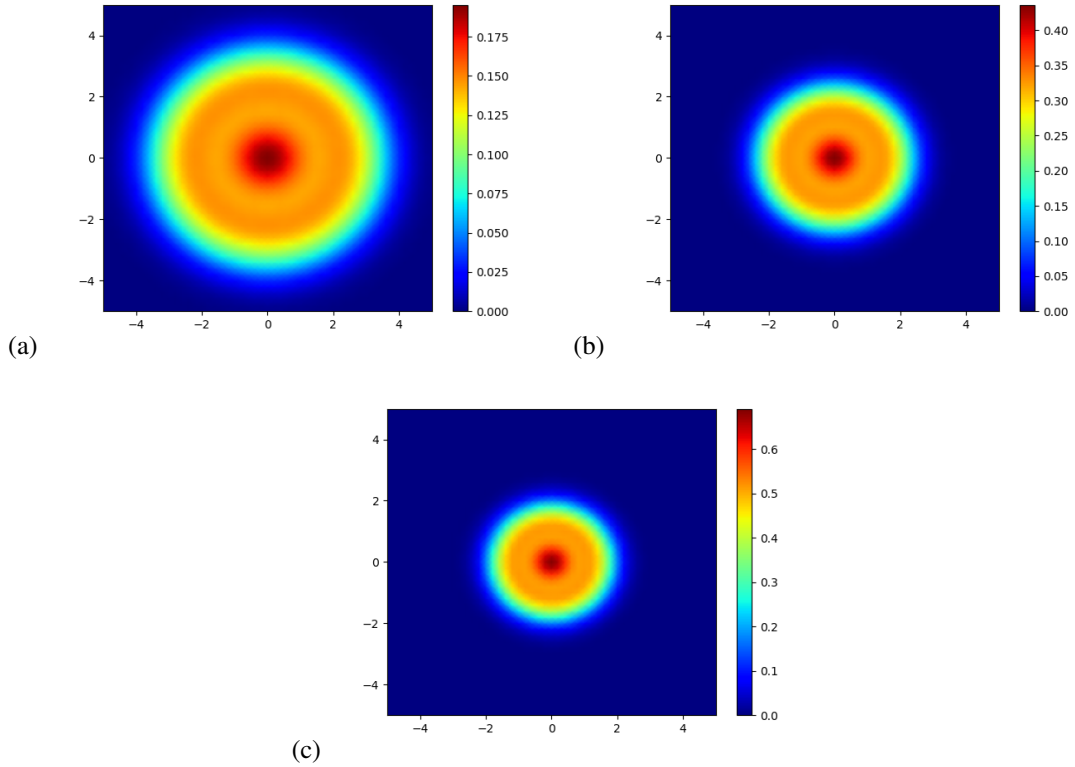

Figure 4.31: Relative motion DFT calculation of electron density for six electrons with total spin 1: $\uparrow+\uparrow+\uparrow+\uparrow+\uparrow+\uparrow=3$. (a) $\omega_0 = 0.5$ (b) $\omega_0 = 1.0$ (c) $\omega_0 = 1.5$. Note that each plot has a unique color bar scale.

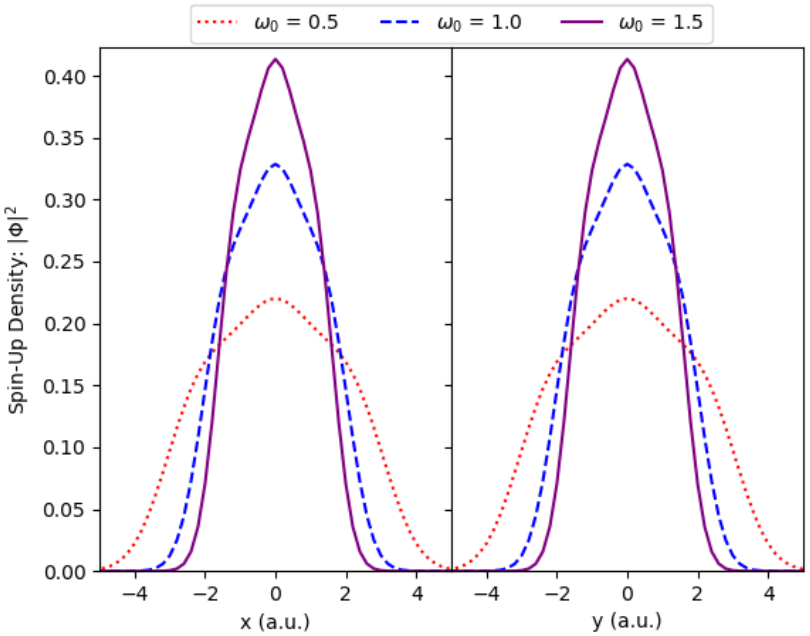

Figure 4.32: Spin-up electron density slices of six-electron system (S = 3) at different confining potential frequencies.

CHAPTER 5

Time-Dependent Density Functional Theory for Strong Cavity-Matter Coupling

Subsection 4.1.1. provides a terse introduction to atom-cavity interactions. Here, we briefly discuss quantum electrodynamical density functional theory (QED-DFT), the investigative conditions necessitating its development, and the benefits its novel, tensor product formulation secures.

5.1 Density Functionalizing Atom-Cavity Interactions

Light-matter coupling in a cavity alters the physical and chemical properties of nanostructures carries implications for polaritonic chemistry [213], nanoplasmonics [214], nonlinear optics [197, 215], quantum information processing [215, 216], and quantum networks [217]. Present theories for practical light-matter calculations go beyond two-level models, tackling coupled Hamiltonians using electron-photon adaptations of well-established quantum many-body methods.

The coupled cluster [210] and stochastic variational approaches [58] solve the electron-photon Schrodinger equations directly, defining coupled electron-photon wave functions, providing photon occupation numbers and accurate, upper bound ground state energies accessible. For extended systems, the many-body electron problem reaches regimes in which the electron density becomes the weathervane of choice. Thus, density functional approaches for cavity-coupling problems have been developed.

The density functional approaches used to solve the equations of motion for many-body electron systems coupled to light in a cavity are referred to as QED-DFTs [63, 200, 209, 218, 219, 220]. Like their electron-only formulations, the kinetic energy and the full Coulombic potential is replaced by effective potentials that are functionals of the electron density. The Maxwell-Kohn-Sham (MKS) approach [61, 221, 222], for example, conveniently couples electrons and photons in a quasi-algorithimic manner, in which the polarization vector still couples to the total dipole, but parameter input is required from a separate, single-photon Maxwell-like equation. Furthermore, unlike the aforementioned wave function-based methods, the electrons and photons do not jointly compose an ansatz, Hilbert-Fock wave function.

In essence, QED-DFT uses coupled nonlinear electron-photon equations for auxiliary electron orbitals to inexpensively generate observables for the real, interacting systems. Dispatching DFT to address cQED questions in this way subsumes then extends the requirements of the exchange-correlation potential. Naturally, QED-DFT absorbs the features of its composite theories: A photon exchange-correlation potential is needed, and due to it and the decoupled nature of the motion variables, the photon dynamics are sealed away, so to speak.

Here, a fully light-matter coupling approach based on the QED-DFT and the motion variables of wave function-based cQED approaches is used to calculate various optical cavity phenomena – a compromise of sorts formed between the wave function approaches and the aforementioned density functional approach.

In this novel formulation, which will be referred to with its own acronym QED-DFT-TP, the electron-photon wave functions of the density functionalized, length gauge Hamiltonian are solve and time propagated on a tensor product of a Fock space and real-space grid. Showing the accuracy of this approach are applications for atoms and molecules in cavities. Shown in [223], examples include the coupling strength and or photon frequency dependence of numerous observables: ground state energies, electron densities, Rabi splitting magnitudes, and optical absorption and HHG spectra in cavities. Here, we focus on the optical absorption spectra of cavity-coupled benzene and hydrogen at different coupling strengths, as well as the HHG spectra of cavity-coupled HF and C_2H_2 (We will occasionally refer to cavity-coupled quantum emitters as being "photonic"). Predictions of polariton states, in one cross section of photonic benzene, by MKS QED-DFT – which we will refer to as "QED-DFT" – and QED-DFT-TP will be compared.

5.1.1 Tensor Product Quantum Electrodynamical Density Functional Theory

The calculations of this chapter being non-periodic, we start from the length gauge Pauli-Fierz Hamiltonian of Eq. 2.193. The general potential term is replaced by a general KS potential. On its surface, the Hamiltonian does not look very different:

$$H = \frac{p^2}{2m} + V_{KS} + \sum_n \left[\omega_n \left(\hat{a}_n^\dagger \hat{a}_n + \frac{1}{2} \right) - \omega_n q_n \boldsymbol{\lambda_n} \cdot \mathbf{D} + \frac{1}{2} (\boldsymbol{\lambda_n} \cdot \mathbf{D})^2 \right], \tag{5.1}$$

the terms, from left to right, being the kinetic energy, the KS potential, the photon Hamiltonian, the photon-dipole interaction, and the dipole self-energy [108]. Since ther are terms coupling the electronic and photonic degrees of freedom, the Hamiltonian is a combination of Hilbert space and Fock space operators. Due to this and the presence of the creation and annihilation operators, the ansatz wave function must be generally expressed as a tensor product of spatial and number state bases.

The tensor product of a general electronic state vector and a photon number state may be projected onto position space to form a real-space and Fock space tensor product:

$$|\phi_m\rangle \otimes |n\rangle = \int d\mathbf{x} \ |\mathbf{x}\rangle\langle\mathbf{x}|\phi_m\rangle \otimes |n\rangle \tag{5.2}$$

$$= \int d\mathbf{x} \ \phi_m(\mathbf{x})(|\mathbf{x}\rangle \otimes |n\rangle), \tag{5.3}$$

where $\mathbf{x} = (x, y, z)$, m is the orbital index, and n refers to the Fock space dimension. These electron-photon

orbitals may be expressed as

$$\Phi_{mn} = \phi_{mn}(\mathbf{x})|n\rangle. \tag{5.4}$$

In this chapter we assume there exists only one dominant photon mode, so we may drop the sum in eq. 5.1 and set n equal to said dominant mode, with frequency ω. A real-space representation is used for the electronic part of the ansatz of eq. 5.4, while the full electron-photon orbitals are defined on 4D grid of composed of the real-space grid and a 1D Fock space. Put differently, for every Fock state (or photon space), there is a real-space grid: one N_x-by-N_y-by-N_z grid and one N_F photon space, making a 4D grid with $N_x N_y N_z (N_F + 1)$ grid points. Note that $N_F = 0$ returns KS-TDDFT. Letting $\mathbf{x}$ represent points on a real-space grid, the orbital matrix is written as

$$\Phi_m(\mathbf{x}) = \begin{bmatrix} \Phi_{m0}(\mathbf{x}) \\ \Phi_{m1}(\mathbf{x}) \\ \vdots \\ \Phi_{mn}(\mathbf{x}) \\ \vdots \end{bmatrix}, \tag{5.5}$$

and the ansatz inner product is a grid integral over the real- and Fock spaces, the latter of which contains orthogonal basis states.

$$\langle \Phi_{mn} | \Phi_{m'n'} \rangle = \delta_{nn'} \sum_{\mathbf{x}} \phi_{mn}(\mathbf{x}) \phi_{m'n'}(\mathbf{x}) \tag{5.6}$$

Each orbital in the electron orbital set $\{\phi_{mn}\}$ is subjected to Gram-Schmidt orthogonalization for each photon space, producing an orthogonal set $\{\hat{\phi}_{mn}\}$ satisfying

$$\sum_{n=0}^{N_F} |\hat{\phi}_{mn}|^2 = 1, \quad \rho(\mathbf{x}) = \sum_{m=1}^{N_{occ}} c_m \sum_{n=0}^{N_F} |\hat{\phi}_{mn}|^2, \tag{5.7}$$

where c_m is the number electrons in the mth orbital. Pulling focus on observables native to the photonic degrees of freedom, one may define the density in a given photon space as

$$p_n(\mathbf{x}) = \sum_{m=1}^{N_{occ}} c_m |\hat{\phi}_{mn}|^2, \tag{5.8}$$

and with this define the photon occupation probability in the nth photon space,

$$P_n = \frac{1}{N} \int d\mathbf{x}\ p_n(\mathbf{x}). \tag{5.9}$$

The largest leap from KS-TDDFT to QED-DFT-TP may be in how the wave equation is evaluated. The

photon operators impacting the form of the electron-photon wave function, the QED-KS equation will simultaneously feature two wave functions in separate photon spaces. To see this explicitly, we operate on the Fock space vectors with the number and photon displacement operators accordingly. The free photon field term in eq. 5.1 gives eigenvalues:

$$\omega\left(\hat{a}^{\dagger}\hat{a}+\frac{1}{2}\right)|n\rangle=\omega\left(n+\frac{1}{2}\right)|n\rangle. \tag{5.10}$$

The photon displacement coordinate q yields,

$$q|n\rangle=\frac{1}{\sqrt{2\omega}}(\sqrt{n}|n-1\rangle+\sqrt{n+1}|n+1\rangle). \tag{5.11}$$

The calculations performed in this chapter assumes only one photon mode and only one photon vector polarization. Moving forward with this assumption, the QED-KS becomes

$$\begin{aligned}\hat{H}\Phi_{mn}=-\frac{\nabla^2}{2}\Phi_{mn}+\left[V_{KS}+\boldsymbol{\lambda}\cdot\mathbf{x}\int d\mathbf{x}\;\boldsymbol{\lambda}\cdot\mathbf{x}\rho(\mathbf{x})+\frac{1}{2}(\boldsymbol{\lambda}\cdot\mathbf{x})^2+\omega\left(n+\frac{1}{2}\right)\right]\Phi_{mn}\\ -\sqrt{\frac{\omega}{2}}(\boldsymbol{\lambda}\cdot\mathbf{x})\left[\sqrt{n}\,\Phi_{mn-1}+\sqrt{n+1}\,\Phi_{mn+1}\right].\end{aligned} \tag{5.12}$$

Note that the traditional KS equation is recovered if the coupling strength is and photon frequency are nullified. Uncoupling the electron system and the photon, but keeping the photon frequency non-zero, just positively shifts the total KS energy.

What happened to the $\boldsymbol{\lambda}\cdot\mathbf{D}$ terms? Before implementing the single-particle approximation, the Hamiltonian takes of the form of eq. 4.3 – which is not a KS Hamiltonian. Therefore, $\mathbf{D}$ has the definition of eq. 2.192, the solution to a volume integral with a delta function in its kernel. In full,

$$\boldsymbol{\lambda}\cdot\mathbf{D}=\boldsymbol{\lambda}\cdot\int_V d\mathbf{x}\,\mathbf{x}\sum_i\delta(\mathbf{x}-\mathbf{x}_i) \tag{5.13}$$

$$=\boldsymbol{\lambda}\cdot\sum_i\mathbf{x}_i, \tag{5.14}$$

and

$$\frac{1}{2}(\boldsymbol{\lambda}\cdot\mathbf{D})^2=\frac{1}{2}\left(\boldsymbol{\lambda}\cdot\int_V d\mathbf{x}\,\mathbf{x}\sum_i\delta(\mathbf{x}-\mathbf{x}_i)\right)\left(\boldsymbol{\lambda}\cdot\int_V d\mathbf{x}'\,\mathbf{x}'\sum_j\delta(\mathbf{x}'-\mathbf{x}_j)\right) \tag{5.15}$$

$$=\frac{1}{2}\left(\boldsymbol{\lambda}\cdot\sum_i\mathbf{x}_i\right)\left(\boldsymbol{\lambda}\cdot\sum_j\mathbf{x}_j\right). \tag{5.16}$$

A complication arises in eq. 5.16, as the dipole self-interaction is shown to be a combination of a one- and

two-body operator. Expanding eq. 5.16 gives

$$\frac{1}{2}\left(\boldsymbol{\lambda}\cdot\sum_i \mathbf{x}_i\right)\left(\boldsymbol{\lambda}\cdot\sum_j \mathbf{x}_j\right) = \frac{1}{2}\left(\sum_i (\boldsymbol{\lambda}\cdot\mathbf{x}_i)^2 + 2\sum_{i>j}(\boldsymbol{\lambda}\cdot\mathbf{x}_i)(\boldsymbol{\lambda}\cdot\mathbf{x}_j)\right). \tag{5.17}$$

In preparing eqs. 5.14 and 5.17 for a density functional calculation – in moving from a many-particle picture to a density picture – we may simply make them consistent with the truncation of the parameter space $\mathbf{x}_1,...,\mathbf{x}_N \to \mathbf{x}$, which is effectively the result of operating on one of the photonic KS orbitals. This yields,

$$\boldsymbol{\lambda}\cdot\sum_i \mathbf{x}_i \to \boldsymbol{\lambda}\cdot\mathbf{x} \tag{5.18}$$

$$\frac{1}{2}\left(\sum_i (\boldsymbol{\lambda}\cdot\mathbf{x}_i)^2 + 2\sum_{i>j}(\boldsymbol{\lambda}\cdot\mathbf{x}_i)(\boldsymbol{\lambda}\cdot\mathbf{x}_j)\right) \to \frac{1}{2}(\boldsymbol{\lambda}\cdot\mathbf{x})^2 + (\boldsymbol{\lambda}\cdot\mathbf{x})(\boldsymbol{\lambda}\cdot\mathbf{x}'). \tag{5.19}$$

The finishing touches are to be applied to eq. 5.19, which must be an operator of just one position variable. Without negating the operational two-particle nature of the second term in eq. 5.19, we restore the definition of the dipole for one of the dot product terms, turning an operator explicitly dependent on $\mathbf{x}'$ into a more general spatial one:

$$\frac{1}{2}(\boldsymbol{\lambda}\cdot\mathbf{x})^2 + (\boldsymbol{\lambda}\cdot\mathbf{x})(\boldsymbol{\lambda}\cdot\mathbf{x}') = \frac{1}{2}(\boldsymbol{\lambda}\cdot\mathbf{x})^2 + \boldsymbol{\lambda}\cdot\mathbf{x}\int d\mathbf{x}\,\boldsymbol{\lambda}\cdot\mathbf{x}\,\rho(\mathbf{x}). \tag{5.20}$$

In [in our paper, 75], the second term on the right-hand side of eq. 5.20 is referred to as a photon-mediated electron-electron interaction. Here, it may be interpreted as a photon-mediated electron-density interaction.

5.2 Rabi Splitting for Cavity-Coupled Benzene

5.2.1 Cavity Polaritons Indicate Strong Coupling

If the Purcell effect is the trademark for the weak cavity coupling regime, then Rabi splitting – the formation of cavity polaritons – is trademark of the strong coupling regime. The strong coupling limit has implications for quantum technology, including information processing [224, 225] and communication [226, 227], and laboratory observations of Rabi splitting in the optical spectra of cavity-coupled systems indicates this regime crossing. The physics of strong light-matter coupling being poorly understood, whatever the theoretical approach, its simulation could help guide experiments and explain their results. With QED-TDDFT-TP in particular, the corpus of photonic and electronic observables in the strong coupling limit can be made available.

Furthermore, the modeling of Rabi splitting, as well as other phenomena induced by strong coupling, by QED-TDDFT-TP might assist with determining the photon exchange-correlation. As we will see, QEDFT

and QED-DFT-TP both yield different upper- and lower-polariton character from splitting the $\pi - \pi^*$ transition peak in benzene – with QED-DFT-TP showing slight spectra fragmentation around frequency lines shifted from the lines given by QEDFT. The opportunity here is the possibility of extracting a form for the photon exchange-correlation from differences between the predictions of QEDFT and QED-DFT-TP.

5.2.2 Optical Absorption and the Polarizability Tensor

To calculate the Rabi splitting for photonic and non-photonic benzene, we must perform a basic optical absorption calculation: the time propagation of electron orbitals perturbed intensely and ephemerally, and the subsequent extraction of the polarizability tensor from the time-dependent dipole moment. Storing the delta kick potential is the external component of the KS potential. This pertubative, delta potential takes the form of a short-lived electric potential. It is defined as

$$V_{EXT} = -e\mathbf{x} \cdot \mathbf{k}_i \delta(0), \tag{5.21}$$

where e and $\mathbf{k}_i$ are the electron charge and the electric field oriented along i, respectively. The $t = 0$ in the delta function indicates the kick takes place during the first time step during time propagation. The selected electric field amplitude falls within the linear response regime.

The electron oscillations initiated by the delta kick generate a time-dependent dipole moment from which an absorption cross section may be calculated. The Fourier transform of the time-dependent dipole moment defines the polarizability tensor:

$$\alpha_{ij}(\omega) = \frac{1}{k_i} \int_0^T dt \, [D_j(t) - D_j(0)] e^{-i\omega t} \, g(t), \tag{5.22}$$

where T is the chosen duration of the dipole oscillations in time, $g(t)$ is a damping function inducing artificial decay of the excited population to smooth the spectrum, and matrix indices i and j represent the direction of the kick and dipole oscillations, respectively. Here, $g(t) = e^{-(\eta t)^2}$, where η is a parameter selected to decrease damping at the end of the propagation. Here, the time-dependent dipole moment is calculated using eq. 2.136.

We simplify eq. 5.22 by neglecting off-diagonal elements. This is justified because the optical absorption spectrum is being calculated from multiple absorption cross sections of benzene: after kicking benzene in directions i and calculating the absorption cross sections in those directions, we calculate the absorption spectrum by averaging over all absorption cross sections. Formally, we do this with the imaginary part of the

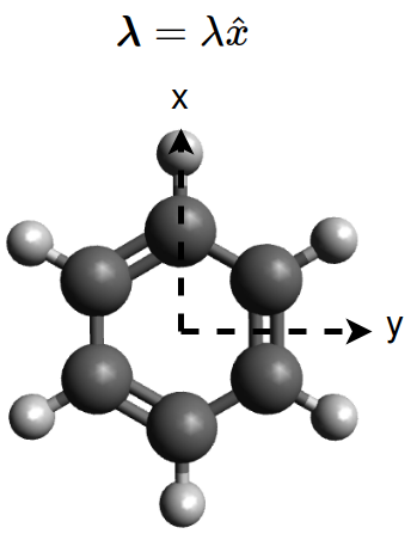

Figure 5.1: The polarization direction of the coupling vector with respect to benzene. Compliment figure for fig. 5.2

polarizability, making the absorption spectrum

$$\begin{aligned} S(\omega) &= \frac{2\omega}{n\pi}\mathrm{Tr}[\mathrm{Im}\{\alpha(\omega)\}] \\ &= \frac{2\omega}{n\pi}\sum_{i}^{n}\mathrm{Im}\{\alpha_{ii}(\omega)\} \end{aligned} \tag{5.23}$$

where n is the number of directions: $n = 3$ for x, y, and z. The physical justification of eq. 5.23 is that the dipole oscillations are dominant in the direction of the kick [228]. Details on how the imaginary part of the polarizability tensor represents absorption is provided in the appendix at the end of this chapter.

As previously mentioned, these calculations are performed on a real-space grid. The QED-DFT-TP calculation for the Rabi splitting in benzene was performed on a uniform grid of dimensions $N_x = N_y = N_z =$ 55 Bohr, with grid spacing $h = 0.5$ Bohr. Using a time step number of 20,000 and time step size of 0.05, the duration of the oscillations was 1000 a.u. The photon frequency was $\omega = 0.25$, the approximate location of the $\pi - \pi^*$ transition, and the polarization of the photon vector was $\boldsymbol{\lambda} = (0, \lambda, 0)$ – parallel to one of the C-H σ bonds (see fig. 5.1).

5.2.3 $\pi - \pi^*$ Splitting and Variable Polariton Doublets

The optical absorption spectrum of benezene and photonic benzene is shown in fig. 5.2. The single, high-intensity Lorentzian peak around 0.25 a.u. is the $\pi - \pi^*$ transition peak for benzene. The other spectra correspond to photonic benzene at different photon coupling strengths, and each case shows Rabi splitting.

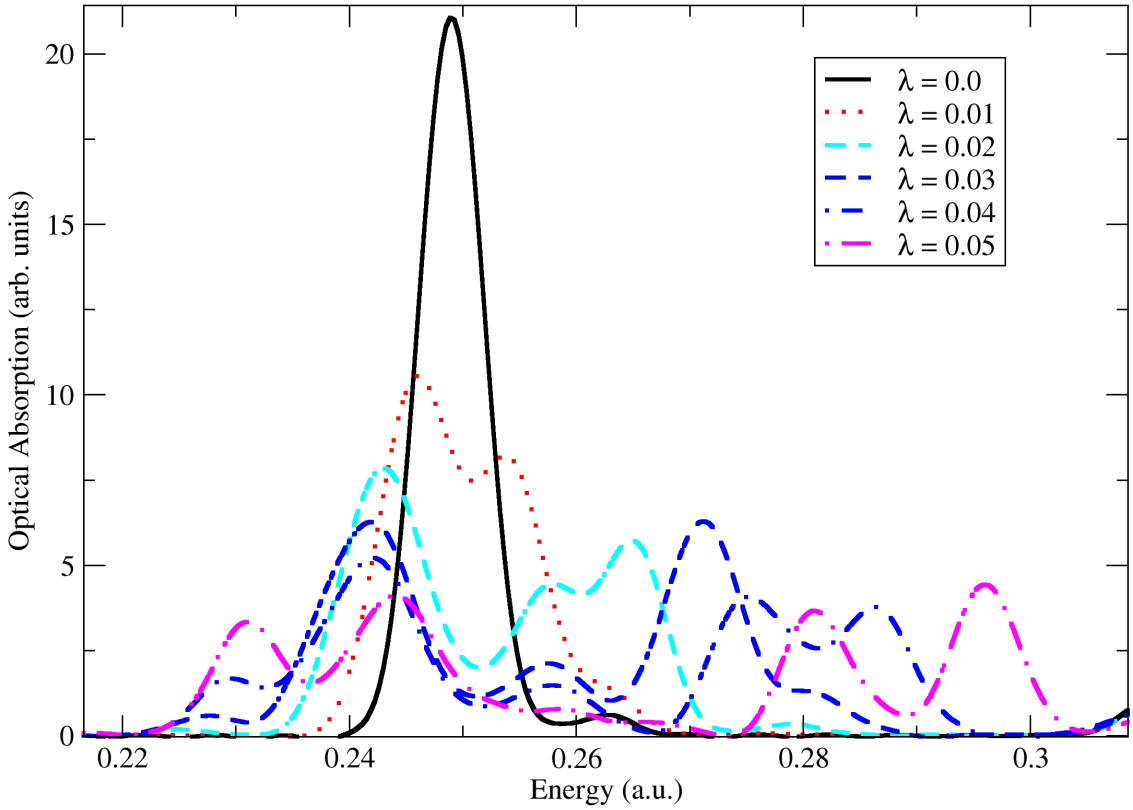

Figure 5.2: Rabi splitting for benzene at different coupling strengths. The simulation parameters are: $N_x = N_y = N_z = 55$; $h = 0.5$ grid spacing; $\delta t = 0.05$, with 1000 time steps; and $\omega = 0.25$.

All upper- and lower-polariton states diverge from the $\pi - \pi^*$ frequency line, which is in agreement with the proportionality between Rabi splitting magnitude and the photon coupling strength.

The splitting magnitude is equal to the energetic difference between an upper- and lower-polariton peak pair at a single coupling strength. Splitting magnitudes predicted by both QED-DFT-TP and QEDFT (from [1]) are reported in table 5.1. As expected, the two approaches follow the same coupling-splitting trend while disagreeing on the splitting magnitudes and state intensities. The exact differences between the two approaches is an open question. Furthermore, as indicated in a comparison between the geometry of the

λ	QED-DFT-TP (eV)	QEDFT (eV)
0.01	0.22	0.33
0.02	0.63	0.69
0.03	0.81	1.02
0.04	1.03	1.35

Table 5.1: Rabi splitting magnitudes at different photon coupling strengths for tensor product QED-DFT and quasi-algorithmic QEDFT. QED-DFT uses simluation parameters from fig. 5.2. QEDFT values are from [1]

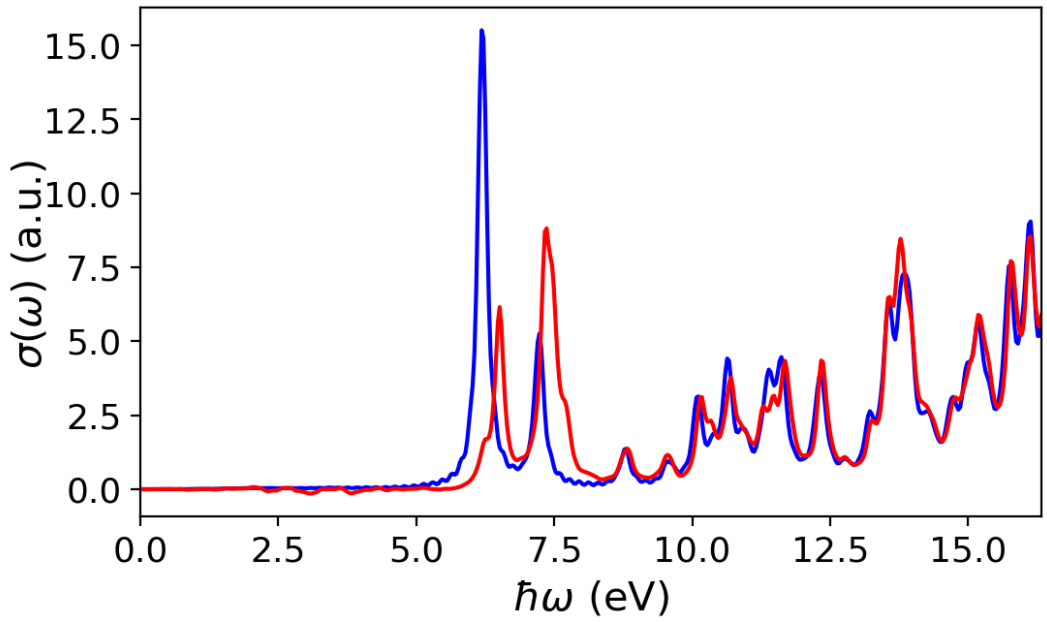

Figure 5.3: Optical absorption spectrum of benezene calculated using the time-dependent forms of QEDFT (blue) and QED-DFT-TP (red). The most prominent transition of both cases is the $\pi - \pi^*$ transition peak. Both calculations used the following parameters: $(N_x, N_y, N_z) = (55, 55, 55)$; $h = 0.5$; $\boldsymbol{\lambda} = \lambda(1,0,0)$; photon frequency $\omega = 0.2496$ a.u.; a time step of $\delta t = 0.05$ used with a total time step number of 100,000.

polariton states reported in [1], there exists the open question of what phenomenon or phenomena introduces the fluctuations in the QED-DFT-TP absorption spectra.

Fig. 5.3 shows absorption cross sections calculated using QEDFT and QED-DFT-TP. Both spectra were generated using a coupling strength of $\lambda = 0.03$, oriented parallel to a C-H σ bond and the kick direction (fig. 5.1 again). In reminder, an absorption cross section is one of three cross sections used to calculated the total absorption spectrum of benzene. The frequencies of the upper- and lower-polaritons, as well as the magnitudes of the Rabi splittings, between the two calculated cross sections are noticeably different. In addition, unlike for QEDFT, QED-DFT-TP does not predict total transparency between the polariton peaks. The most peculiar discrepancy, however, is the manifestation of other peaks in the QED-DFT-TP curve, a difference possible due to the exact representation of the photon exchange-correlation.

Fig. 5.4 shows the effect the coupling has on the $1s$ to $2s-2p$ transition. In this context, the splitting is referred to as electromagnetic induced transparency [229, 230, 231], since most coupling strengths yield near zero peak-to-peak intensities. Both theories predict that the coupling has an effect on the $2s-2p$ transition similar to the DC Stark Effect [232]. (In [19], the effect is compared to the AC Stark Effect). Furthermore, the theories are in extremely close agreement at low coupling strengths, which lends credence to the random phase approximation of the photon exchange-correlation. Note that these calculations included neither

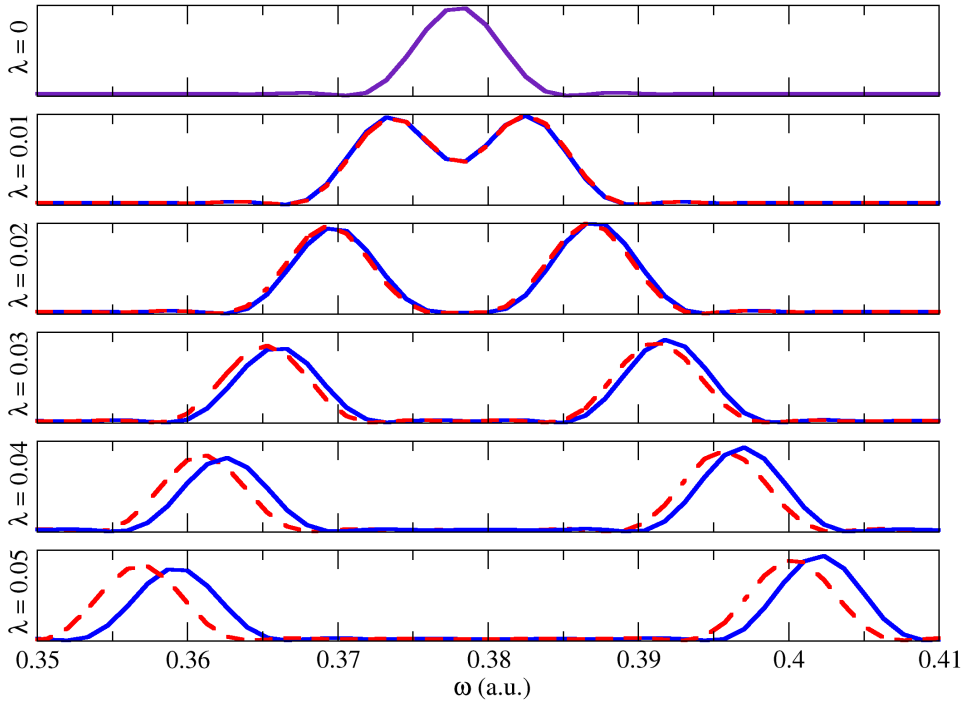

Figure 5.4: Electromagnetic induced transparency of the hydrogen $1s$ to $2s-2p$ transition (purple) at different coupling strengths. The predictions of QED-DFT (red, dotted) and QED-DFT-TP (blue, solid) are compared. The simulation parameters are: $N_x = N_y = N_z = 40$; $h = 0.25$ grid spacing; δt = 0.01, with 100,000 time steps; $\omega = 0.378$; and $\boldsymbol{\lambda} = \lambda(1,0,0)$.

hyperfine effects nor the Lamb shift.

5.3 High Harmonic Generation from Cavity-Coupled Molecules

5.3.1 Upconversion Efficiency in Optical Cavities

High harmonic generation was discussed in the context of KS-TDDFT and OF-TDDFT in chapter 3. What was not discussed in chapter 3 was the low upconversion efficiency of incident electromagnetic radiation to high-order harmonics. In pursuit of extreme ultraviolet tabletop sources – one of the technological promises of HHG – one must improve the upconversion efficiency of the process [233, 234, 235, 236, 237]. Put differently, one must find an effective way to intensify the high-order harmonics. Strong coupling in cavities have been used to modify the nonlinear properties of molecules and enhance second and third harmonic yields [197]. Here, we study the impact strong light-matter coupling has on HHG.

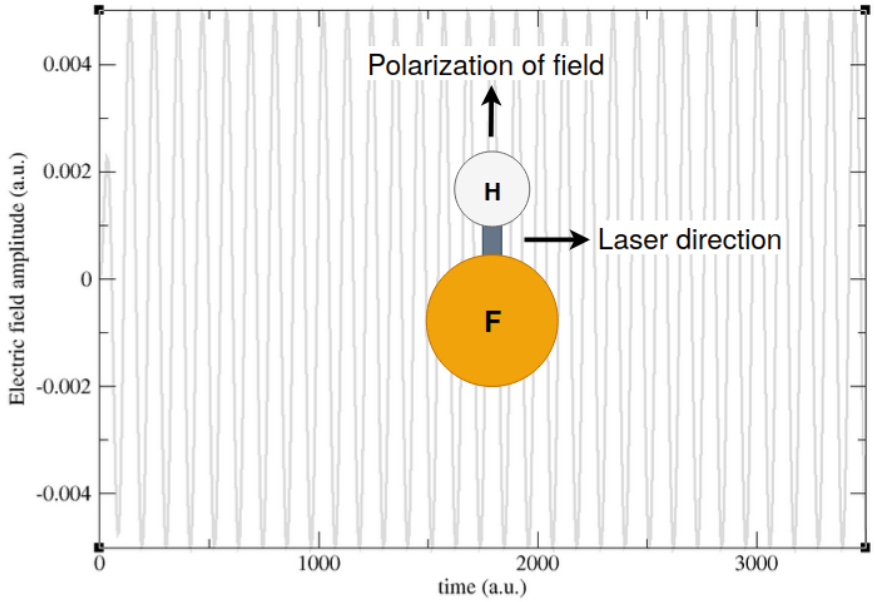

Figure 5.5: Orientation of HF molecule with respect to the complete profile of the continuous laser.

In this section, we calculate the HHG for photonic and bare HF, observing contributions to the intensities of its harmonic yields up to the third order. We do the same for C_2H_2 and observe the impact the cavity has on the harmonics up to the nineteenth order. The photon observables of QED-DFT-TP permit analysis of the dipole changes in each photon space and the interference between them. It will be shown that interference between the dipole fluctuations in separate photon spaces modify both electronic structure and the HHG.

5.3.2 Dipole Acceleration from Continuous Laser Pulse

The common computational details here are the application of a continuous laser pulse and the induced dipole acceleration. The continuous laser takes the form,

$$\mathbf{E}(\mathbf{x},t) = (E_x,0,0)\sin(\pi t/(6T_L))^2\sin(\omega_L t), \tag{5.24}$$

where E_x is the amplitude of the laser, T_L is the laser period, and ω_L is the frequency of the laser. The HHG spectrum is calculated using the dipole acceleration

$$I(\omega) = \left| \int_0^T \frac{\partial^2 \mathbf{D}}{\partial t^2} \mathrm{e}^{-i\omega t} dt \right|^2. \tag{5.25}$$

The photon energy discretely sweeps frequencies equal to half-integer or integer values of the fundamental frequency, starting from the frequency of the laser $\omega_L = 0.057$. Explicitly, $\omega = n\omega_L$, where $n = \{0, 0.5, 1, 1.5, 2, 2.5\}$.

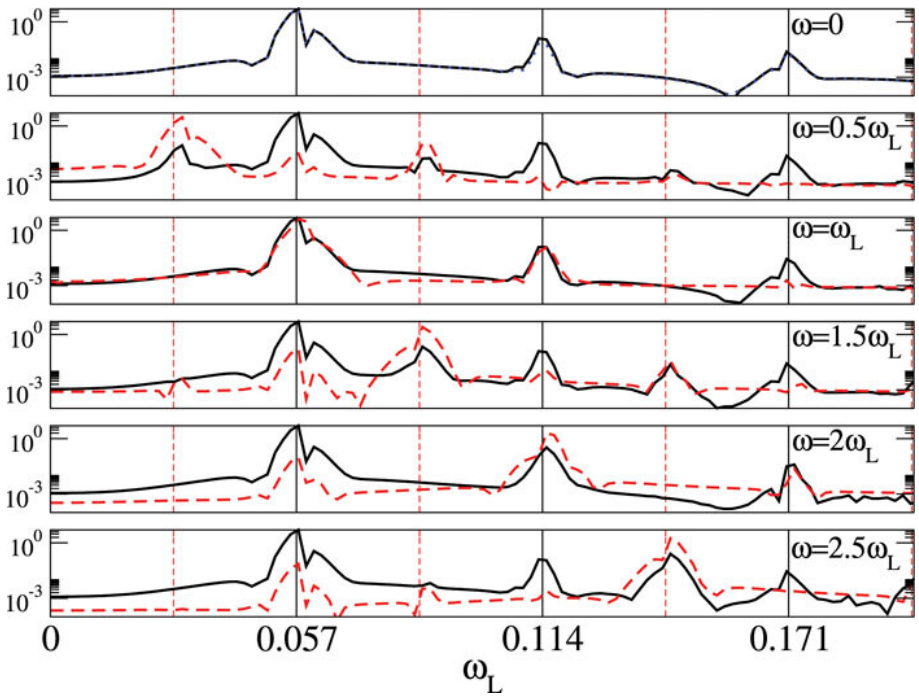

Figure 5.6: HHG spectrum of HF molecule (black lines). The red dashed lines show $|1\rangle$ photon space contribution. The blue dotted lines shows the harmonic yields for HF without the cavity. The vertical axis lists the even- and odd-ordered harmonics, with the dotted lines denoting the half-integer locations. As shown in the fig. 5.5, the axis of the molecule is in the x-direction. The parameters of the simulation are: 1.7229 HF bond length; $(N_x, N_y, N_z) = (51, 51, 51)$; $\boldsymbol{\lambda} = (0.05, 0, 0)$; $\delta t = 0.05$; with laser parameters $\omega_L = 0.057$, which correspond to an 800 nm wavelength, $T_L = 2/\omega_L$, and $E_x = 0.005$.

The principal axis of the molecule is in the x-direction (see fig. 5.5). The bond length of HF is set at 1.7229 Bohr. The real-space grid is a cube of grid point number N = 51. The grid spacing is h = 0.5 Bohr. The polarization vector is $\boldsymbol{\lambda}(0.05, 0, 0)$, and the time step is Δt = 0.05. The amplitude of the electric field E_x = 0.005.

5.3.3 Photon Space Interference Contributes to Harmonic Generation Efficiency

The HHG spectra for bare and photonic HF are shown in Fig. 5.6. Due to the polar nature of HF, it does not have inversion symmetry, and so both even and odd harmonics are present. The bare HF case corresponds to a $|0\rangle$ photon space calculation. When photons are included, a $|0\rangle + |1\rangle$ is involved. When the photon frequency is equal to either a harmonic or half-harmonic, new peaks manifest in the harmonic spectrum at integer and or half-integer positions. These new peaks have larger intensities relative to the bare case. When $\omega = n\omega_L$, the new signals coincide with the frequency of the laser, while the remainder of spectrum remains similar to the HHG of bare HF.

Fig 5.6 also shows the contribution of the $|1\rangle$ photon space. Both $|0\rangle$ and $|1\rangle$ contribute to the dipole

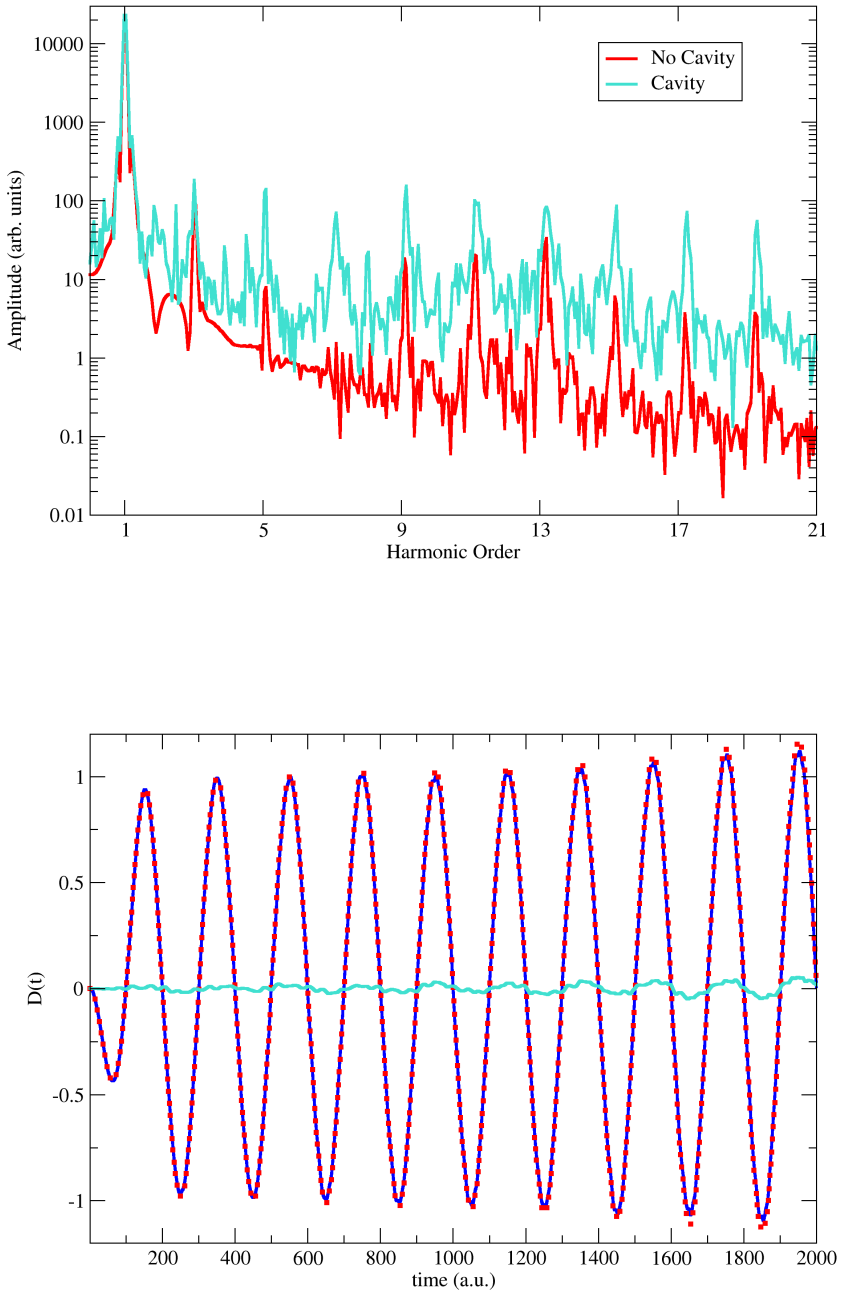

Figure 5.7: HHG spectrum of bare and photonic C_2H_2 (top) and its corresponding dipole spectra in multiple photon space (bottom). The dipole spectra is decomposed into its $|0\rangle$ (blue), $|1\rangle$ (cyan), and $|0\rangle + |1\rangle$ space parts (red, dotted). The parameters of the simulation are: $(N_x, N_y, N_z) = (200, 55, 55)$; $\boldsymbol{\lambda} = (0.05, 0, 0)$, parallel to the molecular axis; $\delta t = 0.05$, implemented up to 2000 a.u.; with laser parameters $\omega_L = 0.031$, which corresponds to an 1450 nm wavelength, and $E_x = 0.03$. The photon frequency is $\omega = 0.248$, which corresponds to the eighth harmonic.

moment, and therefore the HHG spectrum. The total HHG spectrum of the photonic HF is the result of the interference across photon spaces. The contribution of photon space $|1\rangle$ is occasionally large at the integer and half-integer frequencies, inducing new peaks and contributing greatly to the intensities of harmonics.

Fig. 5.7 shows the HHG of C_2H_2 and the dipole spectrum from which the HHG is calculated, shown as it is in the $|0\rangle$ (blue), $|1\rangle$ (cyan), and $|0\rangle + |1\rangle$ photon spaces (red, dotted). The photon polarization lay parallel to the molecular axis. The coupling strength is 0.01, and the photon frequency is equal to the eighth harmonic of the continuous laser generating the harmonics.

Like for the HF case, the bottom figure shows the dipole field interference across photon spaces responsible for changes to the HHG spectrum. The harmonics of the bare C_2H_2 are coherent and without the seventh harmonic (inversion symmetry applies since C_2H_2 is not a polar molecule). Coupled to a cavity, the excited C_2H_2 is predicted to yield higher intensity harmonics, as well as the seventh one absent in the uncoupled case. The intensity contributions are as great as those observed in fig. 5.6, with the fifth, ninth, eleventh, fifteenth, seventeenth, and nineteenth harmonic each being elevated by about one order of magnitude.

This intensification appears to unfold at the expensive of some fraction of the total coherence. The noise baseline in the bare case lay below unity, while the cavity-coupling raises this baseline by about an order of magnitude. In addition, the noise amplitudes are larger and contribute to the slight fragmentation of the harmonic signals.

5.4 Appendix for Chapter 5

5.4.1 Maxwell-Kohn-Sham Quantum Electrodynamical Density Functional Theory

In this chapter, the Maxwell-Kohn-Sham (MKS) QED-DFT [] is referred to as "QED-DFT". With this approach, two coupled equations are solved. The matter equation is a KS Hamiltonian with an added "photonic" potential,

$$i\frac{\partial}{\partial t}\phi_i(\mathbf{x},t) = \left(-\frac{1}{2}\nabla^2 + V_{KS}(q_\alpha;\mathbf{x},t)\right)\phi_i(\mathbf{x},t), \tag{5.26}$$

where ϕ_i is auxillary orbital i. The form of V_{KS}, in length gauge, is

$$V_{KS}([n,q_\alpha];\mathbf{x},t) = V_{\text{ext}}(\mathbf{x},t) + \mathbf{D}\cdot\mathbf{E}_l + V_{XC}(\mathbf{x},t) + V_P(q_\alpha;\mathbf{x},t). \tag{5.27}$$

V_{ext} is the nuclear contribution, $\mathbf{D}\cdot\mathbf{E}_l$ is the dipole interaction between the electron density and the laser field $\mathbf{E}_l$. $V_{XC}(\mathbf{x},t)$ is the Hartree exchange-correlation potential. $V_P(q_\alpha;\mathbf{x},t)$ is the photon exchange-correlation potential. At the time of this writing, the most popular approximation for the photon exchange-correlation

potential is the photon random phase approximation, which is

$$V_P(q_\alpha;\mathbf{x},t) = \sum_{\alpha=1}^{M} \left(\int d\mathbf{x}' \boldsymbol{\lambda}_\alpha \cdot \mathbf{x}' \rho(\mathbf{x}',t) - \omega_\alpha q_\alpha(t) \right) \boldsymbol{\lambda}_\alpha \cdot \mathbf{x}. \tag{5.28}$$

The other coupled equation is a Maxwell-like equation handling the photon dynamics:

$$\left(\frac{\partial^2}{\partial t^2} + \omega_\alpha^2 \right) q_\alpha(t) = -\frac{j_\alpha(t)}{\omega_\alpha} + \omega_\alpha \boldsymbol{\lambda}_\alpha \cdot \mathbf{D}. \tag{5.29}$$

Like in [197], the photon is propagated using eq. 5.29, but with the external charge current $j_\alpha(t)$ equaling zero for all t.

5.4.2 Polarizability and Imaginary Numbers as Wave Attenuators

Like how imaginary potentials in complex electronic Hamiltonians have the effect of attenuating wave functions, the imaginary part of the complex refractive index describes the attenuation of light in a medium. And so, intuitively, the imaginary part of the matrix elements in the polarizability tensor corresponds to the optical absorption of a molecule.

How does this happen? Consider absorptive media and the role the complex absorbing potential plays in the time propagation of electron and electromagnetic waves. Optical absorption is due to the collisional reduction in the kinetic energy of electrons due to lattice ions. In this sense, since the light is not housed for a prolonged period of time, a perfect conductor does not absorb light at all and only reemits. The amplitude of an electric traveling through absorptive media is reduced to zero by the inclusion of a complex refractive index in its complex exponential. Written out for a wave traveling through a bulk absorptive medium along its x-axis, and given the refractive index $\bar{n} = n + i\kappa$ and the complex wave vector being $\bar{k} = 2\pi\bar{n}\lambda^{-1}$,

$$\begin{aligned}
\mathbf{E}(x,t) &= \mathbf{E}_0 \exp\left[i\left(\bar{k}x - \omega t\right)\right] && (5.30)\\
&= \mathbf{E}_0 \exp\left[i\left(\frac{2\pi\bar{n}}{\lambda}x - \omega t \right)\right] && (5.31)\\
&= \mathbf{E}_0 \exp\left[i\left(\frac{2\pi(n+i\kappa)}{\lambda}x - \omega t \right)\right] && (5.32)\\
&= \mathbf{E}_0 \exp\left[i\left(\left(\frac{2\pi n}{\lambda}x + \frac{2\pi i\kappa}{\lambda}x \right) - \omega t \right)\right] && (5.33)\\
&= \mathbf{E}_0 \exp\left[i\frac{2\pi n}{\lambda}x - \frac{2\pi\kappa}{\lambda}x - i\omega t \right] && (5.34)\\
&= \mathbf{E}_0 \exp\left[-\frac{2\pi\kappa}{\lambda}x \right] \exp\left[i\frac{2\pi n}{\lambda}x - i\omega t \right]. && (5.35)
\end{aligned}$$

As one can see, the complex refractive index ceaselessly reduces the field amplitude as it traverses the

medium. This is how the complex absorbing potential functions within time translation operators. Given some time-dependent wave function $\psi(x,t)$, the affect of a complex absorbing potential in a Hamiltonian $H = H' + iW(x)$ is

$$\psi(x,t) = \exp\left[iHt\right]\psi(x) \tag{5.36}$$

$$= \exp\left[i(H' + iW(x))t\right]\psi(x) \tag{5.37}$$

$$= \exp\left[iH't - W(x)t\right]\psi(x) \tag{5.38}$$

$$= \exp\left[iH't - W(x)t\right]\psi(x) \tag{5.39}$$

$$= \exp\left[-W(x)t\right]\exp\left[iH't\right]\psi(x), \tag{5.40}$$

which also has the effect of reducing the amplitude to zero over time, though the explicit spatial dependence of the potential is what normally determines the attenuation length in boundary and scattering problems.

The complex nature of attenuation is responsible for the character of the complex molecular polarizability tensor, which is analogous to the complex refractive index of extended media. Due to the low-dimensional structure of molecules, the attenuation of incident radiation is ephemeral. It is therefore more appropriate to refer to the attenuation of itinerant radiation by a molecule using optical absorption.

One may show that the complex part of the polarizability tensor is contains the absorption information using the Lorentz model [104, 228]. If an electron (density) cloud enshrouding a positively charged molecular lattice is shifted from its equilibrium position, it feels the force of the lattice and a linear drag due to electron-ion collisions, as well as the induced dipole field. The equation of motion is,

$$M\frac{d^2x}{dt^2} = -qE(t) - M\omega_0^2 x(t) - M\gamma\frac{dx}{dt}, \tag{5.41}$$

where M and q are the mass and charge of the cloud, respectively, ω_0 is the resonant frequency, and the γ is the damping parameter. The first term is the electric force contribution, the second term is the harmonic oscillator potential affected by the positive charge, and the last term is a material-dependent linear drag.

Given an electric field of the form

$$E(t) = E_0\exp\left[i(kz - \omega t)\right] \tag{5.42}$$

we look for solutions of the form

$$x(t) = x_0\exp[i(kz - \omega t)], \tag{5.43}$$

where z denotes the trajectory of the wave front. To get the polarizability, we need to know x_0. This can be found by plugging eq. 5.43 into the differential equation eq 5.41. This gives,

$$0 = -M\frac{d^2x}{dt^2} - qE(t) - M\omega_0^2 x(t) - M\gamma\frac{dx}{dt} \tag{5.44}$$

$$= \omega^2 Mx(t) - qE(t) - M\omega_0^2 x(t) + i\omega M\gamma x(t) \tag{5.45}$$

$$= -qE(t) + (\omega^2 - \omega_0^2 + i\omega\gamma)Mx(t), \tag{5.46}$$

which yields the well known result,

$$x(t) = -\frac{(q/M)E(t)}{(\omega^2 + \omega_0^2 - i\omega\gamma)}. \tag{5.47}$$

Recalling that the one-dimensional polarization is defined as $p = -qx = \alpha E$, one can immediately see that the polarizability is

$$\alpha = -q\frac{x(t)}{E(t)} \tag{5.48}$$

$$= \frac{q^2}{M}\sum_j \frac{f_j}{\omega^2 + \omega_0^2 - i\omega\gamma}, \tag{5.49}$$

where the sum comes from generalizing the equation to include collections of electrons.

The resemblance between eq. 5.49 and the general complex refractive index is easy to see:

$$n(\omega)^2 = 1 + A\left[\frac{f_e}{\omega^2 + i\gamma_e\omega} + \sum_j \frac{f_j}{\omega^2 + \omega_0^2 - i\omega\gamma}\right], \tag{5.50}$$

where A stores constants, and f_e and γ_e represent conduction electron oscillator strength and damping, respectively. If the medium only has bound electrons, $f_e = 0$, which eliminates the first term. This gives an expression which further resembles the polarizability. Understanding that the imaginary part of the refractive index handles the absorption abilities of the medium, the similarities between the structures of eqs. 5.49 and 5.50 point to the imaginary part of the polarizability as what captures the absorption properties of the molecule. This also implies that the real part of the polarizability handles the dispersion.

Written out,

$$\alpha = \alpha_r(\omega) + i\alpha_i(\omega). \tag{5.51}$$

The dispersion corresponding to the real part, it physically represents the induced polarization in phase with the driving field. The imaginary part is in quadrature phase due to the damping, the absence of which would make the polarizability a real-valued function of frequency.

CHAPTER 6

Conclusion and Outlook

The aim of this dissertation was to apply novel computational material and electrodynamical approaches to nanoscale systems in which quantum effects are important. Electron density fluctuations in single-species and multi-species nanoparticles, and photon effects in optical cavities, alter the optical properties of their host systems. The former case requires a computational electrodynamics which accounts for the back reaction of the time-dependent density oscillations. The latter case requires a computational quantum electrodynamics which propagates electron-photon states in time.

A "quantum-classical" algorithmic approach constituted of coupled Maxwell and orbital-free density functional equations is used to describe the dynamics of jellium and the density transfer, frequency modulation, and HHG of atomically-detailed nanostructures. "Quantum-quantum" approaches based on NR-QED are used to model the ground state energies, density, and time-dependent dynamics of emitter-cavity coupled systems.

Using Riemann-Silberstein electrodynamics to express the Maxwell equations in Schrodinger-like equation form, the time evolution operator was used to co-propagate coupled light and orbital-free matter equations of motion. This was used to describe the current of and light transmission through lithium jellium, the HHG of periodic semiconductor and metallic sheets, and frequency modulation in a hybrid nanoparticle. The success of these calculations show the promise of the coupled OF-TDDFT approach for modeling metals, especially periodic ones, describing and probing the nature of HHG from solids, and investigating the quantum etiology of nanostructure-related phenomena, such as field frequency modulation through the modulation of interfacial tunneling rates.

Furthermore, using a Pauli-Fierz Hamiltonian divided into center-of-mass and relative parts, spin-polarized LDA density functional theory was used to calculate the density of a harmonically confined many-electron-cavity coupled system, supplying reasonable benchmarks for QED-DFT. A real-space and Fock space tensor product formulation of QED-TDDFT was used to calculate the electromagnetic induced transparency of photonic hydrogen, the Rabi splitting of photonic benzene, and the impact cavity-coupling has on the HHG of C_2H_2 and HF, showing that splitting and HHG efficiency changes may be attributed to the inclusion of photon spaces, wherein the HHG yields are a direct result of photon space interference.

Some possible next steps for coupled OF-TDDFT require advancements in the orbital-free pseudopotential theory for noble metals [238, 239]. The localized *d* shells of noble metals require fine uniform grids or non-uniform grids with a high grid point density near noble ionic cores. One possible approach involves the

inclusion of angular dependence in OF-DFT [240, 241] by confining near-core electron densities in spherical "muffin tin" regions, described by KS-DFT-derived basis functions and onsite density matrices. The density between these regions being smoother, they can be described using OF-DFT. Using nonlocal pseudopotentials with OF-DFT is another possibility [242]. This requires the projection of the nonlocal pseudopotential onto the density functionalize-able non-interacting density matrix. This approach was designed to improve the accuracy of OF-DFT by compensating for the transferability issues of local pseudopotentials, and therefore requires the use of a pre-existing local psuedopotential This imposes limits on its application to noble metals. One can speculate, however, that an inexpensive general local pseudopotential for a metal might work alongside a preexisting nonlocal pseudopotential for a noble metal. In pursuing noble metal local psuedopotentials, a finite difference interpolation method may be used to take advantage of high resolution pseudopotentials while using relatively coarse grids [243]. This could void prohibitive grid spacing requirements for real-space calculations requiring noble metal pseudopotentials.

Applications wise, coupled OF-TDDFT could be useful for investigating plasmon-assisted HHG, such as that reported in [178, 177], the bulk photo-Dember effect [244, 245], the lateral photo-Dember effect [246, 247, 248], and resonant intercluster Coulombic decay [249, 250]. Possible quantum-induced optical phenomena, such as induced transparency by "dark mode" quadruple oscillations in dolmens [251, 51, 252], could be investigated as well.

QED-DFT-TP being used to assist with the creation of a photon exchange-correlation functional was briefly discussed. Stochastic variational method and coupled cluster theory for cavity QED problems may be used to help make electron exchange-correlation functionals for QED-DFT-TP. As mentioned in [223], the HHG of more complex photonic molecules could be studied with QED-DFT-TP. The paper also mentions the opportunity of calculating the hyperpolarizabilities of molecules in cavities using the method in [253].

It appears possible to extend the theory to model chiral cavities [254]. Furthermore, using the velocity gauge form of the Pauli-Fierz Hamiltonian, QED-DFT-TP may be straightforwardly utilized to describe periodic systems, perhaps to study the impact coupling direction and strength has on band structure. Lastly, for nanoclusters and large finite structures there may be an opportunity to devise a single-mode quantum electrodynamical orbital-free density functional theory, though this would likely be a remarkable challenge due to the photons further aggravating the kinetic energy density functional problem.

References

[1] Johannes Flick, Davis M. Welakuh, Michael Ruggenthaler, Heiko Appel, and Angel Rubio. Light-Matter Response in Nonrelativistic Quantum Electrodynamics. *ACS Photonics*, 6(11):2757–2778, nov 2019.

[2] Allan Taflove and Susan C. Hagness. *Computational Electrodynamics: The Finite-Differences Time-Domain Method*. Artech House, Inc., Boston, London, 2 edition, 2000.

[3] John David Jackson. *Classical Electrodynamics*. Wiley, New York, NY, 3rd ed. edition, 1999.

[4] Kane Yee. Numerical solution of initial boundary value problems involving maxwell's equations in isotropic media. *IEEE Transactions on Antennas and Propagation*, 14(3):302–307, 1966.

[5] Allen Taflove and Morris E. Brodwin. Computation of the electromagnetic fields and induced temperatures within a model of the microwave-irradiated human eye. *IEEE Transactions on Microwave Theory and Techniques*, 23(11):888–896, November 1975.

[6] Allen Taflove and Morris E. Brodwin. Numerical solution of steady-state electromagnetic scattering problems using the time-dependent maxwell's equations. *IEEE Transactions on Microwave Theory and Techniques*, 23(8):623–630, August 1975.

[7] Allen Taflove. *Computation of the Electromagnetic Fields and Induced Temperatures within a Model of the Microwave-Irradiated Human Eye.* PhD thesis, USA, 1975. Northwestern University.

[8] W. R. Smythe. *Static and Dynamic electricity*. McGraw-Hill, New York, 1975.

[9] Herbert Goldstein. *Classical Mechanics*. Addison-Wesley, 1980.

[10] Max Born and Emil Wolf. *Principles of Optics: Electromagnetic Theory of Propagation, Interference and Diffraction of Light (7th Edition)*. Cambridge University Press, 7th edition, 1999.

[11] A. L. Fetter and J. D. Walecka. *Quantum Theory of Many-Particle Systems*. McGraw-Hill, Boston, 1971.

[12] J. C. Slater. A simplification of the hartree-fock method. *Phys. Rev.*, 81:385–390, Feb 1951.

[13] G. C. Strinati. Hartree and Hartree-Fock Methods in Electronic Structure. In Franco Bassani, Gerald L Liedl, and Peter Wyder, editors, *Encyclopedia of Condensed Matter Physics*, pages 311–318. Elsevier, Oxford, 2005.

[14] Valerio Magnasco. 7 - Many-Electron Wavefunctions: Slater, Hartree–Fock and Related Methods. In Valerio Magnasco, editor, *Elementary Methods of Molecular Quantum Mechanics*, pages 255–361. Elsevier Science B.V., Amsterdam, 2007.

[15] Efthimios Kaxiras. *Atomic and Electronic Structure of Solids*. Cambridge University Press, 2003.

[16] J. C. Slater. The theory of complex spectra. *Phys. Rev.*, 34:1293–1322, Nov 1929.

[17] Carsten A. Ullrich. *Time-Dependent Density-Functional Theory: Concepts and Applications*. Oxford University Press, 12 2011.

[18] René Jestädt. *Fully coupled Maxwell-Kohn-Sham systems: Electromagnetic field propagation in Schrödinger-like form and ab initio self-consistent light-matter simulations*. PhD thesis, Germany, 2019. Technischen Universität Berlin.

[19] Mark Fox. *Quantum Optics: Ann Introduction*. Oxford master series in atomic, optical, and laser physics. Oxford Univ. Press, Oxford, 2006.

[20] L Allen and J H Eberly. Optical resonance and two-level atoms.

[21] Jonas Larson and Themistoklis Mavrogordatos. *The Jaynes–Cummings Model and Its Descendants*. IOP Publishing, dec 2021.

[22] Shinichiro Ohnuki, Takashi Takeuchi, Tokuei Sako, Yoshito Ashizawa, Katsuji Nakagawa, and Masahiro Tanaka. Coupled analysis of Maxwell-Schrödinger equations by using the length gauge: harmonic model of a nanoplate subjected to a 2D electromagnetic field. *International Journal of Numerical Modelling: Electronic Networks, Devices and Fields*, 26(6):533–544, nov 2013.

[23] Iftikhar Ahmed, Eng Huat Khoo, Erping Li, and Raj Mittra. A hybrid approach for solving coupled maxwell and schrödinger equations arising in the simulation of nano-devices. *IEEE Antennas and Wireless Propagation Letters*, 9:914–917, 2010.

[24] Yongpin P Chen, Wei E I Sha, Lijun Jiang, Min Meng, Yu Mao Wu, and Weng Cho Chew. A unified Hamiltonian solution to Maxwell–Schrödinger equations for modeling electromagnetic field–particle interaction. *Computer Physics Communications*, 215:63–70, 2017.

[25] Christopher Jayun Ryu, Aiyin Y. Liu, Wei E. I. Sha, and Weng Cho Chew. Finite-difference time-domain simulation of the maxwell–schrödinger system. *IEEE Journal on Multiscale and Multiphysics Computational Techniques*, 1:40–47, 2016.

[26] Cody Covington, Daniel Kidd, Haley Buckner, Heiko Appel, and Kálmán Varga. Time propagation of the coupled maxwell and kohn-sham equations using the riemann-silberstein formalism. *Phys. Rev. E*, 100:053301, Nov 2019.

[27] Kevin J. Savage, Matthew M. Hawkeye, Rubén Esteban, Andrei G. Borisov, Javier Aizpurua, and Jeremy J. Baumberg. Revealing the quantum regime in tunnelling plasmonics. *Nature*, 491(7425):574–577, 2012.

[28] Jonathan A. Scholl, Ai Leen Koh, and Jennifer A. Dionne. Quantum plasmon resonances of individual metallic nanoparticles. *Nature*, 483(7390):421–427, 2012.

[29] C Ciracì, R T Hill, J J Mock, Y Urzhumov, A I Fernández-Domínguez, S A Maier, J B Pendry, A Chilkoti, and D R Smith. Probing the Ultimate Limits of Plasmonic Enhancement. *Science*, 337(6098):1072–1074, 2012.

[30] Shu Fen Tan, Lin Wu, Joel K W Yang, Ping Bai, Michel Bosman, and Christian A Nijhuis. Quantum Plasmon Resonances Controlled by Molecular Tunnel Junctions. *Science*, 343(6178):1496–1499, 2014.

[31] Huigao Duan, Antonio I. Fernández-Domínguez, Michel Bosman, Stefan A. Maier, and Joel K.W. Yang. Nanoplasmonics: Classical down to the nanometer scale. *Nano Letters*, 12(3):1683–1689, 2012.

[32] Ferenc Krausz and Misha Ivanov. Attosecond physics. *Rev. Mod. Phys.*, 81:163–234, Feb 2009.

[33] Hongping Xiang, Xu Zhang, Daniel Neuhauser, and Gang Lu. Size-dependent plasmonic resonances from large-scale quantum simulations. *Journal of Physical Chemistry Letters*, 5(7):1163–1169, 2014.

[34] Hongping Xiang, Zhilue Wang, Lin Xu, Xu Zhang, and Gang Lu. Quantum Plasmonics in Nanorods: A Time-Dependent Orbital-Free Density Functional Theory Study with Thousands of Atoms. *Journal of Physical Chemistry C*, 124(1):945–951, 2020.

[35] Hongping Xiang, Jiaxing Zu, Hongwei Jiang, Lin Xu, Gang Lu, and Xu Zhang. Understanding Quantum Plasmonic Enhancement in Nanorod Dimers from Time-Dependent Orbital-Free Density Functional Theory. *Journal of Physical Chemistry C*, 126(10):5046–5054, 2022.

[36] S. A. Sato, K. Yabana, Y. Shinohara, T. Otobe, K.-M. Lee, and G. F. Bertsch. Time-dependent density functional theory of high-intensity short-pulse laser irradiation on insulators. *Phys. Rev. B*, 92:205413, Nov 2015.

[37] Mohammad M Rafiee Fanood, Maurice H M Janssen, and Ivan Powis. Enantioselective femtosecond laser photoionization spectrometry of limonene using photoelectron circular dichroism. *Phys. Chem. Chem. Phys.*, 17(14):8614–8617, 2015.

[38] Valérie Blanchet, Dominique Descamps, Stéphane Petit, Yann Mairesse, Bernard Pons, and Baptiste Fabre. Ultrafast relaxation investigated by photoelectron circular dichroism: an isomeric comparison of camphor and fenchone. *Phys. Chem. Chem. Phys.*, 23(45):25612–25628, 2021.

[39] Luke Bhan, Cody Covington, Jason Rivas, and Kálmán Varga. Simulation of photo-electron spectrum and electron scattering by dual time propagation. *The Journal of Chemical Physics*, 154(11):114110, 03 2021.

[40] S. A. Sato, Y. Shinohara, T. Otobe, and K. Yabana. Dielectric response of laser-excited silicon at finite electron temperature. *Phys. Rev. B*, 90:174303, Nov 2014.

[41] Xiaoqin Zhang, Feng Wang, Lan Jiang, and Yugui Yao. Manipulation of the dielectric properties of diamond by an ultrashort laser pulse. *Phys. Rev. B*, 95:184301, May 2017.

[42] Zi-Yu Chen and Rui Qin. Circularly polarized extreme ultraviolet high harmonic generation in graphene. *Opt. Express*, 27(3):3761–3770, Feb 2019.

[43] Fulong Dong, Qinzhi Xia, and Jie Liu. Ellipticity of the harmonic emission from graphene irradiated by a linearly polarized laser. *Phys. Rev. A*, 104:033119, Sep 2021.

[44] Yuta Murakami and Michael Schüler. Doping and gap size dependence of high-harmonic generation in graphene: Importance of consistent formulation of light-matter coupling. *Phys. Rev. B*, 106:035204, Jul 2022.

[45] Nicolai Klemke, Giuseppe Di Sciacca, Yudong Yang, Giulio M. Rossi, Roland E. Mainz, Nicolas Tancogne-Dejean, Angel Rubio, Franz X. Kärtner, and Oliver D. Mücke. Generation of circularly polarized high-order harmonics in solids driven by single-color infrared pulses. In *Frontiers in Optics 2017*, page JTu3A.18. Optica Publishing Group, 2017.

[46] N. Klemke, N. Tancogne-Dejean, G. M. Rossi, Y. Yang, F. Scheiba, R. E. Mainz, G. Di Sciacca, A. Rubio, F. X. Kärtner, and O. D. Mücke. Polarization-state-resolved high-harmonic spectroscopy of solids. *Nature Communications*, 10(1):1–7, 2019.

[47] Isabella Floss, Christoph Lemell, Georg Wachter, Valerie Smejkal, Shunsuke A. Sato, Xiao-Min Tong, Kazuhiro Yabana, and Joachim Burgdörfer. Ab initio multiscale simulation of high-order harmonic generation in solids. *Phys. Rev. A*, 97:011401, Jan 2018.

[48] Nicolas Tancogne-Dejean, Oliver D. Mücke, Franz X. Kärtner, and Angel Rubio. Impact of the electronic band structure in high-harmonic generation spectra of solids. *Phys. Rev. Lett.*, 118:087403, Feb 2017.

[49] Takashi Nakajima, Tasuku Shinoda, D. M. Villeneuve, and Hiromichi Niikura. High-resolution attosecond imaging of an atomic electron wave function in momentum space. *Phys. Rev. A*, 106:063513, Dec 2022.

[50] Jun Hee Yoon, Florian Selbach, Ludmilla Schumacher, Jesil Jose, and Sebastian Schlücker. Surface Plasmon Coupling in Dimers of Gold Nanoparticles: Experiment and Theory for Ideal (Spherical) and Nonideal (Faceted) Building Blocks. *ACS Photonics*, 6(3):642–648, 2019.

[51] Yu Ren, Siyi Hu, Boyu Ji, Peng Zou, Liwei Liu, and Ye Li. Fano resonance in Al nano-dolmen plasmonic structure for enhanced biosensing. *Sensing and Bio-Sensing Research*, 15:5–11, sep 2017.

[52] Haihua Liu, Thomas E Gage, Prem Singh, Amit Jaiswal, Richard D Schaller, Jau Tang, Sang Tae Park, Stephen K Gray, and Ilke Arslan. Visualization of Plasmonic Couplings Using Ultrafast Electron Microscopy. *Nano Letters*, 21(13):5842–5849, 2021.

[53] Pengchong Liu, Xing Chen, Hepeng Ye, and Lasse Jensen. Resolving Molecular Structures with High-Resolution Tip-Enhanced Raman Scattering Images. *ACS Nano*, 13(8):9342–9351, 2019.

[54] Nathan C. Lindquist, Carlos Diego L. de Albuquerque, Regivaldo G. Sobral-Filho, Irina Paci, and Alexandre G. Brolo. High-speed imaging of surface-enhanced Raman scattering fluctuations from individual nanoparticles. *Nature Nanotechnology*, 14(10):981–987, 2019.

[55] *Handbook of nanophysics. Nanoelectronics and nanophotonics / editor, Klaus D. Sattler.* Handbook of Nanophysics. Taylor Francis, Boca Raton, 2010.

[56] Nariyuki Saito, Peiyu Xia, Faming Lu, Teruto Kanai, Jiro Itatani, and Nobuhisa Ishii. Observation of selection rules for circularly polarized fields in high-harmonic generation from a crystalline solid. *Optica*, 4(11):1333–1336, Nov 2017.

[57] V Apostolopoulos and M E Barnes. THz emitters based on the photo-Dember effect. *Journal of Physics D: Applied Physics*, 47(37):374002, aug 2014.

[58] Alexander Ahrens, Chenhang Huang, Matt Beutel, Cody Covington, and Kálmán Varga. Stochastic variational approach to small atoms and molecules coupled to quantum field modes in cavity qed. *Phys. Rev. Lett.*, 127:273601, Dec 2021.

[59] Matthew Beutel, Alexander Ahrens, Chenhang Huang, Yasuyuki Suzuki, and Kálmán Varga. Deformed explicitly correlated Gaussians. *The Journal of Chemical Physics*, 155(21):214103, 12 2021.

[60] Uliana Mordovina, Callum Bungey, Heiko Appel, Peter J. Knowles, Angel Rubio, and Frederick R. Manby. Polaritonic coupled-cluster theory. *Phys. Rev. Res.*, 2:023262, Jun 2020.

[61] Michael Ruggenthaler, Nicolas Tancogne-Dejean, Johannes Flick, Heiko Appel, and Angel Rubio. From a quantum-electrodynamical light–matter description to novel spectroscopies. *Nature Reviews Chemistry*, 2(3), mar 2018.

[62] Davis M Welakuh and Prineha Narang. Tunable Nonlinearity and Efficient Harmonic Generation from a Strongly Coupled Light–Matter System. *ACS Photonics*, 10(2):383–393, 2023.

[63] I. V. Tokatly. Time-dependent density functional theory for many-electron systems interacting with cavity photons. *Phys. Rev. Lett.*, 110:233001, Jun 2013.

[64] Herbert Spohn. *Dynamics of Charged Particles and their Radiation Field*. Cambridge University Press, 2004.

[65] William C. Witt, Beatriz G. del Rio, Johannes M. Dieterich, and Emily A. Carter. Orbital-free density functional theory for materials research. *Journal of Materials Research*, 33(7):777–795, 2018.

[66] Wenhui Mi, Alessandro Genova, and Michele Pavanello. Nonlocal kinetic energy functionals by functional integration. *The Journal of Chemical Physics*, 148(18):184107, 05 2018.

[67] Cody Covington, Daniel Kidd, Haley Buckner, Heiko Appel, and Kálmán Varga. Time propagation of the coupled maxwell and kohn-sham equations using the riemann-silberstein formalism. *Phys. Rev. E*, 100:053301, Nov 2019.

[68] M Born and R Oppenheimer. Zur Quantentheorie der Molekeln. *Annalen der Physik*, 389(20):457–484, 1927.

[69] *What is Density Functional Theory?*, chapter 1, pages 1–33. John Wiley Sons, Ltd, 2009.

[70] Kálmán Varga and Joseph A. Driscoll. *Computational Nanoscience: Applications for Molecules, Clusters, and Solids*. Cambridge University Press, 2011.

[71] Igor Ying Zhang and Andreas Grüneis. Coupled cluster theory in materials science. *Frontiers in Materials*, 6, 2019.

[72] Rodney J. Bartlett and Monika Musiał. Coupled-cluster theory in quantum chemistry. *Rev. Mod. Phys.*, 79:291–352, Feb 2007.

[73] Ernest R. Davidson, Stanley A. Hagstrom, Subhas J. Chakravorty, Verena Meiser Umar, and Charlotte Froese Fischer. Ground-state correlation energies for two- to ten-electron atomic ions. *Phys. Rev. A*, 44:7071–7083, Dec 1991.

[74] Claudia Filippi and C. J. Umrigar. Multiconfiguration wave functions for quantum Monte Carlo calculations of first-row diatomic molecules. *The Journal of Chemical Physics*, 105(1):213–226, 07 1996.

[75] Yasuyuki Suzuki and Kálmán Varga. *Stochastic Variational Approach to Quantum-Mechanical Few-Body Problems*. Springer Berlin, Heidelberg, 1998.

[76] K. Varga and Y. Suzuki. Precise solution of few-body problems with the stochastic variational method on a correlated gaussian basis. *Phys. Rev. C*, 52:2885–2905, Dec 1995.

[77] W. Kohn. Nobel lecture: Electronic structure of matter—wave functions and density functionals. *Rev. Mod. Phys.*, 71:1253–1266, Oct 1999.

[78] R. O. Jones. Density functional theory: Its origins, rise to prominence, and future. *Rev. Mod. Phys.*, 87:897–923, Aug 2015.

[79] N. Troullier and José Luís Martins. Efficient pseudopotentials for plane-wave calculations. *Phys. Rev. B*, 43:1993–2006, Jan 1991.

[80] Erich Runge and E. K. U. Gross. Density-functional theory for time-dependent systems. *Phys. Rev. Lett.*, 52:997–1000, Mar 1984.

[81] Robert van Leeuwen. Mapping from densities to potentials in time-dependent density-functional theory. *Phys. Rev. Lett.*, 82:3863–3866, May 1999.

[82] Robert van Leeuwen. Causality and symmetry in time-dependent density-functional theory. *Phys. Rev. Lett.*, 80:1280–1283, Feb 1998.

[83] Davood Dar, Lionel Lacombe, and Neepa T. Maitra. The exact exchange–correlation potential in time-dependent density functional theory: Choreographing electrons with steps and peaks. *Chemical Physics Reviews*, 3(3):031307, 09 2022.

[84] L. H. Thomas. The calculation of atomic fields. *Mathematical Proceedings of the Cambridge Philosophical Society*, 23(5):542–548, 1927.

[85] P. A. M. Dirac. Note on exchange phenomena in the thomas atom. *Mathematical Proceedings of the Cambridge Philosophical Society*, 26(3):376–385, 1930.

[86] Eunji Sim, Joe Larkin, Kieron Burke, and Charles W. Bock. Testing the kinetic energy functional: Kinetic energy density as a density functional. *The Journal of Chemical Physics*, 118(18):8140–8148, 04 2003.

[87] Lin-Wang Wang and Michael P. Teter. Kinetic-energy functional of the electron density. *Phys. Rev. B*, 45:13196–13220, Jun 1992.

[88] Enrico Smargiassi and Paul A. Madden. Orbital-free kinetic-energy functionals for first-principles molecular dynamics. *Phys. Rev. B*, 49:5220–5226, Feb 1994.

[89] Yan Alexander Wang, Niranjan Govind, and Emily A. Carter. Orbital-free kinetic-energy functionals for the nearly free electron gas. *Phys. Rev. B*, 58:13465–13471, Nov 1998.

[90] Michael Foley and Paul A. Madden. Further orbital-free kinetic-energy functionals for ab initio molecular dynamics. *Phys. Rev. B*, 53:10589–10598, Apr 1996.

[91] Yan Alexander Wang, Niranjan Govind, and Emily A. Carter. Orbital-free kinetic-energy density functionals with a density-dependent kernel. *Phys. Rev. B*, 60:16350–16358, Dec 1999.

[92] T. G. White, S. Richardson, B. J. B. Crowley, L. K. Pattison, J. W. O. Harris, and G. Gregori. Orbital-free density-functional theory simulations of the dynamic structure factor of warm dense aluminum. *Phys. Rev. Lett.*, 111:175002, Oct 2013.

[93] Y. H. Ding, A. J. White, S. X. Hu, O. Certik, and L. A. Collins. Ab initio studies on the stopping power of warm dense matter with time-dependent orbital-free density functional theory. *Phys. Rev. Lett.*, 121:145001, Oct 2018.

[94] Ilgyou Shin, Ashwin Ramasubramaniam, Chen Huang, Linda Hung, and Emily A Carter. Orbital-free density functional theory simulations of dislocations in aluminum. *Philosophical Magazine*, 89(34-36):3195–3213, 2009.

[95] Shubin Liu and Paul W. Ayers. Functional derivative of noninteracting kinetic energy density functional. *Phys. Rev. A*, 70:022501, Aug 2004.

[96] Robert van Leeuwen and Evert Jan Baerends. Energy expressions in density-functional theory using line integrals. *Phys. Rev. A*, 51:170–178, Jan 1995.

[97] Alex P Gaiduk, Sergey K Chulkov, and Viktor N Staroverov. Reconstruction of Density Functionals from KohnSham Potentials by Integration along Density Scaling Paths. *Journal of Chemical Theory and Computation*, 5(4):699–707, 2009.

[98] M. Pearson, E. Smargiassi, and P. A. Madden. Ab initio molecular dynamics with an orbital-free density functional. *Journal of Physics: Condensed Matter*, 5(19):3221–3240, 1993.

[99] P. Hohenberg and W. Kohn. Inhomogeneous electron gas. *Phys. Rev.*, 136:B864–B871, Nov 1964.

[100] W. Jones and W. H. Young. Density functional theory and the von Weizsäcker method. *Journal of Physics C: Solid State Physics*, 4(11):1322–1330, 1971.

[101] T. D. Newton and E. P. Wigner. Localized states for elementary systems. *Rev. Mod. Phys.*, 21:400–406, Jul 1949.

[102] Tom Lancaster and Stephen J Blundell. *Quantum field theory for the gifted amateur*. Oxford University Press, Oxford, 2014.

[103] Michael E Peskin and Daniel V Schroeder. *An introduction to quantum field theory*. Westview, Boulder, CO, 1995.

[104] Mark (Anthony Mark) Fox. *Optical properties of solids / Mark Fox.* Oxford master series in physics ; 3. Condensed matter physics. Oxford University Press, Oxford [U.K.] ;, second edition. edition, 2010.

[105] Claude Cohen-Tannoudji, Jacques Dupont-Roc, and Gilbert Grynberg. *Photons and atoms: introduction to quantum electrodynamics*. Wiley, New York, NY, 1989. Trans. of : Photons et atomes. Paris, InterEditions, 1987.

[106] A. Vukics, G. Kónya, and P. Domokos. The gauge-invariant Lagrangian, the Power–Zienau–Woolley picture, and the choices of field momenta in nonrelativistic quantum electrodynamics. *Scientific Reports*, 11(1):1–11, 2021.

[107] M Babiker, Rodney Loudon, and George William Series. Derivation of the Power-Zienau-Woolley Hamiltonian in quantum electrodynamics by gauge transformation. *Proceedings of the Royal Society of London. A. Mathematical and Physical Sciences*, 385(1789):439–460, 1983.

[108] Vasil Rokaj, Davis M Welakuh, Michael Ruggenthaler, and Angel Rubio. Light–matter interaction in the long-wavelength limit: no ground-state without dipole self-energy. *Journal of Physics B: Atomic, Molecular and Optical Physics*, 51(3):34005, jan 2018.

[109] Jun John Sakurai and Jim Napolitano. *Modern quantum mechanics; 2nd ed.* Addison-Wesley, San Francisco, CA, 2011.

[110] Luca Pierantoni, Davide Mencarelli, and Tullio Rozzi. A new 3-d transmission line matrix scheme for the combined schrÖdinger–maxwell problem in the electronic/electromagnetic characterization of nanodevices. *IEEE Transactions on Microwave Theory and Techniques*, 56(3):654–662, 2008.

[111] Shinichiro Ohnuki, Takashi Takeuchi, Tokuei Sako, Yoshito Ashizawa, Katsuji Nakagawa, and Masahiro Tanaka. Coupled analysis of maxwell-schrödinger equations by using the length gauge: harmonic model of a nanoplate subjected to a 2d electromagnetic field. *International journal of numerical modelling electronic networks, devices and fields.*, 26(6), 2013-11.

[112] Iftikhar Ahmed, Eng Huat Khoo, Erping Li, and Raj Mittra. A hybrid approach for solving coupled maxwell and schrödinger equations arising in the simulation of nano-devices. *IEEE Antennas and Wireless Propagation Letters*, 9:914–917, 2010.

[113] Ludwig Silberstein. Elektromagnetische grundgleichungen in bivektorieller behandlung. *Annalen der Physik*, 327(3):579–586, 1907.

[114] Ludwig Silberstein. Nachtrag zur abhandlung über elektromagnetische grundgleichungen in bivektorieller behandlung". *Annalen der Physik*, 329(14):783–784, 1907.

[115] Iwo Bialynicki-Birula. V Photon Wave Function. volume 36 of *Progress in Optics*, pages 245–294. Elsevier, 1996.

[116] Iwo Bialynicki-Birula and Zofia Bialynicka-Birula. The role of the Riemann–Silberstein vector in classical and quantum theories of electromagnetism. *Journal of Physics A: Mathematical and Theoretical*, 46(5):53001, jan 2013.

[117] René Jestädt, Michael Ruggenthaler, Micael J T Oliveira, Angel Rubio, and Heiko Appel. Light-matter interactions within the Ehrenfest–Maxwell–Pauli–Kohn–Sham framework: fundamentals, implementation, and nano-optical applications. *Advances in Physics*, 68(4):225–333, 2019.

[118] Adam Kiejna. Stabilized jellium—simple model for simple-metal surfaces. *Progress in Surface Science*, 61(5):85–125, 1999.

[119] K. Jakobi. 3.1.1.2 the jellium model: Datasheet from landolt-börnstein - group iii condensed matter · volume 24b: "electronic and vibrational properties" in springermaterials (https://doi.org/10.1007/10086058_8). Copyright 1994 Springer-Verlag Berlin Heidelberg.

[120] Alejandro Varas, Pablo García-González, Johannes Feist, F. J. García-Vidal, and Angel Rubio. Quantum plasmonics: from jellium models to ab initio calculations. *Nanophotonics*, 5(3):409–426, 2016.

[121] W. Ekardt. Dynamical polarizability of small metal particles: Self-consistent spherical jellium background model. *Phys. Rev. Lett.*, 52:1925–1928, May 1984.

[122] M. J. Puska, R. M. Nieminen, and M. Manninen. Electronic polarizability of small metal spheres. *Phys. Rev. B*, 31:3486–3495, Mar 1985.

[123] W. Ekardt. Size-dependent photoabsorption and photoemission of small metal particles. *Phys. Rev. B*, 31:6360–6370, May 1985.

[124] W. Ekardt. Collective multipole excitations in small metal particles: Critical angular momentum l^{cr} for the existence of collective surface modes. *Phys. Rev. B*, 32:1961–1970, Aug 1985.

[125] D. E. Beck. Self-consistent calculation of the eigenfrequencies for the electronic excitations in small jellium spheres. *Phys. Rev. B*, 35:7325–7333, May 1987.

[126] Jorge Zuloaga, Emil Prodan, and Peter Nordlander. Quantum Description of the Plasmon Resonances of a Nanoparticle Dimer. *Nano Letters*, 9(2):887–891, 2009.

[127] D C Marinica, A K Kazansky, P Nordlander, J Aizpurua, and A G Borisov. Quantum Plasmonics: Nonlinear Effects in the Field Enhancement of a Plasmonic Nanoparticle Dimer. *Nano Letters*, 12(3):1333–1339, 2012.

[128] T. V. Teperik, P. Nordlander, J. Aizpurua, and A. G. Borisov. Robust subnanometric plasmon ruler by rescaling of the nonlocal optical response. *Phys. Rev. Lett.*, 110:263901, Jun 2013.

[129] Tatiana V. Teperik, Peter Nordlander, Javier Aizpurua, and Andrei G. Borisov. Quantum effects and nonlocality in strongly coupled plasmonic nanowire dimers. *Opt. Express*, 21(22):27306–27325, Nov 2013.

[130] Lorenzo Stella, Pu Zhang, F J García-Vidal, Angel Rubio, and P García-González. Performance of Nonlocal Optics When Applied to Plasmonic Nanostructures. *The Journal of Physical Chemistry C*, 117(17):8941–8949, 2013.

[131] Vlasta. Bonacic-Koutecky, Piercarlo. Fantucci, and Jaroslav. Koutecky. Quantum chemistry of small clusters of elements of groups Ia, Ib, and IIa: fundamental concepts, predictions, and interpretation of experiments. *Chemical Reviews*, 91(5):1035–1108, 1991.

[132] Seth M Morton, Daniel W Silverstein, and Lasse Jensen. Theoretical Studies of Plasmonics using Electronic Structure Methods. *Chemical Reviews*, 111(6):3962–3994, 2011.

[133] Luke Bhan, Cody Covington, and Kálmán Varga. Signatures of atomic structure in subfemtosecond laser-driven electron dynamics in nanogaps. *Phys. Rev. B*, 105:085416, Feb 2022.

[134] M. E. J. (Mark E. J.) Newman. *Computational physics*. [Createspace], Place of publication not identified, 2012.

[135] J G Muga, J P Palao, B Navarro, and I L Egusquiza. Complex absorbing potentials. *Physics Reports*, 395(6):357–426, 2004.

[136] David E. Manolopoulos. Derivation and reflection properties of a transmission-free absorbing potential. *The Journal of Chemical Physics*, 117(21):9552–9559, 11 2002.

[137] Cody Covington, Justin Malave, and Kálmán Varga. Coupled maxwell and time-dependent orbital-free density functional calculations. *Phys. Rev. B*, 103:075119, Feb 2021.

[138] J. Itatani, J. Lavesque, D. Zeidler, Hiromichi Niikura, H. Pépin, J. C. Kieffer, P. B. Corkum, and D. M. Villeneuve. Tomographic imaging of molecular orbitals. *Nature*, 432(7019):867–871, 2004.

[139] Brian K. McFarland, Joseph P. Farrell, Philip H. Bucksbaum, and Markus Gühr. High harmonic generation from multiple orbitals in n¡sub¿2¡/sub¿. *Science*, 322(5905):1232–1235, 2008.

[140] A. Baltuška, Th. Udem, M. Uiberacker, M. Hentschel, E. Goulielmakis, Ch. Gohle, R. Holzwarth, V. S. Yakovlev, A. Scrinzi, T. W. Hänsch, and F. Krausz. Attosecond control of electronic processes by intense light fields. *Nature*, 421(6923):611–615, Feb 2003.

[141] Shambhu Ghimire, Anthony D. Dichiara, Emily Sistrunk, Pierre Agostini, Louis F. Dimauro, and David A. Reis. Observation of high-order harmonic generation in a bulk crystal. *Nature Physics*, 7(2):138–141, 2011.

[142] D. Golde, T. Meier, and S. W. Koch. High harmonics generated in semiconductor nanostructures by the coupled dynamics of optical inter- and intraband excitations. *Phys. Rev. B*, 77:075330, Feb 2008.

[143] G. Vampa, C. R. McDonald, G. Orlando, D. D. Klug, P. B. Corkum, and T. Brabec. Theoretical analysis of high-harmonic generation in solids. *Phys. Rev. Lett.*, 113:073901, Aug 2014.

[144] Takuya Higuchi, Mark I. Stockman, and Peter Hommelhoff. Strong-field perspective on high-harmonic radiation from bulk solids. *Phys. Rev. Lett.*, 113:213901, Nov 2014.

[145] Mengxi Wu, Shambhu Ghimire, David A. Reis, Kenneth J. Schafer, and Mette B. Gaarde. High-harmonic generation from bloch electrons in solids. *Phys. Rev. A*, 91:043839, Apr 2015.

[146] Georges Ndabashimiye, Shambhu Ghimire, Mengxi Wu, Dana A. Browne, Kenneth J. Schafer, Mette B. Gaarde, and David A. Reis. Solid-state harmonics beyond the atomic limit. *Nature*, 534(7608):520–523, 2016.

[147] Lun Yue and Mette B. Gaarde. Introduction to theory of high-harmonic generation in solids: tutorial. *J. Opt. Soc. Am. B*, 39(2):535–555, Feb 2022.

[148] V. E. Nefedova, S. Fröhlich, F. Navarrete, N. Tancogne-Dejean, D. Franz, A. Hamdou, S. Kaassamani, D. Gauthier, R. Nicolas, G. Jargot, M. Hanna, P. Georges, M. F. Ciappina, U. Thumm, W. Boutu, and H. Merdji. Enhanced extreme ultraviolet high-harmonic generation from chromium-doped magnesium oxide. *Applied Physics Letters*, 118(20):201103, 05 2021.

[149] Naotaka Yoshikawa, Tomohiro Tamaya, and Koichiro Tanaka. High-harmonic generation in graphene enhanced by elliptically polarized light excitation. *Science*, 356(6339):736–738, 2017.

[150] Hanzhe Liu, Yilei Li, Yong Sing You, Shambhu Ghimire, Tony F. Heinz, and David A. Reis. High-harmonic generation from an atomically thin semiconductor. *Nature Physics*, 13(3):262–265, 2017.

[151] Hassan A. Hafez, Sergey Kovalev, Jan Christoph Deinert, Zoltán Mics, Bertram Green, Nilesh Awari, Min Chen, Semyon Germanskiy, Ulf Lehnert, Jochen Teichert, Zhe Wang, Klaas Jan Tielrooij, Zhaoyang Liu, Zongping Chen, Akimitsu Narita, Klaus Müllen, Mischa Bonn, Michael Gensch, and Dmitry Turchinovich. Extremely efficient terahertz high-harmonic generation in graphene by hot Dirac fermions. *Nature*, 561(7724):507–511, 2018.

[152] O. Schubert, M. Hohenleutner, F. Langer, B. Urbanek, C. Lange, U. Huttner, D. Golde, T. Meier, M. Kira, S. W. Koch, and R. Huber. Sub-cycle control of terahertz high-harmonic generation by dynamical Bloch oscillations. *Nature Photonics*, 8(2):119–123, 2014.

[153] Yong Sing You, David A. Reis, and Shambhu Ghimire. Anisotropic high-harmonic generation in bulk crystals. *Nature Physics*, 13(4):345–349, 2017.

[154] Jeffrey L. Krause, Kenneth J. Schafer, and Kenneth C. Kulander. High-order harmonic generation from atoms and ions in the high intensity regime. *Phys. Rev. Lett.*, 68:3535–3538, Jun 1992.

[155] K. J. Schafer, Baorui Yang, L. F. DiMauro, and K. C. Kulander. Above threshold ionization beyond the high harmonic cutoff. *Phys. Rev. Lett.*, 70:1599–1602, Mar 1993.

[156] P. B. Corkum. Plasma perspective on strong field multiphoton ionization. *Phys. Rev. Lett.*, 71:1994–1997, Sep 1993.

[157] Paul B. Corkum. Recollision physics. *Physics Today*, 64(3):36–41, 03 2011.

[158] M. Lewenstein, Ph. Balcou, M. Yu. Ivanov, Anne L'Huillier, and P. B. Corkum. Theory of high-harmonic generation by low-frequency laser fields. *Phys. Rev. A*, 49:2117–2132, Mar 1994.

[159] W. L. Schaich. Calculations of second-harmonic generation for a jellium metal surface. *Phys. Rev. B*, 61:10478–10483, Apr 2000.

[160] A. T. Georges and N. E. Karatzas. Theory of multiple harmonic generation in reflection from a metal surface. *Applied Physics B: Lasers and Optics*, 81(4):479–485, 2005.

[161] Xin-Qiang Wang and Xue-Bin Bian. Model-potential method for high-order harmonic generation in monolayer graphene. *Phys. Rev. A*, 103:053106, May 2021.

[162] A A Romanov, A A Silaev, T S Sarantseva, M V Frolov, and N V Vvedenskii. Simulation of High Harmonic Generation in Xenon Based on Time-Dependent Density-Functional Theory. *Journal of Physics: Conference Series*, 2249(1):12005, apr 2022.

[163] Roi Baer, Daniel Neuhauser, Petra R. Ždánská, and Nimrod Moiseyev. Ionization and high-order harmonic generation in aligned benzene by a short intense circularly polarized laser pulse. *Phys. Rev. A*, 68:043406, Oct 2003.

[164] Jie Liu, Zhenyu Guo, Jin Sun, and Wanzhen Liang. Theoretical studies on electronic spectroscopy and dynamics with the real-time time-dependent density functional theory. *Frontiers of Chemistry in China*, 5(1):11–28, 2010.

[165] Emmanuel Penka Fowe and Andre D. Bandrauk. Nonlinear time-dependent density-functional-theory study of ionization and harmonic generation in co_2 by ultrashort intense laser pulses: Orientational effects. *Phys. Rev. A*, 81:023411, Feb 2010.

[166] Shunsuke Yamada, Tomohito Otobe, David Freeman, Anatoli Kheifets, and Kazuhiro Yabana. Propagation effects in high-harmonic generation from dielectric thin films. *Phys. Rev. B*, 107:035132, Jan 2023.

[167] Shambhu Ghimire and David A. Reis. High-harmonic generation from solids. *Nature Physics*, 15(1):10–16, 2019.

[168] Murat Sivis, Marco Taucer, Giulio Vampa, Kyle Johnston, André Staudte, Andrei Yu. Naumov, D M Villeneuve, Claus Ropers, and P B Corkum. Tailored semiconductors for high-harmonic optoelectronics. *Science*, 357(6348):303–306, 2017.

[169] Seunghwoi Han, Hyunwoong Kim, Yong Woo Kim, Young-Jin Kim, Seungchul Kim, In-Yong Park, and Seung-Woo Kim. High-harmonic generation by field enhanced femtosecond pulses in metal-sapphire nanostructure. *Nature Communications*, 7(1):13105, Oct 2016.

[170] G. Vampa, B. G. Ghamsari, S. Siadat Mousavi, T. J. Hammond, A. Olivieri, E. Lisicka-Skrek, A. Yu Naumov, D. M. Villeneuve, A. Staudte, P. Berini, and P. B. Corkum. Plasmon-enhanced high-harmonic generation from silicon. *Nature Physics*, 13(7):659–662, Jul 2017.

[171] Nicolas Tancogne-Dejean and Angel Rubio. Atomic-like high-harmonic generation from two-dimensional materials. *Science Advances*, 4(2):eaao5207, 2018.

[172] Baojing Zhou, Yan Alexander Wang, and Emily A. Carter. Transferable local pseudopotentials derived via inversion of the kohn-sham equations in a bulk environment. *Phys. Rev. B*, 69:125109, Mar 2004.

[173] Chen Huang and Emily A Carter. Transferable local pseudopotentials for magnesium{,} aluminum and silicon. *Phys. Chem. Chem. Phys.*, 10(47):7109–7120, 2008.

[174] Chen Huang and Emily A. Carter. Nonlocal orbital-free kinetic energy density functional for semiconductors. *Phys. Rev. B*, 81:045206, Jan 2010.

[175] Beatriz G del Rio, Johannes M Dieterich, and Emily A Carter. Globally-Optimized Local Pseudopotentials for (Orbital-Free) Density Functional Theory Simulations of Liquids and Solids. *Journal of Chemical Theory and Computation*, 13(8):3684–3695, 2017.

[176] Jan-Christoph Deinert, David Alcaraz Iranzo, Raúl Pérez, Xiaoyu Jia, Hassan A Hafez, Igor Ilyakov, Nilesh Awari, Min Chen, Mohammed Bawatna, Alexey N Ponomaryov, Semyon Germanskiy, Mischa Bonn, Frank H L Koppens, Dmitry Turchinovich, Michael Gensch, Sergey Kovalev, and Klaas-Jan Tielrooij. Grating-Graphene Metamaterial as a Platform for Terahertz Nonlinear Photonics. *ACS Nano*, 15(1):1145–1154, 2021.

[177] Xiao-Yuan Wu, Hao Liang, Xiao-Shuang Kong, Qihuang Gong, and Liang-You Peng. Enhancement of high-order harmonic generation in two-dimensional materials by plasmonic fields. *Phys. Rev. A*, 103:043117, Apr 2021.

[178] Joel D. Cox, Andrea Marini, and F. Javier García de Abajo. Plasmon-assisted high-harmonic generation in graphene. *Nature Communications*, 8(1):14380, Feb 2017.

[179] I. Pupeza, M. Högner, J. Weitenberg, S. Holzberger, D. Esser, T. Eidam, J. Limpert, A. Tünnermann, E. Fill, and V. S. Yakovlev. Cavity-enhanced high-harmonic generation with spatially tailored driving fields. *Phys. Rev. Lett.*, 112:103902, Mar 2014.

[180] A. K. Mills, S. Zhdanovich, M. X. Na, F. Boschini, E. Razzoli, M. Michiardi, A. Sheyerman, M. Schneider, T. J. Hammond, V. Süss, C. Felser, A. Damascelli, and D. J. Jones. Cavity-enhanced high harmonic generation for extreme ultraviolet time- and angle-resolved photoemission spectroscopy. *Review of Scientific Instruments*, 90(8):083001, 08 2019.

[181] Haihua Liu, Thomas E. Gage, Prem Singh, Amit Jaiswal, Richard D. Schaller, Jau Tang, Sang Tae Park, Stephen K. Gray, and Ilke Arslan. Visualization of plasmonic couplings using ultrafast electron microscopy. *Nano Letters*, 21(13):5842–5849, Jul 2021.

[182] Howard DeVoe. Optical Properties of Molecular Aggregates. I. Classical Model of Electronic Absorption and Refraction. *The Journal of Chemical Physics*, 41(2):393–400, 07 2004.

[183] Edward M. Purcell and Carlton R. Pennypacker. Scattering and Absorption of Light by Nonspherical Dielectric Grains. , 186:705–714, December 1973.

[184] Bruce T. Draine and Piotr J. Flatau. Discrete-dipole approximation for scattering calculations. *J. Opt. Soc. Am. A*, 11(4):1491–1499, Apr 1994.

[185] M A Yurkin and A G Hoekstra. The discrete dipole approximation: An overview and recent developments. *Journal of Quantitative Spectroscopy and Radiative Transfer*, 106(1):558–589, 2007.

[186] Otto Laporte and William F. Meggers. Some rules of spectral structure∗. *J. Opt. Soc. Am.*, 11(5):459–463, Nov 1925.

[187] David J. Griffiths and Darrell F. Schroeter. *Introduction to Quantum Mechanics*. Cambridge University Press, 3 edition, 2018.

[188] A. Perot and Charles Fabry. On the Application of Interference Phenomena to the Solution of Various Problems of Spectroscopy and Metrology. , 9:87, February 1899.

[189] Anonymous. Proceedings of the american physical society. *Phys. Rev.*, 69:674–674, Jun 1946.

[190] Mikhail V. Rybin, Sergei F. Mingaleev, Mikhail F. Limonov, and Yuri S. Kivshar. Purcell effect and lamb shift as interference phenomena. *Scientific Reports*, 6(1):20599, Feb 2016.

[191] Serge Haroche and Daniel Kleppner. Cavity Quantum Electrodynamics. *Physics Today*, 42(1):24–30, 01 1989.

[192] Herbert Walther, Benjamin T H Varcoe, Berthold-Georg Englert, and Thomas Becker. Cavity quantum electrodynamics. *Reports on Progress in Physics*, 69(5):1325, apr 2006.

[193] E.T. Jaynes and F.W. Cummings. Comparison of quantum and semiclassical radiation theories with application to the beam maser. *Proceedings of the IEEE*, 51(1):89–109, 1963.

[194] Thomas W Ebbesen. Hybrid Light–Matter States in a Molecular and Material Science Perspective. *Accounts of Chemical Research*, 49(11):2403–2412, 2016.

[195] Arkajit Mandal, Michael Taylor, Braden Weight, Eric Koessler, Xinyang Li, and Pengfei Huo. Theoretical advances in polariton chemistry and molecular cavity quantum electrodynamics. *ChemRxiv*, 2022.

[196] D. N. Basov, Ana Asenjo-Garcia, P. James Schuck, Xiaoyang Zhu, and Angel Rubio. Polariton panorama. *Nanophotonics*, 10(1):549–577, 2020.

[197] Davis M. Welakuh and Prineha Narang. Tunable nonlinearity and efficient harmonic generation from a strongly coupled light–matter system. *ACS Photonics*, 10(2):383–393, Feb 2023.

[198] Kuidong Wang, Marcus Seidel, Kalaivanan Nagarajan, Thibault Chervy, Cyriaque Genet, and Thomas Ebbesen. Large optical nonlinearity enhancement under electronic strong coupling. *Nature Communications*, 12(1):1486, Mar 2021.

[199] Anton Frisk Kockum, Vincenzo MacRì, Luigi Garziano, Salvatore Savasta, and Franco Nori. Frequency conversion in ultrastrong cavity QED. *Scientific Reports*, 7(1), dec 2017.

[200] Johannes Flick and Prineha Narang. Ab initio polaritonic potential-energy surfaces for excited-state nanophotonics and polaritonic chemistry. *The Journal of Chemical Physics*, 153(9):094116, 09 2020.

[201] James A. Hutchison, Andrea Liscio, Tal Schwartz, Antoine Canaguier-Durand, Cyriaque Genet, Vincenzo Palermo, Paolo Samorì, and Thomas W. Ebbesen. Tuning the work-function via strong coupling. *Advanced Materials*, 25(17):2481–2485, 2013.

[202] Dominik Sidler, Christian Schäfer, Michael Ruggenthaler, and Angel Rubio. Polaritonic Chemistry: Collective Strong Coupling Implies Strong Local Modification of Chemical Properties. *The Journal of Physical Chemistry Letters*, 12(1):508–516, 2021.

[203] Johannes Feist and Francisco J. Garcia-Vidal. Extraordinary exciton conductance induced by strong coupling. *Phys. Rev. Lett.*, 114:196402, May 2015.

[204] R. Balili, V. Hartwell, D. Snoke, L. Pfeiffer, and K. West. Bose-einstein condensation of microcavity polaritons in a trap. *Science*, 316(5827):1007–1010, 2007.

[205] Johannes Schachenmayer, Claudiu Genes, Edoardo Tignone, and Guido Pupillo. Cavity-enhanced transport of excitons. *Phys. Rev. Lett.*, 114:196403, May 2015.

[206] Bo Xiang, Raphael F. Ribeiro, Matthew Du, Liying Chen, Zimo Yang, Jiaxi Wang, Joel Yuen-Zhou, and Wei Xiong. Intermolecular vibrational energy transfer enabled by microcavity strong light–matter coupling. *Science*, 368(6491):665–667, 2020.

[207] Lorenz S. Cederbaum. Polaritonic states of matter in a rotating cavity. *The Journal of Physical Chemistry Letters*, 12(26):6056–6061, Jul 2021.

[208] Chen Li. Exact Analytical Solution of the Ground-State Hydrogenic Problem with Soft Coulomb Potential. *Journal of Physical Chemistry A*, 125(23):5146–5151, jun 2021.

[209] Michael Ruggenthaler, Johannes Flick, Camilla Pellegrini, Heiko Appel, Ilya V. Tokatly, and Angel Rubio. Quantum-electrodynamical density-functional theory: Bridging quantum optics and electronic-structure theory. *Phys. Rev. A*, 90:012508, Jul 2014.

[210] Tor S. Haugland, Enrico Ronca, Eirik F. Kjønstad, Angel Rubio, and Henrik Koch. Coupled cluster theory for molecular polaritons: Changing ground and excited states. *Phys. Rev. X*, 10:041043, Dec 2020.

[211] Chenhang Huang, Alexander Ahrens, Matthew Beutel, and Kálmán Varga. Two electrons in harmonic confinement coupled to light in a cavity. *Phys. Rev. B*, 104:165147, Oct 2021.

[212] Thomas W. Ebbesen. Hybrid light–matter states in a molecular and material science perspective. *Accounts of Chemical Research*, 49(11):2403–2412, Nov 2016.

[213] Raphael F Ribeiro, Luis A Martínez-Martínez, Matthew Du, Jorge Campos-Gonzalez-Angulo, and Joel Yuen-Zhou. Polariton chemistry: controlling molecular dynamics with optical cavities. *Chem. Sci.*, 9(30):6325–6339, 2018.

[214] Denis G. Baranov, Battulga Munkhbat, Elena Zhukova, Ankit Bisht, Adriana Canales, Benjamin Rousseaux, Göran Johansson, Tomasz J. Antosiewicz, and Timur Shegai. Ultrastrong coupling between nanoparticle plasmons and cavity photons at ambient conditions. *Nature Communications*, 11(1):2715, Jun 2020.

[215] Pengfei Yang, Xiuwen Xia, Hai He, Shaokang Li, Xing Han, Peng Zhang, Gang Li, Pengfei Zhang, Jingping Xu, Yaping Yang, and Tiancai Zhang. Realization of nonlinear optical nonreciprocity on a few-photon level based on atoms strongly coupled to an asymmetric cavity. *Phys. Rev. Lett.*, 123:233604, Dec 2019.

[216] William Huie, Shankar G. Menon, Hannes Bernien, and Jacob P. Covey. Multiplexed telecommunication-band quantum networking with atom arrays in optical cavities. *Physical Review Research*, 3, 12 2021.

[217] Stephan Ritter, Christian Nölleke, Carolin Hahn, Andreas Reiserer, Andreas Neuzner, Manuel Uphoff, Martin Mücke, Eden Figueroa, Joerg Bochmann, and Gerhard Rempe. An elementary quantum network of single atoms in optical cavities. *Nature*, 484(7393):195–200, Apr 2012.

[218] Christian Schäfer, Michael Ruggenthaler, and Angel Rubio. Ab initio nonrelativistic quantum electrodynamics: Bridging quantum chemistry and quantum optics from weak to strong coupling. *Phys. Rev. A*, 98:043801, Oct 2018.

[219] Tor S. Haugland, Christian Schäfer, Enrico Ronca, Angel Rubio, and Henrik Koch. Intermolecular interactions in optical cavities: An ab initio QED study. *The Journal of Chemical Physics*, 154(9):094113, 03 2021.

[220] Johannes Flick, Christian Schäfer, Michael Ruggenthaler, Heiko Appel, and Angel Rubio. Ab Initio Optimized Effective Potentials for Real Molecules in Optical Cavities: Photon Contributions to the Molecular Ground State. *ACS Photonics*, 5(3):992–1005, 2018.

[221] Christian Schäfer, Michael Ruggenthaler, Heiko Appel, and Angel Rubio. Modification of excitation and charge transfer in cavity quantum-electrodynamical chemistry. *Proceedings of the National Academy of Sciences*, 116(11):4883–4892, 2019.

[222] Dominik Sidler, Christian Schäfer, Michael Ruggenthaler, and Angel Rubio. Polaritonic chemistry: Collective strong coupling implies strong local modification of chemical properties. *The Journal of Physical Chemistry Letters*, 12(1):508–516, Jan 2021.

[223] Justin Malave, Alexander Ahrens, Daniel Pitagora, Cody Covington, and Kálmán Varga. Real-space, real-time approach to quantum-electrodynamical time-dependent density functional theory. *The Journal of Chemical Physics*, 157(19):194106, 11 2022.

[224] K. Hennessy, A. Badolato, M. Winger, D. Gerace, M. Atatüre, S. Gulde, S. Fält, E. L. Hu, and A. Imamoğlu. Quantum nature of a strongly coupled single quantum dot–cavity system. *Nature*, 445(7130):896–899, Feb 2007.

[225] C. Monroe. Quantum information processing with atoms and photons. *Nature*, 416(6877):238–246, Mar 2002.

[226] Hoi-Kwong Lo and H. F. Chau. Unconditional security of quantum key distribution over arbitrarily long distances. *Science*, 283(5410):2050–2056, Mar 1999.

[227] H. J. Kimble. The quantum internet. *Nature*, 453(7198):1023–1030, Jun 2008.

[228] J.L. McHale. *Molecular Spectroscopy*. CRC Press, 2017.

[229] D Solovyev, V K Dubrovich, and G Plunien. Investigation of the electromagnetically induced transparency in the era of cosmological hydrogen recombination. *Journal of Physics B: Atomic, Molecular and Optical Physics*, 45(21):215001, sep 2012.

[230] Stephen E. Harris. Electromagnetically Induced Transparency. *Physics Today*, 50(7):36–42, 07 1997.

[231] Yong-Chun Liu, Bei-Bei Li, and Yun-Feng Xiao. No Title. *Nanophotonics*, 6(5):789–811, 2017.

[232] S. Weinberg. *Lectures on Quantum Mechanics*. Cambridge University Press, 2015.

[233] Natsuki Kanda, Tomohiro Imahoko, Koji Yoshida, Akihiro Tanabashi, A. Amani Eilanlou, Yasuo Nabekawa, Tetsumi Sumiyoshi, Makoto Kuwata-Gonokami, and Katsumi Midorikawa. Opening a new route to multiport coherent xuv sources via intracavity high-order harmonic generation. *Light: Science & Applications*, 9(1):168, Sep 2020.

[234] M Kretschmar, M J J Vrakking, and B Schütte. Intense XUV pulses from a compact HHG setup using a single harmonic. *Journal of Physics B: Atomic, Molecular and Optical Physics*, 54(20):20LT01, nov 2021.

[235] B. Major, O. Ghafur, K. Kovács, K. Varjú, V. Tosa, M. J. J. Vrakking, and B. Schütte. Compact intense extreme-ultraviolet source. *Optica*, 8(7):960–965, Jul 2021.

[236] François Labaye, Maxim Gaponenko, Norbert Modsching, Pierre Brochard, Clément Paradis, Stéphane Schilt, Valentin Johannes Wittwer, and Thomas Südmeyer. Xuv sources based on intra-oscillator high harmonic generation with thin-disk lasers: Current status and prospects. *IEEE Journal of Selected Topics in Quantum Electronics*, 25(4):1–19, 2019.

[237] S Sebban, A Depresseux, E Oliva, J Gautier, F Tissandier, J Nejdl, M Kozlova, G Maynard, J P Goddet, A Tafzi, A Lifschitz, H T Kim, S Jacquemot, P Rousseau, P Zeitoun, and A Rousse. Toward compact and ultra-intense laser-based soft x-ray lasers. *Plasma Physics and Controlled Fusion*, 60(1):14030, nov 2017.

[238] Baojing Zhou and Emily A. Carter. First principles local pseudopotential for silver: Towards orbital-free density-functional theory for transition metals. *The Journal of Chemical Physics*, 122(18):184108, 05 2005.

[239] Chen Huang and Emily A. Carter. Toward an orbital-free density functional theory of transition metals based on an electron density decomposition. *Phys. Rev. B*, 85:045126, Jan 2012.

[240] Youqi Ke, Florian Libisch, Junchao Xia, Lin-Wang Wang, and Emily A. Carter. Angular-momentum-dependent orbital-free density functional theory. *Phys. Rev. Lett.*, 111:066402, Aug 2013.

[241] Youqi Ke, Florian Libisch, Junchao Xia, and Emily A. Carter. Angular momentum dependent orbital-free density functional theory: Formulation and implementation. *Phys. Rev. B*, 89:155112, Apr 2014.

[242] Qiang Xu, Cheng Ma, Wenhui Mi, Yanchao Wang, and Yanming Ma. Nonlocal pseudopotential energy density functional for orbital-free density functional theory. *Nature Communications*, 13(1):1385, Mar 2022.

[243] Deena Roller, Andrew M. Rappe, Leeor Kronik, and Olle Hellman. Finite difference interpolation for reduction of grid-related errors in real-space pseudopotential density functional theory. *Journal of Chemical Theory and Computation*, 19(13):3889–3899, Jul 2023.

[244] Harry Dember. Über eine photoelektronische kraft in kupferoxydul-kristallen. *Z. Phys*, 32:554, 1931.

[245] V. Apostolopoulos and M. E. Barnes. THz emitters based on the photo-Dember effect. *Journal of Physics D: Applied Physics*, 47(37), 2014.

[246] M. E. Barnes, S. A. Berry, P. Gow, D. McBryde, G. J. Daniell, H. E. Beere, D. A. Ritchie, and V. Apostolopoulos. Investigation of the role of the lateral photo-dember effect in the generation of terahertz radiation using a metallic mask on a semiconductor. *Opt. Express*, 21(14):16263–16272, Jul 2013.

[247] Chang-Hua Liu, You-Chia Chang, Seunghyun Lee, Yaozhong Zhang, Yafei Zhang, Theodore B. Norris, and Zhaohui Zhong. Ultrafast lateral photo-dember effect in graphene induced by nonequilibrium hot carrier dynamics. *Nano Letters*, 15(6):4234–4239, Jun 2015.

[248] G. Klatt, F. Hilser, W. Qiao, M. Beck, R. Gebs, A. Bartels, K. Huska, U. Lemmer, G. Bastian, M.B. Johnston, M. Fischer, J. Faist, and T. Dekorsy. Terahertz emission from lateral photo-dember currents. *Opt. Express*, 18(5):4939–4947, Mar 2010.

[249] Rasheed Shaik, Hari R. Varma, Mohamed El-Amine Madjet, Fulu Zheng, Thomas Frauenheim, and Himadri S. Chakraborty. Plasmonic resonant intercluster coulombic decay. *Phys. Rev. Lett.*, 130:233201, Jun 2023.

[250] S. Barth, S. Joshi, S. Marburger, V. Ulrich, A. Lindblad, G. Öhrwall, O. Björneholm, and U. Hergenhahn. Observation of resonant Interatomic Coulombic Decay in Ne clusters. *The Journal of Chemical Physics*, 122(24):241102, 06 2005.

[251] Alexei Halpin, Christiaan Mennes, Arkabrata Bhattacharya, and Jaime Gómez Rivas. Visualizing near-field coupling in terahertz dolmens. *Applied Physics Letters*, 110(10):101105, 03 2017.

[252] Valentin Flauraud, Gabriel D. Bernasconi, Jeremy Butet, Massimo Mastrangeli, Duncan T. L. Alexander, Olivier J. F. Martin, and Jürgen Brugger. Mode evolution in strongly coupled plasmonic dolmens fabricated by templated assembly. *ACS Photonics*, 4(7):1661–1668, Jul 2017.

[253] Vladimir A. Goncharov and Kalman Varga. Real-space, real-time calculation of dynamic hyperpolarizabilities. *The Journal of Chemical Physics*, 137(9):094111, 09 2012.

[254] Hannes Hübener, Umberto De Giovannini, Christian Schäfer, Johan Andberger, Michael Ruggenthaler, Jerome Faist, and Angel Rubio. Engineering quantum materials with chiral optical cavities. *Nature Materials*, 20(4):438–442, Apr 2021.